Characterisation of freshly emitted mineral dust aerosols determined by scanning electron microscopy

Insights from in situ measurements at source locations

Zur Erlangung des Grades eines Doktors der Naturwissenschaften (Dr. rer. nat.)
Genehmigte Dissertation von Agnesh Panta aus Nawalparasi, Nepal
Tag der Einreichung: 19.07.2023, Tag der Prüfung: 31.08.2023

1. Referent: Prof. Dr. Konrad Kandler
2. Referent: Prof. Dr. Carlos Pérez García-Pando
Prüfer: Prof. Dr. Moritz Bigalke
Prüfer: Prof. Dr. Christoph Schüth
Vorsitzender: Prof. Dr. Andreas Henk
Darmstadt, Technische Universität Darmstadt

TECHNISCHE UNIVERSITÄT DARMSTADT

Fachbereich Material- und Geowissenschaften
Institut für Angewandte Geowissenschaften
Fachgebiet Atmosphärisches Aerosol

Characterisation of freshly emitted mineral dust aerosols determined by scanning electron microscopy
Insights from in situ measurements at source locations

Genehmigte Dissertation von Agnesh Panta

Tag der Einreichung: 19.07.2023
Tag der Prüfung: 31.08.2023

Darmstadt, Technische Universität Darmstadt

बालुवाका दानालाई सानो भनौ भने एक कणमा सूक्ष्मदर्शी यन्त्रले र विज्ञानले विश्वोको झिलिमिली जादूगरी दर्शाइरहेचन।
-लक्ष्मीप्रसाद देवकोटा (के नेपाल सानो छ?)

To my family...

Erklärungen laut Promotionsordnung

§ 8 Abs. 1 lit. c PromO

Ich versichere hiermit, dass die elektronische Version meiner Dissertation mit der schriftlichen Version übereinstimmt.

§ 8 Abs. 1 lit. d PromO

Ich versichere hiermit, dass zu einem vorherigen Zeitpunkt noch keine Promotion versucht wurde. In diesem Fall sind nähere Angaben über Zeitpunkt, Hochschule, Dissertationsthema und Ergebnis dieses Versuchs mitzuteilen.

§ 9 Abs. 1 PromO

Ich versichere hiermit, dass die vorliegende Dissertation selbstständig und nur unter Verwendung der angegebenen Quellen verfasst wurde.

§ 9 Abs. 2 PromO

Die Arbeit hat bisher noch nicht zu Prüfungszwecken gedient.

Darmstadt, 19.07.2023

A. Panta

Preface

The study presented herein was conducted as part of the FRontiers in dust minerAloGical coMposition and its Effects upoN climate (FRAGMENT) project. The project has received funding from the European Research Council (ERC) under the Horizon 2020 research and innovation programme via the ERC Consolidator Grant. FRAGMENT aims to understand the global mineralogical composition of soil dust aerosols and their impact on climate. Earth System Models typically assume a uniform composition of dust aerosols, but regional variations in mineralogy are known to influence their effect. However, limited knowledge of global soil mineral content and incomplete understanding of particle size distribution hinder the representation of global dust mineralogy. The project will use an ensemble of measurement campaigns to understand the size-resolved mineralogy of dust at emission and its relationship with parent soil. It will also evaluate available remote hyperspectral imaging to improve knowledge of global soil mineral content. Finally, the project will generate integrated knowledge of the role of dust mineralogy in dust-radiation, dust-chemistry, and dust-cloud interactions based on modeling experiments constrained with theoretical innovations and field measurements.

The work conducted for this thesis was part of two intensive measurement campaigns carried out under the FRAGMENT project. The first intensive campaign took place in 2019 at the edge of the Sahara desert in Morocco, while the second campaign was conducted in the Dyngjunsandur desert of Iceland in 2021. Both of these locations are a major source of freshly emitted mineral dust. The primary objective of this thesis was to utilize computer-controlled scanning electron microscopy (SEM) with energy-dispersive X-ray analysis for mineral dust research. This involved particle sampling using various instrumentation, as well as complementing single particle analysis with results from other techniques.

The first FRAGMENT campaign was coordinated by Barcelona Supercomputing Center with Spanish National Research Council (CSIC) and Technical University of Darmstadt (TUDa) the main partner. There was collaboration with Karlsruhe Institute of Technology (KIT), National Aeronautics and Space Administration (NASA), Planetary Science Institute

(PSI), Desert Research Institute (DRI), and National Research Institute for Agriculture, Food and Environment (INRAE). The different groups had their own objectives and focused on the different optical, physical, and chemical properties of the freshly emitted dust and parent soil.

The second FRAGMENT campaign took place in Iceland. This time it was a joint effort with with projects funded by German Science Foundation (HiLDA), Helmholtz Association of German Research Centers (Helmholtz Young Investigator Group on Mineral Dust), NASA (EMIT), Icelandic Centre for Research (Rannís), Czech Science Foundation (GACR), and National Power Company of Iceland (Landsvirkjun). During the intensive campaign, more than 50 state-of-the-art and custom built instruments were deployed on one main site and multiple sub-sites to investigate the aerosol composition, soil properties and processes that govern dust emission and long-range transport towards the High Arctic and Europe along with its influence on the earth's climate.

List of publications in the scope of and with contribution to or from this work:

Panta, A., Kandler, K., Alastuey, A., González-Flórez, C., González-Romero, A., Klose, M., Querol, X., Reche, C., Yus-Díez, J., and Pérez García-Pando, C.: Insights into the single-particle composition, size, mixing state, and aspect ratio of freshly emitted mineral dust from field measurements in the Moroccan Sahara using electron microscopy, *Atmospheric Chemistry and Physics*, https://doi: 10.5194/acp-23-3861-2023.

Panta, A., Kandler, K., Schepanski, K., Alastuey, A., González-Flórez, C., González-Romero, A., Klose, M., Querol, X., Reche, C., Yus-Díez, J., and Pérez García-Pando, C.: Electron microscopy of freshly emitted Icelandic dust: insights into particle chemistry, size, shape, and mixing state, *in preparation for submission to a peer-reviewed journal*

González-Flórez, C., Klose, M., Alastuey, A., Dupont, S., Escribano, J., Etyemezian, V., Gonzalez-Romero, A., Huang, Y., Kandler, K., Nikolich, G., **Panta, A.**, Querol, X., Reche, C., Yus-Díez, J., Pérez García-Pando, C.: Insights into the size-resolved dust emission from field measurements in the Moroccan Sahara, *Atmospheric Chemistry and Physics*, https://doi.org/10.5194/acp-23-7177-2023.

González-Romero, A., González-Flórez, C., **Panta, A.**, Yus-Díez, J., Reche, C., Córdoba. P., Alastuey, A., Kandler, K., Klose, M., Baldo, C., Clark, R.N., Shi, Z., Querol, X. and and Pérez García-Pando, C.: Variability in grain size, mineralogy, and mode of occurrence of Fe in surface sediments of preferential dust-source inland drainage basins: The case of the Lower Drâa Valley, S Morocco, *under review in Atmospheric Chemistry and Physics* https://doi.org/10.5194/egusphere-2023-1120.

Results were presented as

Oral Presentation

- Emission partitioning between desert soils and mineral dust based on single particle analysis data. Forschungsseminar 2019, Darmstadt
- Characterization of freshly emitted mineral dust using electron microscopy. Forschungsseminar 2022, Darmstadt

Poster Presentation

- American Geophysical Union Fall Meeting, December 1-17, 2020, online
- International Atmospheric Chemistry Conference, September 11-15, 2022, Manchester, UK

Abstract

Mineral dust is a key component of the Earth system, affecting the radiation balance, cloud properties, biogeochemical cycles and impacting atmospheric circulation, air quality, aviation, and solar energy generation. Understanding of these processes is currently limited by a lack of in situ measurements resulting in a large uncertainty in the chemical, microphysical, optical, and radiative properties of mineral dust.

This thesis presents an analysis of dust measurements obtained during the FRontiers in dust minerAloGical coMposition and its Effects upoN climaTe (FRAGMENT) campaigns which took place in August-September 2019 over Southern Morocco and August-September 2021 over Iceland. Samples are collected for offline analysis using SEM/EDX and are used to provide insights into the chemical composition, particle size distribution (PSD), mixing state, and the shape and morphology of airborne dust. It focuses on the description and comparison of dust samples from northern Africa (Morocco) and high-latitude region (Iceland) which are the two distinct source regions.

Moroccan dust particles are mineralogically dominated by (alumino) silicates such as clay minerals, quartz, and feldspar with varying amounts of carbonates, and iron-bearing minerals. An exhaustive analysis of the PSD and potential mixing state of different particle types is made, focusing largely on iron-rich (Fe oxide-hydroxides) and feldspar particles, which are key to the effects of dust upon radiation and clouds, respectively. Nearly pure or externally mixed Fe oxide-hydroxides are present mostly in diameters smaller than 2 µm, with the highest fraction below 1 µm at about 3.75 % abundance by mass. Fe oxide-hydroxides tend to be increasingly internally mixed with other minerals, especially clays, as particle size increases; i.e., the volume fraction of Fe oxide-hydroxides in aggregates decreases with particle size. Pure (externally mixed) feldspar represented 3.2 % of all the particles by mass, of which an estimation of about a 10th is K-feldspar. The externally mixed total feldspar and K-feldspar abundances are relatively invariant with particle size, in contrast to the increasing abundance of feldspar-like (internally mixed) aggregates with particle size with mass fractions ranging from 5 % to 18 %. The median aspect ratio is

rather constant across particle size and mineral groups, although slightly higher aspect ratios for internally mixed particles is observed.

Icelandic dust particles are heterogeneous in size, shape, and elemental composition, with particle group medium aluminium silicates (most probably glass-like) making up the largest fraction across all size ranges (35 % - 93 % by volume). Sulfate particles were found on few of the samples, suggesting volcanic emission contribution to the aerosol load. Fe-rich and Ti-rich particles represented 3.5 % and 1.8 % respectively of the particle volume and were present mainly in the fine fraction. Particle median aspect ratio is observed to be size dependent and increases with particle size. The overall composition was consistent between the main studied area and the regional outflow areas except for one specific location which was rather less affected by the local emission.

This work highlights that at an individual particle level Moroccan (Saharan) dust and Icelandic dust have some key differences. Icelandic dust shows elevated levels of Fe and Ca and slightly reduced Al compared to Moroccan dust. A major difference was the almost absence of K in Icelandic dust particles, whereas it is detected in the Moroccan dust particles. Further, the Fe contribution to the single particles was observed to be higher compared to the Moroccan dust with median Fe index of 0.1 for Icelandic dust and 0.06 for Moroccan dust. The median aspect ratio of the particles varied between 1.34 to 1.67, increasing as particle size increased. This is in contrast with Moroccan dust where the median aspect ratio was 1.46 and showed little dependence with size. However, the overall shape distribution is observed to be rather similar between Icelandic and Saharan dust.

Single-particle analysis in this work shows that dust particles are mostly internally mixed, predominantly aspherical, and morphologically complex. Many Earth system models still assume globally uniform mineralogical composition or oversimplified compositional and physical parameters and therefore introduce errors in the assessment of regional forcing of dust. The detailed information on the chemical composition and morphology of freshly emitted individual dust particles and quantitative analysis of their mixing state presented here can be used to constrain climate models including mineral species in their representation of the dust cycle.

Zusammenfassung

Mineralstaub ist eine Schlüsselkomponente des Erdsystems. Die Hebung, der Transport und die Ablagerung von Mineralstaub beeinflussen das Klima durch Strahlungseffekte und durch die Ablagerung von Staub im Ozean. Das Verständnis dieser Prozesse ist derzeit durch einen Mangel an In-situ-Messungen begrenzt, was zu einer großen Unsicherheit in Bezug auf die chemischen, mikrophysikalischen, optischen und Strahlungseigenschaften von Mineralstaub führt.

Diese Arbeit stellt eine Analyse von Staubmessungen vor, die während der FRontiers in dust minerAloGical coMposition and its Effects upoN climaTe (FRAGMENT) Kampagnen durchgeführt wurden, die im August-September 2019 über Südmarokko und im August-September 2021 über Island stattfanden. Die Proben werden für Offline-Analysen mit SEM/EDX gesammelt und dienen dazu, Einblicke in die chemische Zusammensetzung, die Partikelgrößenverteilung (PSD), den Mischungszustand sowie die Form und Morphologie von luftgetragenem Staub zu gewinnen. Der Schwerpunkt liegt auf der Beschreibung und dem Vergleich von Staubproben aus zwei unterschiedlichen Herkunftsregionen, Nordafrika (Marokko) und den hohen Breitengraden (Island).

Die marokkanischen Staubpartikel bestehen mineralogisch überwiegend aus (Alumino-)Silikaten wie Tonmineralien, Quarz und Feldspat mit unterschiedlichen Mengen an Karbonaten und eisenhaltigen Mineralien. Es wird eine umfassende Analyse der PSD und des potenziellen Mischungszustands verschiedener Partikeltypen durchgeführt, wobei der Schwerpunkt auf eisenreichen (Fe-Oxid-Hydroxide) und Feldspatpartikeln liegt, die für die Auswirkungen des Staubs auf die Strahlung bzw. die Wolken entscheidend sind. Nahezu reine oder extern gemischte Fe-Oxid-Hydroxide sind meist in Durchmessern kleiner als 2 µm vorhanden, wobei der höchste Anteil unter 1 µm bei etwa 3.75 % Massenanteil liegt. Fe-Oxid-Hydroxide neigen dazu mit zunehmender Pratikelgröße intern mit anderen Mineralien, insbesondere Tonen, sich zu vermischen, d. h. der Volumenanteil von Fe-Oxid-Hydroxiden in Aggregaten nimmt mit der Partikelgröße ab. Reiner (extern gemischter) Feldspat machte 3.2 % der Masse aller Partikel aus, von denen schätzungsweise etwa ein

Zehntel K-Feldspat ist. Die Häufigkeit von extern gemischtem Feldspat und K-Feldspat ist mit der Partikelgröße relativ unveränderlich, während die Häufigkeit von feldspatähnlichen (intern gemischten) Aggregaten mit der Partikelgröße zunimmt, wobei die Massenanteile von 5 % bis 18 % reichen. Das mittlere Aspektverhältnis ist über die Partikelgröße und Mineralgruppen hinweg ziemlich konstant, obwohl bei intern gemischten Partikeln ein etwas höheres Aspektverhältnis beobachtet wird.

Die isländischen Staubpartikel sind hinsichtlich Größe, Form und elementarer Zusammensetzung heterogen, wobei die Partikelgruppe der mittleren Aluminiumsilikate (höchstwahrscheinlich glasartig) über alle Größenbereiche hinweg den größten Anteil ausmacht (35 % - 93 % nach Volumen). Sulfatpartikel wurden in wenigen Proben gefunden, was auf einen Beitrag vulkanischer Emissionen zur Aerosolbelastung schließen lässt. Fe-reiche und Ti-reiche Partikel machten 3.5 % bzw. 1.8 % des Partikelvolumens aus und waren hauptsächlich in der Feinfraktion vorhanden. Außerdem wurde beobachtet, dass der Eisenanteil in den einzelnen Partikeln intern mit den Silikatphasen vermischt ist. Das mediane Aspektverhältnis der Partikel ist größenabhängig und nimmt mit der Partikelgröße zu. Die Gesamtzusammensetzung war zwischen dem Hauptuntersuchungsgebiet und den regionalen Ausströmungsgebieten konsistent, mit Ausnahme eines bestimmten Ortes, der von der lokalen Emission weniger betroffen war.

Diese Arbeit unterstreicht, dass marokkanischer (Sahara-)Staub und isländischer Staub auf der Ebene der einzelnen Partikel eine relativ ähnliche elementare Zusammensetzung, aber eine grundlegend andere Mineralogie aufweisen, was auf die unterschiedlichen geologischen Ausgangssedimente zurückzuführen ist. Hinsichtlich der Fe-Verteilung auf die Partikel wurden Unterschiede zwischen isländischem und marokkanischem Staub festgestellt. Die allgemeine Formverteilung von isländischem und saharischem Staub ist recht ähnlich, obwohl eine Abhängigkeit von der Größe bei isländischem Staub, nicht aber bei marokkanischem Staub beobachtet wird.

Die Einzelpartikelanalyse in dieser Arbeit zeigt, dass Staubpartikel meist intern gemischt, überwiegend asphärisch und morphologisch komplex sind. Viele Erdsystemmodelle gehen immer noch von einer global einheitlichen mineralogischen Zusammensetzung oder von zu stark vereinfachten Zusammensetzungs- und physikalischen Parametern aus und führen daher zu Fehlern bei der Bewertung des regionalen Einflusses von Staub. Die hier vorgestellten detaillierten Informationen über die chemische Zusammensetzung und Morphologie einzelner, frisch emittierter Staubpartikel und die quantitative Analyse ihres Mischungszustands können verwendet werden, um Klimamodelle einzuschränken, die mineralische Arten in ihre Darstellung des Staubkreislaufs einbeziehen.

Table of Contents

Preface vii

1 Introduction 1
- 1.1 Introduction . . . 1
- 1.2 Atmospheric aerosols . . . 1
- 1.3 FRAGMENT project . . . 3
- 1.4 Motivation and overview of the thesis . . . 5

2 Basics 9
- 2.1 Aeolian dust . . . 9
  - 2.1.1 Dust cycle . . . 9
  - 2.1.2 Dust sources . . . 11
    - 2.1.2.1 Mineral dust from warm desert regions . . . 11
    - 2.1.2.2 High-latitude dust . . . 13
- 2.2 Aerosol particle size distribution . . . 15
- 2.3 Dust diameter types . . . 15
- 2.4 Mixing state . . . 17
- 2.5 Climate effects . . . 18
  - 2.5.1 Interactions with radiation . . . 19
  - 2.5.2 Interactions with the clouds . . . 21
  - 2.5.3 Interactions with atmospheric chemistry . . . 23
  - 2.5.4 Interactions with the cryosphere . . . 24
  - 2.5.5 Interactions with biogeochemistry . . . 25
- 2.6 Dust observations . . . 27

3 Material and Methods 31
- 3.1 Particle sampling . . . 31
  - 3.1.1 Flat plate sampler . . . 31
  - 3.1.2 Cascade impactor . . . 32

3.1.3 Free-wing impactor . . . 32
3.1.4 Ancillary data . . . 33
3.2 Analysis . . . 33
3.2.1 Scanning Electron Miscroscopy (SEM) coupled with Energy dispersive spectrometry (EDX) . . . 33
3.2.2 Automated single particle analysis in SEM . . . 36
3.2.3 Particle classification method . . . 37
3.2.4 Particle morphology characterization . . . 38
3.2.4.1 Aspect Ratio . . . 38
3.2.4.2 Projected-area and volume-equivalent diameters . . . 38
3.3 Determining the size distributions from the freewing impactor measurements 40
3.4 Calculation of the feldspar indices . . . 41

4 Results and Discussion – Part 1: Morocco 43
4.1 Study area . . . 43
4.2 Particle classes . . . 44
4.2.1 Oxides/Hydroxides . . . 46
4.2.2 Quartz-like and complex quartz-like . . . 46
4.2.3 Feldspar-like and pure feldspar abundance . . . 46
4.2.4 Ca-rich . . . 47
4.2.5 Clay minerals . . . 47
4.2.6 Other silicates . . . 47
4.2.7 Mixtures and other . . . 48
4.2.8 Sulfates . . . 48
4.2.9 Silicate composition . . . 48
4.3 Comparison of PSD of different techniques for particle collection . . . 49
4.4 Particle composition . . . 50
4.4.1 Particle abundances using different techniques . . . 54
4.4.2 Temporal variability . . . 56
4.4.3 Iron distribution . . . 58
4.4.4 Feldspar . . . 62
4.5 Particle shape . . . 63

5 Results and Discussion – Part 2: Iceland 67
5.1 Study area and sampling sites . . . 67
5.2 Particle-type characterization . . . 68
5.2.1 Medium Al mixed silicates . . . 69
5.2.2 Silicate mixtures . . . 70

5.2.3 Iron-rich particles . . . 70
5.2.4 Pyroxene/amphibole-like . . . 71
5.2.5 Sulfate . . . 71
5.3 Relative Abundances of Various Types of Particles . . . 72
5.4 Iron distribution in Icelandic dust . . . 73
5.5 Particle shape . . . 75
5.6 Composition at Outflow Regions . . . 78
5.7 Discussion . . . 80
5.7.1 Aerosol composition . . . 80
5.7.2 Iron distribution . . . 81
5.7.3 Particle shape . . . 82
5.7.4 Comparison with Saharan dust . . . 83

6 Conclusions and Further Work **87**
6.1 Summary and conclusions . . . 87
6.2 Suggestions for future work . . . 89

Appendix **93**

List of Figures **105**

List of Tables **113**

Bibliography **117**

Acknowledgement **147**

1 Introduction

1.1 Introduction

Between 1900s to 2017, the Earth's average temperature increased by approximately 1°C (likely between 0.8°C and 1.2°C) and is increasing at 0.2°C (likely between 0.1°C and 0.3°C) per decade (IPCC, 2018). This increase in temperature is a response to a perturbation in the energy balance of the Earth's top-of-atmosphere energy budget. Two of the most important causes of this perturbation are greenhouse gases, and atmospheric aerosols.

Greenhouse gases act to absorb and emit infrared radiation back towards the Earth's surface, thereby causing a net warming. Mineral dust (one of atmospheric aerosol type), however, depending on their composition and particle size distribution (PSD), are able to reflect solar radiation back out to space, causing a cooling, or absorb solar and infrared radiation, which can have a warming effect. These processes are known as the direct radiative effect (DRE). Recent study has reported a net dust DRE of -0.15 ± 0.35 W m^{-2}, meaning that the dust DRE could either slightly warm or substantially cool the planet, or it could have little net impact (Kok et al., 2023). This is in contrast to a net positive DRE of 3.32 ± 0.29 W m^{-2} (IPCC, 2018) from well-mixed greenhouse gases which causes warming. Therefore, the investigation of airborne mineral dust requires further attention to quantify its role in global climate.

1.2 Atmospheric aerosols

Atmospheric aerosols are defined as solid or liquid particles suspended in a gas (Seinfeld & Pandis, 2016). They can be natural or anthropogenic in origin. Windblown desert dust are one example of natural aerosol species. Other examples of natural aerosols include sea salt, volcanic ash, smoke from forest fires, sea salt, and water droplets. Anthropogenic aerosol sources can include combustion of fuels, industrial enterprises, agriculture (soil plowing,

planned burning out of forests), etc. Figure 1.1 depicts the distribution of these different aerosols which is a model simulation by supercomputers of the National Aeronautics and Space Administration (NASA).

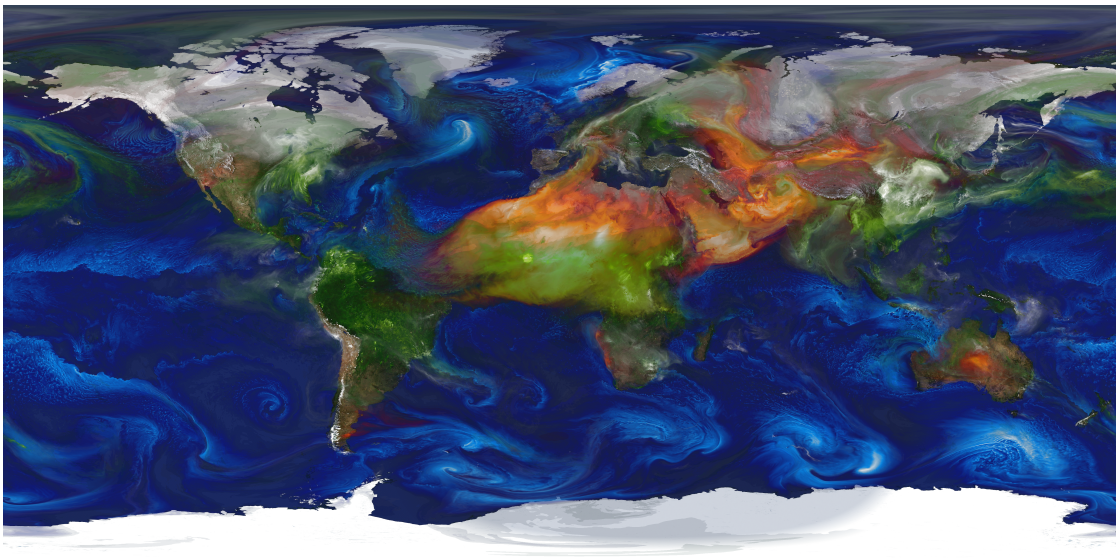

Figure 1.1: Model simulation showing four essential aerosol types and their global occurrence: mineral dust from deserts (orange/red), sea salt (blue), organics and black carbon from fires (green) and sulfates from fossil fuel combustion and volcanoes (white). This simulation used GEOS-5 and the Goddard Chemistry Aerosol Radiation and Transport (GOCART) Model. Image from: http://svs.gsfc.nasa.gov/30637.

Mineral dust, as one of the most important natural aerosols in the atmosphere, is a key player in influencing the global climate system (Shao et al., 2011). It is the most abundant aerosol type in terms of mass (Choobari et al., 2014; Textor et al., 2006), with an estimated emission flux between 3400 and 8900 Tg yr^{-1} for particles smaller than 20 µm geometric diameter (Kok et al., 2021b). In particular, Northern Africa is responsible for an estimated 50 % of global windblown mineral dust emissions (Engelstaedter et al., 2006; Kok et al., 2021a). Dust affects directly the Earth's radiative budget via scattering and absorption of radiation (Pérez et al., 2006; Sokolik et al., 2001; Strong et al., 2018), and indirectly by influencing cloud development on a microphysical level by acting as cloud condensation nuclei and ice nuclei (Froyd et al., 2022; Hoose & Möhler, 2012; Kumar et al., 2011b; Zimmermann et al., 2008), and thus impacting cloud optical properties and radiation. Once uplifted over the source areas, dust can travel thousands of kilometers away from these and can act as a carrier for micronutrients, such as iron and phosphorous,

to the ocean (Jickells et al., 2005; Myriokefalitakis et al., 2022; Rodríguez et al., 2021; Schulz et al., 2012) and the Amazon rainforest (Yu et al., 2015), with implications for biogeochemical cycles and ocean uptake of atmospheric carbon dioxide by promoting phytoplankton growth (Mahowald et al., 2009). Additionally, dust can be deposited on snow or ice thereby reducing snow/ice reflectance (surface darkening) and consequently changing the climate and water cycle by accelerating snow melting (Painter et al., 2010; Sarangi et al., 2020). Dust can also interact with air pollutants by acting as a catalyst and providing a surface for heterogeneous reactions (Cwiertny et al., 2008; Ndour et al., 2008). Finally, dust might negatively impact human health (Giannadaki et al., 2014; Pérez García-Pando et al., 2014; Querol et al., 2019), induce a decrease in solar energy yield by dust deposition to solar panels (Piedra & Moosmüller, 2017), and negatively impact aircraft operations due to reduced visibility (Middleton, 2017; Monteiro et al., 2022). Most of these processes rely not only on the total mass of dust but also on its microphysical properties and mineral composition (Mahowald et al., 2014).

1.3 FRAGMENT project

Soil dust aerosols are mixtures of different minerals, whose relative abundances, particle size distribution (PSD), shape, surface topography and mixing state influence their effect upon climate. At present, Earth System models represent poorly the local/regional variations in dust mineral composition mainly because 1) our knowledge of the global soil-surface mineralogical composition is limited due to a lack of observations, and 2) there is an incomplete understanding of the emitted dust PSD in terms of its constituent minerals that results from the fragmentation of soil aggregates during wind erosion. The first challenge is being tackled by the Earth Surface Mineral Dust Source Investigation (EMIT), which uses a hyperspectral sensor mounted to the exterior of the International Space Station (ISS) to determine the mineral composition of natural sources that produce dust aerosols around the world. The second challenge is to be tackled by the project **FR**ontiers in dust miner**A**lo**G**ical co**M**position and its **E**ffects upo**N** clima**T**e (FRAGMENT). It is a European Research Council Consolidator Grant project with the aim to fundamentally advance the treatment of dust mineralogy in earth system models by fulfilling the following objectives as shown in Fig. 1.2:

Objective 1: Contribute new fundamental understanding to reduce the large uncertainties in the emitted dust PSD. This will be achieved by evaluating and extending current theoretical paradigms based on an ensemble of coordinated measurement field campaigns and laboratory analyses. Additionally, the study will address the size-resolved mineralogy

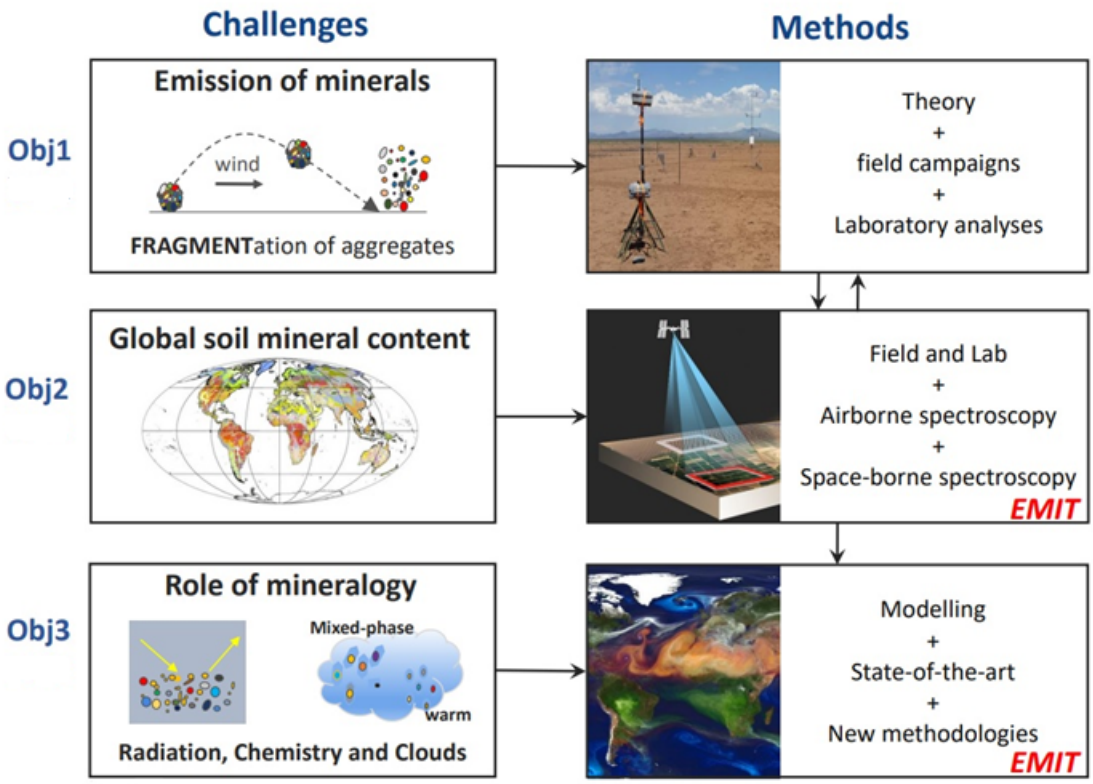

Figure 1.2: Conceptual scheme of FRAGMENT with the three objectives (Obj. 1, Obj. 2, and Obj. 3). Image credit: C. Pérez García-Pando, principal investigator of FRAGMENT.

of dust at emission and its relationship with the parent soil, both experimentally and theoretically.

Objective 2: To obtain precise knowledge of dust mineral content, more detailed and widespread measurements of soil mineralogy are necessary. Available airborne and space-borne hyperspectral imaging will be evaluated and utilized to improve global atlases of soil mineralogy for dust modelling. The methods and understanding developed in this study will anticipate the future innovation of retrieving soil mineralogy through high-quality spaceborne hyperspectral measurements.

Objective 3: Although the potential impact of dust mineralogy on climate is significant, the interconnection of mechanisms has been overlooked in the few models that account for

mineral variations. The study aims to generate comprehensive and quantitative knowledge of how dust mineral composition affects atmospheric radiation, chemistry, and clouds by conducting modelling experiments that incorporate theoretical innovations and field measurements.

With these three objectives, the overarching goal of FRAGMENT is then to understand, constrain and calculate the global mineralogical composition of dust along with its effects upon climate.

1.4 Motivation and overview of the thesis

Why should we care about the details of the atmospheric aerosols? Studying aerosols is very interesting simply from a chemistry and physics perspective, but they have many relevant effects as outlined in the section above. Despite their potentially large relevance, aerosols still pose one of the largest uncertainties in our understanding of aerosol-climate interactions. The impacts of mineral dust aerosols on the Earth's climate system depend largely on the physical (PSD, particle shape and morphology) and chemical (mineralogy, mixing state) properties of the dust. Therefore, a detailed characterization of different mineral dust types is necessary for its implementation in climate models that consider mineralogical variations. Many earth system models assume that mineral dust aerosol have a globally uniform composition (Myhre et al., 2013; Stocker et al., 2013), despite the fact that there are local and regional variations in the mineralogical composition of the sources (Claquin et al., 1999; Journet et al., 2014; Nickovic et al., 2012). Most of the modelling studies have focused on constraining dust sources (Ginoux et al., 2001; Tegen et al., 2002; Zender et al., 2003b), emission (Cakmur et al., 2006), and PSD (Cakmur et al., 2006; Mahowald et al., 2014; Tegen & Lacis, 1996). While this minimal representation has led to great advances in dust and climate research over the past decade, the omission of dust mineralogy has hindered further understanding the role of dust aerosols in the Earth system.

The chemical and mineralogical composition of atmospheric mineral dust can be characterized by a variety of sampling and analytical techniques (Rodríguez et al., 2012), having their own advantages and limitations. The bulk composition of mineral dust (and its parent sediments) can be given as a mineralogical composition primarily determined by X-ray diffraction (XRD) or as a chemical composition determined by different analytical techniques such as Atomic Absorption Spectroscopy (AAS), Inductively Coupled Plasma Mass Spectrometry (ICP-MS), X-ray Fluorescence analysis (XRF), Proton Induced X-ray Emission (PIXE), among others.

Besides the above-mentioned bulk analytical techniques giving bulk composition, the properties of the individual particles can be of particular interest, as several properties could differ considerably on a particle-to particle basics. There are different approaches available for single particle measurement, namely single particle mass spectrometry e.g., aerosol time-of-flight mass spectrometry (ATOFMS) (Fitzgerald et al., 2015), optical and electron microscopy including scanning electron microscopy (SEM) and transmission electron microscopy (TEM), X-ray microscopy, etc., all of which have advantages and limitations (Li et al., 2016).

The major dust source regions in the world includes low-latitude dust (mostly 0–35°N), high-latitude dust ($\geq$ 50°N and $\geq$ 40°S) (Meinander et al., 2022), and the so-called "global dust belt" (Prospero et al., 2002), referring to dusty source regions stretching from the northern Africa over the Middle East, central, and East Asia and southwestern North America (Ginoux et al., 2012). Figure 1.3 displays some of the major hot-spots for dust emission. The intensive field campaign conducted within the framework of this thesis is located at two of the major dust source region and is marked by a star symbol. The measurements were carried out between 03 September - 01 October 2019 in Morocco and between 08 August - 07 September 2021 in Iceland.

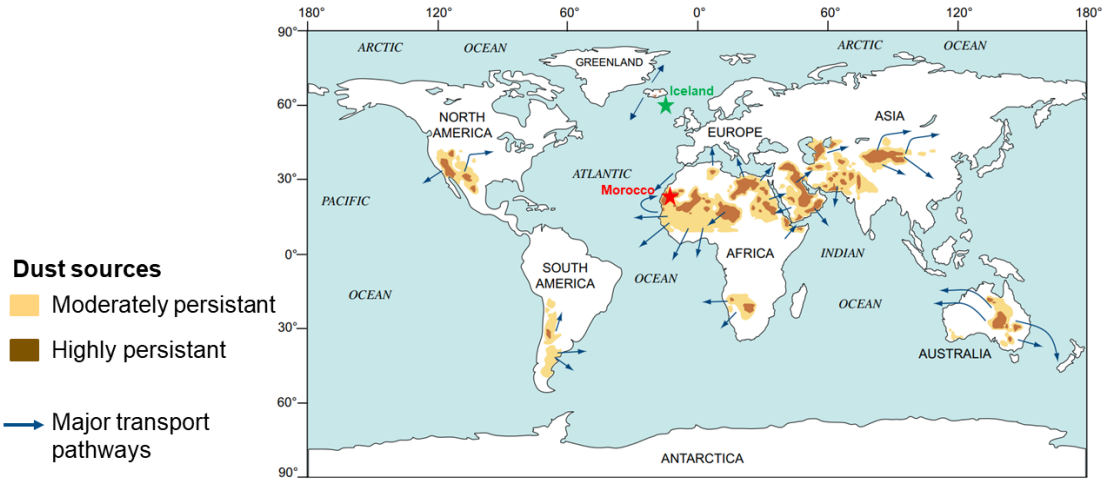

Figure 1.3: Map of the measurement locations, dust sources, and major transport pathways. The study area in Morocco, denoted by red star, is near M'Hamid el Ghizlane, into the Drâa basin at the edge of Sahara desert. The measurement site in Iceland, denoted by green star, is in Dyngjusandur located at the northern edge of the Vatnajökull ice cap where the river Jökulsá á Fjöllum originates. Image adapted from Muhs (2013).

In this work, automated individual particle analysis using SEM coupled with an energy-dispersive X-ray (EDX) is used to determine the size-segregated chemical and physical properties of mineral dust aerosol using measurement data from intensive field campaigns carried out at two distinct source regions:

1. L'Bour, Morocco which is a small ephemeral lake located in the lower Drâa valley of Morocco and lies at the edge of the Sahara approximately 15 km to the west of the small village of M'Hamid El Ghizlane, see Chapter 3.
2. Dyngjusandur, Iceland is one of the most prominent dust source region in Iceland and is located at the northern edge of the Vatnajökull ice cap where the river Jökulsá á Fjöllum originates, see Chapter 4.

The thesis is organized into several chapters, each focusing on a different aspect of the study. Chapter 2 provides an explanation of the fundamental concepts related to mineral dust aerosol. Chapter 3 describes the measurement methods and techniques used in the study. The results of the analysis of Moroccan and Icelandic dust are presented in Chapters 4 and 5, respectively. Finally, Chapter 6 provides a summary of the findings and discusses their implications, as well as outlining potential areas for future research.

The detailed knowledge of individual dust particles generated in this study would potentially help in understanding and constraining the mineralogical composition of dust and its effects upon climate by improved representation of mineral dust in ESM - the overarching goal of the FRAGMENT project of which this thesis is a part.

2 Basics

2.1 Aeolian dust

Mineral dust emission, transport, and deposition caused by the wind are referred to as *aeolian processes*, after the Greek god Aeolus, the keeper of the winds (Kok et al., 2012). Windblown fine sand, silt, and clay are key components in desert, arid-land and sparsely vegetated areas, such as dry lake beds. The global dust loading is estimated to be around 22-29 Tg (Kok et al., 2021a). Approximately 10 Tg yr^{-1} is deposited to the Amazon rainforest (Kok et al., 2021a) as dust mobilized by winds undergoes long range transport following the major wind system (Prospero, 1999; Zhao, Huang et al., 2022). Because of the diurnal behaviour of dust emission, there is a strong temporal and spatial variability in aerosol concentrations.

In the following section, the most important factors concerning Aeolian dust are described.

2.1.1 Dust cycle

Mineral dust in the atmosphere is the dominant aerosol type by mass (Textor et al., 2006) whose diameters can vary in size from less than 1 nm to more than 100 µm in diameter (Mahowald et al., 2014; Ryder et al., 2019; van der Does et al., 2018). The dust cycle (Fig. 2.1) involves three main processes: emission, transport, and the deposition of mineral dust (Shao et al., 2011). Currently, there is a considerable discrepancy between earth system model simulations and observations in representing the dust cycle (Evan et al., 2014; Zhao, Ryder & Wilcox, 2022).

Minerals that are present in the topmost layer of Earth's crust are more prone to physical, chemical, and biological weathering (Christiansen & Hamblin, 2014). Mineral dust is emitted when the surface winds are sufficient to break soil cohesion which usually happens with no vegetation cover and dry soil. Furthermore, human activities due to, for example, urbanization and agriculture may be a source of soil mineral dust or disturb soils and

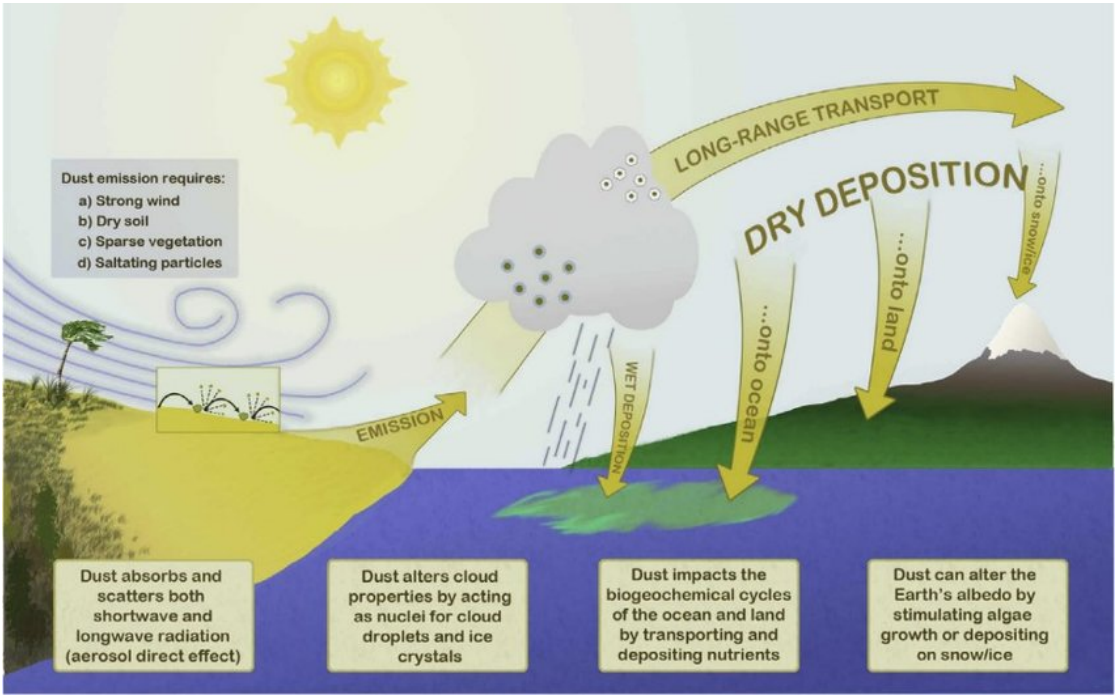

Figure 2.1: Schematic diagram of mineral dust cycle and interactions between dust and climate and biogeochemistry, taken from Mahowald et al. (2014).

enhance wind erosion (Ginoux et al., 2012). The dust production mechanism is based on the physical phenomena such as creeping, saltation, and sandblasting of soil aggregates (Alfaro et al., 1998; Gomes et al., 1990). For the dust to be lifted from the surface, surface winds need to reach a threshold velocity of wind erosion. The value of this wind erosion threshold depends on land-surface conditions like soil moisture, soil texture, roughness length, and particle size, and the presence of obstacles like pebbles, rocks, and vegetation (Gillette & Passi, 1988; Gillette et al., 1980; Marticorena & Bergametti, 1995; Pu et al., 2020; Raupach et al., 1993; Zender et al., 2003a), and this therefore varies spatially and temporally (Helgren & Prospero, 1987; Kurosaki & Mikami, 2007).

The atmospheric lifetime of mineral dust is proportional to particle size; as larger particles are more likely to deposit due to their inertia (Kok et al., 2012) which is governed by the Stokes equation (Stokes, 1901). The settling of larger particles has been observed in various field studies (Denjean et al., 2016; Maring et al., 2003; Ryder et al., 2013b). However, strong winds, turbulence, strong convective clouds, and triboelectrification can

result in long range transport of giant dust particles ($>$ 63 µm) (van der Does et al., 2018; Varga et al., 2021). Furthermore, with increasing distance away from the source, the size distribution changes and the count median diameter shift towards smaller particle size (Kandler et al., 2011a). These changes are often linked with changes in dust mineralogy and morphology (Glaccum & Prospero, 1980; Kandler et al., 2011b; Reid et al., 2003a). In addition, dust originating from north Africa gets deposited into the ocean providing an important source of micronutrients for oceanic phytoplankton (Jickells et al., 2005) and soil in the Amazon rainforest (Bristow et al., 2010). Similarly, Asian dust originating from deserts in China and Mongolia can also undergo long-range transport and could be a potential contributor to the regional climate of Artic (Huang et al., 2015; Zhao, Huang et al., 2022) and tropical north pacific (Duce et al., 1980) as well as impact the environment and human health in Japan (Onishi et al., 2015, 2012) and Taiwan (Kong et al., 2022; Liu et al., 2006).

2.1.2 Dust sources

Large sources for mineral dust are the major wind erosion regions (Shao, 2008), loading the atmosphere with $\sim$ 26 million tonnes of dust (Kok et al., 2023). Hugh troughs and areas with dry loess sediments combined with strong winds are providing material for uplift. The African, American, Australian, Chinese and Mongolian deserts are large sources for mineral dust in the atmosphere. Dust from East Asia dominates the atmospheric load over China and Mongolia, Korea, Japan, and the North Pacific Ocean. But the Saharan Desert and the Sahel is the world's most important source for mineral dust aerosol with $\sim$ 50% of global dust emission ($\sim$ 2100 Tg yr^{-1}) and mass loading of $\sim$ 13 Tg (Kok et al., 2021a). Similarly, the Asian deserts contribute $\sim$ 40 % ($\sim$ 200 Tg yr^{-1} and $\sim$ 10 Tg), and the North American and Southern Hemisphere deserts and high latitude regions another $\sim$ 10 % ($\sim$ 500 Tg yr^{-1} and $\sim$ 3 Tg) (Kok et al., 2021a). Although much of the dust is deposited close to source regions, a substantial fraction is transported vast distances. For example, plumes of African dust regularly travel across the tropical North Atlantic, reaching the southwestern USA and the Amazon Basin.

2.1.2.1 Mineral dust from warm desert regions

Low-latitude deserts are by far the largest contributors to natural dust in the atmosphere with $\sim$ 50, 40, and 10 % of global dust loadings (20 µm in diameter) from North Africa, Asia, and North American and Southern Hemisphere regions, respectively. These areas can be further divided into nine source regions, which include (1) western North Africa,

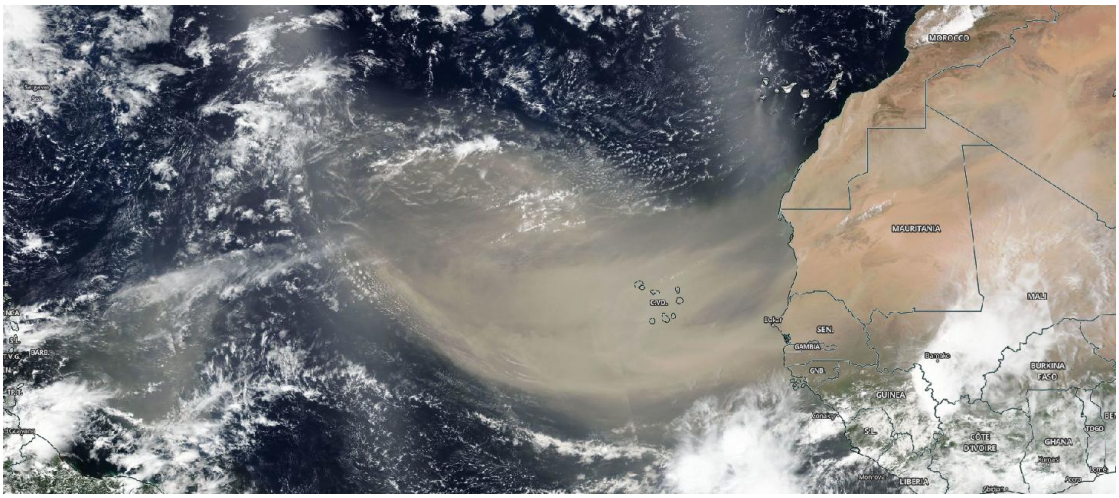

Figure 2.2: Satellite captured image of a Saharan dust plume by the National Aeronautics and Space Administration (NASA)-National Oceanic and Atmospheric Administration (NOAA) Suomi National Polar-orbiting Partnership on June 18, 2020. The dust plume (in light brown) is being transported off the west coast of northern Africa into the Atlantic Ocean. Image and caption obtained from NASA Worldview.

(2) eastern North Africa, (3) the southern Sahara and Sahel, (4) the Middle East and central Asia (which includes the Horn of Africa), (5) East Asia, (6) North America, (7) Australia, (8) South America, and (9) southern Africa.

Despite the fact that mineral dust is generally composed of quartz, clay, feldspar, gypsum, calcite, hematite, and goethite minerals, its chemical and mineralogical composition is still source dependent. For example, illite/kaolinite ratios in the clay fraction of mineral dust have been used to identify dust source regions because dust from northern Africa is known to contain a lower illite/kaolinite ratio (< 2) compared to Asian dust (> 5). Calcite content in mineral dust also varies with source location, as calcite content in dust source regions decreases with increasing annual rainfall. However, the identification of dust source regions based off the mineralogical analysis of collected samples is not always conclusive; instead, satellite imagery and air mass back trajectory models are also used to predict the original sources of atmospheric dust.

2.1.2.2 High-latitude dust

Although hot subtropical deserts are considered the largest contributors to the global dust cycle (Kok et al., 2021a), recent research has identified cold deserts at high latitudes as an important yet neglected dust source (Bullard et al., 2016; Meinander et al., 2022). High-latitude dust (HLD) regions are defined as north of $\geq$ 50 °N and south of $\geq$ 40 °S and include the Arctic as a sub-region $\geq$ 60 °N (Meinander et al., 2022) Model simulations indicate that high-latitude dust (HLD) sources contribute an estimated 1-5 % of global dust emission (Bullard et al., 2016; Groot Zwaaftink et al., 2016; Meinander et al., 2022), while their impact might be much higher due to their presence in an otherwise pristine, but sensitive environment (Schmale et al., 2021). HLD regions include Alaska, Antarctica, Canada, Greenland, Iceland, New Zealand, Patagonia, and Svalbard. In contrast to hot subtropical deserts, HLD is often formed by glaciers during the abrasion by ice over sediments, which can displace, disintegrate, and expose sediments producing fine particles that can be transported by surface winds (Bullard, 2013). HLD source regions cover a significantly smaller land area compared to lower-latitude deserts. However, many HLD sources are located in pro-glacial regions, or regions that are in close proximity to glacier activity. These areas are typically characterised by their cold, dense air with high intensity of turbulence resulting in strong wind speed that are more efficient in suspending particles than the warmer winds of low-latitude regions (Bullard et al., 2016; Neuman, 1993). Moreover, it has been argued that HLD sources associated with glaciers will be increasingly active in the future as temperatures increase and glaciers retreat (Bullard, 2013; Bullard et al., 2016).

In the northern hemisphere, Iceland is a major high-latitude dust source in the Arctic (Arnalds et al., 2001; Arnalds et al., 2016). While Iceland as a whole is humid from a climatological point of view, some regions in the interior are semi-arid due to shielding by the surrounding mountains (Arnalds et al., 2016). Therefore, it is one of the most active aeolian areas on Earth consisting of sandy deserts that undergoes intensive aeolian processes (Arnalds et al., 2001; Arnalds et al., 2016). Glaciers cover about 11 % of Iceland's land surface (Björnsson & Pálsson, 2008). Glacier activity results in the production of glacial sediment of which in particular the fine fraction is transported by glacial meltwater. After drying, these fine sediments are prone to wind erosion (Bullard et al., 2016) and frequently emit dust (Arnalds, 2010; Arnalds et al., 2016). The sandy areas of Iceland have dark surfaces consisting of mostly basaltic volcanic glass (Arnalds et al., 2001). Hence, due to the different geological origin and a different weathering regime compared to lower latitudes with a different climate, the properties of Icelandic dust are significantly different compared to northern African and Asian dust (Baldo et al., 2023, 2020).

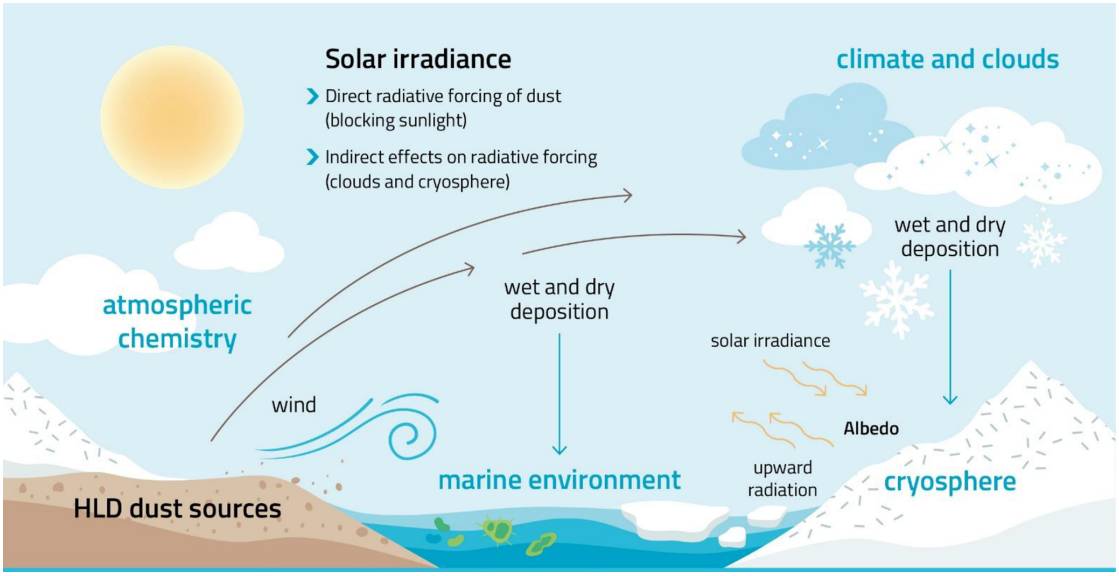

Figure 2.3: Climatic and environmental impacts of HLD include direct radiative forcing (blocking sunlight), indirect radiative forcing (clouds and cryosphere), as well as effects on atmospheric chemistry and the marine environment. Figure and caption taken from Meinander et al. (2022).

Icelandic dust serves as ice-nucleating particles population type across the North Atlantic and Arctic (Kawai et al., 2023; Paramonov et al., 2018; Sanchez-Marroquin et al., 2020). However, the abundance, sources, and nature of INPs in the high latitudes remain poorly understood (Murray et al., 2021; Xi et al., 2022). Furthermore, Icelandic dust can be strongly light-absorbing due to the presence of magnetite-like particles (Yoshida et al., 2016). In addition, it has different shapes, lower densities, higher porosity, increased roughness, and darker colors compared to other desert dusts (Butwin et al., 2020; Richards-Thomas et al., 2021). Icelandic dust provides a large surface for heterogeneous reactions with SO_2 uptake, thus providing a major sink of sulfur in volcanic clouds (Lasne et al., 2022; Urupina et al., 2019). Icelandic dust also has a strong influence on the mass balance of glaciers in Iceland (Wittmann et al., 2017) and thereby have a stronger positive direct radiative forcing on climate (Baldo et al., 2023), as indicated by its optical properties alone. Emitted Icelandic dust can be transported towards the North Atlantic Ocean (Dagsson-Waldhauserova et al., 2013; Moroni et al., 2018) as well as to glaciers in Greenland (Meinander et al., 2016). The transported dust could also potentially influence marine biota within ecosystems in the Arctic Ocean (Dagsson-Waldhauserova et al., 2017).

2.2 Aerosol particle size distribution

Mineral dust particles size span more than three orders of magnitude from a few nanometers to several hundreds of micrometers (Mahowald et al., 2014; van der Does et al., 2018). A full assessment and understanding of the dust cycle (emission, transport, and deposition phases) requires knowledge of processes related to dust emissions and the spatial evolution of dust load and its size distribution with transport and deposition (Mahowald et al., 2014). Aerosol particles are usually classified by their size diameter as the properties of dust particles are size-dependent with the formation, transformation and removal of atmospheric particles change with the particle size. For example, coarse dust particles scatter and absorb both the shortwave and longwave radiation whereas fine dust particles principally scatter shortwave radiation. Therefore, the overall fraction of coarse to fine dust present in the atmosphere could dictate the sign and magnitude of the dust direct radiative effect on the global climate system (Adebiyi & Kok, 2020; Di Biagio et al., 2020; Kok et al., 2023, 2017). Furthermore, coarse particles dominate the deposited dust mass which is expected to be more prevalent closer to the source regions and also supplies nutrients into the marine and terrestrial ecosystems, consequently affecting biogeochemical cycles (Jickells et al., 2005; Yu et al., 2015).

2.3 Dust diameter types

Four different types of diameters have been used for measurement and studies of atmospheric dust and its various impacts - aerodynamic diameter, optical diameter, projected area-equivalent diameter, and volume-equivalent/geometric diameter (Huang et al., 2021). First, the aerodynamic diameter of a particle is defined as that of a sphere, whose density is 1 g cm^{-3} (cf. density of water), having the same terminal velocity as the particle settling under the influence of gravity (Hinds, 1999). This diameter is obtained from aerodynamic classifiers such as cascade impactors. The aerodynamic diameter is used in assessing aerosol impacts on human health and in defining the air quality standards for pollution, namely $PM_{2.5}$ and PM_{10}, defined as particulate matter (PM) having an aerodynamic diameter less than 2.5 µm and 10 µm, respectively (WHO, 2021). Second, the optical diameter is the diameter of a calibration particle (usually a polystyrene latex sphere) with given optical properties that scatter the same amount of radiation into a particular direction as the dust particle (Mahowald et al., 2014). The optical diameter is commonly used in optical sizing instruments like the optical particle counters - the most widely used instrument to measure the PSD of dust aerosols in field campaigns (Formenti et al., 2011; Reid et al., 2003b). Third, the projected area-equivalent diameter is the diameter

of a circle with the same area as dust particle projected on a two-dimensional image. It is commonly measured using electron and light microscopy on particles collected on filters (Kandler et al., 2007; Reid et al., 2003a) and is used to quantify size-resolved dust mineralogy and morphology (Kandler et al., 2007, 2011b) and occasionally dust PSDs (Chou et al., 2008; Ryder et al., 2018). Finally, the volume-equivalent (also known as geometric diameter) describes the diameter of a sphere with the same volume and density as an irregularly shaped dust particles (Hinds, 1999). The geometric diameter can be determined for instance using a Coulter counter, a technique that is common for measuring dust size in ice and marine sediment cores (Delmonte et al., 2002). Although hard to measure, attempts have been made in previous studies using shadowing techniques to derive the third dimension and merged it with the area-equivalent information to acquire the geometric diameter (Anderson et al., 1996; Okada et al., 2001; Reid et al., 2003a). Unlike the aerodynamic, optical, or projected area-equivalent diameter, the geometric diameter is the primary diameter type used in global aerosol models to quantify dust size (Mahowald et al., 2014). Usually dust with geometric diameter $\leq$ 20 µm is considered most relevant to dust impacts on weather and climate (Adebiyi & Kok, 2020), although coarser dust also produces important impacts (Ryder et al., 2019, 2013a). For a given dust particle, values of these different diameter types could vary widely, and the conversion among the four diameter types is not straightforward (Huang et al., 2021; Reid et al., 2003a). This is partially due to the assumption made regarding particle shape - that it is spherical. However, numerous in situ measurements have shown that dust is highly aspherical, with typical particle length-to-width (aspect ratio) and height-to-width ratios often deviating from unity (Chou et al., 2008; Huang et al., 2020; Kandler et al., 2007; Okada et al., 2001). Because aspherical dust has different aerodynamic, optical, and geometric properties than spherical dust, spherical particle shape assumption is problematic and accurate conversion between different diameter types is important (Huang et al., 2021). For example, if a dust particle is approximated as a tri-axial ellipsoid, its drag force is higher than if the same dust were represented as a geometric sphere (Huang et al., 2020; Mallios et al., 2020). This difference in asphericity contributes to the fact that dust particles expressed in aerodynamic diameter are on average 45% larger than the same dust particle expressed in geometric diameter (Huang et al., 2021). Furthermore, the conversion between aerodynamic and geometric diameter also depends on the difference between dust and water densities (Hinds, 1999). In addition, knowledge of dust's index of refraction and dust shape is important for converting optical diameter to other diameter types. Therefore, uncertainties in dust asphericity, dust density, and index of refraction can lead to errors when converting from one diameter type to another, especially for coarse dust particles (Huang et al., 2021).

2.4 Mixing state

Airborne mineral dust particles are often complex mixtures of various chemical species, have different morphologies, and their composition can vary substantially with particle size. Furthermore, for a given size, particles may range from consisting mainly of individual species to aggregates of numerous components. One of the properties, which characterize their ensemble, is the aerosol mixing state and it can have a considerable impact on radiative forcing and climate. Generally, in cases where a detailed knowledge is special interest, a complete and rigorous description of aerosol composition and mixing state may require information on each individual particle. The mixing state describes how various species are mixed at the individual particle level. Aerosol particles mixing state is defined as the distribution of chemical compounds across the particle population (Winkler, 1973). A distribution of particles is a homogeneous mixture, if the ensemble of particles has uniform composition and properties throughout.

In the case of **external mixture**, the particles have different chemical composition and exist independently in the particle distribution. An **internal mixture** is when different species are present within one particle and not homogeneously distributed in the volume of each particle (Riemer et al., 2019) as seen in Fig. 2.4.

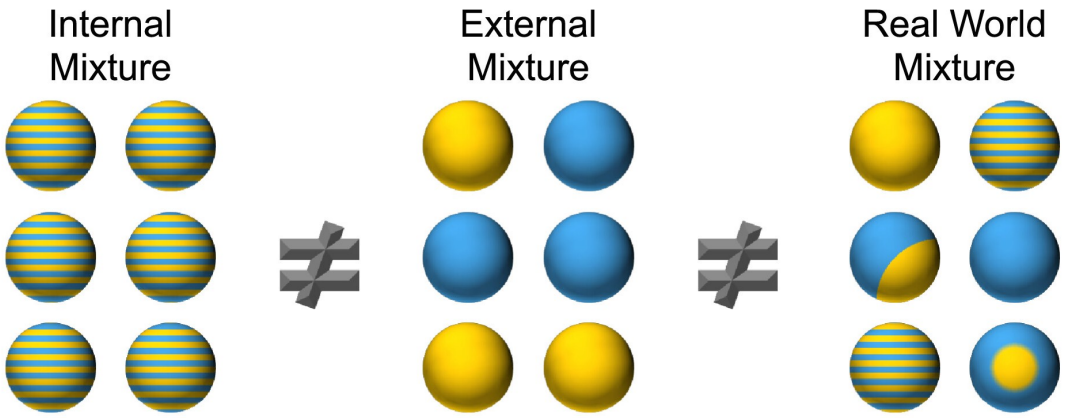

Figure 2.4: The image on the left illustrates an instance of a fully internal mixture, where species are uniformly mixed inside each particle, as indicated by the blue and yellow striped particles in this case. In the middle, an external mixture is portrayed, where each particle contains only one species. The population on the right represents an example that lies somewhere between the external and internal mixture, while also emphasizing that the arrangement of the species within the particle can vary. Figure from Riemer et al. (2019) John Wiley and Sons, used with permission.

2.5 Climate effects

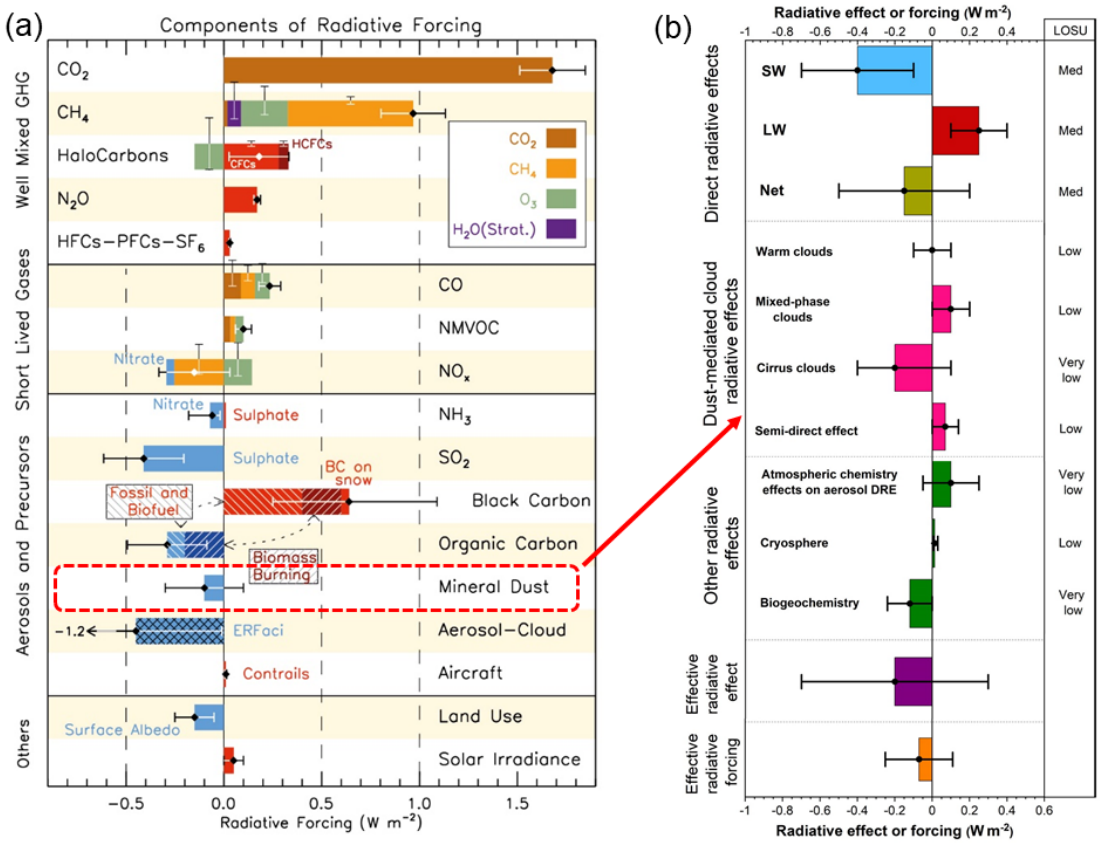

Figure 2.5: (a) Radiative forcing estimates bar chart for the period 1750–2011 based on emitted compounds (gases, aerosols or aerosol precursors) or other changes and aggregated uncertainties for the main drivers of climate change. (b) **Global mean radiative effects and forcing of dust at the top of atmosphere**. Dust-related perturbations to the radiation budget through direct radiative effects, dust-mediated cloud radiative effects (pink bars), other radiative effects (green bars), their sum (effective radiative effect; purple bar) and the proportion of the latter linked to dust increases since pre-industrial times (effective radiative forcing; orange bar). Error bars denote the 90 % confidence range. The level of scientific understanding (LOSU) describes confidence in the assessment of each radiative effect, following past practice (Solomon et al., 2007). The global mean dust effective radiative effect and radiative forcing are uncertain in sign and magnitude, but are more likely to cool the climate than to warm the climate. SW, shortwave; LW, longwave. Figure and caption from Kok et al. (2023) Springer Nature, used with permission.

Energy in the Earth-atmosphere system is received from the sun as incoming solar radiation. This radiation is absorbed by the earth and some of it (about 30 percent) is reflected back into space. The balance between incoming and outgoing energy is known as “radiative

forcing" and can ultimately have either a net cooling or net warming of the planet (Seinfeld & Pandis, 2016). Many factors, including reflectivity of the Earth's surface, the physical properties of gases in the atmosphere such as carbon dioxide, clouds, and polar ice have an effect on this balancing act with each of these parameters having its own level of uncertainty and its own difficulties in being precisely measured (Seinfeld & Pandis, 2016). In order to forecast the planet's future climate scenario, global climate models must be able to quantify the extent to which anthropogenic and natural emissions will influence radiative forcing. However, chemically diverse species like aerosols pose a significant uncertainty in estimating the radiative forcing in a changing climate (Stocker et al., 2013). Among the different aerosol types, the contribution of mineral dust aerosols to radiative forcing is uncertain as dust interacts with the earth system via multiple mechanisms which can both cool and warm the climate system resulting in an uncertain the net effect (Kok et al., 2023). Accordingly, the sign and magnitude of radiative perturbations due to increase in dust since the pre-industrial era are also uncertain, meaning that it is unknown whether dust changes have enhanced or opposed anthropogenic warming (Kok et al., 2023).

2.5.1 Interactions with radiation

Direct radiative effect (DRE) of dust is defined as the perturbation of the energy budget with change in radiation flux due to the presence of dust particles suspended in the atmosphere (Schepanski, 2018). Mineral dust can influence DRE through scattering and absorption of light by individual particles. As dust sizes spans a wide range from few nanometers to 100 µm (Mahowald et al., 2014), it interacts with shortwave (SW) (centred around 550 nm wavelength) and longwave (LW) (centred around 10 µm wavelength) radiation (Sokolik & Toon, 1999; Tegen & Lacis, 1996). The sign and magnitude of the dust DRE depend on the balance between these interactions. For example, fine particles mostly cool the climate via scattering of SW radiation as it dominates spectral absorption, whereas coarse particles tend to cause warming by absorption of both SW and LW radiation. Therefore, the balance between cooling from SW scattering and warming from SW absorption and LW scattering and absorption dictate the dust DRE.

Much of the uncertainty in DRE stems from the uncertainties in the dust mineralogy and its evolution during transport (Baker & Croot, 2010; Hand et al., 2004; Shao et al., 2011). Mineral dust is typically internally mixed and comprised of a wide range of minerals (Falkovich et al., 2001). The ability of a particle to scatter and absorb light depends greatly on the particle's mineralogy (Nousiainen & Kandler, 2015). As a result, direct radiative forcing depends greatly on the mineralogy of the dust in the atmosphere. There have

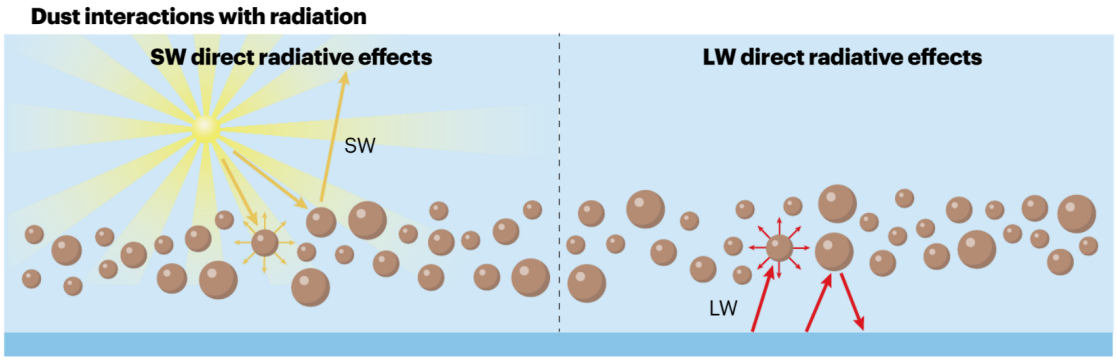

Figure 2.6: Dust direct interactions with shortwave (SW) and longwave (LW) radiation. Yellow arrows represent SW radiation and red arrows represent LW radiation. Figure and caption from Kok et al. (2023) Springer Nature, used with permission.

been many studies that demonstrate the effect of mineralogy on radiative forcing – for example, it has been shown that iron oxides and oxi-hydroxides are a major factor that determines the capacity of the dust to absorb radiation because their imaginary part of the refractive index is order(s) of magnitude higher than that of clay minerals (Sokolik & Toon, 1999; Zhang et al., 2015). They can exist as separate grains, but also mixed with clay mineral aggregates (Deboudt et al., 2012; Jeong et al., 2016; Kandler et al., 2007). Clay minerals usually contribute the majority of the atmospheric dust mass and number and are therefore among the most relevant for optical aspects like short-wave radiation scattering and long-wave absorption and emission, but less so for short-wave absorption due to their low imaginary part of the refractive index (Sokolik & Toon, 1999; Sokolik et al., 1998).

The shape of mineral dust particles is highly variable and rarely spherical, and this asphericity can greatly influence the optical properties of the dust. Accurate quantification of dust shape is therefore important for calculating dust impact on radiative forcing (Ito et al., 2021) and the terminal velocity of dust particles (Ginoux, 2003; Huang et al., 2020), albeit with high uncertainties for both of these effects (Nousiainen et al., 2011). Mineral dust also contributes significantly to the atmospheric aerosol mass loadings which are retrieved from satellite measurements and ground-based lidar measurements applying algorithms that use particle shape as one of the input parameters. Dust aerosols in most climate models are usually assumed to be spherical (Mahowald et al., 2014). The importance of realistic size equivalence and shape of spheroidal Saharan dust particles on optical properties and the radiative effect was studied by (Otto et al., 2011) during SAMUM-1 in

Morocco. Furthermore, SEM was used to characterize the mineralogical composition and shape of mineral dust particles collected during the SAMUM campaign over Morocco in 2006 (Lindqvist et al., 2014). They found great variation between the scattering properties of spheres, spheroids, and mineral dust particles characterized by SEM (Lindqvist et al., 2014).

2.5.2 Interactions with the clouds

Dust particles influence cloud development on a microphysical level by changing the thermodynamic environment and by acting as both cloud condensation nuclei (CCN) (Bègue et al., 2015; Karydis et al., 2011) and ice-nucleating particles (INPs) (Boose et al., 2016; DeMott et al., 2010). These interactions can cause radiative perturbations on warm clouds, mixed-phase clouds, and cirrus (ice) clouds, as well as through semi-direct effects on low clouds. The aerosol-cloud interactions pose a major challenge in understanding the sign (positive or negative effect) and magnitude of aerosol impacts on clouds in particular and water cycle and energy budget of Earth in general (Stevens & Feingold, 2009).

Dust particles can affect warm clouds by increasing the concentration of cloud condensation nuclei (CCN) (Koehler et al., 2009; Kumar et al., 2011a), reducing the concentration of non-dust CCN, and acting as giant CCN which can form cloud droplets and suppress overall cloud droplet formation (Kok et al., 2023). The effect of dust on warm clouds is complex, with some models suggesting that dust decreases cloud droplet number concentrations (CDNC) (Karydis et al., 2017), while others suggest that dust increases CDNC (McGraw et al., 2020; Sagoo & Storelvmo, 2017) and has a net cooling effect. Past research are not conclusive regarding the net global effects of dust on warm clouds, with general agreement that the sign and magnitude of the dust contribution to CDNC is highly heterogeneous in both space and time (Karydis et al., 2017; McGraw et al., 2020). The perturbation to Earth's TOA radiation budget through changes to warm clouds due to dust is likely negative but close to zero, with an uncertainty range of -0.10 to +0.10 W m^{-2} and low confidence due to limited research (Kok et al., 2023).

Dust particles can impact mixed-phase clouds (MPCs) by acting as ice nucleating particles (INPs). MPCs are clouds that contain both supercooled liquid droplets and ice crystals and occur at temperatures between approximately -40°C and 0°C (Korolev et al., 2017). In an INP-limited environment, MPCs will be optically thick with liquid cloud tops (Morrison et al., 2012) and only small amounts of ice in the cloud interior or below cloud base. However, a dust-enriched environment can lead to partial or complete glaciation of MPCs, which reduces cloud albedo and causes a positive (warming) radiative effect. An increase

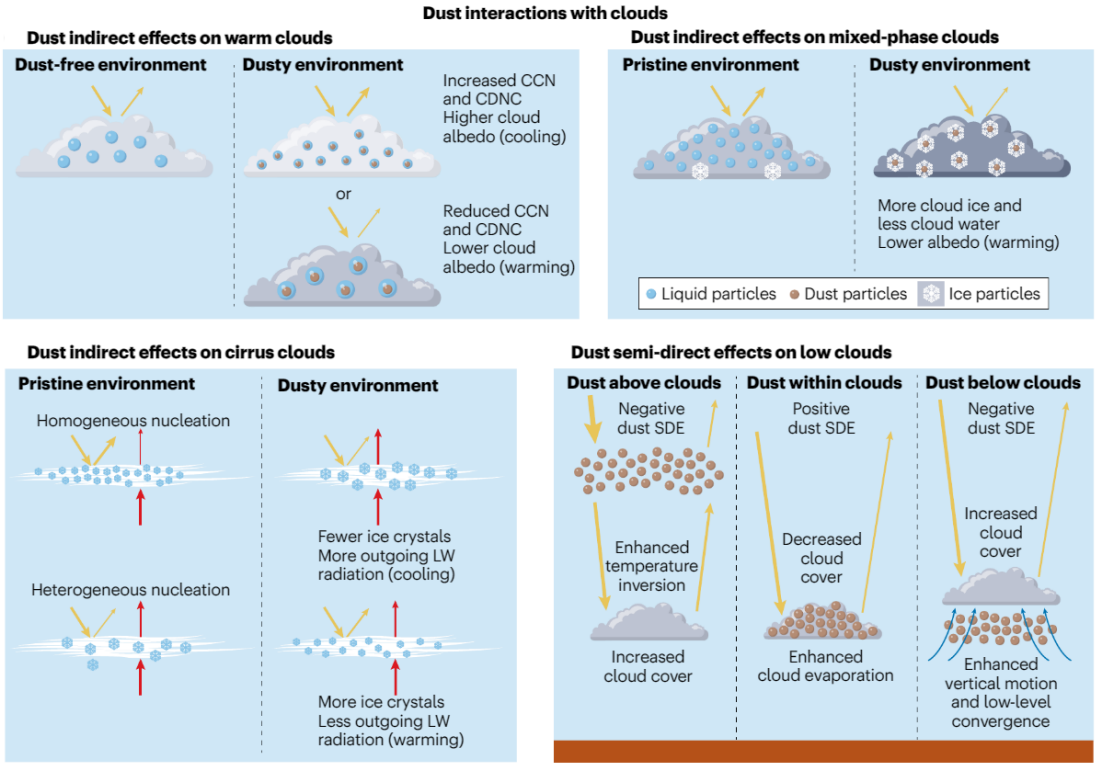

Figure 2.7: Dust indirect effects on warm clouds, mixed-phase clouds, cirrus clouds, and semi-direct effects on low clouds. Figure from Kok et al. (2023) Springer Nature, used with permission.

in dust loading, and thus INPs, is likely to cause a warming effect on climate by reducing the cooling effect of MPCs (Kok et al., 2023). Global simulations and satellite observations suggest that dust effects on MPCs can perturb the TOA radiation budget by approximately 0.10 W m^{-2}, but there is a large uncertainty range of 0 to 0.20 W m^{-2} and low confidence due to limited research (Kok et al., 2023).

Dust particles play a major role in the formation of cirrus clouds (Cziczo et al., 2013; Froyd et al., 2022) in the upper troposphere at temperatures below approximately -38°C. Cirrus clouds have a net warming effect on climate by reducing the emission of LW radiation to space more effectively than they reflect SW radiation (Heymsfield et al., 2017). Cirrus clouds can form by two different mechanisms: homogeneous and heterogeneous nucleation (Kanji et al., 2017). The impact of dust on cirrus clouds depends on whether non-dust INPs are present. When INPs are present, additional dust INPs would add ice

crystals and reduce their size, making cirrus clouds optically thicker and extending their lifetimes. However, when INPs are not present, additional dust could reduce the number of ice crystals and increase their size (Storelvmo, 2017), resulting in an optical thinning of cirrus clouds. The overall radiative effect of dust on cirrus clouds is estimated to be -0.20 W m^{-2}, with a range from -0.40 to +0.10 W m^{-2}. However, the assessment of this effect is given low confidence due to limited research (Kok et al., 2023).

Dust particles can have a semi-direct effect (SDE) on clouds by modifying the temperature profile (Huang et al., 2014) and atmospheric stability, moisture profile, and secondary circulations (Amiri-Farahani et al., 2017; Perlwitz & Miller, 2010). This effect depends on the relative position of the dust and cloud layers within the atmospheric column and the amount of radiation absorbed by the dust layer (Amiri-Farahani et al., 2017; Perlwitz & Miller, 2010). The pathways for dust SDEs can be categorized into cases where the dust layer is above, within or near, and below the cloud layer. The overall impact of dust on cloud cover is complex and depends on various factors such as the location and altitude of the clouds and the amount of radiation absorbed by the dust layer (Amiri-Farahani et al., 2017; Perlwitz & Miller, 2010). Satellite observations show that annual dust SDE is negative over the North Atlantic Ocean (Amiri-Farahani et al., 2017), but global observational estimates of dust SDE are currently not available (Samset et al., 2018). Climate model simulations have reported a net positive global annual mean dust SDE (Amiri-Farahani et al., 2019; McGraw et al., 2020), but there are uncertainties in dust absorption properties, the vertical distributions of dust and clouds, an underestimate of LW radiative cooling by coarse dust, and the parameterization of cloud processes (Ansmann et al., 2017; O'Sullivan et al., 2020; Sand et al., 2021). Therefore, the overall estimate of the dust SDE is 0.07 ± 0.07 W m^{-2}, but with low confidence due to these possible biases and limited research (Kok et al., 2023).

2.5.3 Interactions with atmospheric chemistry

Mineral dust can significantly impact atmospheric chemistry through its interactions with trace gases and aerosols. Although freshly emitted mineral dust aerosols are typically insoluble, they can become reactive when exposed to trace acidic gases resulting from anthropogenic pollutants and sea salt. Studies in various fields and laboratory settings have shown that mineral dust can provide a reactive surface that removes and transforms inorganic (SO_2, NO_2, N_2O_5, and O_3) and organic trace gases (Usher et al., 2003).

Moreover, mineral dust can act as a sink for volatile organic compounds (VOCs) in the atmosphere. Formaldehyde, acetone, and glyoxal are examples of VOCs that can absorb or

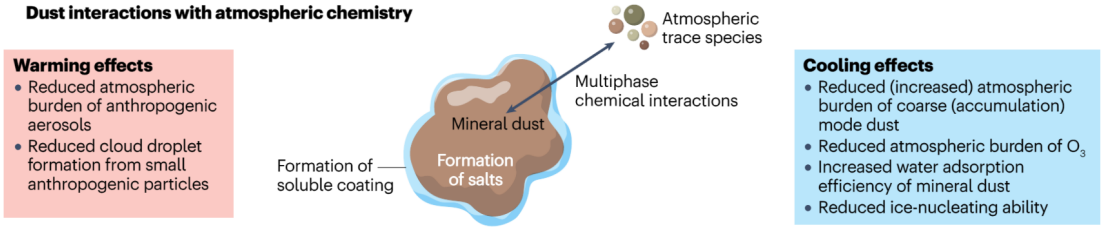

Figure 2.8: Influence of dust on atmospheric chemistry and radiative fluxes at the top-of-atmosphere, leading to either warming (left) or cooling (right) effects on global climate. The brown core depicts the freshly emitted insoluble dust particle, while the blue area represents the soluble coating acquired through interactions with atmospheric chemistry. Figure and caption from Kok et al. (2023) Springer Nature, used with permission.

adsorb onto the surface of mineral dust particles, effectively reducing their concentration in the gas phase. Additionally, mineral dust aerosols containing Ti and Fe oxides can uptake nitrogen dioxide (NO_2) from the atmosphere and are photo-chemically active substrates that can interact with NO_2 through a process called heterogeneous chemistry. This process involves the adsorption of NO_2 onto the surface of the dust particles, followed by a series of chemical reactions that can lead to the formation of nitrogen-containing compounds such as nitrates in the presence of light (Ndour et al., 2009, 2008).

Chemical aging of dust through various reactions can modify its hygroscopicity (Laskin et al., 2005), which, in turn, affects its ice-nucleating ability (Cziczo et al., 2009), water solubility, and oceans fertilization capabilities (Paris et al., 2011; Shi et al., 2012). Overall, the interactions of mineral dust with trace species in the atmosphere are complex and can have important implications for air quality, climate, and human health.

2.5.4 Interactions with the cryosphere

The interaction of dust with the cryosphere affects climate through the dust DRE and indirect radiative effect (Kok et al., 2023). Mineral dust once deposited on clean snow and ice surfaces causes darkening and decrease their albedo. Due to the snow albedo effect, snow and glacier are melting faster (Painter et al., 2010; Skiles et al., 2018) and causes a positive surface albedo feedback (Hall, 2004) which leads to further warming (Flanner et al., 2007).

The concentration of dust in snow (Dang et al., 2015), the optical properties of dust (defined by its PSD and chemical composition) (Dang et al., 2015; Flanner et al., 2021),

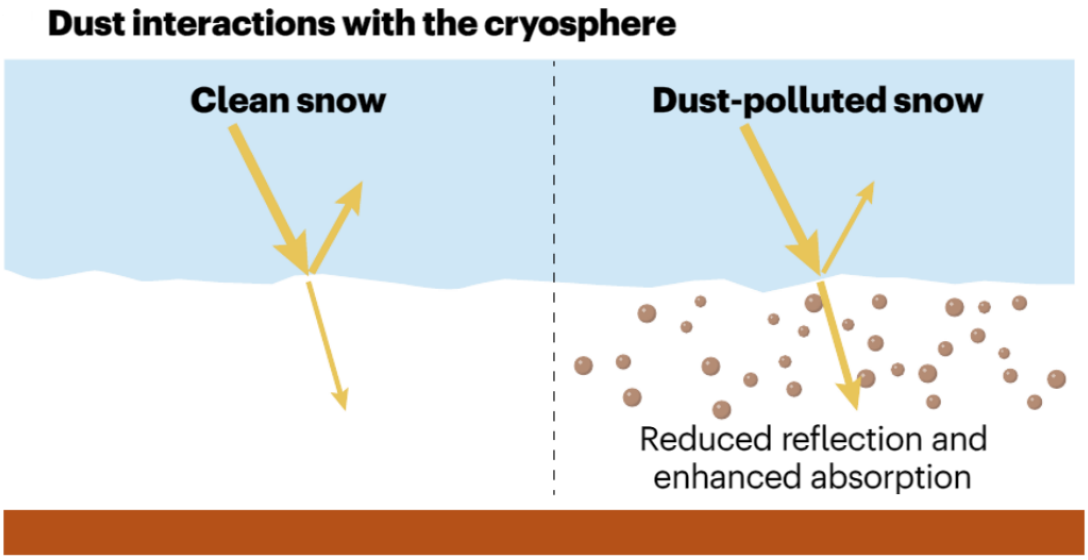

Figure 2.9: Radiative effects of dust deposited on snow and ice, illustrated by snow reflectivity without (left) and with (right) dust deposited onto the snowpack. Figure and caption from Kok et al. (2023) Springer Nature, used with permission.

the mixing state of dust and snow (He et al., 2019; Liou et al., 2014), the size and shape of the snow grains (Liou et al., 2014), the characteristics of the snowpack (He et al., 2017; Warren & Wiscombe, 1980), and illumination conditions (Dang et al., 2015; He, 2022) all have an impact on the dust-induced snow albedo effect. Observations have shown significant differences in dust concentrations in snow and ice which leads to huge variations in associated surface radiative effects. Because of the large uncertainties caused by complicated and poorly constrained dust–snowpack–radiation interactions, Kok et al. (2023) have assigned low confidence to the dust-induced snow albedo effect.

2.5.5 Interactions with biogeochemistry

Atmospheric carbon dioxide (CO_2) concentration and therefore Earth's climate is profoundly influenced by the exchange of CO_2 between atmosphere and ocean (Falkowski et al., 2000; Krishnamurthy et al., 2009) which is controlled by the bio-productivity in the ocean surface water. Several studies have shown that the bio-productivity is controlled by nutrient supply (Bristow et al., 2017; Hamilton et al., 2022). Usually the nutrients close

to the continents are supplied by riverine input (Cotrim da Cunha et al., 2007), while the vast majority of the oceans depend on atmospheric input (Thompson & Ridgwell, 2002).

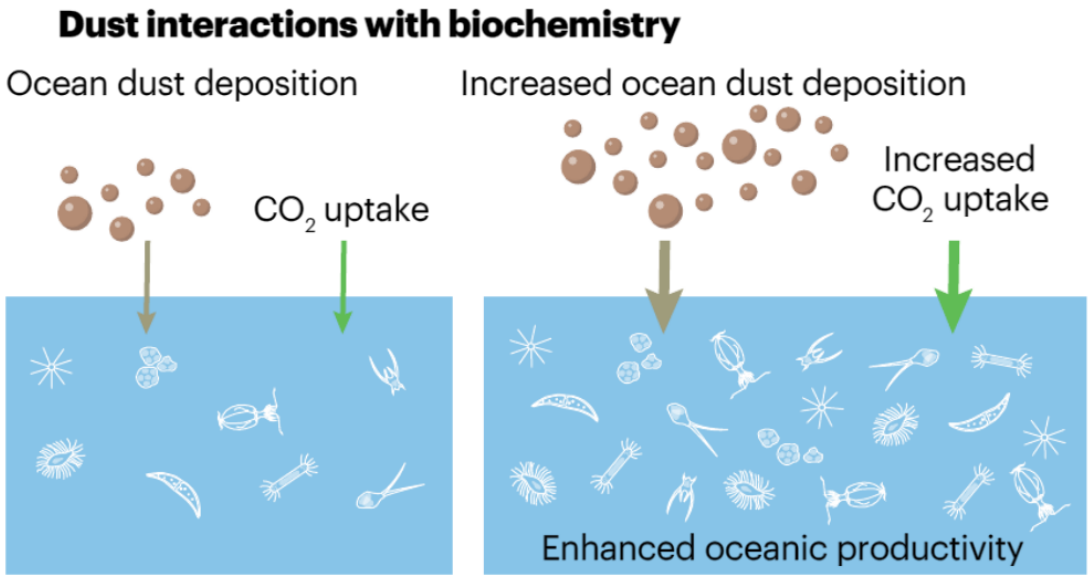

Figure 2.10: Effect of dust in modifying CO_2 concentrations via ocean biogeochemical process. Figure and caption from Kok et al. (2023) Springer Nature, used with permission.

Mineral dust deposition into the oceans exceeds several hundreds of Tg anually (Huneeus et al., 2011) in total and supplies an estimated 15 Tg yr^{-1} as potential nutrient (Jickells et al., 2005; Luo et al., 2008; Mahowald et al., 2009). Of that potential nutrients - namely iron and phosphorus compounds, usually only a fraction is bio-available. Iron is an important micro-nutrient which affects the ocean bio-productivity as marine phytoplankton use it during both photosynthesis and respiration processes (Morel et al., 1991; Ye & Völker, 2017). The Fe bio-availability in the ocean top layers varies between 0.01 % and 80 % of total mineral dust (Mahowald et al., 2009), with an average of around 4 % (Luo et al., 2008). This iron solubility in the oceanic surface water is however depends on the mineralogical composition of the deposited dust with certain Fe-containing minerals such as clays, possessing much higher solubility as compared to others, such as magnetite, hematite, and goethite (Journet et al., 2008). Therefore, the soluble iron content is different in soils from dust-source areas compared to sediments derived from glacial processes (glacial flour). Glacial flour is common in high latitude dust and the iron content is primarily contained in the form of iron-containing amorphous glass which have higher

levels of soluble iron compared to soils from low latitude regions, which contains a larger fraction of iron oxides and hydroxides (Baldo et al., 2020). In addition, the solubility and bio-availability can be altered via acid processing (Baker & Croot, 2010; Raiswell & Canfield, 2012; Shi et al., 2009), photochemical reactions (Rubasinghege et al., 2010), as well as, at a later stage, sea water composition (Baker & Croot, 2010). Furthermore, atmospheric effects in the ice phase might enhance the solubility (Jeong et al., 2012).

Another consideration is the particle mixing state and its effects on nutrient supply. For iron, the mixing state (the distribution of iron inside the single particles) is known to play a key role on its bioavailability due to the different surface area to volume ratio or due to direct uptake of iron nanoparticles by marine microorganisms (Rubin et al., 2011; Shi et al., 2012). Furthermore, atmospheric processing can alter the solubility as well as the bioavailability of the iron contained in mineral dust. For example, atmospheric processing can lead to the formation of iron nanoparticles which enhances its bioavailability (Shi et al., 2009, 2011). Such inclusions are also reported in individual cases for mineral dust aerosols (Lieke et al., 2011). In addition, the significance of mixing state for bioavailability is corroborated by the positive correlation between iron solubility and particle sulfate content (Chen & Siefert, 2004) as a reaction can only occur in internal mixture components of different sources (Baker & Croot, 2010). For phosphorus, the nutrient availability from mineral phases found in atmospheric dust remains unknown (Okin et al., 2011; Vet et al., 2014). Additionally, it is unclear how phosphorus is transported to the oceans - whether it is carried in high-phosphorus particles or distributed in smaller quantities across numerous particles. Previous research suggests the latter, but studies with a statistically significant number of particles are lacking (Kandler et al., 2011b; Scheuvens et al., 2011). While minerals like iron and phosphorus are commonly discussed component of mineral dust in relation to biogeochemical cycling of metals, there are other minor and trace elements such as cobalt, nickel, manganese, copper, arsenic, lead, and cadmium that are essential for primary production (Fishwick et al., 2018; Jickells et al., 2005).

2.6 Dust observations

Mineral dust can be observed using various techniques depending on the objective. Figure 2.11 shows the different approaches to study dust: aircraft, ground based, laboratory simulation, and remotely.

Aircraft measurements are a useful approach for measuring mineral dust in the atmosphere, particularly for studying the vertical distribution of dust particles. Aircraft can be equipped with instruments such as nephelometers, particle counters, and filter samples to measure

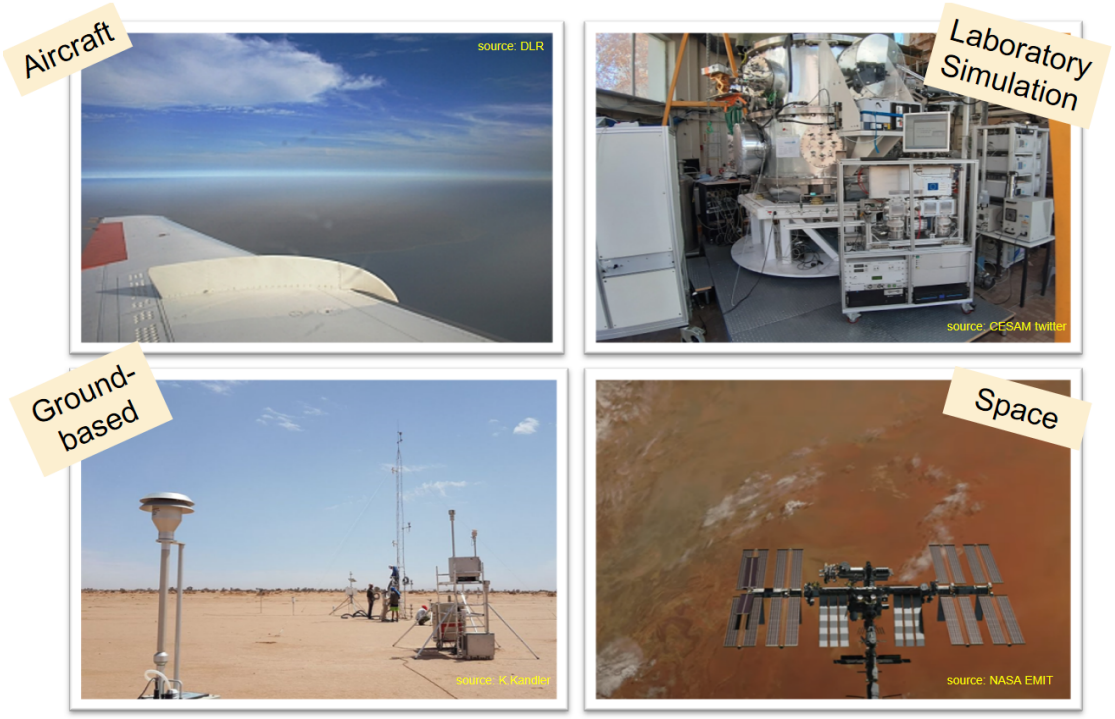

Figure 2.11: Various techniques for observing mineral dust, including aircraft, ground-based, laboratory simulation, and remote sensing.

the chemical and physical properties of dust particles in real-time. In many cases, it presents the only way to examine aerosol particles and their interactions with clouds (Wendisch & Brenguier, 2013). However, this method is challenging due to the high speeds involved, particularly for coarse-mode aerosols. Their high inertia makes it difficult for them to follow the air streamlines when they are distorted by the aircraft fuselage and the inlet, which can lead to artificial depletion or enhancement (Brockmann, 2011; Hinds, 1999). Therefore inlet design and characterisation of the sampling system present in a research aircraft is imperative (Sanchez-Marroquin et al., 2019).

Ground-based in situ measurements involve collecting samples of mineral dust directly from the atmosphere in the vicinity of dust sources. It involve the use of instruments such as filter samplers, particle counters, and spectrometers to measure and characterize the properties of dust particles. The filter samples can later be analyzed in the laboratory to determine their physical and chemical properties, such as size distribution, mineralogy

and morphology. However, field measurements are quite challenging due to the difficulty in dust sampling at source areas, as source areas are often remote harsh environments. Also, frequent dust storms result in high particulate concentrations and filter overload, which pose a challenge not only for automated single particle analysis by SEM but also could potentially damage the state of the art instrumentation by the extreme atmospheric conditions.

Remote sensing has enabled monitoring and investigation of mineral dust sources on a global scale. Remote sensing of dust includes retrievals of parameters like backscatter and extinction coefficient, depolarisation, aerosol optical depth, and flux densities. Remote sensing techniques include LIDAR applications , Hyperspectral Imaging, Long-Wave Infrared, Multispectral Imaging, Radiometrics. This approach is useful for studying large-scale dust transport, but provides limited information on the size and composition of individual dust particles.

Use of laboratory simulation enables reproducible investigations into precisely controlled atmospheric-chemical mechanisms. This makes it possible to perform experiments in realistic conditions to recreate and investigate processes at play in the atmosphere. It is however limited in its ability to reproduce the complex atmospheric processes that affect the behavior of dust particles in the real atmosphere.

Finally, data analysis approaches involve analyzing existing datasets of atmospheric dust measurements to extract meaningful insights and patterns. This can involve statistical analysis, machine learning, and other computational techniques to identify trends and relationships between dust properties and other environmental variables.

All of these different approaches has its own strengths and limitations and therefore a synergistic approach should be taken. The choice of approach mainly depends on the specific research question and available resources. A combination of different approaches is often needed to fully understand the behavior and impact of mineral dust in the atmosphere. Additionally, the model parameters should be regularly reviewed and compared with results from in situ measurements.

3 Material and Methods

3.1 Particle sampling

Particles were collected using 3 different sampling techniques namely: flat-plate sampler (FPS), free-wing impactor (FWI), and a micro-orifice uniform deposit impactor (MOUDI, MSP Corp. Model 110) all of which are briefly described in the section below. All aerosol samples were collected on pure carbon adhesive substrates (Spectro Tabs, Plano GmbH, Wetzlar, Germany) mounted to standard SEM aluminum stubs. Pure carbon substrate was chosen because of the low-Z background providing a contrast between particles and background as well as the different elemental composition of the background and the substances of interest. All adhesive samples were stored in standard SEM storage boxes (Ted Pella Inc., Redding, CA, USA) in dry conditions at room temperature. FWI and MOUDI samples were collected twice per day with a typical sampling duration of a few minutes to an hour whereas the exposure time was 8–48 h for the FPS. The sample substrate exposure time was dependent on the estimated aerosol concentrations in order to have a statistically significant number of particles on the substrate for individual particle analysis. The combination of three different techniques allows sampling of particles spanning over a wide size range which is generally the case for mineral dust.

3.1.1 Flat plate sampler

The flat-plate sampler used in this work is taken from the original geometry of flat-plate sampler used in Ott und Peters (2008). It consists of two round brass plates (top-plate diameter of 203 mm, bottom plate 127 mm, thickness 1 mm each) mounted with a distance of 16 mm separating them. The plates protect the substrate from precipitation and reduce the effects of wind speed by reducing the smallest turbulences to the distance between the parallel plates. Larger droplets (> 1 mm) are prevented by this setup from reaching the SEM stub surface at low wind speeds (Ott & Peters, 2008). The main triggers

for particle deposition on the substrate are diffusion, gravity settling, and turbulent inertial forces.

3.1.2 Cascade impactor

Sampling was conducted using a 5-stage Micro-Orifice Uniform Deposit Impactor (MOUDI, MSP Corp., MN, USA) with a 100 L min^{-1} flow rate. The impactor has stages available with 50% cut-point aerodynamic diameter (D_a) of 10, 2.5, 1.0, and 0.25 µm. Particles were collected on 25-mm sticky carbon substrates attached to the 75-mm impaction plate using a double-sided adhesive. The sampling time was chosen to provide optimum particle loading for single particle analysis which was usually limited to a few minutes. The short sampling time resulted in fewer particle collection in the first two stages and therefore only the third and fourth stages are chosen for detailed analysis.

Particle bounce can be an issue with an inertial impactor such as the MOUDI and occurs when particles are impacted on the collection substrate but are not retained. Studies have shown that particle bounce reduces at the relative humidity of > 70 % depending on the chemical composition of particles (Bateman et al., 2014; Fang et al., 1991; Vasiliou et al., 1999). During the Morocco campaign, the relative humidity was usually below 60 % with a maximum of 71 %. Therefore, particle bounce can occur which could lead to biases in the particles collected. Additionally, the shattering and asphericity of dust particles can further induce bias in collected particles.

3.1.3 Free-wing impactor

A free-rotating wing impactor (Kandler et al., 2018, 2009; Waza et al., 2019) was used to collect particles larger than approximately 3 µm (projected diameter). The FWI has a carbon adhesive impaction surface attached to a rotating arm that moves through the air; particles deposit on the moving plate due to their inertia. The rotating arm is moved at a constant speed by a stepper motor, which is fixed on a wind vane, aligning the FWI to the wind direction. The substrate itself is oriented perpendicular to the air stream vector (resulting from wind and rotation speeds) which is maintained by a small wind vane attached to the rotating arm. The particle size cutoff is defined by the impaction parameter, i.e., by rotation speed, wind speed, and sample substrate geometry.

3.1.4 Ancillary data

Aerosol PSDs of suspended mineral dust were obtained by using an Optical Particle Counter (OPC, FIDAS 200, Palas GmbH, Germany). The measurement range of FIDAS was 0.2 - 19 µm with a time resolution of 2 min and a flow of 4.80 L min^{-1}. Data acquisition was performed by a data logger, averaging measurements over 2 min. In addition, meteorological data were acquired with a time resolution of 1 s. Air temperature and relative humidity were measured by HC2A-S3 sensor (Campbell Scientific) and wind speed, and wind direction were recorded by a two-dimensional sonic anemometer (Campbell Scientific WINDSONIC4-L) during the sampling period at approximately 0.4 m, 0.8 m, 2 m , 5 m and 10 m height facing north above ground level.

3.2 Analysis

3.2.1 Scanning Electron Miscroscopy (SEM) coupled with Energy dispersive spectrometry (EDX)

Scanning Electron Microscopy (SEM) is one of the most frequently used methods for routine analysis and characterization of single particles. The SEM uses a focused beam with accelerated electrons to produce a variety of signals after interacting with the sample.The schematic of electron-matter interaction is shown in Fig. 3.1 which is generally carried out in a vacuum chamber. The incident electron beam is focused on the sample surface and an image is created by scanning the electron beam line by line through a rectangular (raster) pattern (Johnson, 1996). As the scanning is done from point to point by the moving beam, the generated signal varies in strength reflecting the differences within the sample.

When electron beam enters the sample, some of them are scattered back out of the sample by elastic collisions with the atomic nuclei of sample atoms, as shown in Fig 3.1. These are called backscattered electrons (BSE) and have high energy leading to a larger specific volume of interaction and degrades the resolution of BSE images (Johnson, 1996). BSE produce images whose contrast comes mainly point to point differences in the average atomic number of the elements present within the sample. This is due to the beam interacting with higher atomic number nuclei results in greater elastic scattering and a greater flux of backscattered electrons at the detector creating bright areas in the image (Johnson, 1996). Other electrons in the beam are scattered inelastically by electrons present at the sample surface. Secondary electrons (SE) are sample atom electrons that have been ejected by interactions with the incident beam (primary) electrons. The SE are generally ejected with low kinetic energy. Because of their low energy they can escape

only from a very shallow region at the sample surface and thus results in the best imaging resolution. The images produced by SE depend on the sample topography. The interaction volume is more close to the sample surface and hence more SE can escape at the top of a peak than at the bottom of a valley resulting in peaks appearing bright and valley appearing dark in the image (Johnson, 1996). Therefore, the interpretation of SE is quite intuitive.

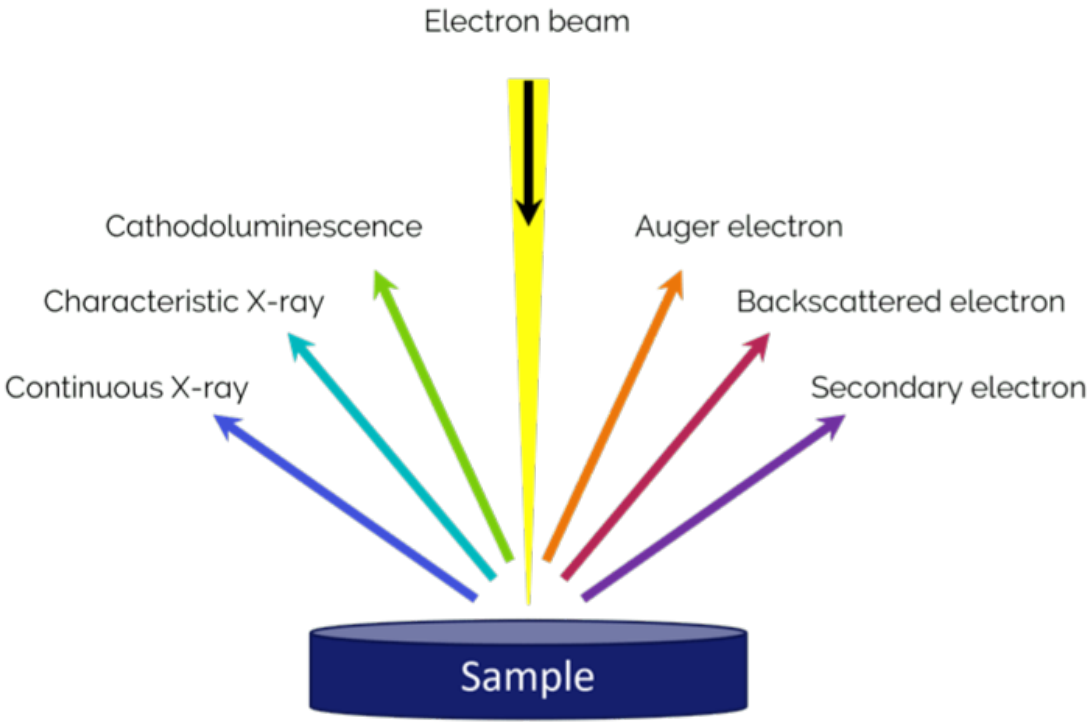

Figure 3.1: Electron — matter interactions: the different types of signals which are generated. The most commonly used signals are secondary electrons, backscattered electrons, and characteristic X-rays. Image extracted on 24/04/2023 from https://nano.oxinst.com/campaigns/what-is-eds/edx

Energy-dispersive X-ray spectrometry (EDX) is an SEM-based analytical technique for determining the chemical characterization/elemental analysis of a sample. It relies on the X-ray generation from a sample when excited with an electron beam. The X-rays are produced within a sample-beam interaction volume and are of two types: characteristic X-rays and X-ray continuum as seen in Fig. 3.2. The atoms in the sample interact with the incident electron beam and as a result emit X-rays that has a characteristic spectrum based on its atom of origin. These X-rays are of sharply defined energies with the position of the

peaks in the spectrum used to identify what elements the sample is made of, whereas the intensity of the signal represents the concentration of the element. Bremsstrahlung (braking radiation) or X-ray continuum creates a spectral background that is automatically eliminated by the software in order to precisely measure the energies of the characteristic X-rays. Lower spatial resolutions are caused by an increase in the sample beam interaction volume at higher electron beam energy. In contrast, higher resolution analysis is provided by low beam energy analysis.

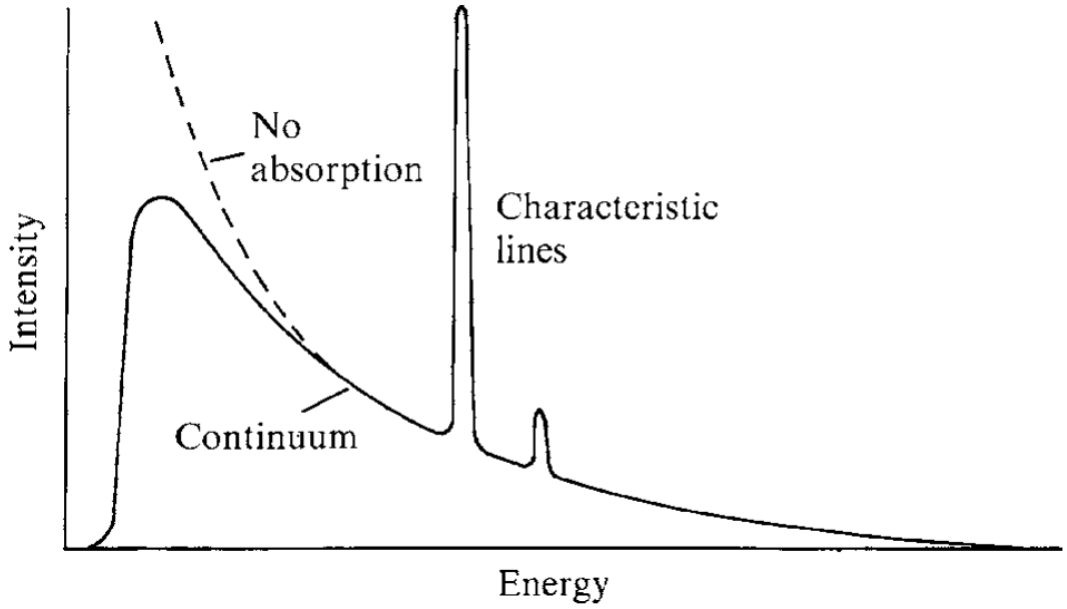

Figure 3.2: Schematic representation of the types of X-ray spectrum produced by bombardment of incident electron against photon energy, taken from (Reed, 2005).

SEM-EDX is one of the most used techniques for characterization of individual aerosol particles (Chou et al., 2008; Engelbrecht et al., 2016; Eriksen Hammer et al., 2019, 2018; Kandler et al., 2007, 2018, 2009; Krejci et al., 2005; Laskin et al., 2006; Price et al., 2018; Reid et al., 2003a; Ryder et al., 2018; Scheuvens et al., 2011; Waza et al., 2019; Young et al., 2016). Most of these studies used atmospheric or laboratory-generated aerosol samples that were collected onto different substrates with deposition techniques or using impactors, or on top of filters via filtration. The substrates containing aerosol particles are later subjected to SEM analysis to visually examine some of these particles or measure

their morphological features like size distribution and shape. EDX is also frequently used during these analyses to determine the chemical composition of the particles. This is often done to quantify the presence of several aerosol species within the sample or to further characterise properties of specific individual aerosol particles such as their mixing state or coatings.

Using SEM-EDX system to study the composition of aerosol particles has limitations beyond those inherent in the technique itself. As explained above, after the EDX detector targets a spot in the sample, the generated X-rays are being emitted by certain interaction volume (shown in Fig 3.1), which is inversely proportional to the particle mean atomic number (Z) and proportional to the energy of the incident electrons used. Therefore, a part of the EDX signal is contributed by the sample substrate for particles smaller than the interaction volume (Laskin & Cowin, 2001). This issue can be partially avoided by choosing a substrate made of a material which is generally absent in the atmosphere, or choosing a substrate with a very low EDX signal (Laskin et al., 2002, 2003). The well suited sampling substrates for aerosol size and composition for SEM analysis are pure carbon substrates (Kandler et al., 2007, 2018, 2011b) or polycarbonate filters (Chou et al., 2008; Engelbrecht et al., 2016; Reid et al., 2003a; Young et al., 2016). Therefore, the concentrations of elements present in these background materials (i.e. carbon and oxygen) cannot be detected reliably when classifying the particles according to their elemental composition. Boron substrates are sometimes used to enable quantification of carbon (Choël et al., 2005; Ebert et al., 2016; Eriksen Hammer et al., 2019). There are also different limitations depending on the choice of electron signal for particle characterisation. Some studies choose BSE (Kandler et al., 2007, 2018, 2011b; Price et al., 2018; Reid et al., 2003a; Young et al., 2016) while some other use SE (Krejci et al., 2005). Since the contrast in BSE images is mainly coming from point to point differences in the average atomic number of the sample (Johnson, 1996), aerosol particles with a similar composition to the background might be difficult to interpret under this detector. This is particularly important for small carbonaceous particles (e.g. soot) on top of carbon substrate or polycarbonate filters (Laskin & Cowin, 2001).

3.2.2 Automated single particle analysis in SEM

For analysing a large number of particles in an efficient way, data collection was performed by the AztecFeature software expansion. In the SEM, the stub was positioned at a working distance of approximately 10 mm. The SEM's electron beam had an accelerating voltage of 12.5 keV, beam current of 18 nA, and spot size 5 (beam diameter $\sim$ 3 nm) to produce the optimum number of input counts in the EDX detector. Scanning resolution was tuned

to particle size. For the FPS, 160 nm per pixel were used to identify particles up to 0.5 µm (equivalent projected area diameter) and for the FWI, 360 nm per pixel was used to identify the largest particles (mainly particles larger than 2.5 µm). Chemistry information is derived by EDX. The internal ZAF correction (Z – atomic number, A – absorption, F – fluorescence, accounting for material-dependent efficiencies) of the detector/software system–based on inter-peak background radiation absorption measurements for correction–was used for obtaining quantitative results.

To distinguish particles from the background, a brightness and contrast threshold with upper and lower bounds corresponding to pixels with specific shades of gray was manually adjusted by the operator for each image. Based on a manually set brightness and contrast threshold, AztecFeature identifies pixels within the boundaries as aerosol particles and provides particle quantification such as area, aspect ratio, breadth, projected area equivalent diameter, length, perimeter, and shape. Each region is selected in the software and the particle detection threshold is manually adjusted. The Z position of the stage is also manually adjusted for each image to generate a well-focused image. An image scan and the EDX acquisition is then performed automatically.

3.2.3 Particle classification method

SEM-EDX detects the elemental composition of individual dust particles. Some minerals have well-defined composition and can therefore be identified relatively easy (e.g. gypsum, quartz, calcite). Others, e.g. clay minerals, are variable by nature, so their identification is more ambiguous. Moreover, dust particles are commonly found in the form of aggregates rather than in their pure mineral forms, and therefore the method used in this study identifies the major mineral type in each particle. Furthermore, to assess artefacts, a few clean blank samples taken during the campaign were scanned and certain particle populations were identified as contaminants and thus discarded from the analysis. The contaminants detected consisted of pure iron (apparently already from the manufacturing process) and F+Si. The contaminants were mostly rare compared to the abundance of dust particles.

Based on the single particle composition quantification, an elemental index for the element X is defined as the atomic ratio of the concentration of the element considered and the sum of the concentrations of the element quantified (Kandler et al., 2007, 2018)

$$|X| = \frac{X}{Na + Mg + Al + Si + P + S + Cl + K + Ca + Ti + Cr + Mn + Fe + Co}, \tag{3.1}$$

where the element symbols represent the relative contribution in atom % measured for each particle. Note that the given method cannot be used to quantify the percentage of C, N, and O due to their high uncertainty and substrate contributions. Classification is done using a set of rules, which use the elemental index and additional elemental ratios and are defined by the dominance of one or more specific elements or their ratios (e.g. Al, Si, Ca, Fe, Al/Si). Particle classes are named for their most prevalent component(s), which may contain terms for mineral phases to simplify the naming (e.g. gypsum, quartz). Those mineral phases were chosen as the most prevalent components that matched the reported elemental composition, but no real phase identification of individual particles (e.g., by transmission electron microscopy) was carried out. Therefore, all the particle classes are termed '-like' to express the similarity in chemical fingerprints.

3.2.4 Particle morphology characterization

3.2.4.1 Aspect Ratio

The two-dimensional (2D) shape of individual dust particles is presented here as aspect ratio (AR) and was calculated by the image analysis integrated into the SEM-EDX software AZtec. AZtec software manual defines AR as the ratio of the major (L) to the minor axis ($W_{ellipse}$) of the elliptical fit on the projected particle area (Fig. 3.3). Features having shape like spheres have an AR that is approximately 1 whereas ovals or needles have an AR that is greater than 1. A caveat of 2-D imaging is that it can yield different shapes of 3-D particles depending on their orientations on the sampling substrate (Huang et al., 2020).

3.2.4.2 Projected-area and volume-equivalent diameters

In this study, the image analysis integrated into the SEM-EDX software AZtec is used to determine the size of particles as a projected area diameter. Projected area diameter, d_p is the diameter of a circle having the same area as the dust particle projected in a two-dimensional image (Fig. 3.3) and is calculated as:

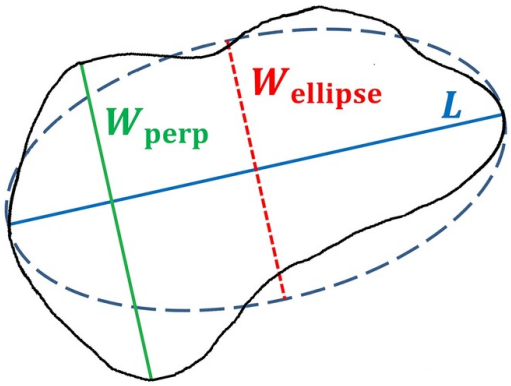

Figure 3.3: Top view of two-dimensional (2-D) projected area (within the black line) of a dust particle with the two common quantifications of dust width. The first definition records the maximum distance between two points on the outline that is perpendicular to the length (*L*) as the width W_{perp} (green line). The second definition records the width $W_{ellipse}$ (red dashed line) as the minor axis of an area-equivalent ellipse (blue dashed line) with *L* as its major axis. Image and caption taken from Huang et al. (2020).

$$d_p = \sqrt{\frac{4 \cdot A}{\pi}}, \tag{3.2}$$

in which *A* is the area covered by the particle on the sample substrate.

Following Ott und Peters (2008), the volume-equivalent diameter (sphere with the same volume as an irregular shaped particle) also called the geometric diameter, d_v, is estimated from the projected area diameter via a volumetric shape factor expressed by particle projected area and perimeter (*P*) as follows:

$$d_v = \frac{4\pi A}{P^2} d_p = \frac{1}{P^2}\sqrt{64\pi A^3}. \tag{3.3}$$

All particle diameters presented in this thesis are converted from projected area-equivalent diameter to volume-equivalent (geometric) diameter (unless stated otherwise). The reason for this conversion is that geometric diameter is used in global aerosol models to quantify dust size (Mahowald et al., 2014).

Particle volume is computed as

$$V = \frac{\pi}{6} \cdot d_v^3. \tag{3.4}$$

3.3 Determining the size distributions from the freewing impactor measurements

For calculating the atmospheric size distribution from the FWI, the collection efficiency of the FWI has to be considered.

The collection efficiency E(P) is parameterized from the experimentally determined values for discs given by May und Clifford (1967) as a function of impaction parameter *P*:

$$P = \frac{S}{D}, \tag{3.5}$$

where *S* is the stopping distance and *D* is the characteristic dimension, here 12 mm.

While *P* equals to the Stokes number within the Stokes regime, in the current work the particle Reynolds numbers are considerably higher. In this regime, in analogy to Hinds (1999) the stopping distance (*S*) can be approximated with better than 3 % accuracy as

$$S = \frac{\rho_{amb} \cdot d_{amb}}{\rho_a \cdot \sqrt{\gamma}} \left[Re_p^{1/3} - \sqrt{6} \,\text{tan inverse} \left(\frac{Re_p^{1/3}}{\sqrt{6}} \right) \right], \tag{3.6}$$

where ρ_{amb} is the ambient particle density, estimated from chemical composition, ρ_a is air density, and γ is aerodynamic shape factor. Results of the trigonometric function must be given in radian. The dry aerodynamic shape factor is assumed as constant similar to Ott und Peters (2008).

The particle Reynolds number is calculated as

$$Re_p = \frac{\rho_a \cdot v_i \cdot d_{amb}}{\eta \cdot \sqrt{\gamma}} \tag{3.7}$$

where $v_i = \sqrt{v_r^2 + v^2}$ is the impaction velocity

$v_r = 2\pi l f_r$ is the speed of the collector in the plane of rotation

l is the collector arm length

f_r is the rotation frequency

v is the wind speed

η is air viscosity

The collection E(P) efficiency for P>0.125 is then parameterized and the according correction is

$$c_e = \frac{1}{E(P)} = exp\left(\frac{0.28}{P}\right) \tag{3.8}$$

The total investigated volume (V_i) for the concentration calculations is determined by

$V_i = Av_it_i$, where

A is the analyzed area,

t_i is the sample collection time.

3.4 Calculation of the feldspar indices

The index values show the closeness of a particle composition to pure feldspar. They are composed of three properties, the overall contribution of feldspar-specific elements to the particle composition and the closeness to the feldspar Al/Si ratio as well as to the K/Si or alkali/Si ratio. The overall contribution of specific elements is calculated as

$$r_{Sil} = \frac{|Na| + |Al| + |Si| + |K| + |Ca|}{|Na| + |Al| + |Si| + |K| + |Ca| + |Mg| + |P| + |S| + |Cl| + |Ti| + |Fe|} \tag{3.9}$$

Closeness w.r.t Al/Si is determined as

$$r_{fsp,Al/Si} = \frac{|Al|}{|Si|}\frac{3|Na| + 3|K| + 2|Ca|}{|Na| + |K| + 2|Ca|} \tag{3.10}$$

$$Q_{fsp,Al/Si} = \begin{cases} 1 - \left| lg(r_{fsp,Al/Si}) \right| & \forall \quad 0.1 \leq r_{fsp,Al/Si} \leq 10 \\ 0 & \forall \quad r_{fsp,Al/Si} < 0.1 \\ 0 & \forall \quad r_{fsp,Al/Si} > 10 \end{cases} \tag{3.11}$$

Closeness w.r.t K and alkali ratio is calculated as

$$r_{fsp,K/Si} = \frac{3|K|}{|Si|} \tag{3.12}$$

$$Q_{fsp,Al/Si} = \begin{cases} 1 - \left| lg(r_{fsp,K/Si}) \right| & \forall \quad 0.1 \leq r_{fsp,K/Si} \leq 10 \\ 0 & \forall \quad r_{fsp,K/Si} < 0.1 \\ 0 & \forall \quad r_{fsp,K/Si} > 10 \end{cases} \tag{3.13}$$

$$r_{fsp,NaKCa/Si} = \frac{3|Na| + 3|K| + 2|Ca|}{|Si|} \tag{3.14}$$

$$Q_{fsp,Al/Si} = \begin{cases} 1 - \left| lg(r_{fsp,NaKCa/Si}) \right| & \forall \quad 0.1 \leq r_{fsp,NaKCa/Si} \leq 10 \\ 0 & \forall \quad r_{fsp,NaKCa/Si} < 0.1 \\ 0 & \forall \quad r_{fsp,NaKCa/Si} > 10 \end{cases} \tag{3.15}$$

The similarity of a particle's composition to pure feldspar in expressed then as

$$P_{fsp} = r_{Sil} Q_{fsp,Al/Si} Q_{fsp,NaKCa/Si} \tag{3.16}$$

and to pure K-feldspar as

$$P_{fsp,K} = r_{Sil} Q_{fsp,Al/Si} Q_{fsp,K/Si} \tag{3.17}$$

For example, the P_{fsp} value becomes 1 for pure microcline or plagioclase and 0 for sodium chloride or quartz.

4 Results and Discussion – Part 1: Morocco

4.1 Study area

In situ aerosol sampling was conducted in a small study area in SE Morocco during FRAGMENT wind erosion and dust emission field campaign between 03 September and 01 October 2019. A suite of meteorological and aerosol instruments was deployed as depicted in Fig. 4.1 to measure key meteorological and aerosol quantities. Below we describe only the instruments and measurements used in this contribution. Measurements performed during the campaign with other instruments displayed in Fig. 4.1b are discussed in companion papers (González-Flórez et al., 2022; Yus-Díez et al., 2023). The study area, locally known as L'Bour (29°49'30" N, 5°52'25" W $\approx$ 500 m a.s.l.), is a small ephemeral lake located in the Lower Drâa Valley of Morocco and lies at the edge of the Saharan Desert approximately 15 km to the west of the small village M'Hamid El Ghizlane. The region is characterized by high aerosol optical depth (Ginoux et al., 2012). The location was chosen primarily based on its dust emission potential and logistical feasibility. L'Bour is approximately flat and devoid of vegetation or other obstacles within a radius of $\sim$1 km and is surrounded by small sand dune fields. The surface consists of a smooth hard crust (paved sediment) mostly resulting from drying and aeolian erosion of paleo-sediments that is analyzed in detail in a companion paper (González-Romero et al., 2023). Under favorable weather conditions, dust is frequently emitted from this source area (González-Flórez et al., 2022). PSDs of the paved sediment were analyzed using dry dispersion (minimally dispersed) and wet dispersion (fully dispersed) techniques and displayed two prominent modes at $\sim$ 100 µm and $\sim$ 10 µm (González-Romero et al., 2023). According to the fully dispersed PSD, the texture of the surface paved sediment is loam (Valentin & Bresson, 1992).

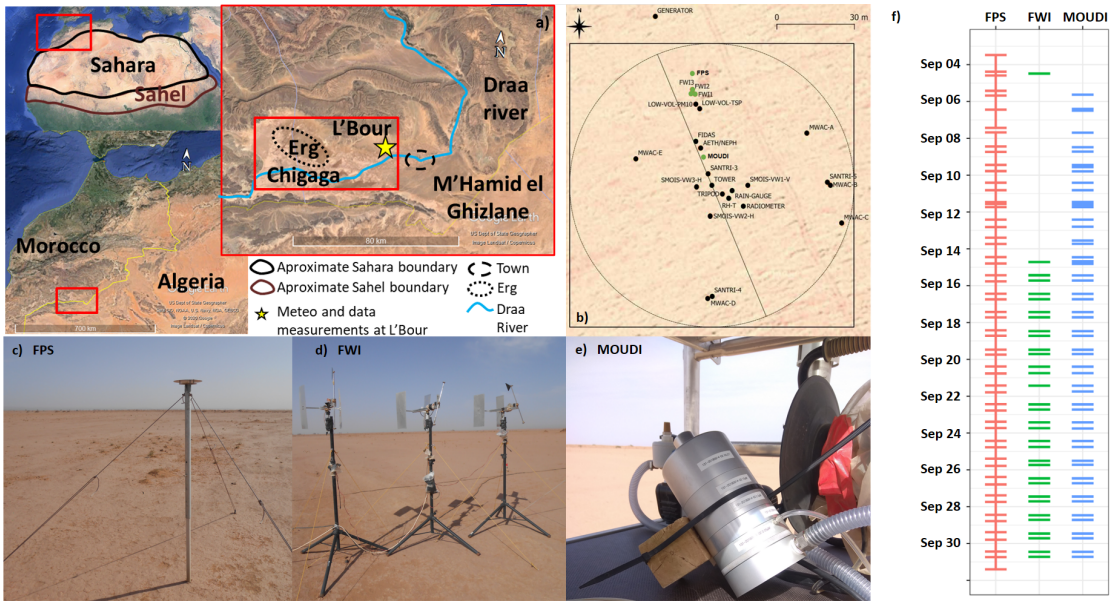

Figure 4.1: (a) Northwestern Africa showing area of operation of FRAGMENT campaign. The main location L'Bour is shown by a star sign which is located close to the Drâa river basin. (b) Schematic representation of different instruments used in the campaign with green dots highlighting those instruments used for single particle analysis. (c) Flat-plate deposition sampler (FPS). (d) Free-wing impactor (FWI). (e) Cascade impactor (MOUDI). (f) Sampling schedule of particle collection using different techniques. The horizontal bar represents start and end of sampling time. Note that due to very short sampling time for FWI and MOUDI, the two bars (start and end) appear as one. Image (a) was created using Google Earth (US Dept of State Geographer, Data SIO, NOAA, US Navy, NGA, GEBCO, ©2020 Google, Image Landsat/ Copernicus).

4.2 Particle classes

Typical chemical compositions of a set of minerals and boundary rules were used to define particle groups (see section S1 in the Supplement). Based on set classification rules, particles were assigned to different types. Figure 4.2 show the average elemental composition of these groups. However, it is important to treat this classification scheme with caution as each particle can be composed of different minerals, which in part can have variable or ambiguous compositions. As a result the groups used do not uniquely identify a mineral, but instead show the most probable mineral matching a particle composition. This is reflected in the suffix -like used in the group nomenclature.

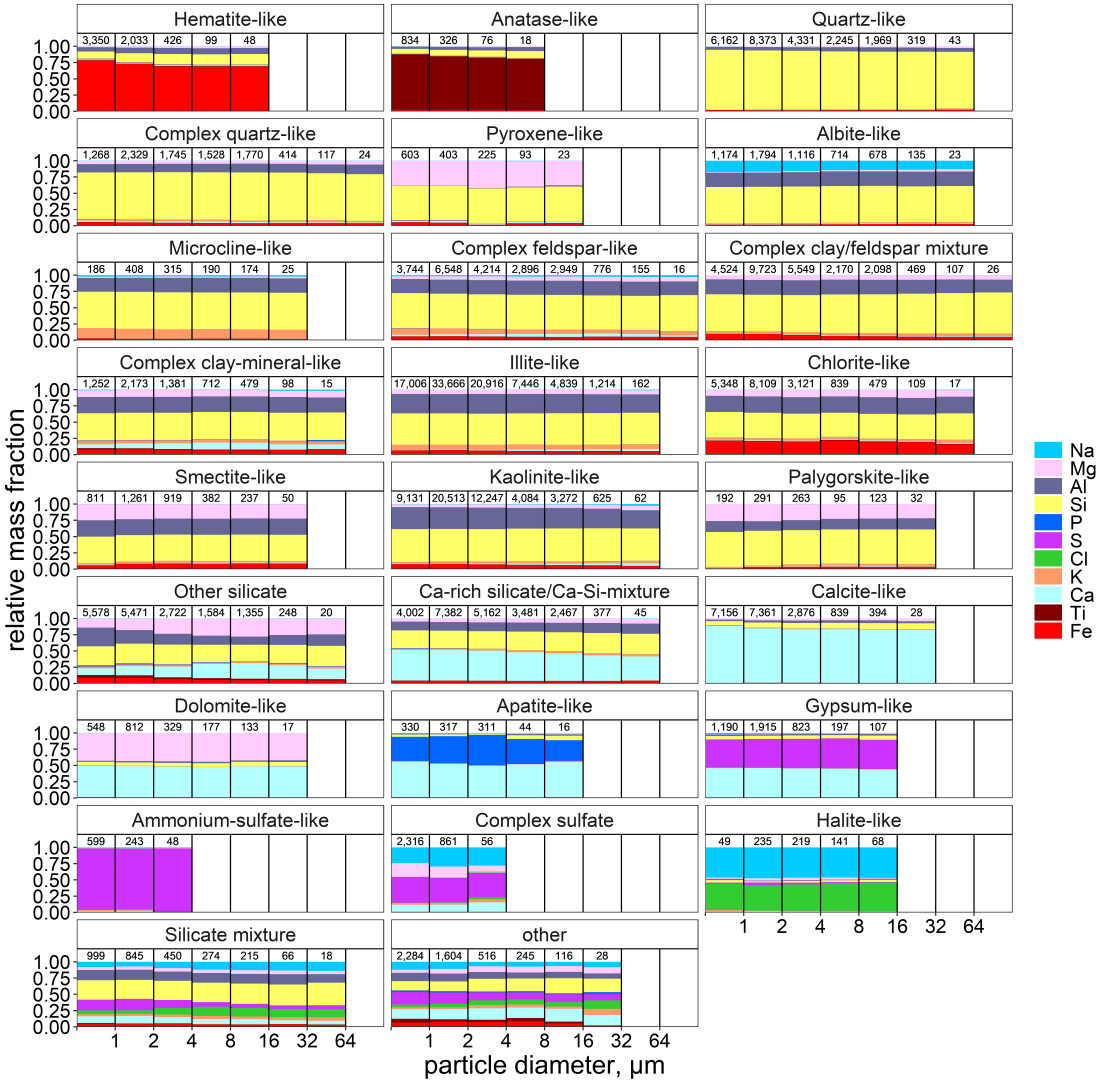

Figure 4.2: Average elemental composition as a function of particle size for different particle groups. The legend shows element index for each respective element. The numbers on top represent total particle counts in the given size bin. Abundance bars are not shown for size bins with fewer than 10 particles.

4.2.1 Oxides/Hydroxides

This class consists of hematite-like and anatase-like particles with Fe and Ti X-ray signals dominating, respectively. Both particle types were found mainly in particles with $d_v <$ 2.5 µm with anatase-like particles being rare. Iron (Fe) oxides are present both in pure crystalline form and as small impurities attached to other minerals. Moreover, Fe is present in other particle groups as well, mainly in clays and silicates. However, the presence of Fe can be due to not only Fe oxi(hydroxi)des but also to structural Fe. Fe oxides tend to exist as separate individual particles in sizes $d_v <$ 2 µm and with increasing aggregate size could be distributed as small grains throughout the aggregate volume. The number abundance of this class was usually below 2 % in the collected samples.

4.2.2 Quartz-like and complex quartz-like

The classification of particles into quartz-like is relatively straightforward with a dominant Si signal. Some of the particles with high Si were also found with slightly higher Al content associated with them and are therefore classified as complex quartz-like. Fe content of quartz-like particles is generally low and variable, suggesting that Fe oxides are not an integral part of the quartz-like particles. The particle number abundance of quartz-like particles was $\sim$ 8 % and complex quartz-like particles ranged from 1 % to 15 % depending on particle size.

4.2.3 Feldspar-like and pure feldspar abundance

The feldspar group is characterized by Si:Al:K / Si:Al:Na signal ratios of approximately 3:1:1 for microcline-like (K-feldspar) and albite-like (Na-feldspar), respectively. Ca-feldspar-like particles are quite rare in the samples. Na-feldspar particles are present across all size ranges ranging from 1.5 % in particles with $d_v <$ 2.5 µm to around 3 % in particles with $d_v >$ 2.5 µm. K-feldspar particles on the contrary are present in $<$1 % and are found mainly in particles with $d_v <$ 5 µm. The complex feldspar-like and complex clay/feldspar mixture have Si:Al signal ratios of approximately 3:1 with additional elements such as Ca, Fe and Mg, suggesting a more complex aggregate than a pure feldspar. Complex feldspar-like particles were found in the range of 5 - 8 % in particles with $d_v <$ 20 µm. For particles with $d_v >$ 20 µm , its occurrence was about 15 %. Similar number abundances were also observed for complex clay/feldspar mixtures.

Regarding the identification of feldspars, there are two approaches: One is based on the classical ‘classification’ scheme, where a fixed limit around the usual composition of

feldspars is used (detailed formalism in section 3.4), and the other is the feldspar-specific index approach, where a distance from the ideal composition is calculated. Both form different shapes in the x-dimensional element space and therefore lead to different results. The index approach has the advantage that it shows how close a particle is to an ideal composition. In this case, the feldspar indices regard the overall contribution of feldspar-specific elements to the particle and the specific Al/Si as well as alkali/Si or K/Si ratios. It was found that an index value of > 0.80 is suitable to distinguish between pure feldspar grains and other silicates. Details of the index calculation are given in S3.

4.2.4 Ca-rich

Calcium-rich particles include calcite-like, apatite-like, dolomite-like, and gypsum-like and these are characterized by high Ca, Ca+P, Ca+Mg, and Ca+S content, respectively. In gypsum-like the Ca:S weight ratio is ~ 1 and in dolomite-like particles the Ca:Mg weight ratio is ~ 1. Apatite-like particles were quite rare and only present in a few samples. The majority of the particles were calcite-like and their abundance was usually around 10 % for $d_v < 2.5$ µm and around 5 % for $2.5 < d_v < 10$ µm. This group did not include particles with appreciable Fe contents in contrast to other classes.

4.2.5 Clay minerals

Clay minerals can be divided into four subgroups: kaolinite-like, illite-like, smectite-like, and chlorite-like, with illite and kaolinite having a similar average Si-to-Al signal ratio (1.6 and 1.5 respectively), but with illite-like containing K, Fe and Mg whereas in kaolinite-like particles K is present in trace amount. These are the most abundant particle types found in the collected sample with number abundances of 25 % and 15 %, respectively. Smectite-like particles are clay minerals containing Fe and Mg, as well as small amounts of Ca and are found across all size ranges in small proportions (< 1 %). Chlorite-like particles are characterized by slightly higher Fe content compared to other clay minerals and their relative contribution is around 6 % in particles with $d_v < 2.5$ µm and 5 % in particles with $2.5 < d_v < 62.5$ µm.

4.2.6 Other silicates

The other silicate class group are characterized by the presence of Si and Al together with trace amounts of Mg, Ca, and Fe. Another silicate group in this class are Ca-rich silicates/Ca-Si-mixtures. These are typically clay minerals particles that are internally

mixed with Ca carbonates (e.g. calcite). Furthermore, Fe is also a minor component in this particle class suggesting an additional contribution of Fe oxides. The particle number abundance of other silicates class is $\sim$ 5 % and that of Ca-Si mixtures varies between 5 % to 12 % depending on particle size.

4.2.7 Mixtures and other

The silicate mixture group are dominated by Si along with the presence of other elements in varying amount and therefore does not belong to any other defined silicate group. The so-called 'other' group contains all particles that are not classified by the applied scheme into any of the groups described above. Therefore, it represents a mixture of different minerals or rare species. The relative number abundance for mixtures was around 4 % in the collected sample and the number percentage of the 'other' group is substantially low ($<$ 0.5 %).

4.2.8 Sulfates

In the sulfate group, mainly ammonium sulfate-like particles were present (i.e. only S was detected in a particle). They make up a very small amount in the total sample ($<$ 0.25 %) as individual particles and are mostly observed in particles with $d_v < 2$ µm. Ammonium sulfate is the prevalent sulfate species in atmospheric aerosols and generally of anthropogenic origin.

4.2.9 Silicate composition

The dominating composition in mineral dust is silicates which are composed of different minerals. Figure 4.3 shows the highly variable chemical composition of the silicate particles with (Mg+Fe)/Si ratio (x-axis), Al/Si ratio (y-axis), and the (Na+K+Ca)/Si ratio (z-axis, colour-coded) for each single particle. The three main clusters visible in Fig. 4.3 are numbered 1 (quartz-like), 2 (feldspar), and 3 (most other particles). As mentioned in Kandler et al. (2011b), the Al/Si ratio exhibits the least measurement uncertainty and varies significantly for different minerals. The (Mg+Fe)/Si ratio is an indicator for clay mineral aggregates as feldspar does not usually contain these elements (Anthony et al., 2003). The (Na+K+Ca)/Si ratio can be used to differentiate between feldspar and clay minerals as feldspar shows much higher values as compared to clay minerals. However, it can be also seen that this distinction is usually not clear-cut as all dust particles are usually 'contaminated' with other minerals and the aggregates have ambiguous compositions.

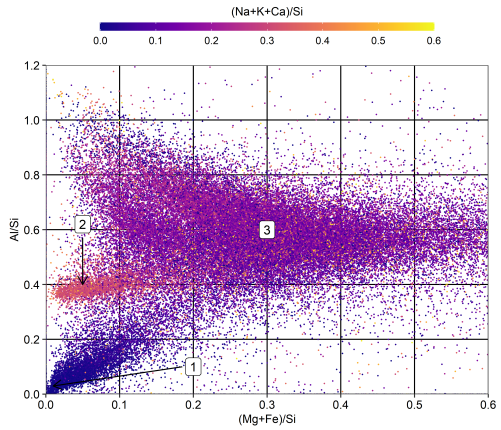

Figure 4.3: Scatter-plot for silicate particle composition. The three main clusters are marked by numbers: (1) quartz cluster, (2) feldspar cluster, and (3) clay mineral/aggregate cluster.

4.3 Comparison of PSD of different techniques for particle collection

Figure 4.4 (a) presents normalized PSD obtained by FPS, MOUDI, and OPC as described in section 2.5.2. The normalization allows to easily compare the shape of the PSD obtained with the different techniques, i.e, the relative contribution of particles of different sizes.

The PSD obtained by the FPS shows good agreement with that obtained from the OPC. The PSD of the measured volume equivalent diameter is towards the higher end of the cut-off aerodynamic diameter expected on individual MOUDI stages. In stage 3, the mode is at around 3 µm (nominal cut point 2.5 µm) and for stage 4 the mode is at 1 µm (nominal cut point 1 µm). Figure 4.4 (b) shows the PSD obtained by the FWI and is compared with the PSD from the OPC. A clear discrepancy is observed between FWI and OPC that is larger than the statistical uncertainties. Here, the FWI substantially underestimates particles < 10 µm. The collection efficiency of the FWI is 50 % for 11 µm aerodynamic diameter particles (Kandler et al., 2018) and therefore for fine mode particles the efficiency correction function can result in unrealistic values. For diameters > 10 µm, the shape of the PSD is similar to that of the OPC but the observed concentrations are still an order of magnitude smaller. The discrepancy may be linked to one or more of the following potential sources of uncertainty: not well defined efficiency curve for the FWI, and particle density

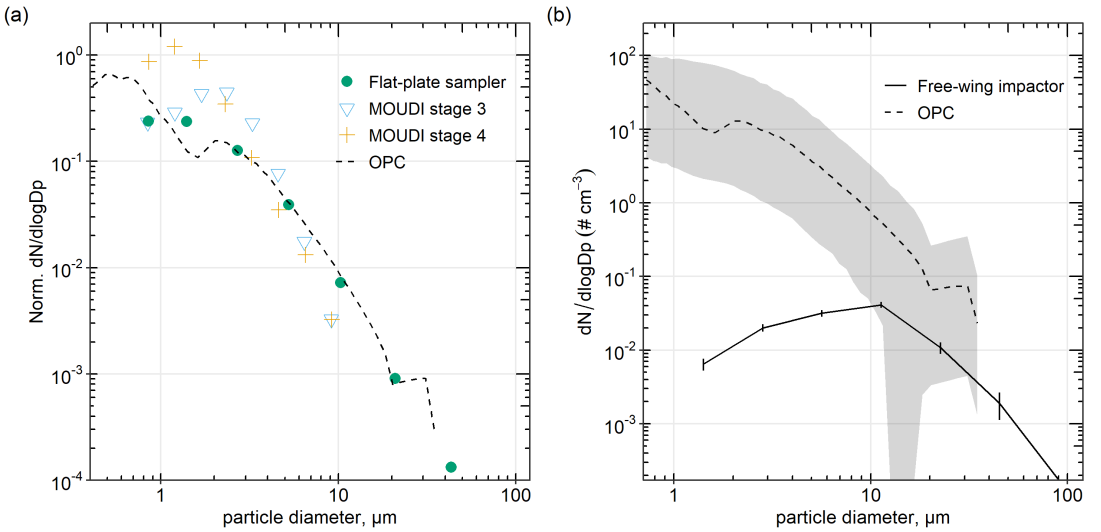

Figure 4.4: (a) Normalized particle size distribution obtained by different sampling techniques averaged over the entire campaign period. (b) Comparing the atmospheric particle size distribution between FWI and OPC. The bold line is for FWI with error bar showing the Poisson counting error and dashed line indicates the field campaign mean size distribution from OPC and the shaded region shows the 95th and 5th percentile. Note that below $\sim$ 15 µm diameter, the collection efficiency of the FWI drops significantly.

estimation from SEM to calculate volume equivalent diameter for efficiency correction. In this contribution, the shape (and not absolute concentrations) of the PSD is relevant and is quite similar among the different measurement techniques used and OPC. It therefore provides confidence in the derived size-resolved elemental composition by SEM.

4.4 Particle composition

The dependence of composition on size is shown in Fig. 4.5 and Table 4.1 for aerosol samples collected with three different sampling techniques. Since the composition of the aerosol particles in each sample does not exhibit a large sample-to-sample variability (see Appendix for individual samples), all of the dust sample compositions were merged for further comparison. Furthermore, the collection efficiency by size is less relevant to the fractional contribution of each mineral type per size and therefore integrating all the techniques together improves the statistics per each size with higher number of particles

analysed.

A clear trend is seen among the different particle groups based on their size. Clay minerals are the most abundant and are present across all size ranges. Quartz-like particles are found in each size class with almost similar mass abundance (around 5-8 %) whereas the mass fraction for complex quartz-like grows with particle size from 2 % in $d_v < 1$ µm to 22 % in $d_v > 64$ µm. This suggests that as particle size increases, quartz particles get internally mixed with elements like Al and Fe forming complex aggregates. Likewise, a similar trend is observed for feldspar particles where complex feldspar-like particles increase with particle size as a result of the inclusion of other elements creating a complex mixture. This observation is consistent with Engelbrecht et al. (2017, 2016) that found larger particles to be generally present as aggregates and coatings on other mineral particles. A detailed discussion on feldspar particles is addressed further in Sect. 3.3.4. Fe-rich particles are present in low quantities and and their contribution decreases with particle size. As they are highly relevant in controlling spectral shortwave refractive index (Caponi et al., 2017; Di Biagio et al., 2019; Engelbrecht et al., 2016), they are further discussed in detail in section 3.3.3. Furthermore, iron is detected across all the size classes and present in most of the particle groups. This could further have implications for the absorption as absorption increases with particle size which could be further enhanced because of the iron content. Similarly, the proportion of Ca-rich particles (calcite, dolomite as well as gypsum and apatite) are mainly confined to particles smaller than 4 µm. The Ca-Si mixture is slightly enhanced at $d_v > 4$ µm which could be due to the availability of more silicates to form aggregates with calcite and also the depletion of illite-like particles could partly form aggregates with calcite too. Sulfate-like particles are mainly present in the smallest size bin of < 1 µm. These are most probably anthropogenic/secondary aerosol as corroborated with measurements of optical properties (Yus-Díez et al., 2023) and PSD (González-Flórez et al., 2022).

Studies on individual particle analysis of mineral dust by SEM/EDX have provided insights into the compositional variability, size and morphological characteristics of dust particles from different regions. Kandler et al. (2009) presents composition of Saharan mineral dust collected during the SAMUM campaign from in situ measurements at Tinfou, Morocco in May/June 2006 and thus providing an ideal comparison to our findings. On average, their particle composition between 0.5 µm and 50 µm diameter is also primarily alumino-silicates with a smaller contribution of quartz and calcium-rich particles.

However, one finding of note from Kandler et al., 2009 is the observation of quartz fraction to increase with particle size, mainly for particles larger than 20 µm in diameter. Although our result reveal the quartz/complex-quartz-like to increases with particle size,

Table 4.1: Size resolved mass fraction (%) of particles in each particle class (number fraction in parentheses).

	Size class in µm						
Particle type	0.1-1	1-2	2-4	4-8	8-16	16-32	32-64
Hematite-like	3.75 (4.15)	1.40 (1.62)	0.57 (0.62)	0.33 (0.32)	0.16 (0.21)		
Anatase-like	0.84 (1.03)	0.22 (0.26)	0.09 (0.11)	0.06 (0.06)			
Quartz-like	7.99 (7.64)	6.76 (6.70)	5.97 (6.10)	8.40 (7.47)	7.95 (8.31)	6.34 (6.22)	5.41 (5.13)
Complex quartz-like	1.72 (1.58)	1.98 (1.87)	2.68 (2.51)	5.78 (5.09)	7.59 (7.43)	8.93 (8.38)	16.62 (14.24)
Pyroxene-like	0.56 (0.75)	0.31 (0.32)	0.39 (0.33)	0.25 (0.31)	0.08 (0.10)		
Albite-like	1.64 (1.46)	1.45 (1.43)	1.51 (1.58)	2.69 (2.34)	2.72 (2.77)	2.66 (2.62)	2.97 (3.03)
Microcline-like	0.24 (0.23)	0.38 (0.33)	0.45 (0.44)	0.65 (0.62)	0.71 (0.72)	0.45 (0.53)	
Complex feldspar-like	5.08 (4.64)	5.34 (5.25)	6.36 (6.01)	10.48 (9.50)	12.29 (12.13)	15.95 (15.29)	18.33 (18.79)
Illite-like	22.11 (21.09)	27.85 (26.93)	30.31 (29.76)	21.54 (23.85)	20.79 (19.78)	23.38 (23.72)	17.86 (19.72)
Chlorite-like	6.80 (6.63)	6.16 (6.48)	4.15 (4.41)	2.31 (2.68)	1.96 (2.01)	1.96 (2.07)	2.04 (2.10)
Smectite-like	1.01 (1.01)	1.01 (1.01)	1.41 (1.31)	1.08 (1.21)	1.03 (0.98)	0.90 (0.99)	
Kaolinite-like	12.42 (11.33)	16.94 (16.40)	17.13 (17.18)	12.82 (13.29)	14.60 (14.07)	11.85 (12.78)	7.50 (7.58)
Palygorskite-like	0.23 (0.24)	0.25 (0.23)	0.36 (0.37)	0.32 (0.32)	0.56 (0.51)	0.58 (0.62)	
Ca-rich silicate/Ca-Si-mixture	5.06 (4.97)	6.11 (5.91)	7.48 (7.35)	12.19 (11.71)	9.21 (10.17)	7.23 (7.32)	6.12 (5.60)
Calcite-like	8.00 (8.87)	5.42 (5.88)	3.49 (4.06)	2.77 (2.88)	1.35 (1.66)	0.44 (0.53)	
Dolomite-like	0.70 (0.68)	0.60 (0.65)	0.43 (0.48)	0.62 (0.59)	0.50 (0.54)	0.25 (0.35)	
Apatite-like	0.35 (0.41)	0.26 (0.25)	0.67 (0.65)	0.09 (0.15)	0.06 (0.07)		
Gypsum-like	1.39 (1.47)	1.31 (1.53)	0.89 (1.17)	0.57 (0.66)	0.38 (0.47)		
Ammonium-sulfate-like	0.58 (0.74)	0.13 (0.19)	0.06 (0.07)				
Complex sulfate	2.19 (2.87)	0.40 (0.69)	0.05 (0.08)				
Halite-like	0.09 (0.09)	0.23 (0.23)	0.28 (0.31)	0.52 (0.49)	0.24 (0.29)		

it is not the dominant component as reported in Kandler et al. (2009). Marsden et al. (2019) present the mineralogy and mixing state of particles smaller than 2.5 µm in laboratory-suspended northern African dust using SEM. They found a dominance of clay minerals in the size < 2.5 µm which is similar to the observations reported in the current study. Scheuvens et al. (2011) observed compositional homogeneity of dust over southern Morocco, consistent with our results indicating dust at source regions to be not usually affected by anthropogenic components. Additionally, compositional and morphological homogeneity was also reported by Chou et al. (2008) for dust samples taken over Niger. Nevertheless, our study shows distinct compositional signatures of prominent source area (e.g. occurrence of apatite-like particles, elevated Ca-rich content). For the Middle East, Jish Prakash et al. (2016) reported relative mass abundance of 45-75 % clay minerals, 5–54 % feldspar, and 0.1–10.2 % quartz as main components, while calcite, dolomite, gypsum, and iron oxides were the minor constituents of individual dust particles in the size range 0.5–38 µm. This is quite similar to our results if the 'complex' part of the quartz and feldspar fraction together with its 'mineral-like' component is considered as one fraction suggesting a similarity between Arabian and Saharan dust. A separate study from Engelbrecht et al. (2009) found quartz and feldspars to be dominant particle type in Kuwait while calcite and dolomite were major components in the dust particles from the UAE and Iraq. This is quite different to the mineralogy in our study and could be due to the different chemical weathering regime and the composition of the parent sediments. In Asia, Jeong (2008) reported mineralogical properties of Asian dust to mainly consist of

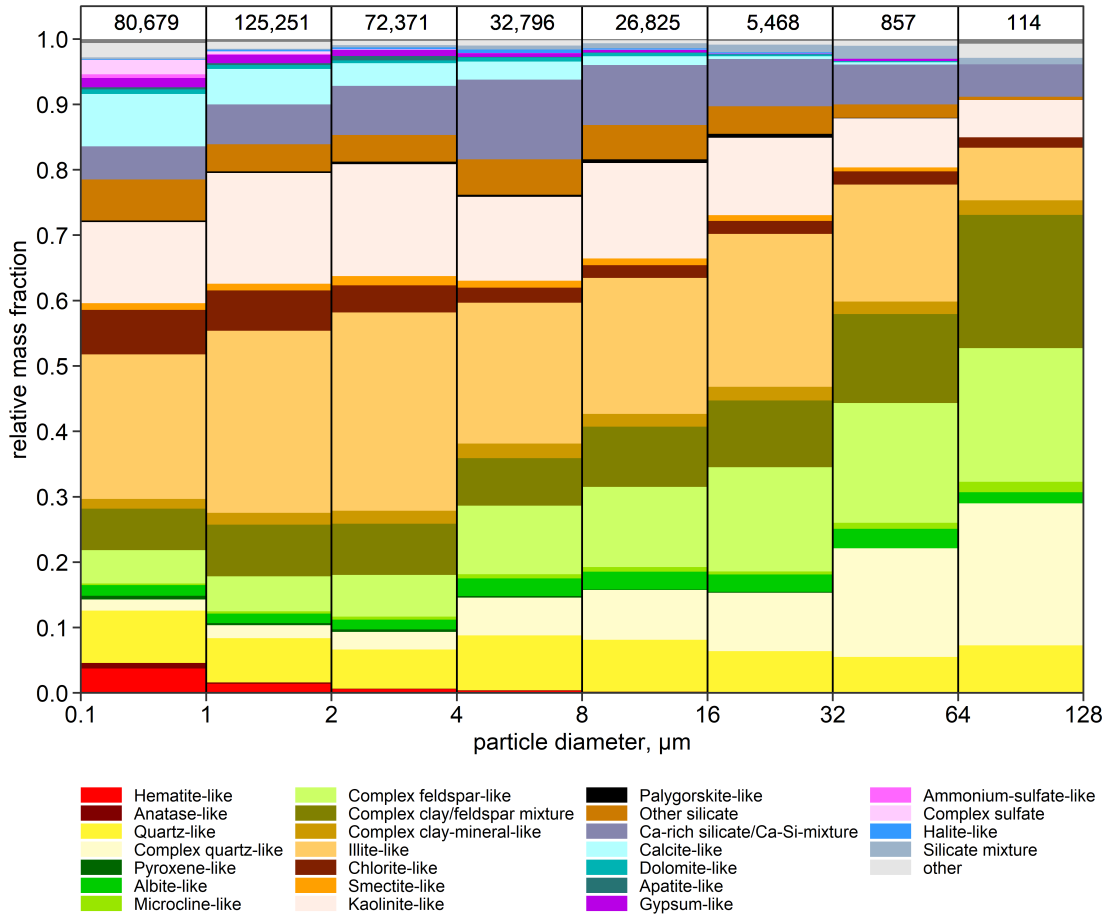

Figure 4.5: Average size-resolved mass abundance of different particle groups. The numbers on top represent total particle counts in the given size bin.

clay aggregates (48 %), quartz (22 %), plagioclase (11 %), calcite (6 %), and K-feldspar (5%). The mineral composition of Asian dust therefore has a higher K-feldspar content compared to our findings in Morocco while illite is observed in both the Asian dust and our study as major clay mineral.

4.4.1 Particle abundances using different techniques

Figure 4.6 shows the compositional information for dust samples obtained using 3 different collection techniques. These techniques have different collection efficiencies, target size ranges, and sampling intervals. The goal was to get a representative number of particles across a wide size distribution, which is usually the case for mineral dust. However, the collection of particles larger than a few micrometres is relatively difficult due to the poor collection efficiency of many instruments. Therefore, in this work an inlet-free impactor i.e. FWI was used to sample particles with $d_v > 3$ µm whereas FPS and MOUDI were used primarily for particles having $d_v < 3$ µm. The non-parallel sampling time of the sampling techniques during the present field campaign could not be avoided as FWI and MOUDI operate actively while the FPS operates passively. The active samplers have a much higher collection velocity. This requires short sampling time for the two active samplers. On the contrary, the passive sampler (i.e., FPS) require a much longer sampling time. Using the same collection time would result in either underloading of the passive or overloading of the active samplers.

In the MOUDI sample, most of the collected particles ($>$ 97%) had $d_v < 5$ µm. In stage 3, 56 % of the collected particles were within the specified stage size range; the size of half of the remaining particles was below the lower cutoff and that of the other half was above the upper cutoff. The major constituents were illite-like, kaolinite-like, quartz-like, Ca-silicate mixture, complex clay/feldspar mixture, and calcite-like with feldspar-like, quartz-like, hematite-like and sulfates as minor constituents. A similar trend was also observed in stage 4 of MOUDI except for an enhanced abundance of kaolinite-like and complex clay particles. In the FPS samples, the number of collected particles in the size range $0.1 < d_v < 5$ µm is quite comparable to stage 3 of MOUDI. For particles with $d_v > 5$ µm, the composition changes only slightly by increasing quartz-like and decreasing calcite-like particles. In the FWI samples, more than 70 % of particles had $d_v > 5$ µm. The number abundance of feldspar-like, quartz-like, complex feldspar-like and complex clay/feldspar mixture particles increases with increasing particle size, while the number abundance of clay-like particles tends to decrease. In contrast, calcite-like, gypsum-like, and sulfates are virtually absent in samples from FWI in $d_v < 3$ µm which is the size range where they are typically observed. However, the number of particles analysed in the given size is significantly less compared to FPS or MOUDI. Note that it was not possible to perform sampling with FWI and MOUDI under the highest dust concentrations due to the high concentrations and as a consequence extremely short sampling times, which would have been necessary.

Differences in abundance for some of the classes among the different techniques might

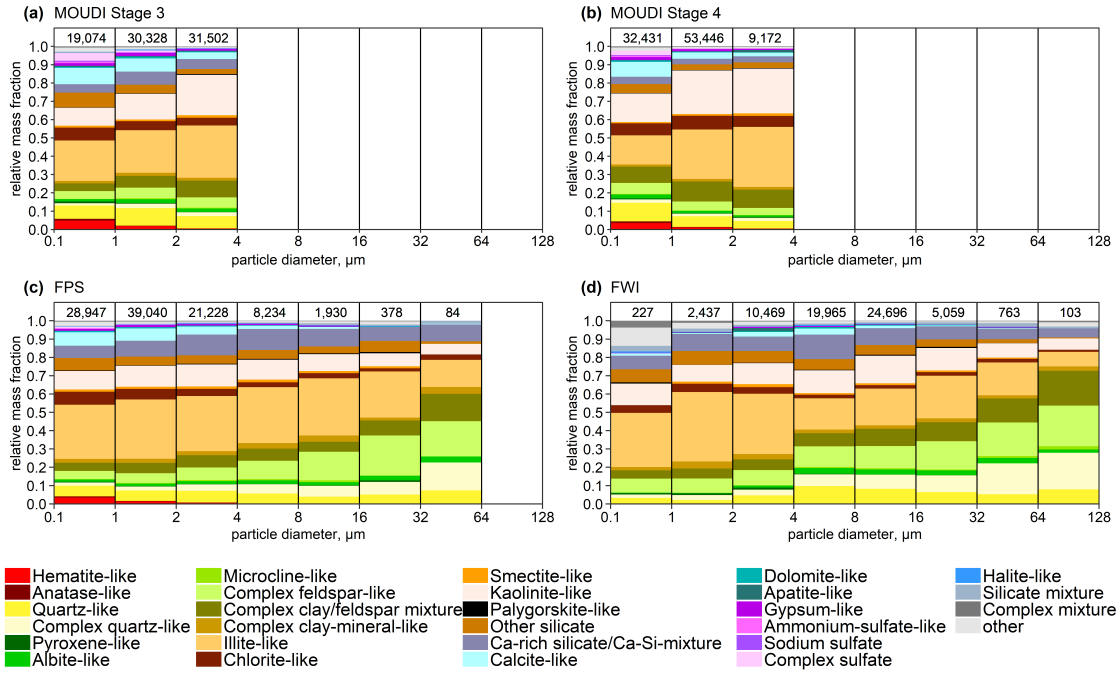

Figure 4.6: Average size-resolved mass abundance of different particle groups using different sampling techniques collected over the campaign period. The numbers on top represent total particle counts in the given size bin. Abundance bars are not shown for size bins with fewer than 30 particles.

be due to the way by which particles reach the substrate. In MOUDI and FWI, particles are impacted on the substrate whereas in FPS particles are deposited by gravitational settling and turbulent diffusion. One hypothesis for such difference is that in the MOUDI the high impaction speed experienced by particle aggregates on the top stages may break some of them into smaller ones and get carried away along the air streams onto the lower stages. Such a hypothesis is consistent with the enhancement of clay-like aggregates in MOUDI. Other observed differences between the sampling techniques could be related to the non-parallel sampling times. MOUDI and FWI samples represent a few minutes compared to the usually half-day exposure time for FPS. However, as variations in the composition are fairly similar for all of our analysed samples, the latter is most likely not a major aspect.

4.4.2 Temporal variability

Figure 4.7 displays time series of number abundances in three size ranges for the different particle groups observed in deposition samplers. While the dependence of particle size distribution on sample mineralogy is quite strong, the temporal variation of the major particle groups does not show significant variability. This behaviour is to be expected as sampling was done in the source region, and the average daily composition is relatively constant.

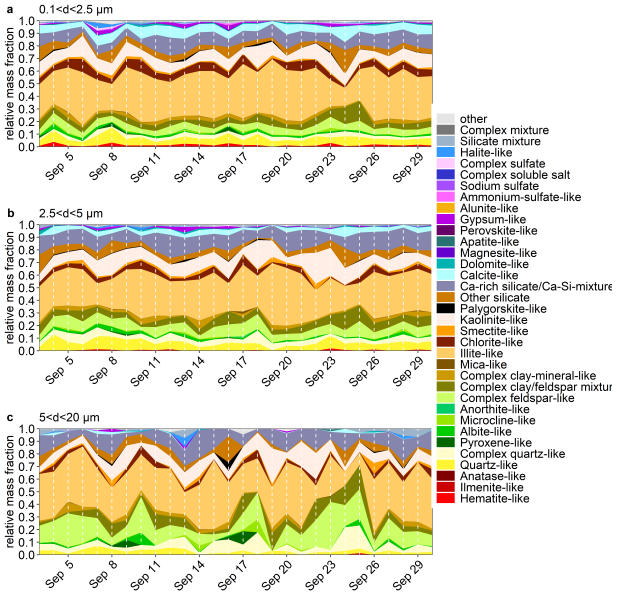

Figure 4.7: Time series of chemical composition for particles in (a) $0.1 < d < 2.5$ µm, (b) $2.5 < d < 5$ µm and (c) $5 < d < 20$ µm in L'Bour.

Nevertheless, looking at specific samples we can observe distinct compositional differences. Figure 4.8 shows chemical composition for four different situations. Secondary sulfates were dominant in particle $d_v < 2$ µm in samples collected during 8-10 September when the wind comes from the east (i.e. M'Hamid) suggesting anthropogenic origin which is further corroborated with measurements of optical properties (Yus-Díez et al., 2023) and PSD (González-Flórez et al., 2022). This was also observed for small particles in the SAMUM campaign in Tinfou, Morocco (Kaaden et al., 2009). Apatite-like particles were almost non-existent in our samples except for some specific days (20 and 23 September). They were identified by the presence of Ca and P. Furthermore, manual inspection of

the particles showed it to be not beam-sensitive with no Cl and F signals detected. Even though hydroxyapatite [$Ca_5OH(PO_4)_3$] is not commonly found in the Morocco phosphate deposits, the absence of Cl and F suggests it to be OH-apatite originating from a distinct geogenic source. Most of these particles were confined to size d_v 2-4 µm. In these particles, phosphorus is attached to the crystal lattice which is one of the important dust-derived nutrients for marine and terrestrial ecosystems controlling phytoplankton productivity and carbon uptake (Stockdale et al., 2016). The sampling day of 24 September is characterized by elevated Ca-rich particles making it the most calcium-rich day and were present mainly in $d_v < 1$ µm. Here it was present in 30 % compared to the average of 5 %. This observation could be due to advection from a prominent dust source. Furthermore, the iron-rich particle is also quite pronounced on this day indicating a special source imprint.

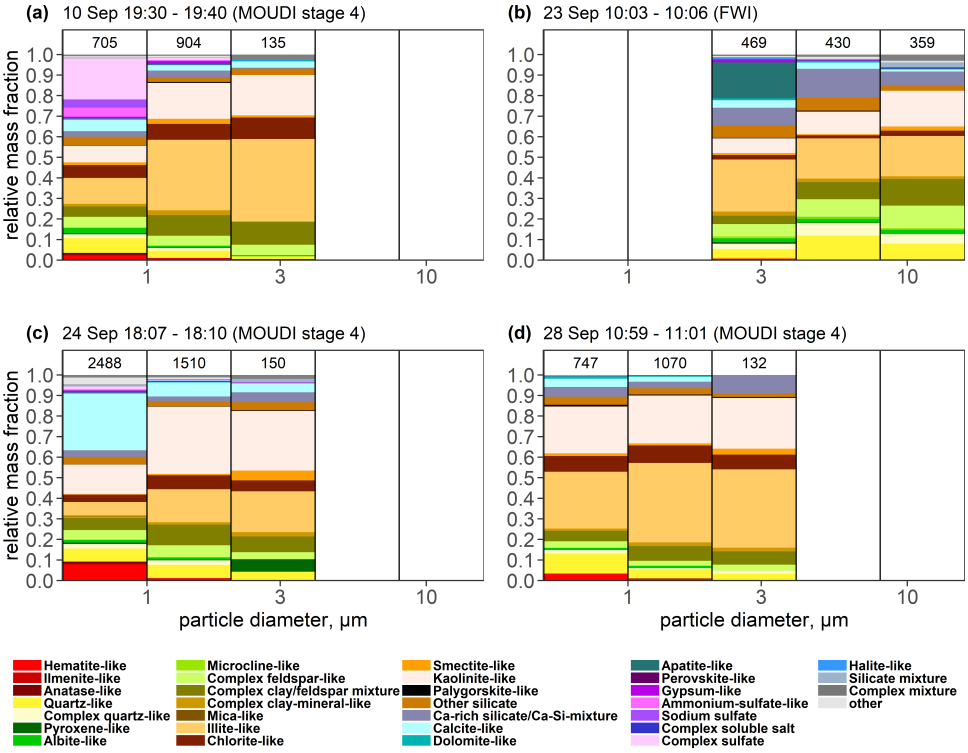

Figure 4.8: Phase compositions of size bins for samples collected under specific meteorological conditions at specific times and on certain days: (a) sulfate episode (b) apatite particle (c) Ca-rich episode and (d) typical average composition. The total number of analyzed particles is given for each size class with fewer than 30 particles not shown.

4.4.3 Iron distribution

Clay minerals and Fe-oxi/hydroxides such as hematite, goethite and magnetite, contain Fe, which is a key ingredient to numerous climatic, environmental and biological processes affected by dust (Schulz et al., 2012). Fe in minerals can be broadly classified into structural Fe, which is typically found in the crystal lattice of clay minerals, and Fe in the form of oxide or hydroxide particles (mainly hematite and goethite) (Kandler et al., 2009; Scheuvens et al., 2011). The amount of free Fe-oxi/hydroxides along with its size, and aggregation or mixing state (internal vs external mixing) with other minerals determine the degree of absorption of solar radiation by dust (Di Biagio et al., 2019; Moosmüller et al., 2012; Sokolik & Toon, 1999; Zhang et al., 2015), and the potential Fe solubility (Baker & Jickells, 2006; Marcotte et al., 2020) of the deposited dust that fertilizes the ocean. In addition, it has been suggested that ocean primary productivity depends not only on the dissolved Fe but also on suspended solid Fe particles and their mineralogical components (Hettiarachchi et al., 2021). Furthermore, dust absorptive properties vary in different source regions mainly due to variations in the Fe oxides fraction (Lafon et al., 2006). While SEM cannot distinguish between structural and free Fe, by providing the total Fe content on a particle-by-particle basis, it can provide some useful clues on the mixing state of Fe-oxi/hydroxides.

To understand the Fe content and to some extent the mixing state along with the type of particles that Fe is associated with, Fig. 4.9a shows the relative abundance of particles classified into nine categories according to their Fe content as a function of particle size, and Fig. 4.9b further displays the relative abundances of particles for each of the nine Fe categories and particle size ranges according to three Al/Si ratio categories. The Al/Si ratio is chosen because it has little measurement uncertainty, and varies significantly for different mineral groups as discussed in section S 2.9 of the Supplement. High Al/Si ratios indicate dominance of structural Fe-containing clay minerals, like illite, smectite and chlorite, which also tend to be internally mixed with Fe-oxi/hydroxides (Kandler et al., 2011b). Low Al/Si ratios tend to be associated with quartz-like particles.

The relative mass of particles with Fe fractions above 0.1 decreases with increasing particle size. Among these, particles with Fe fractions above 0.5 are hematite-like particles as shown in Fig. 4.9a; their relative abundance is $\sim$ 4 % below 1 µm, which decreases steeply with size to the extent that no appreciable amounts are observed above 4 µm. Given the amount of Fe, these hematite-like particles are mostly composed of Fe-oxi/hydroxides and to first order could be taken as externally mixed Fe-oxi/hydroxide particles. However, they still show some degree of aggregation with other minerals that increase with particle size. This can be appreciated in Fig. 4.2, where hematite-like particles show increasing amounts

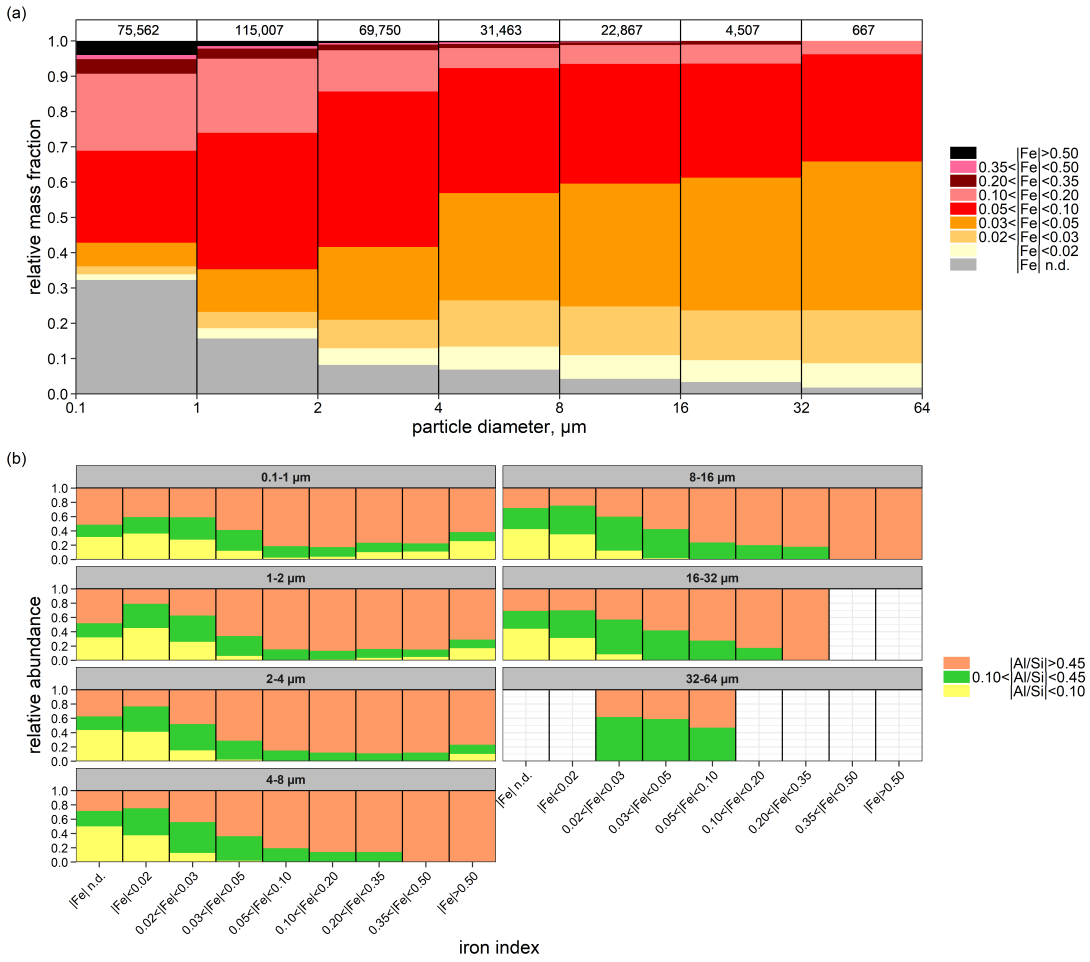

Figure 4.9: (a) Size resolved iron indices for silicate particles. “n.d.” means Fe not detected. The numbers on top represent total particle counts in the given size bin. (b) Silicate particle with iron association based on Al/Si ratio. Abundance bars are not shown for size intervals with fewer than 30 particles because of high statistical uncertainty.

of Si, Al and Mg with size. Figure 4.9b shows that aggregation of Fe-oxi/hydroxides (Fe $>$ 0.5) in hematite-like particles happens mainly with clays (high Al/Si ratios), but particles with low Al/Si ratios were also observed for diameters $<$ 4 µm. These are most likely for a fraction of particles (e.g. complex quartz-like) with some free Fe (oxy-hydr)oxides (e.g., goethite and hematite) assemblages.

Particles with Fe fractions between 0.2 and 0.5 follow a similar decrease in relative abundance with particle size although there are still appreciable amounts of particles up to 8 µm. Such particles are mostly classified as chlorite-like; in Fig. 4.2 chlorite particles feature Fe fractions above 0.2, and in Fig. 4.5 the abundance of chlorite-like particles decreases with particle size. However, the presence of Fe-oxi/hydroxide internal mixtures is very likely, particularly in particles with Fe contents towards the higher end of the 0.2-0.5 range. The relative number of particles with Fe fractions between 0.1 and 0.2 also decreases with particle size; such particles have mainly a high Al/Si ratio (clay minerals, such as illite, smectite and chlorite) (Fig. 4.9b). Interestingly, the relative mass abundance of particles with no Fe detected reaches $\sim$ 0.32 below 1 µm and thereafter also decreases with particle size. All in all, these results show that Fe-oxi/hydroxides tend to be increasingly internally mixed with other minerals, especially clays, as particle size increases. In other words, the volume fraction of Fe-oxi/hydroxides in aggregates decreases with particle size.

Conversely, with increasing particle size, the relative number of particles with Fe fractions between 0.03 - 0.05 increase, and that of particles with intermediate Fe content (0.05 - 0.10) tend to increase for particle sizes between 0.1 and 4 µm (26 % to 44 %) while remaining approximately invariant ($\sim$ 30 %) above 4 µm. Such increasing trends with particle size are also visible for particles with Fe contents below 0.03. The increase in particles with lower Fe content with particle size is mostly due to the increasing amount of complex clay-feldspar mixtures, complex feldspar-like and quartz-like aggregates (Fig. 4.5) with lower Al/Si ratios (Fig. 4.9b).

The mean Fe abundance is 0.09 and is dependent on size with values of 0.095 in the size range $0.1 < d < 2.5$ µm and 0.06 for particles $2.5 < d < 64$ µm. This is consistent with observations in Tinfou, Morocco (mean 0.053) for particles between 1 and 20 µm (Kandler et al., 2009).

Figure 4.10a shows the relative contribution of each particle type to Fe in every particle class. In comparison to the particle type fractions displayed in Fig. 4.5, the hematite-like and chlorite-like particles have an increased proportion because of their higher contribution in terms of Fe content, and the calcite-like and Ca-rich silicate group gets substantially diminished due to the absence of Fe in carbonate minerals. It is remarkable to see that the iron contribution of clay-like aggregates (illite, smectite and kaolinite) increases with particle size up to $\sim$ 4-8 µm, which suggests (and further confirms) increased internal mixing with Fe-oxi-hydroxides. Figure 4.10b shows the mass fraction of elemental Fe as a function of particle size and is calculated by dividing the average estimated mass of Fe in a particle by the average estimated mass of particle. The total Fe in dust is greatly reduced

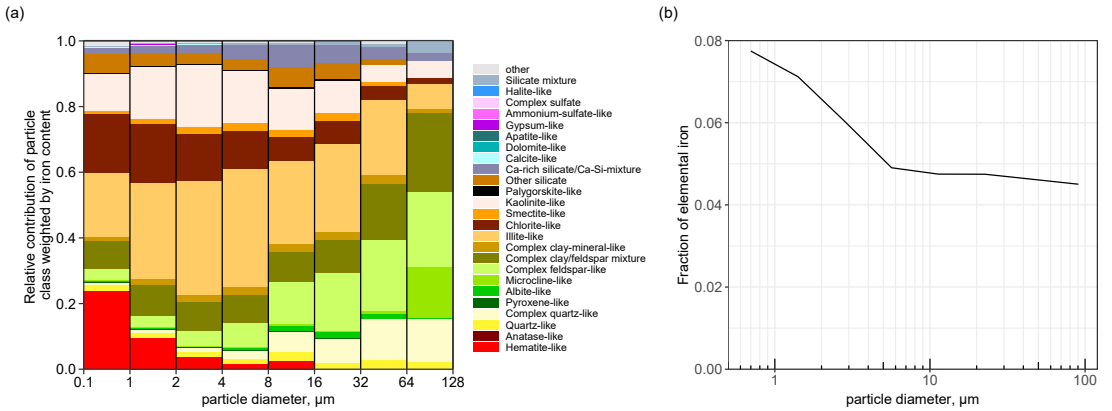

Figure 4.10: (a) Relative contribution of each particle type to total iron and (b) fraction of elemental iron by mass with respect to all the other elements.

with size, particularly up to $\sim$ 5 µm, going from $\sim$ 8 % below 1 micron to less than 5 % in particles above 6 µm. This is slightly higher than the values of fractional mass of elemental iron obtained for Moroccan soil using X-ray Fluorescence (XRF) analysis which was reported to be 3.6 % for $PM_{10.6}$ (Caponi et al., 2017; Di Biagio et al., 2019).

Overall, our results suggest that fine dust particles are more enriched with Fe due to both the presence of small-sized Fe-oxi-hydroxide (hematite-like) and the increase in feldspar and quartz with particle size, which reduces the fractional abundance of clay-like particles internally mixed with Fe-oxi-hydroxides. Scheuvens et al. (2011) also observed Fe-rich particles to be relatively scarce ($<$ 1.5 % in particle number fraction). In contrast, less proportion of Fe-rich was observed from more southerly source areas (Chou et al., 2008). Usually Fe-rich particles are associated with alumosilicates (Deboudt et al., 2012; Moskowitz et al., 2016; Reynolds et al., 2014; Scheuvens et al., 2011) and are often located at the particle surface and has implications for particle refractive index. All these observations are complementary to the laboratory results obtained by Baddock et al. (2013) that showed abrasion from saltating particles can release Fe-rich nanoparticles from larger aggregates. As fine dust particles are more prone to long-range transport, this might provide an increased amount of soluble Fe. However, due to the association of Fe in different particle groups, it is difficult to estimate the fraction of soluble Fe available after deposition in ocean biogeochemistry and thereby the global carbon cycle or terrestrial ecosystem as a nutrient with the method used in this work. Nevertheless, as observed by Marcotte et al. (2020), the Fe solubility (% dissolved Fe/total Fe in the mineral) in

pure Fe-bearing clay materials was higher by an order of magnitude than in pure Fe oxide minerals so the dust transported from this region could be a major source of nutrient.

4.4.4 Feldspar

Feldspar, and in particular K-rich feldspar, are discussed as the most efficient ice nuclei among the different mineral constituents found in dust (Atkinson et al., 2013; DeMott et al., 2018; Harrison et al., 2016) and are therefore of interest for atmospheric processes.

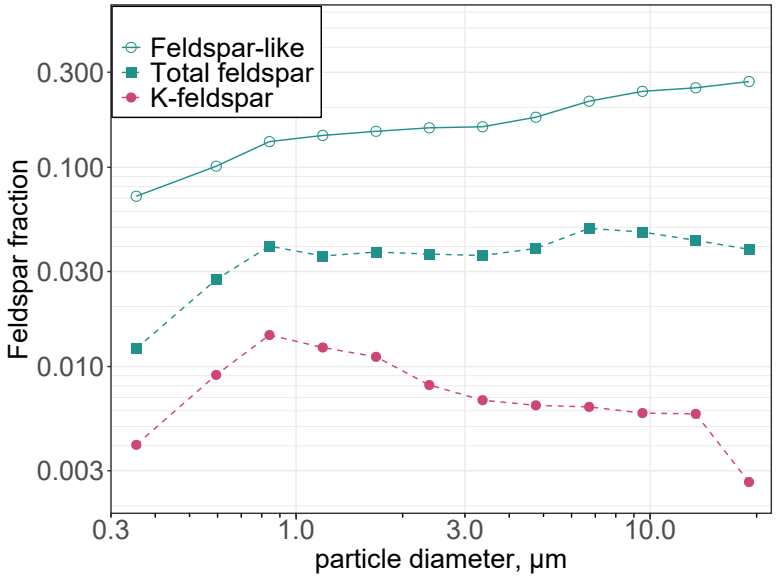

Figure 4.11: Mass ratio of Feldspar-like, Total feldspar (more strict criterion), and K-feldspar (more strict criterion) to total particles.

Figure 4.11 shows the feldspar relative mass ratio for K-feldspar and total feldspar to total particles as determined by the feldspar index approach (see Section S2.3 in the Supplement for the distinction between the two different approaches for feldspar characterization). Here the total feldspar includes K-feldspar, Na-feldspar, and other feldspar. For comparison, the 'relaxed' in contrast to strict classification scheme of feldspar-like particles is also shown which includes albite-like, microcline-like, anorthite-like, complex feldspar-like, and complex clay/feldspar mixture. In general, our analysis shows that approximately 3 % of the dust aerosols are relatively pure, externally mixed feldspar particles whereas relatively pure, externally mixed K-feldspar particles are less than 0.5 % by mass. With

the inclusion of internally mixed feldspar, an increasing trend is observed with particle size. Studies have found the K-feldspar content of dust to be highly variable with values up to 25 % for Moroccan dust (Atkinson et al., 2013). Since the PSD of K-feldspar at the source determines how much of it is transported across long distances, our finding shows that the relative amount of externally mixed K-feldspar particle is size independent up to 10 µm. For long-range transported dust over Barbados, no significant variation was reported for K-feldspar under different dust conditions but are slightly lower than the values reported here using the same technique as in this study (Harrison et al., 2022; Kandler et al., 2018).

4.5 Particle shape

Dust particles were found to be highly aspherical and displayed a wide range of AR values for the size range 0.5 $< D_p <$ 100 µm, which is consistent with previous studies of Northern African dust (Chou et al., 2008; Kandler et al., 2009). The median AR of particles is 1.46 and is almost independent of particle diameter as seen in Fig. 4.12 (b). It is slightly lower than the one found in previous AR measurements of Moroccan dust (median 1.6) (Kandler et al., 2009) but is similar to the Asian dust (median 1.4) (Okada et al., 2001) and those observed in Niger during aircraft campaign (Matsuki et al., 2010). These are also substantially lower than values reported for long-range transported Saharan dust (Coz et al., 2009; Reid et al., 2003a). The discrepancy in observations at the point of the source region and transported dust could be the preferential removal of lower AR particles at the source due to their higher gravitational settling velocity than elongated particles of the same volume (Yang et al., 2013). Other median values found in the literature at the source location are 1.7 during African Monsoon Multidisciplinary Analysis (AMMA) campaign in Niger (Chou et al., 2008), 1.55 during Geostationary Earth Radiation Budget Intercomparisons of Longwave and Shortwave radiation (GERBILS) campaign over Mauritania, Mali and Niger (Klaver et al., 2011). A median value of 1.3 was found during the Fennec campaign in the central Sahara (Rocha-Lima et al., 2018) for particles $<$ 5 µm and during AERosol Properties - Dust (AER-D) aircraft measurement median of 1.3-1.44 for 0.5 to 5 µm, 1.30 for 5 to 10 µm and 1.51 for 10 to 40 µm was observed for dust particles collected in the Saharan Air Layer and the marine boundary layer (Ryder et al., 2018). It should be noted that the AR calculation done in several of the studies mentioned are not directly comparable as systematic difference occur as function of the measurement approach (Huang et al., 2020). While the values here are corrected after Huang et al. (2020), a bias might still remain.

The density distribution with respect to the AR can be parameterized by a modified log-normal distribution (Kandler et al., 2007):

$$h(AR) = \frac{1}{\sqrt{2\pi} \cdot (AR-1) \cdot \sigma} \times exp\left[-\frac{1}{2}\left(\frac{ln(AR-1)-\mu}{\sigma}\right)^2\right] \tag{4.1}$$

Figure 4.12 (a) shows the parameterization curve together with the measured values for all particles and in Table 4.2 the fitting parameters σ and μ along with the median value are given for different particle classes. Most of the particle groups have a similar median AR of 1.46 except for dolomite, which has the lowest median AR of 1.35. While the AR is generally independent of particle size and particle types, slightly higher aspect ratios are observed for internally mixed particles. Differences with other locations could then be at least partly explained by differences in mineralogical composition and mixing state.

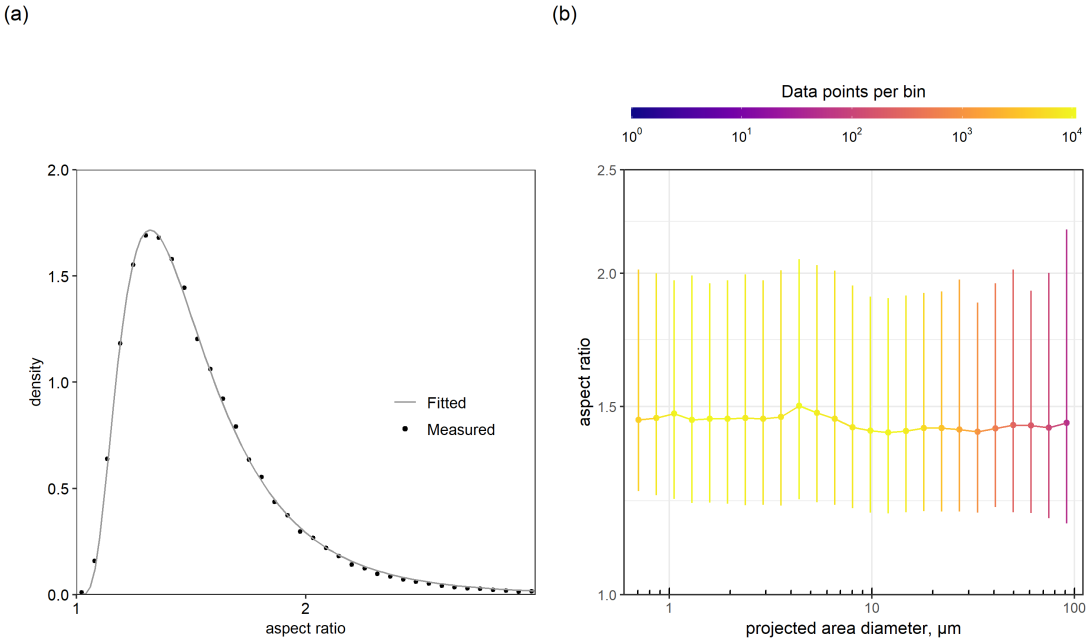

Figure 4.12: (a) Measured and parameterized (solid line) aspect ratio density distribution of dust particles (b) Size-resolved particle aspect ratio. The bar range represents the range between 0.1 and 0.9 quantiles with dot being the median and the bins are color coded by the number of data points within each bin.

Table 4.2: Parameters of the aspect ratio density distribution, mean, median, and standard deviation (SD) for different particle classes

Particle type	σ	μ	Mean	Median	SD
Hematite-like	0.5754	-0.7942	1.51	1.44	0.30
Quartz-like	0.5917	-0.7965	1.54	1.45	0.40
Complex quartz-like	0.5991	-0.7793	1.54	1.45	0.44
Microcline-like	0.5701	-0.7263	1.53	1.46	0.30
Albite-like	0.5852	-0.7493	1.53	1.46	0.33
Complex feldspar-like	0.6204	-0.7894	1.54	1.45	0.38
Complex clay/feldspar mixture	0.5990	-0.8248	1.52	1.43	0.34
Complex clay−mineral−like	0.6008	-0.7078	1.57	1.49	0.35
Illite−like	0.5936	-0.7500	1.55	1.47	0.34
Chlorite−like	0.5928	-0.7268	1.55	1.47	0.34
Smectite−like	0.6113	-0.7390	1.55	1.46	0.35
Kaolinite−like	0.6056	-0.8136	1.52	1.44	0.35
Ca−rich silicate/Ca−Si−mixture	0.6183	-0.7006	1.58	1.50	0.40
Calcite−like	0.5904	-0.7572	1.55	1.46	0.37
Dolomite−like	0.5931	-0.9837	1.44	1.35	0.30
Gypsum−like	0.6505	-0.7287	1.60	1.46	0.49
All	0.6024	-0.7744	1.55	1.46	0.38

5 Results and Discussion – Part 2: Iceland

5.1 Study area and sampling sites

The intensive campaign was carried out in the highlands of Iceland for a period of 6 weeks during August-September 2021. During these weeks, measurements were carried out in Dyngjusandur as well as the outflow region as shown in Fig.5.1.

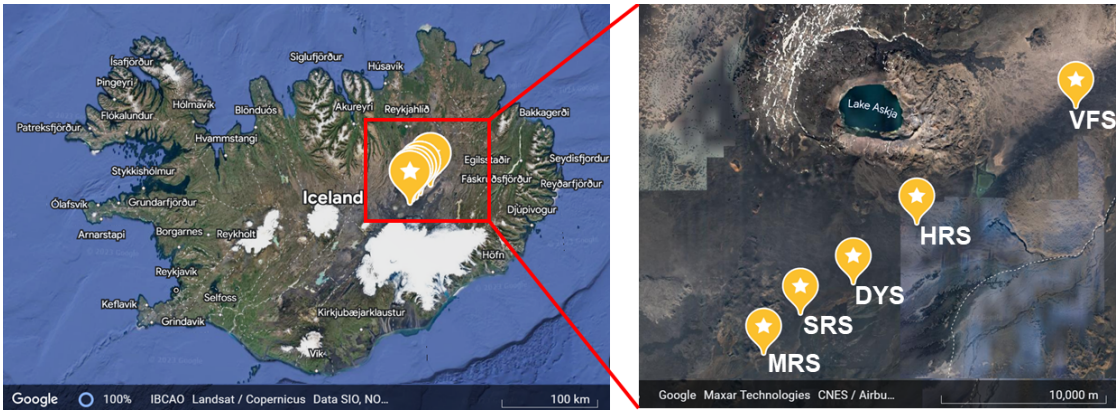

Figure 5.1: Location of the study area. The label DYS represent the location of main measurement site whereas labels MRS, SRS, HRS, and VFS represent the outflow regions where a deposition sampler was placed.

Dyngjusandur lies north of Vatnajökull glacier in the interior of Northeast Iceland and is characterized by various surface pathways of aeolian sediments. It has a dry, cold climate with an annual precipitation of less than 400 mm and is known to be one of the most extensive dust source area in Iceland with frequent dust events observed during summer (Arnalds et al., 2016). The main measurement site, denoted by DYS in Fig. 5.1, is a ephemeral lake of the major river Jökulsá á Fjöllum, formed due to the glacier discharge channel obturation by the Holuhraun lava field (Geiger et al., 2016; González-Romero

et al., in prep). The area is topographically mostly flat and is devoid of vegetation or other obstacles. It has however melt water channels due to the glacier discharge causing size-segregated glacio-fluvial sediment to be frequently replenished. The finer, non-aggregated particles are found on top of the sediment layer and are prone to dust emissions under favorable conditions (González-Romero et al., in prep).

5.2 Particle-type characterization

Chemical compositions of more than 128 000 particles were measured from the samples collected at Dyngjusandur. An additional 62 400 particles were analysed from surrounding locations. Based on the chemical composition derived from EDX, the particles were classified into different particle groups. The criteria for some of the major particle types are given in Table 5.1 while the full classification can be found in the supplement.

Table 5.1: Classification criteria for different particle groups. The full list is provided in the supplement.

Group	Criteria
Medium Al mixed silicates	(Al+Si+Na+Mg+K+Ca+Fe) / X_f [a]=0.7 .. 1.01 & Al/Si=0.25 .. 0.5 & Mg/Si=0 .. 0.5 & Fe/Si=0 .. 0.5 & Ca/Si=0 .. 0.5 & K/Si=0 .. 0.5 & Na/Si=0 .. 0.5 & (Na+K+Ca)/Si=0.125 .. 0.7 & (Na+Cl+2*S) / (Al+Si)=0 .. 0.25
Interm.-Plag.-like	(Na+Ca+Al+Si) / X_f [a]=0.7 .. 1.01 & Na/(Na+Ca)=0.3 .. 0.7 & Al*(3-Ca/(Na+Ca))/(Si*(1+Ca/(Na+Ca)))=0.7 .. 1.3 & (Na+Ca)/(Na+Ca+Al+Si)=0.15 .. 0.25 & K/(K+Al+Si)=0 .. 0.1 & Fe/(Fe+Al+Si)=0 .. 0.15 & (Cl+2*S)/Na=0 .. 0.3 & (Cl+2*S) / (Al+Si)=0 .. 0.125
Pyroxene/amphibole-like	(Ca+Mg+Fe+Si) / X_f [a]=0.7 .. 1.01 & Al/Si=0 .. 0.25 & (Mg+Ca+Fe)/Si=0.8 .. 1.6 & Fe/X_f [a]=0 .. 0.4999
Fe-oxide/Fe-hydroxide-like	Fe/X_f [a]=0.5 .. 0.98999 & Cr/(Cr+Fe)=0 .. 0.1 & Cl/(Cl+Fe)=0 .. 0.1 & Ti/(Ti+Fe)=0 .. 0.1 & (F+Si)/(F+[a])=0 .. 0.499
Titanomagnetite-like	(Fe+Ti)/X_f [a]=0.7 .. 1.01 & Ti/(Ti+Fe)=0.1 .. 0.25
Ammonium-sulfate-like	S/X_f [a]=0.7 .. 1.01 & Na/S=0 .. 1.01 & Cl / (Cl+S)=0 .. 0.3 & Cl/S=0 .. 0.2 & Si/S=0 .. 0.5 & (Al+Si)/S=0 .. 0.25

[a] X_f = Na+Mg+Al+Si+P+S+Cl+K+Ca+Ti+Cr+Mn+Fe

The classification scheme is primarily based on our previous work (Kandler et al., 2007, 2018; Panta et al., 2023). However, as the geology of Iceland is different to that of low-latitude dust sources, other mineralogical particle groups are required and, therefore, new boundary conditions were developed. Dyngjusandur is mainly characterised by basaltic volcanic glasses formed below Vatnajökull glacier during subglacial eruptions with pyroxene, olivine and plagioclase as other significant phases (Baratoux et al., 2011).

Dust resuspension of surface sediment samples from five major Icelandic dust hotspots including Dyngjusandur also showed amorphous basaltic materials to be dominant with around 70 wt % observed for Dyngjusandur sample (Baldo et al., 2020). In the following the major particle groups found are described.

5.2.1 Medium Al mixed silicates

The most frequent particles in Dyngjusandur are classified as Medium Al mixed silicates (MAS) based on our elemental classification scheme. The name is chosen to be generic and descriptive, as they most probably do not represent a single mineral. Figure 5.2 presents the size-resolved average elemental composition and a 2D histogram of MAS particles. It is characterized by the presence of elements such as Si, Al, Fe, Ca, Mg, and Na in EDX spectra with Al/Si of 0.33 ± 0.03 (mean ± standard deviation), Ca/Si of 0.21 ± 0.05, Mg/Si of 0.17 ± 0.05. The Fe/Si ratio is slightly high in fine mode with 0.28 ± 0.07 whereas in coarse mode it is 0.22 ± 0.04. We further analysed few individual glass particles manually by SEM and in Fig. 5.2b show the derived elemental ratios together with the classification done by ccSEM. As the Dyngjusandur sediments primarily consist of amorphous basaltic material (Baldo et al., 2020), it can be partly inferred that MAS are probably glassy particles.

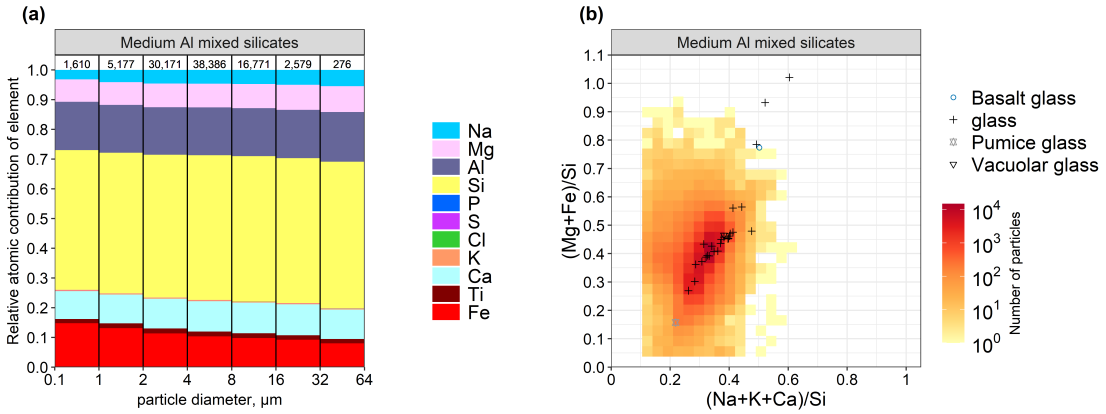

Figure 5.2: (a) Average elemental composition (atomic fraction) as a function of particle size for the Medium Al mixed silicates (MAS) particles at Dyngjusandur from deposition plate and free-wing impactor samples. The numbers on top represent total particle counts in the given size bin. (b) Two-dimensional histogram with respect to element atomic concentrations ratios for MAS particles. In addition, positions and classifications of particles identified manually by composition and morphology are shown.

5.2.2 Silicate mixtures

The groups ‘Other silicates´, ‘Complex silicate (high Al)´ and ‘Complex silicate (moderate Al-low alkali)´ show no matches with the common mineral phases. Nevertheless, they form distinct point clusters. This indicates that they have a specific chemical composition depending on the group, but cannot be assigned to any mineral phase. Their position between compositions of mineral phases indicates that the particles are structurally still in the process of fractionation from the igneous melt glass.

5.2.3 Iron-rich particles

Iron-rich particles were characterized by high relative fraction of Fe, with varying amount of mainly Si, Ca, and Ti present and can be divided into two main caterogries: (a) Fe-oxide/Fe-hydroxide-like and (b) Titanomagnetite-like. These are also observed in previous studies of surface sediment samples from Dyngjusandur (Baldo et al., 2020). Hematite occurs mostly as a secondary product of weathering in soils (Deer et al., 2013). As the sediments from Dyngjusandur show low degree of chemical weathering (Arnalds et al., 2016; Baldo et al., 2020), the Fe-oxide/Fe-hydroxide group are more likely to be magnetite-like than hematite-like. The Titanomagnetite-like group is characterized with relatively high concentration of Ti in magnetite. Both of these particle types are observed mainly in diameters smaller than 4 µm and are generally mixtures of different minerals rather than pure component.

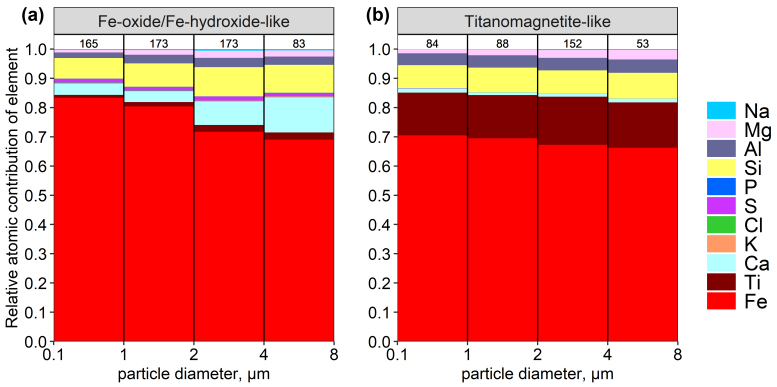

Figure 5.3: Average elemental composition as a function of particle size for (a) Fe-oxide/Fe-hydroxide-like and (b) Titanomagnetite-like. The legend shows element index for each respective element. The numbers on top represent total particle counts in the given size bin.

5.2.4 Pyroxene/amphibole-like

Pyroxenes are rock-forming inosilicate minerals and have the general formula $XY(Si,Al)_2O_6$, where X and Y are most commonly sodium, magnesium, calcium, or iron. Pyroxene minerals usually have volcanic origin and are generally not present in low latitude mineral dust. Previous studies have reported pyroxene (augite) to be the dominant mineral phases present in Dyngjusandur (Baldo et al., 2020; Baratoux et al., 2011). These particles can potentially have an influence on ambient ice nucleating particle as recent work with volcanic tephra samples (volcanic ash) indicates that some pyroxene phases can onset freezing at temperatures near −10 °C (Maters et al., 2019).

5.2.5 Sulfate

Sulfate aerosol particles are produced in the atmosphere through the oxidation of sulfur dioxide emitted by various sources. Volcanic emissions are the primary natural source of sulfur dioxide SO_2 (Carn et al., 2017), accounting for about 25 % of tropospheric sulfate aerosol burden (Lamotte et al., 2021). The emitted SO_2 undergoes oxidation in the atmosphere to form gaseous sulfuric acid, which then converts to sulfate aerosol particles. The 2014-2015 tropospheric effusive eruption of the Holuhraun volcano in Iceland affected the cloud-drop effective radius, highlighting the potential impact of volcanic emissions on atmospheric properties (Ilyinskaya et al., 2017). Sulfate particles typically appeared to be spherical with presence of a deposition 'ring' of small droplets around the core particles as seen in Fig. 5.4 although some extreme aspect ratios were also observed due to needle-like structure of these particles.

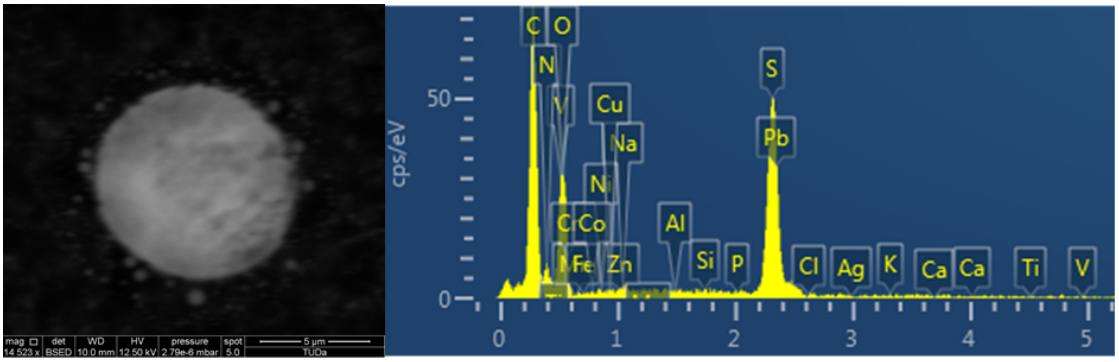

Figure 5.4: Typical sulfate particle with presence of a deposition 'ring' of small droplets around the core.

5.3 Relative Abundances of Various Types of Particles

Figure 4.5 shows the relative volume abundance of the various particle types observed in the Dyngjusandur samples. During the measurement campaign, the composition of the aerosol particles in each sample did not exhibit a large sample-to-sample variability except for few sulfate intrusion events (see appendix figures 6.4 and 6.5 for individual samples collected on a deposition plate and free-wing, respectively). Therefore, for further comparison all of the dust sample compositions are merged and separated by sulfate intrusion periods. This was done primarily because the collection efficiency by size is less relevant to the fractional contribution of each mineral type per size, and therefore integrating all the techniques together improves the statistics for each size with a higher number of particles analyzed. Excluding the sulfate episodic samples, in the 0.1–1 µm size, the dominant particle class are MAS (38 %) and other silicate (13 %) followed by Complex silicate with moderate Al (8 %), Interm-Plag.-like (6 %), Pyroxene/amphibole-like (6 %) with Fe-oxide/Fe-hydroxide (3 %) and Titanomagnetite-like (2 %) occurring mostly in this size interval. Also observed were trace amount of salt and sulfate mixtures. In the 1-2 µm size, the relative volume fractions of MAS, Interm-Plag.-like, other silicate, and Pyroxene/amphibole-like are 58 %, 9 %, 7 %, and 6 % respectively with Fe-oxide/Fe-hydroxide at 1 %. In general, the MAS shows an increasing frequency with particle size and Fe-rich particles are limited to diameters smaller than 2 µm. A decrease in relative fraction is also observed for Titanomagnetite-like particles (0.9 %) in this size range. From particle diameters between 2 and 8 µm 75-85 % of the particles fall under MAS with Interm-Plag.-like and Pyroxene/amphibole-like the other two main particle types at around 6 % and 4 % respectively. The contribution of Fe-rich particles is less than 0.5 % while Titanomagnetite-like particles is < 0.2 %. Finally, for the particle size greater than 8 µm, more than 90 % of the particles are MAS with Fe-rich and Titanomagnetite-like particles virtually absent.

The major compositional variability between sampling days is due to the presence of sulfate particles. Especially, the number abundance of the ammonium-sulfate-like particles exhibits large differences. Ammonium sulfate particles are present in significant proportion during the periods 16 to 21 August and on 02, 03, and 05 September mainly in particles $d_v < 4$ µm. On other days, they are almost absent or occur in minor amounts. As all of the collected particles are freshly emitted and of local origin, the observation of a high content of ammonium-sulfate particles particles in few of the sample highlights the influence of volcanic emission in aerosol load as sulfur is a notable indicator of volcanic emission (Carn et al., 2009).

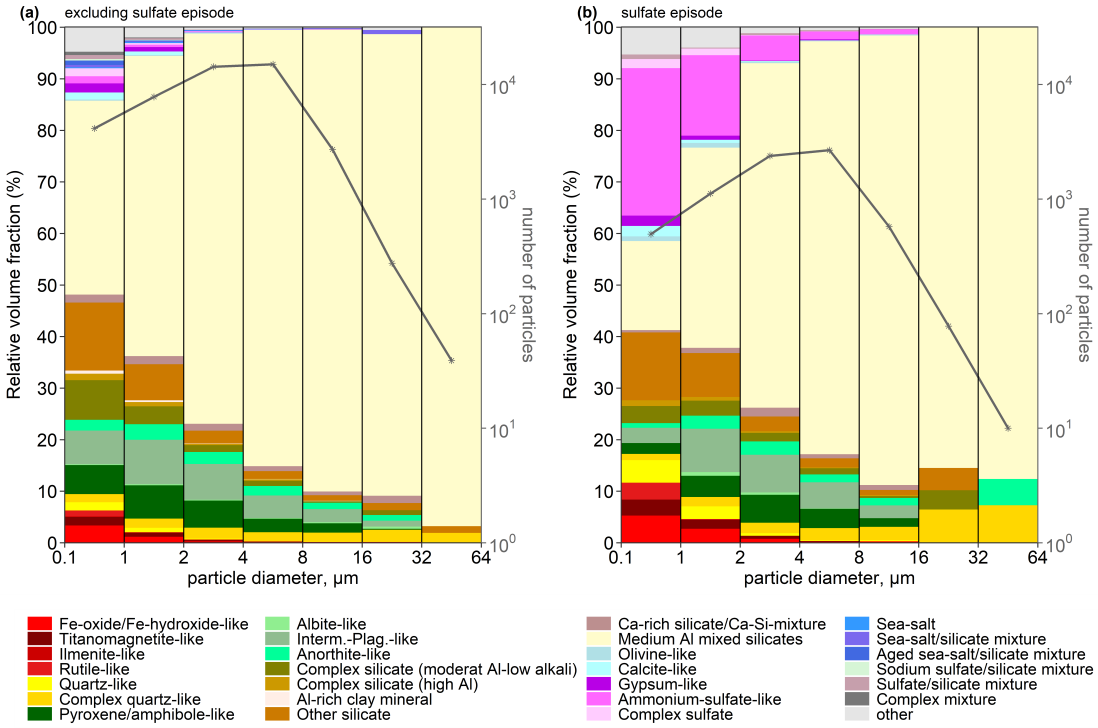

Figure 5.5: Size-resolved relative volume fraction of different particle groups.

5.4 Iron distribution in Icelandic dust

Icelandic dust is rich in iron (Fe) (Arnalds et al., 2014) which is a key mineral affecting climatic, environmental, and biological processes (Schulz et al., 2012). Fe in Icelandic volcanic rocks (andesite and basalts) varies between 6.5 to 12.5 wt. % (Jakobsson et al., 2008). For Dyngjusandur the reported Fe content is $\sim$ 10 wt. %, consisting primarily of volcanic glass (Baldo et al., 2020; Baratoux et al., 2011). Fe in Icelandic dust can be broadly classified into structural Fe (typically contained in pyroxene and amorphous glass) and Fe oxide-hydroxide (derived via sequential extractions) such as hematite and goethite (Baldo et al., 2020). While SEM cannot distinguish between structural and free Fe, by providing the total Fe content on a particle-by-particle basis, it can provide some useful clues on the mixing state of Fe oxide-hydroxides.

To quantitatively evaluate the Fe distribution on large number of particles, Fig. 5.6a shows the size-resolved abundance of silicate particles classified by their Fe content in

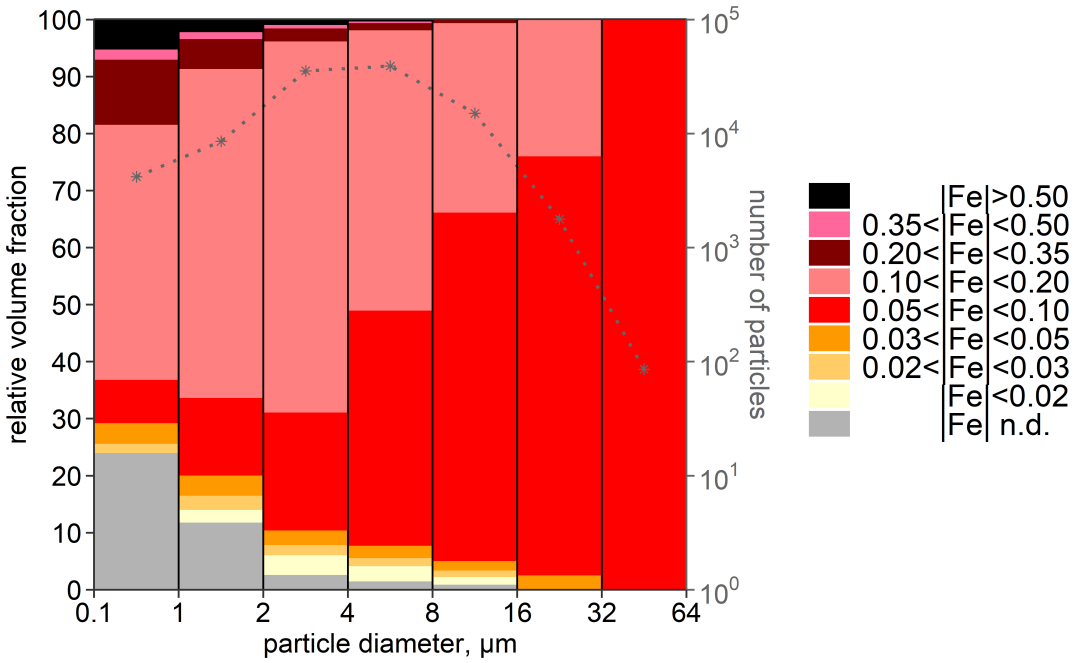

Figure 5.6: Size resolved iron indices for silicate particles. “n.d.” means Fe not detected.

Dyngjusandur. Four main particle types can be distinguished in the plot: (a) particles with high Fe content ($|Fe| > 0.5$), (b) particles with intermediate Fe content $0.1 < |Fe| < 0.5$, (c) particles with low Fe content ($|Fe| < 0.1$), and (d) particles without detectable Fe. High Fe content is mainly associated with particles of diameters less than 2 µm. In general, most particles have Fe index between 0.05 and 0.2 suggesting that most of the Fe is internally mixed in the particle, either embedded into the crystal structure or as small (hydr)oxide grains (Kandler et al., 2020, 2011b).

Figure 5.7a shows the relative contribution of each particle type to Fe in every particle class. In comparison to the particle type fractions displayed in Fig. 4.5, the Fe-oxide/Fe-hydroxide-like and Titanomagnetite-like particles have an increased proportion because of their higher contribution in terms of Fe content, and the sulfates, quartz, and other group gets substantially diminished due to the absence of Fe in them. It can be seen that the iron contribution coming from MAS particles follows a similar trend as observed in its size resolved composition, which suggests that these primarily glassy particles have substantial iron present in them. Figure 5.7b shows the mass fraction of elemental Fe as a

function of particle size. The total Fe in dust shows a decreasing trend with size which is also observed for Moroccan dust (Panta et al., 2023). This is observed particularly up to $\sim$ 10 µm, going from $\sim$ 13 % below 1 µm to less than 8 % in particles above 10 µm.

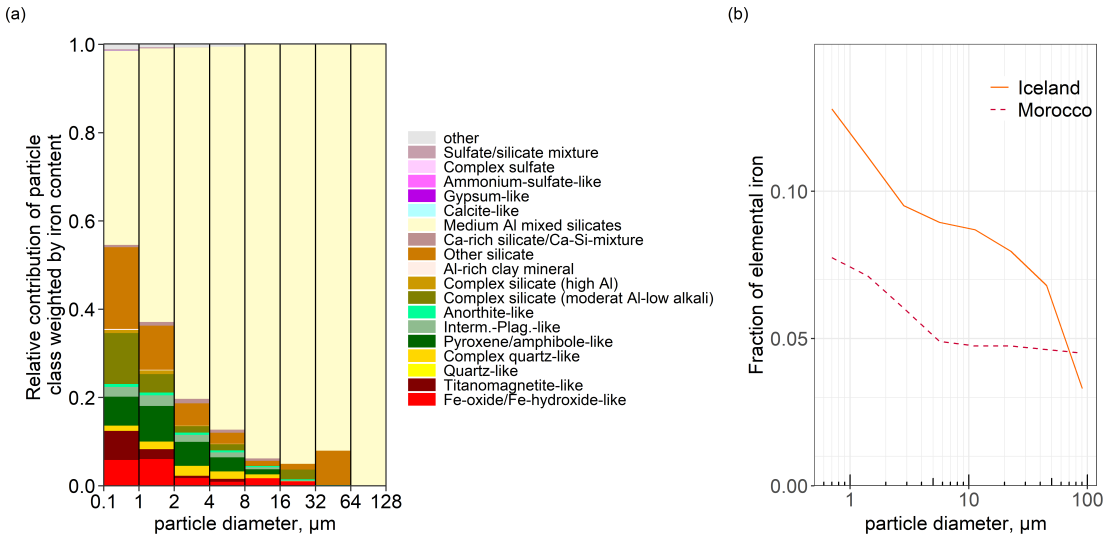

Figure 5.7: (a) Relative contribution of each particle type to total iron and (b) fraction of elemental iron by mass with respect to all the other elements. For comparison iron fraction from Saharan dust is also shown from Panta et al. (2023).

5.5 Particle shape

The size-resolved aspect ratio (AR) distribution, defined as the ratio of the major to minor axis of the elliptical fit, is shown in 5.8 and listed in Table 5.2. The results highlights a positive trend between higher AR and increasing particle size. The collected aerosol particles in this study had AR ranging from 1.03 to 19.65. However, the majority ($\sim$ 99 %) of particles had a measured AR < 3 (see also Figure S4 in the supplement). The mean value for sulfate particles was observed to be highest (2.05) indicating extreme elongated (needle-like) structure for some of these particles. The median was however significantly lower (1.35). The size dependence of the median AR as well as its variability (0.1–0.9 quantiles) is shown in Fig. 5.8. For comparison the size resolved median AR for Moroccan dust is also shown. It can be seen that the for Moroccan dust the AR is relatively constant up to 5 µm and a slight decrease after that. However, for Icelandic dust the AR is

consistently increasing with particle size. Note that the number of particles available in size bins greater than 60 µm is low.

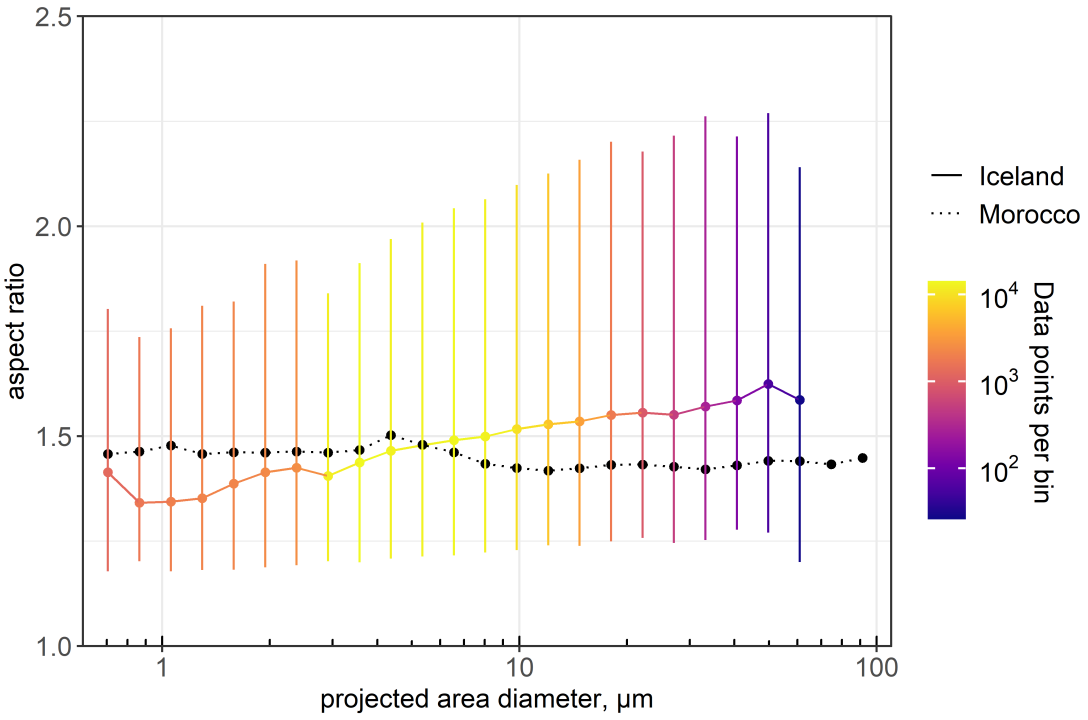

Figure 5.8: Size-resolved particle AR. The shaded area represents the range between 0.1 and 0.9 quantiles with dot being the median and the bins are color coded by the number of data points within each bin. For comparison the median AR of freshly emitted Saharan dust is also shown from Morocco.

The density distribution of the AR of Icelandic dust can be characterized by analysing sufficient number of individual particles using a modified log-normal function Kandler et al. (2007) with high accuracy:

$$h(AR) = \frac{1}{\sqrt{2\pi} \cdot (AR-1) \cdot \sigma} \times exp\left[-\frac{1}{2}\left(\frac{ln(AR-1)-\mu}{\sigma}\right)^2\right] \tag{5.1}$$

with σ and μ the distribution parameters. The AR distribution is shown in Fig. 5.9 for different size fractions. For comparison, the distribution of Saharan dust (Panta et al., 2023) is also shown. The distribution is slightly narrow for the fine range with a median of 1.37. In the coarse and super-coarse range the AR distribution is slightly broader with a median 1.46 and 1.53 respectively. The broad AR distribution in the coarse and super-coarse compared to fine range reflects the high variability in AR of MAS particles. The shape of the overall distribution is however relatively similar to that observed at Morocco for Saharan dust (Panta et al., 2023).

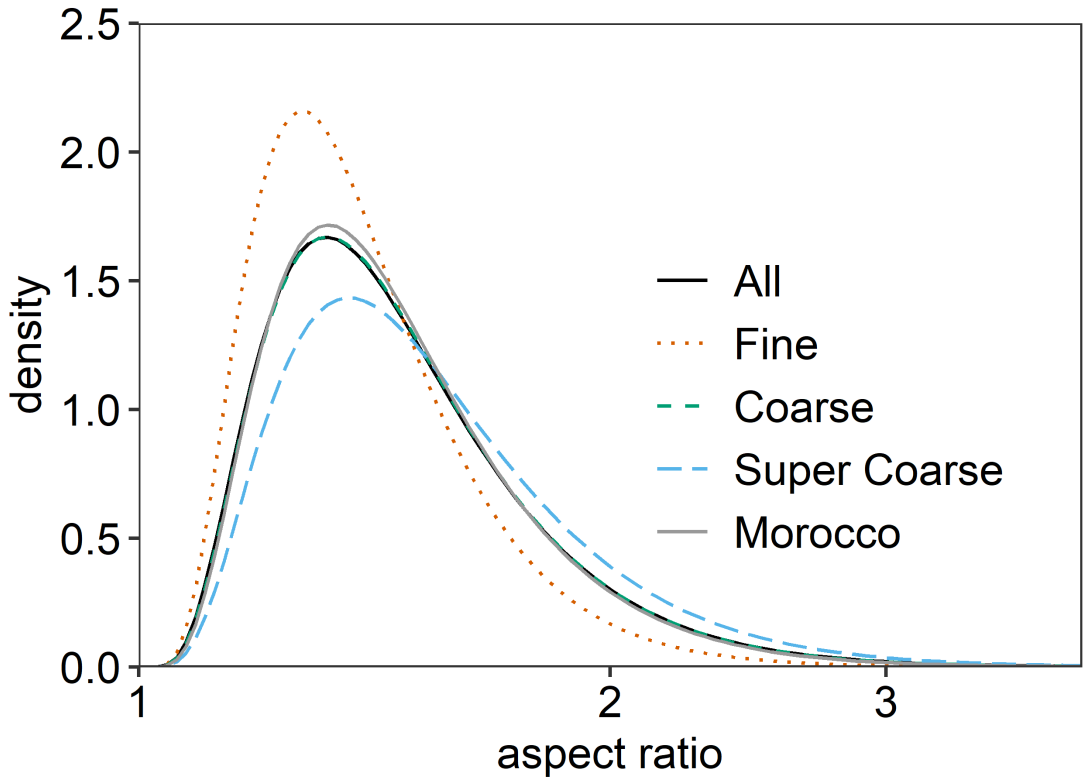

Figure 5.9: Parameterized aspect ratio density distributions for fine, coarse, and super-coarse dust as well as distribution for Saharan dust from Panta et al. (2023).

Table 5.2: Aspect ratio mean, median and standard deviation (SD) for particle group in fine, coarse, and super-coarse dust mode. Values are not shown for size intervals with less than 40 particles.

Particle type	Fine dust ($d_p < 2.5$ µm)			Coarse dust ($2.5 \leq d_p < 10$ µm)			Super-coarse dust ($10 \leq d_p < 62.5$ µm)		
	Mean	Median	SD	Mean	Median	SD	Mean	Median	SD
Fe-oxide/Fe-hydroxide-like	1.41	1.34	0.27	1.55	1.46	0.39			
Titanomagnetite-like	1.39	1.34	0.28	1.43	1.39	0.22			
Quartz-like	1.52	1.39	0.38	1.56	1.45	0.34			
Complex quartz-like	1.48	1.42	0.32	1.55	1.48	0.33	1.62	1.52	0.36
Pyroxene/amphibole-like	1.44	1.35	0.27	1.57	1.49	0.33	1.64	1.55	0.38
Albite-like				1.48	1.40	0.26			
Interm.-Plag.-like	1.42	1.34	0.28	1.51	1.44	0.30	1.56	1.50	0.32
Anorthite-like	1.43	1.35	0.27	1.53	1.45	0.32	1.63	1.55	0.37
Complex silicate (moderat Al-low alkali)	1.43	1.35	0.27	1.46	1.39	0.28	1.47	1.42	0.25
Complex silicate (high Al)	1.46	1.35	0.36	1.56	1.47	0.35			
Al-rich clay mineral	1.52	1.45	0.30	1.54	1.46	0.31			
Other silicate	1.51	1.41	0.37	1.54	1.46	0.35	1.68	1.58	0.50
Ca-rich silicate/Ca-Si-mixture	1.53	1.44	0.38	1.58	1.50	0.39	1.63	1.55	0.37
Medium Al mixed silicates	1.46	1.37	0.32	1.55	1.47	0.34	1.63	1.53	0.40
Olivine-like				1.62	1.54	0.35			
Calcite-like	1.41	1.34	0.26	1.53	1.44	0.37			
Gypsum-like	1.54	1.40	0.64	1.74	1.53	0.72			
Ammonium-sulfate-like	1.45	1.34	0.39	2.06	1.36	1.82	2.61	1.28	2.99
Complex sulfate	1.57	1.42	0.42	1.47	1.38	0.35			
Sulfate/silicate mixture	1.69	1.44	0.49	1.42	1.36	0.26			
Other	1.61	1.45	0.53	1.68	1.43	0.70			
All	1.47	1.37	0.34	1.55	1.46	0.42	1.63	1.53	0.47

5.6 Composition at Outflow Regions

Flat-plate samplers were placed at 4 different outflow regions to gain insights into the local/regional transport of dust aerosols and understand its diverse chemical compositions (Fig.5.10). The codes HRS, MRS, SRS, and VFS are given to the different outflow regions with DYS representing the main site and are shown in Fig. 5.1. The average exposure in the outflow regions were $\sim$ 48 hours. Overall, the chemical composition of the collected aerosol particles in locations HRS, MRS, and SRS does not show a significant variability and is relatively similar to the aerosol composition at the main site. Similar to the aerosol composition at the main site, we also see episodes of sulfate intrusions on HRS (17 - 21 August), MRS (17 - 19 August), and SRS (17 - 21 August). The site VFS was relatively less influenced by local emission as observed in its particle composition.

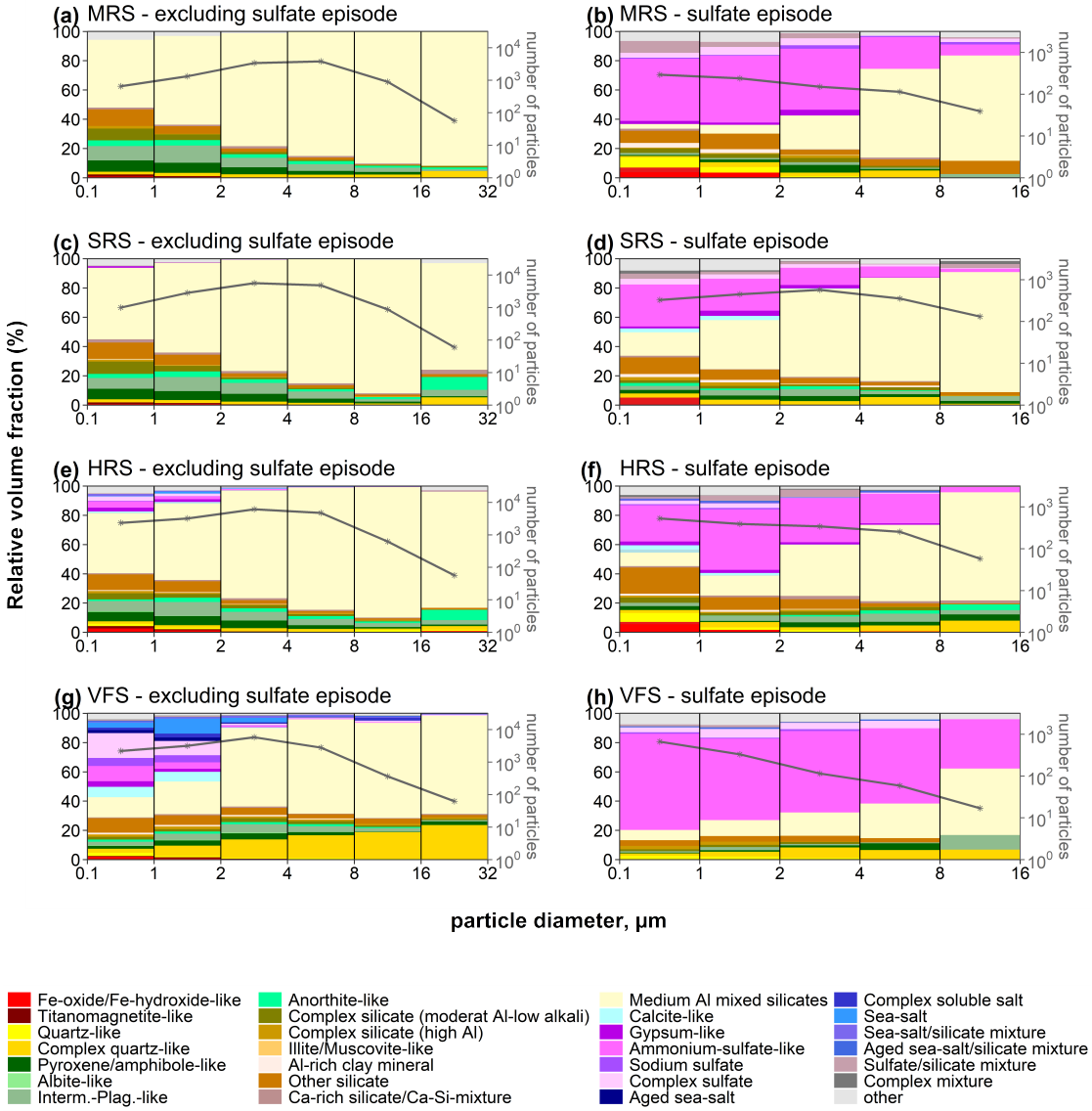

Figure 5.10: Size-resolved volume-averaged composition of the aerosol at different outflow regions during sulfate intrusion period.

5.7 Discussion

5.7.1 Aerosol composition

Using the elemental ratio based classification analysis from the single-particle analysis, we derived an empirical mineralogical classification scheme. With the exception of few sulfate intrusion events (to be discussed below), aerosol composition at Dyngjusandur was remarkably stable.

As around 20 % ($>$ 20 000 km^2) of Iceland is covered by volcaniclastic sandy deserts with active aeolian processes containing sediments from both volcanic systems and eroded glaciofluvial soils (Arnalds et al., 2001; Arnalds et al., 2016), glass, a main constituent of abraded hyaloclastite is expected as a signature compound. In hot deserts, soils tend to undergo mineralogical fractionation due to size segregation during dust emission. Emitted Saharan dust, for example, tends to be comprised primarily of illite and kaolinite, along with non-clay minerals including feldspar, quartz, calcite, and iron oxides (Panta et al., 2023). However, mineralogical fractionation is quite unlikely in most of Icelandic dust due to the low weathering, which would produce minerals from the glassy compounds, and the absence of coarse and super-coarse mineral grains such as quartz, feldspar and clays (Baldo et al., 2020).

From previous analysis of Icelandic dust at Dyngjusandur (e.g. Baldo et al., 2020; Baratoux et al., 2011), the composition of dust aerosols tends to be comprised primarily of basaltic glass. This is consistent with the elemental data and the corresponding classification scheme in this study. Around 52 % of aerosol population number and 62 % of mass can be attributed to MAS - most likely glass particles - in the fine range. A further $\sim$ 77 % and 91 % of number and $\sim$ 82 % and 92 % of mass can be grouped into MAS particles in the coarse and super-coarse range respectively. Baratoux et al. (2011) found high iron content up to 10 % in Dyngjusandur and a similar high iron content of 15 % was also observed by Baldo et al. (2020). Titanomagnetite-like particles were mainly present in the fine mode at $\sim$ 0.6 % by mass and were also identified in previous studies of dust and sediments (Baldo et al., 2020; Baratoux et al., 2011; Dagsson-Waldhauserova et al., 2015; Moroni et al., 2018).

The observed enhancement in sulfate particles on certain days, probably reflects the influence of the volcanic emissions from Fagradalsfjall, which in general is expected to have higher sulfur content (Carn et al., 2009). The sulfate enrichment occurs on 16-17 August, 19-20 August, 02-03 September, and 05 September as seen from deposition sampler and free-wing impactor measurements. Furthermore, this coincides with very strong

accumulation mode visible in the SMPS measurements that are probably condensates from SO_2. Although the direct sulfate emission from volcanoes is relatively small, the lifetime of SO_2 near the tropopause is $\sim$ a week (Carn et al., 2016) allowing for long-range transport during which it forms sulfate aerosols via oxidation.

Regarding the composition of the aerosols collected at the outflow regions, VFS site was more diverse compared to those at other outflow sites. As shown in Fig. 5.10, in the fine mode, sea-salt and calcium-rich particles along with their mixtures were present, whereas they were not observed at other sites. As sea-salt and ca-rich particles can be from ocean, samples collected at HRS indicates the influence of transport rather than locally emitted. In addition, considerable amounts of complex quartz-like particles were observed in the coarse and super-coarse fraction. The most abundant fraction nevertheless were MAS particles in the coarse and super-coarse fraction.

5.7.2 Iron distribution

Figure 5.7a showed the Fe distribution among the individual silicate particles as a function of particle size. The relative fraction of Fe-rich ($|\mathrm{Fe}| > 0.2$) particles is higher in fine mode particles which gets transported easily over long distances and could potentially influence ocean bio-geochemistry. Mineralogy of Icelandic soil surfaces of several active erosion regions including Dyngjusandur is documented (Baldo et al., 2020; Baratoux et al., 2011) with the dust having basaltic composition containing relatively high Fe oxides and the total Fe content reported to be 10 % – 13 % for suspended dust generated in atmospheric chamber (Baldo et al., 2020).

On average, externally mixed Fe-rich particles are scarce. The aspect ratio associated with these particles is slightly influenced by particle size (Table 5.2). We find that the median AR is lower for fine fractions compared to coarse fractions, indicating coarse fractions are more irregular. The observed trend of AR is also seen in other particle groups indicating that fine particles are more regular in shape than are coarse. Further, Fe is detected in virtually all (> 99.9 %) of the MAS particles, which accounts for the highest relative fraction of particles observed by ccSEM and $\sim$ 88 % of total aerosol population in Dyngjusandur. This indicates that most of the particles in Icelandic dust has some iron associated with them.

Comparison of iron distribution in particles between Icelandic and Saharan dust shows both similarities and differences in the Fe index trends. For example, most of the Fe-rich particles ($|\mathrm{Fe}| > 0.5$) are concentrated in particles smaller than 1 µm in both Icelandic dust and Saharan dust (Kandler et al., 2020, 2011b; Panta et al., 2023) accounting for around 5

% and 4 % volume fraction for Icelandic and Saharan dust respectively. These particles tend to be externally mixed. Also similar are the relative fractions of particles in which iron is not detected. The in-between range is however completely different; there is a considerable higher fraction of particles with $0.1 < |\mathrm{Fe}| < 0.2$ at Dyngjusandur, and increases up to 4 µm and then decreases while in L'Bour, Morocco it decreases with increasing particle size. Similarly, the index range $0.05 < |\mathrm{Fe}| < 0.10$ increases with particle size at Dyngjusandur whereas in Morocco it remains relatively constant. The higher Fe contribution to the single particles at Dyngjusandur indicates low chemical weathering regime of Icelandic soils (Baldo et al., 2020) leading to higher Fe content compared to Moroccan soil. The higher iron content of the emitted dust at Dyngjusandur could potentially be a source of micronutrient for marine biota in the Artic Ocean (Dagsson-Waldhauserova et al., 2013) as Fe from the glass is relatively mobile and therefore potentially bio-available (Baldo et al., 2020).

5.7.3 Particle shape

In section 5.5, it was demonstrated that Icelandic dust exhibits an increased level of asphericity with increasing size. This observation aligns with the findings of Richards-Thomas et al. (2021) regarding volcaniclastic dust particles, although their study utilized sphericity as a shape descriptor rather than aspect ratio (AR). Nevertheless, the observed trend implies a similar relationship, where fine particles tend to possess a more regular shape compared to coarse particles. This could have potential implications on the lifetime of dust in the atmosphere as aspherical particle experience an increased drag force reducing their settling velocity (Yang et al., 2013). Recently, Huang et al. (2020) compared the settling velocity of dust by approximating it as randomly oriented tri-axial ellipsoidal and spheres of the same volume. Their finding suggests an increased dust lifetime with respect to gravitational settling by $\sim$ 20 % when dust is considered non-spherical. Therefore, the increased asphericity with size could lead to longer atmospheric lifetime of coarse Icelandic dust as $\sim$ 10 % of these particles have AR $>$ 2.

When comparing AR data from this study to Saharan dust (Panta et al., 2023), we observed increasing median AR with size in Icelandic dust whereas in Saharan dust it remains relatively constant. One reason to explain this discrepancy is related to the differences in the age and mechanical history of the dust particles. In the case of Morocco, the particles are transported down from rivers and contain clay minerals which may aggregate into soil mineral grains that are larger than their original size. Furthermore, due to their older age, the particles may have experienced more extensive mechanical abrasion and erosion, resulting in a more rounded shape and a decrease in AR for Saharan dust particles. In

contrast, Icelandic dust particles is composed of a bulk material that undergoes abrasion and experience less mechanical weathering, resulting in a higher proportion of edges and consequently higher AR.

5.7.4 Comparison with Saharan dust

The mean elemental mass ratios in our work— 3.15 (Si/Al), 1.38 (Fe/Al), and 1.41 (Fe/Ca)—are in good agreement to results with the XRF analysis reported by Baldo et al. (2020) for their Dyngjusandur (D3) sample (3.26, 1.42, and 1.41, respectively).

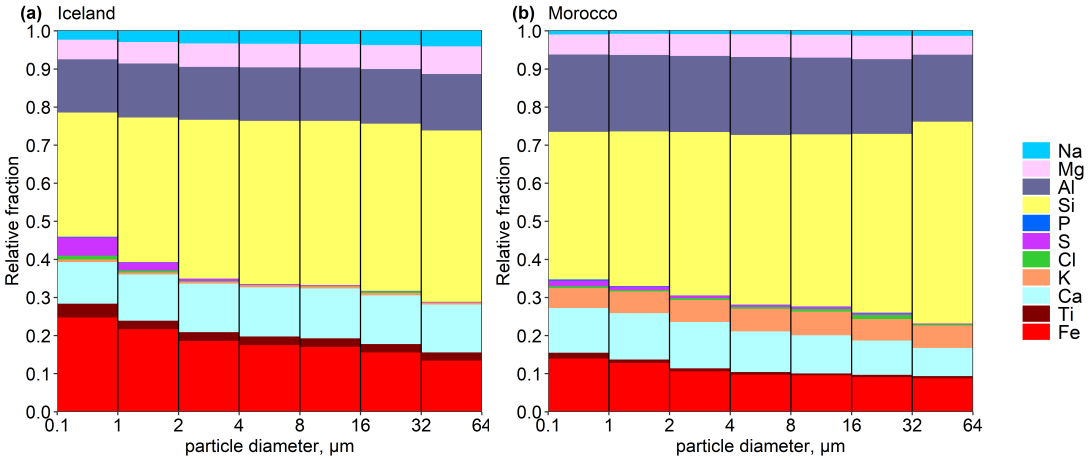

Figure 5.11: Size-resolved average elemental composition for (a) Icelandic dust and (b) Moroccan dust.

Compared to elemental composition of Moroccan dust at L'Bour (Panta et al., 2023), Icelandic dust at Dyngjusandur exhibited lower Al/Si and higher Fe/Al ratios. The difference is mostly related to the high iron content observed in Icelandic dust as compared to northern African dust (Baldo et al., 2020; González-Romero et al., in prep). The average elemental composition of all particle types can be seen in Fig. 5.11 (a) and (b) for Icelandic and Moroccan dust respectively. The most striking feature is clearly the Fe content which is almost double in Icelandic dust. In addition, there is slight enhancement of Ca and less Al in Icelandic dust. A key difference between them is the almost absence of K in Icelandic dust particles, while it is present in the Moroccan dust particles. Moreover, Ti is present almost exclusively only in the fine fraction of the Moroccan dust and present in $\sim$ 18 % of the silicate particles (Panta et al., 2023) whereas in Icelandic dust it is detected across

the entire size range with more than ∼ 86 % of silicate particles containing Ti. This is consistent with the findings of Sanchez-Marroquin et al. (2020) for the Icelandic dust collected on an aircraft. Therefore, Ti could act as a potential tracer for the identification of Icelandic mineral dust particle.

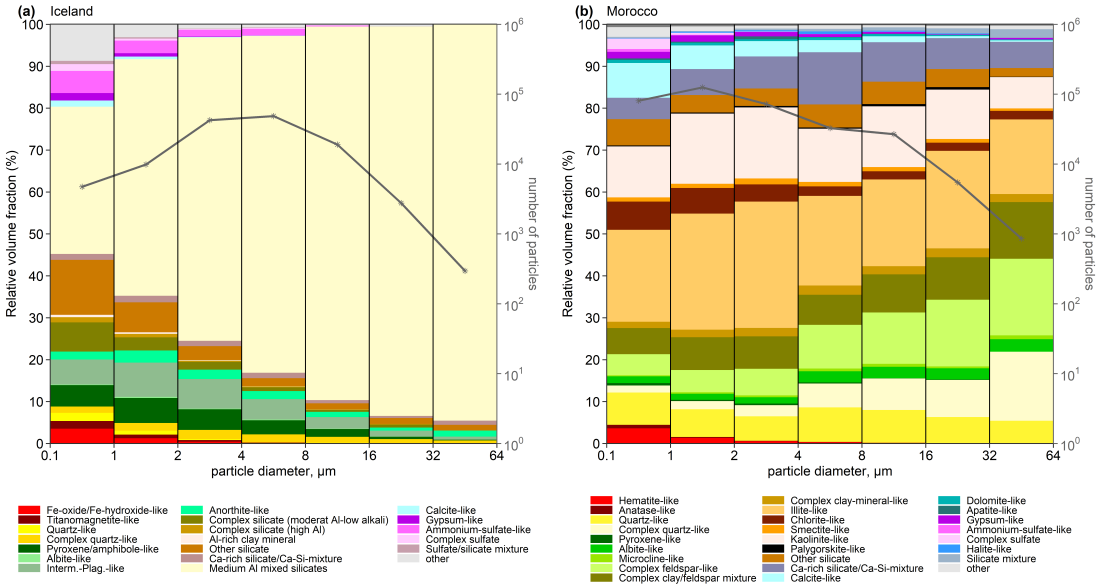

Figure 5.12: Size-resolved average mineralogical composition for (a) Icelandic dust and (b) Moroccan dust.

With respect to comparison of particle type classification for Icelandic and Moroccan dust, it is important to note that the particle identification scheme is based on elemental composition of the particles derived from EDX. This alone is not sufficient to accurately identify the mineral phase because the same elemental composition can form different mineral phases. As the parent sediments of Icelandic and Moroccan dust are different (Baldo et al., 2020; González-Romero et al., in prep), some of the mineral groups in the used classification scheme can have the same rule but different names for the analysed Icelandic and Moroccan dust. For example, Fe-oxide/Fe-hydroxide-like, MAS in Icelandic dust are named as hematite-like and complex feldspar-like respectively in Moroccan dust based on the regional mineralogical composition. Figure 5.12 (a) and (b) shows the average mineralogical composition of all particle types for Icelandic and Moroccan dust respectively. It becomes evident that Moroccan dust is primarily composed of clay minerals whilst for Icelandic dust, glass particles are the major group. As the adopted quantification method

is same for samples analysed from both locations, it can be concluded that Icelandic and Moroccan dust have slightly different elemental composition with regard to individual particle but completely different mineralogy.

6 Conclusions and Further Work

6.1 Summary and conclusions

The overall aim of this thesis was to characterize the chemical and physical properties of freshly emitted mineral dust from two distinct source regions namely Morocco and Iceland. The specific research objectives were to gain insights into the single-particle composition, size, mixing state, and aspect ratio of Moroccan and Icelandic dust using ccSEM/EDX.

Chapter 1 introduced atmospheric aerosol and presented the motivation and overview of the thesis.

Chapter 2 reviewed basics of aeolian dust along with its effects on the earth's climate system.

Chapter 3 presented the experimental methods for sampling freshly emitted mineral dust suitable for SEM/EDX analysis as well as principles of SEM method.

Chapter 4 described the mineralogical and morphological properties of Saharan dust collected at L'Bour, Morocco during 2019 FRAGMENT campaign. We investigated the single particle composition of freshly emitted mineral dust aerosols using SEM-EDX. Samples were collected between 4-30 September 2019 during intensive field campaign on the edge of the Saharan desert in Morocco. A total of more than 300 000 individual particles were classified into eight major particle classes based on their elemental composition and were: (i) oxides/hydroxides, (ii) feldspar, (iii) clay minerals, (iv) quartz-like and complex quartz-like, (v) other silicates (vi) Ca-rich, (vii) sulfates, and (viii) mixtures and others. Our analysis shows that clay minerals (illite-like, kaolinite-like) were the most abundant across the size range $d_v < 64$ µm (25 %–48 % in relative mass abundance). In contrast, calcite-like and chlorite-like particles were present mainly in the size range $d_v < 4$ µm, (3.5 %–8 %). Quartz-like particles were present in a relatively constant quantity across different size bins (5.5 % –8.5 %) whereas complex quartz-like particles were present primarily in the size range $d_v > 4$ µm, (5 %–22 %). A similarly high fraction of quartz,

feldspars, and clay minerals were reported for Morocco during SAMUM (Kandler et al., 2009), except for Ca-rich particles which are significantly less in our sample whereas in Kandler et al. (2009) appear as a log-normal mode centred around 3 µm. Particles with high iron content (Fe oxides and hydroxides) were also identified which are crucial for assessing the radiative effect of mineral dust as well as are essential nutrients for marine and terrestrial ecosystems.

The time series of the overall composition of mineral dust showed relative homogeneity over the campaign. Nevertheless, elevated contents of apatite, calcite, and sulfates were observed on certain days suggesting the presence of a strong local source.

Most particle groups have median aspect ratios of around 1.46. Slightly higher aspect ratios are observed for internally-mixed particles whereas dolomite-like particles have the lowest median value of 1.35. This implies that dust aggregates with higher internal mixture fractions tend to have higher aspect ratios, which will change the radiative properties of dust. Studies have shown a trend of increasing aspect ratios for Northern African dust after transatlantic advection (Huang et al., 2020).

We provided a more exhaustive analysis of Fe-oxi/hydroxides and feldspar, including their PSD and potential aggregation or mixing state, which are key to the effects of dust upon radiation and clouds. Compared to clay minerals and quartz, iron-rich particles (either dominated by or externally-mixed Fe-oxi/hydroxides) are present mainly in diameters smaller than 1 µm at about 3.75 % abundance by mass. Our analysis suggests that Fe-oxi/hydroxides tend to be increasingly internally mixed with other minerals, especially clays, as particle size increases, with the volume fraction of Fe-oxi/hydroxides in aggregates decreasing with particle size. All in all, smaller particles are more enriched with Fe due to both the presence of Fe-oxi-hydroxide (hematite-like) and the increase in feldspar and quartz with particle size, which reduces the fractional abundance of clay-like particles internally mixed with Fe-oxi-hydroxides. The externally-mixed total feldspar and K-feldspar abundances are relatively constant in contrast to the increasing abundance of feldspar-like (internally-mixed) aggregates with particle size.

Chapter 5 described the mineralogical and morphological properties of high-latitude dust collected at Dyngjusandur, Iceland during 2021 FRAGMENT campaign. The chemistry and morphology data of Icelandic dust particles were identified by ccSEM/EDX. We discussed the different particle types observed and explored their properties. The most abundant particle class were Medium Al mixed particles (glassy) at all of the locations. Sulfate intrusion periods were observed on selected days with higher abundance of ammonium sulfate particles in both the fine and coarse size range. The anomalous chemistry associated with sulfate intrusion event is probably related to volcanic emission from Fagradalsfjall.

The composition at regional outflow regions were also found to be similar to that observed in Dyngjusandur except for a hill top site which had influence of transported aerosol.

We observed that the particles solely dominated by Fe are found mainly in fine fractions. Furthermore, a higher total Fe content within individual particle is observed in Icelandic dust which can affect the modelled dust-radiation interaction as well as the for the supply of nutrients to terrestrial and marine ecosystems. The high Fe content in Icelandic dust is associated with the composition of the parent sediments (González-Romero et al., in prep) as most of the glass particles have structural iron present. The iron content of dust is key to several climate processes including radiative effect and biogeochemical cycle which modulates atmospheric carbon dioxide. Baldo et al. (2020) estimated Fe solubility of 0.6 % for Dyngjusandur which supplies Fe to the North Atlantic Ocean. The optical properties of airborne aerosol depends on its composition, particle size distribution, and shape. Icelandic dust is strongly light absorbing (Zubko et al., 2019) with greater absorption towards the near-infrared most likely due to the high magnetite content (Baldo et al., 2023). The direct radiative forcing of Icelandic dust was recently estimated by Baldo et al. (2023). The mineral composition data used in their model included surface sediment sample from Dyngjusandur resuspended in smog chamber. Since the mineralogical composition and the Fe speciation of Icelandic dust are different to that of northern African and Asian dust (Baldo et al., 2020), the spectral optical properties would be different.

The shape (aspect ratio) of the particles was found to be dependent on particle size. The median aspect ratio increased with increasing particle size. The density distribution was slightly narrow for fine mode particles compared to coarse and super-coarse suggesting more spread of aspect ratio values in them.

Our results highlight that at an individual particle level Icelandic dust and Moroccan (Saharan) dust have some similarity with respect to its elemental composition. However, the mineralogy is fundamentally different due to the different geological parent sediment. With regard to the distribution of Fe among the particles, differences were for Icelandic and Moroccan dust. The overall shape distribution between Icelandic and Saharan dust was observed to be rather similar.

6.2 Suggestions for future work

The work in this thesis has been able to use SEM/EDX to characterize mineral dust from two distinct source regions during the FRAGMENT campaigns, obtained over Saharan desert in Morocco and from over the high-latitude region in Iceland. The results have

provided insights into the single-particle composition, size, mixing state, and aspect ratio of freshly emitted mineral dust. However, there are some questions that require further investigation for future work and are described below:

- The results analyzed and discussed here were based on intensive field campaigns at two distinct source location. It would be desirable to have permanent long-term measurements at other key locations using e.g. standard aerosol optical measurements besides a full chemical and physical analysis of the aerosol. This will provide complementary data to the intensive field campaigns that happen on a very sporadic basis and helps for a more robust assessment.

- The relationship between mineral composition and size distribution of particles from parent soil to suspended mineral dust is highly important. Understanding this relationship is key to include mineralogical dependencies in climate models. For this, future laboratory work should focus on analyzing different soils and generate different size classes and then measure and validate them by more than one technique to assess reliability of each technique. These samples should then be analysed by SEM-EDX to get quantitative results.

- Data on the third dimension of dust particles and surface roughness are important for optical modeling of mineral dust in the atmosphere. The third dimension (height or depth of a particle) and surface roughness can affect radiative properties. Therefore, having accurate information on the 3D shape and surface roughness of dust particles is important for accurately modeling how they interact with radiation and how they impact the Earth's climate. SEM and AFM (atomic force microscopy) are two techniques that can be used to obtain information on the 3D shape and surface roughness of dust particles. SEM can provide high-resolution images of the surface of particles, while AFM can provide information on surface topography at the nanoscale level. By combining these techniques and conducting correlative analyses, it may be able to obtain more accurate and detailed information on the shape and surface roughness of dust particles.

- The research presented in this thesis was conducted as part of the ERC FRAGMENT project, which included additional field campaign in Jordan, as well as a soil campaign in the USA. Therefore, future studies should compare and contrast the outcomes from different source regions.

- Develop and refine models of mineral dust emissions and transport: Accurately modeling mineral dust emissions and transport is important for understanding its impacts on the Earth's climate and environment. Future studies could develop and

refine models of mineral dust emissions and transport using the data and insights gained from this study.

The results presented here provide insight into chemical and physical composition and properties of freshly emitted mineral dust aerosols and help us better understand their role in atmospheric chemistry and the Earth's climate system. Many Earth system models still assume globally uniform mineralogical composition and therefore introduce errors in the assessment of regional forcing of dust. The detailed single-particle analysis of freshly emitted dust particles in this study is one key element in understanding the relationship of the emitted size-resolved composition to that of the parent soil. Recently, the field of imaging spectrometry satellite missions has progressed with the development of new instruments, and projects like the Earth Surface Mineral Dust Source Investigation (EMIT) (Green et al., 2020), Environmental Mapping and Analysis Program (EnMAP) (Guanter et al., 2015), and DLR Earth Sensing Imaging Spectrometer (DESIS) (Müller et al., 2016) that will retrieve global surface mineralogy. Together, all of these efforts will help advance our knowledge of dust effects upon climate.

Appendix

In this study, a scanning electron microscope (FEI ESEM Quanta 400 FEG instrument, Eindhoven, The Netherlands) equipped with an X-Max 150 Energy-Dispersive X-ray spectroscopy (EDX) silicon drift X-ray detector (Oxford, Oxfordshire, UK) was used for obtaining the elemental composition of individual particle. The table inserted below is a description of the classification scheme and the observed particle groups. Note that the given method cannot be used to quantify the percentage of C, N, and O due to their high uncertainty and substrate contributions. Particle classes are named for their most prevalent component(s), which may contain terms for mineral phases to simplify the naming (e.g. gypsum, quartz). Those mineral phases were chosen as the most prevalent components that matched the reported elemental composition, but no real phase identification of individual particles (e.g., by transmission electron microscopy) was carried out. Therefore, all the particle classes are termed '-like' to express the similarity in chemical fingerprints.

```
;Oxides/Hydroxides

[Fe-rich]
Name=Hematite-like
Class=Oxides/Hydroxides
AdditionalTitle=Density
Additional=5
Fe/(Na+Mg+Al+Si+P+S+Cl+K+Ca+Ti+Cr+Mn+Fe)=0.5 .. 0.98999
Cr/(Cr+Fe)=0 .. 0.1
Cl/(Cl+Fe)=0 .. 0.1
(F+Si)/(F+Na+Mg+Al+Si+P+S+Cl+K+Ca+Ti+Cr+Mn+Fe)=0 .. 0.499
Ti/Fe=0 .. 0.24999
~kappa_upper=Cl+S>0 ? (1-f_dust_upper)*(0.68*142.04/2.66*S + 1.12*58.44/2.17*Cl)/(142.04/2.66*S + 58.44/2.17*Cl) : (1-f_dust_upper)*(0.8) :
~kappa_lower=Cl+S>0 ? (1-f_dust_lower)*(0.68*142.04/2.66*S + 1.12*58.44/2.17*Cl)/(142.04/2.66*S + 58.44/2.17*Cl) : (1-f_dust_lower)*(0.8) :

[Ti-rich]
Name=Rutile-like
Class=Oxides/Hydroxides
AdditionalTitle=Density
Additional=4.1
Ti/(Na+Mg+Al+Si+P+S+Cl+K+Ca+Ti+Cr+Mn+Fe)=0.7 .. 1.01
Ca/(Ca+Ti)=0 .. 0.3
~kappa_upper=Cl+S>0 ? (1-f_dust_upper)*(0.68*142.04/2.66*S + 1.12*58.44/2.17*Cl)/(142.04/2.66*S + 58.44/2.17*Cl) : (1-f_dust_upper)*(0.8) :
~kappa_lower=Cl+S>0 ? (1-f_dust_lower)*(0.68*142.04/2.66*S + 1.12*58.44/2.17*Cl)/(142.04/2.66*S + 58.44/2.17*Cl) : (1-f_dust_lower)*(0.8) :

[Ti-Ca-rich]
Name=Perovskite-like
Class=Oxides/Hydroxides
AdditionalTitle=Density
Additional=4.1
(Ti+Ca)/(Na+Mg+Al+Si+P+S+Cl+K+Ca+Ti+Cr+Mn+Fe)=0.7 .. 1.01
Ca/(Ca+Ti)=0.3 .. 0.7
~kappa_upper=Cl+S>0 ? (1-f_dust_upper)*(0.68*142.04/2.66*S + 1.12*58.44/2.17*Cl)/(142.04/2.66*S + 58.44/2.17*Cl) : (1-f_dust_upper)*(0.8) :
~kappa_lower=Cl+S>0 ? (1-f_dust_lower)*(0.68*142.04/2.66*S + 1.12*58.44/2.17*Cl)/(142.04/2.66*S + 58.44/2.17*Cl) : (1-f_dust_lower)*(0.8) :

[Ilmenit]
Name=Ilmenite-like
Class=Oxides/Hydroxides
AdditionalTitle=Density
Additional=4.72
(Fe+Ti)/(Na+Mg+Al+Si+P+S+Cl+K+Ca+Ti+Cr+Mn+Fe)=0.7 .. 1.01
Ti/Fe=0.25 .. 4
~kappa_upper=Cl+S>0 ? (1-f_dust_upper)*(0.68*142.04/2.66*S + 1.12*58.44/2.17*Cl)/(142.04/2.66*S + 58.44/2.17*Cl) : (1-f_dust_upper)*(0.8) :
~kappa_lower=Cl+S>0 ? (1-f_dust_lower)*(0.68*142.04/2.66*S + 1.12*58.44/2.17*Cl)/(142.04/2.66*S + 58.44/2.17*Cl) : (1-f_dust_lower)*(0.8) :
```

```
;Silikate

[Quartz]
Name=Quartz-like
Class=silicates
Si/(Na+Mg+Al+Si+P+S+Cl+K+Ca+Ti+Cr+Mn+Fe)=0.7 .. 1.01
(Na+Mg+K+Ca+Al)/Si=0 .. 0.2
F/(F+Si)=0 .. 0.499
~kappa_upper=Cl+S>0 ? (1-f_dust_upper)*(0.68*142.04/2.66*S + 1.12*58.44/2.17*Cl)/(142.04/2.66*S + 58.44/2.17*Cl) : (1-f_dust_upper)*(0.8) :
~kappa_lower=Cl+S>0 ? (1-f_dust_lower)*(0.68*142.04/2.66*S + 1.12*58.44/2.17*Cl)/(142.04/2.66*S + 58.44/2.17*Cl) : (1-f_dust_lower)*(0.8) :

[Ca-Si Mix]
Name=Ca-rich silicate/Ca-Si-mixture
Class=silicates
(Ca+Al+Si) / (Na+Mg+Al+Si+P+S+Cl+K+Ca+Ti+Cr+Mn+Fe)=0.7 .. 1.01
Ca/(Al+Si)=0.3 .. 3.333
(Na+Cl+2*S) / (Al+Si)=0 .. 0.25
~kappa_upper=Cl+S>0 ? (1-f_dust_upper)*(0.68*142.04/2.66*S + 1.12*58.44/2.17*Cl)/(142.04/2.66*S + 58.44/2.17*Cl) : (1-f_dust_upper)*(0.8) :
~kappa_lower=Cl+S>0 ? (1-f_dust_lower)*(0.68*142.04/2.66*S + 1.12*58.44/2.17*Cl)/(142.04/2.66*S + 58.44/2.17*Cl) : (1-f_dust_lower)*(0.8) :


[Pyroxene]
Name=Pyroxene-like
Class=silicates
Al/Si=0 .. 0.1
(Ca+Mg+Fe+Si) / (Na+Mg+Al+Si+P+S+Cl+K+Ca+Ti+Cr+Mn+Fe)=0.7 .. 1.01
(Na+Mg+K+Ca+Al+Fe)/Si=0.8 .. 1.2
IsNotInOtherGroup=yes
~kappa_upper=Cl+S>0 ? (1-f_dust_upper)*(0.68*142.04/2.66*S + 1.12*58.44/2.17*Cl)/(142.04/2.66*S + 58.44/2.17*Cl) : (1-f_dust_upper)*(0.8) :
~kappa_lower=Cl+S>0 ? (1-f_dust_lower)*(0.68*142.04/2.66*S + 1.12*58.44/2.17*Cl)/(142.04/2.66*S + 58.44/2.17*Cl) : (1-f_dust_lower)*(0.8) :

[complex QuartzMix]
Name=Complex quartz-like
Class=silicates
(Al+Si+Na+Mg+K+Ca+Fe) / (Na+Mg+Al+Si+P+S+Cl+K+Ca+Ti+Cr+Mn+Fe)=0.7 .. 1.01
Al/Si=0.05 .. 0.25
(Na+K+Ca)/Si=0 .. 1
Fe/Si=0 .. 0.5
Ca/Si=0 .. 0.5
K/Si=0 .. 0.5
Mg/Si=0 .. 0.5
Na/Si=0 .. 0.5
(Na+Cl+2*S) / (Al+Si)=0 .. 0.25
IsNotInOtherGroup=yes
~kappa_upper=Cl+S>0 ? (1-f_dust_upper)*(0.68*142.04/2.66*S + 1.12*58.44/2.17*Cl)/(142.04/2.66*S + 58.44/2.17*Cl) : (1-f_dust_upper)*(0.8) :
~kappa_lower=Cl+S>0 ? (1-f_dust_lower)*(0.68*142.04/2.66*S + 1.12*58.44/2.17*Cl)/(142.04/2.66*S + 58.44/2.17*Cl) : (1-f_dust_lower)*(0.8) :

[other silicate]
Name=Other silicate
Class=silicates
(Al+Si+Na+Mg+K+Ca+Fe+Ti) / (Na+Mg+Al+Si+P+S+Cl+K+Ca+Ti+Cr+Mn+Fe)=0.7 .. 1.01
(Na+Cl+S) / (Al+Si+Fe)=0 .. 0.25
IsNotInOtherGroup=yes
~kappa_upper=Cl+S>0 ? (1-f_dust_upper)*(0.68*142.04/2.66*S + 1.12*58.44/2.17*Cl)/(142.04/2.66*S + 58.44/2.17*Cl) : (1-f_dust_upper)*(0.8) :
~kappa_lower=Cl+S>0 ? (1-f_dust_lower)*(0.68*142.04/2.66*S + 1.12*58.44/2.17*Cl)/(142.04/2.66*S + 58.44/2.17*Cl) : (1-f_dust_lower)*(0.8) :
```

```
;clay minerals

[Kaolinite]
Name=Kaolinite-like
Class=clay minerals
(Al+Si) / (Na+Mg+Al+Si+P+S+Cl+K+Ca+Ti+Cr+Mn+Fe)=0.7 .. 1.01
Al/Si=0.5 .. 1.5
Fe/(Al+Si)=0 .. 0.2
Mg/(Al+Si)=0 .. 0.2
Ca/(Al+Si)=0 .. 0.2
Na/(Al+Si)=0 .. 0.15
K/(Si)=0 .. 0.1
(Na+Cl+2*S)/(Al+Si)=0 .. 0.25
~kappa_upper=Cl+S>0 ? (1-f_dust_upper)*(0.68*142.04/2.66*S + 1.12*58.44/2.17*Cl)/(142.04/2.66*S + 58.44/2.17*Cl) : (1-f_dust_upper)*(0.8) :
~kappa_lower=Cl+S>0 ? (1-f_dust_lower)*(0.68*142.04/2.66*S + 1.12*58.44/2.17*Cl)/(142.04/2.66*S + 58.44/2.17*Cl) : (1-f_dust_lower)*(0.8) :

[Illit]
Name=Illite-like
Class=clay minerals
(K+Al+Si) / (Na+Mg+Al+Si+P+S+Cl+K+Ca+Ti+Cr+Mn+Fe)=0.7 .. 1.01
Al/Si=0.45 .. 1.5
Mg/(Al+Si)=0 .. 0.2
Fe/(Al+Si)=0 .. 0.2
(Na+Ca)/(Al+Si)=0 .. 0.2
K/(Si)=0.1 .. 1.01
(Na+Cl+2*S) / (Al+Si)=0 .. 0.25
~kappa_upper=Cl+S>0 ? (1-f_dust_upper)*(0.68*142.04/2.66*S + 1.12*58.44/2.17*Cl)/(142.04/2.66*S + 58.44/2.17*Cl) : (1-f_dust_upper)*(0.8) :
~kappa_lower=Cl+S>0 ? (1-f_dust_lower)*(0.68*142.04/2.66*S + 1.12*58.44/2.17*Cl)/(142.04/2.66*S + 58.44/2.17*Cl) : (1-f_dust_lower)*(0.8) :

[Smectit/Montmorrillonit später Plot da hier auch Palygorskit]
Name=Smectite-like
Class=clay minerals
(Mg+Al+Si) / (Na+Mg+Al+Si+P+S+Cl+K+Ca+Ti+Cr+Mn+Fe)=0.7 .. 1.01
Al/Si=0.5 .. 1.5
Fe/(Al+Si)=0 .. 0.2
Mg/(Al+Si)=0.2 .. 1.01
Ca/(Al+Si)=0 .. 0.2
Na/(Al+Si)=0 .. 0.2
K/(Si)=0 .. 0.1
(Na+Cl+2*S) / (Al+Si)=0 .. 0.25
~kappa_upper=Cl+S>0 ? (1-f_dust_upper)*(0.68*142.04/2.66*S + 1.12*58.44/2.17*Cl)/(142.04/2.66*S + 58.44/2.17*Cl) : (1-f_dust_upper)*(0.8) :
~kappa_lower=Cl+S>0 ? (1-f_dust_lower)*(0.68*142.04/2.66*S + 1.12*58.44/2.17*Cl)/(142.04/2.66*S + 58.44/2.17*Cl) : (1-f_dust_lower)*(0.8) :

[Chloritgruppe]
Name=Chlorite-like
Class=clay minerals
(Mg+Fe+Al+Si) / (Na+Mg+Al+Si+P+S+Cl+K+Ca+Ti+Cr+Mn+Fe)=0.7 .. 1.01
Al/Si=0.5 .. 1.5
Fe/(Al+Si)=0.2 .. 1.01
Ca/(Al+Si)=0 .. 0.3
(Na+Cl+2*S) / (Al+Si)=0 .. 0.25
~kappa_upper=Cl+S>0 ? (1-f_dust_upper)*(0.68*142.04/2.66*S + 1.12*58.44/2.17*Cl)/(142.04/2.66*S + 58.44/2.17*Cl) : (1-f_dust_upper)*(0.8) :
~kappa_lower=Cl+S>0 ? (1-f_dust_lower)*(0.68*142.04/2.66*S + 1.12*58.44/2.17*Cl)/(142.04/2.66*S + 58.44/2.17*Cl) : (1-f_dust_lower)*(0.8) :
```

```
;feldspar

[K-Feldspar]
Name=Microcline-like
Class=feldspar
(K+Al+Si) / (Na+Mg+Al+Si+P+S+Cl+K+Ca+Ti+Cr+Mn+Fe)=0.7 .. 1.01
Al/Si=0.2 .. 0.45
K/Si=0.15 .. 0.5
Ca/Si=0 .. 0.1
Na/Si=0 .. 0.1
(Cl+2*S)/Na = 0 .. 0.3
(Cl+2*S) / (Al+Si)=0 .. 0.125
~kappa_upper=Cl+S>0 ? (1-f_dust_upper)*(0.68*142.04/2.66*S + 1.12*58.44/2.17*Cl)/(142.04/2.66*S + 58.44/2.17*Cl)   (1-f_dust_upper)*(0.8) :
~kappa_lower=Cl+S>0 ? (1-f_dust_lower)*(0.68*142.04/2.66*S + 1.12*58.44/2.17*Cl)/(142.04/2.66*S + 58.44/2.17*Cl) : (1-f_dust_lower)*(0.8) ;

[Na-Feldspar]
Name=Albite-like
Class=feldspar
(Na+Al+Si) / (Na+Mg+Al+Si+P+S+Cl+K+Ca+Ti+Cr+Mn+Fe)=0.7 .. 1.01
Al/Si=0.2 .. 0.45
Na/Si=0.15 .. 0.5
Ca/Si=0 .. 0.1
K/Si=0 .. 0.1
(Cl+2*S)/Na = 0 .. 0.3
(Cl+2*S) / (Al+Si)=0 .. 0.125
~kappa_upper=Cl+S>0 ? (1-f_dust_upper)*(0.68*142.04/2.66*S + 1.12*58.44/2.17*Cl)/(142.04/2.66*S + 58.44/2.17*Cl) : (1-f_dust_upper)*(0.8) :
~kappa_lower=Cl+S>0 ? (1-f_dust_lower)*(0.68*142.04/2.66*S + 1.12*58.44/2.17*Cl)/(142.04/2.66*S + 58.44/2.17*Cl) : (1-f_dust_lower)*(0.8) :

[Ca-Feldspar]
Name=Anorthite-like
Class=feldspar
(Ca+Al+Si) / (Na+Mg+Al+Si+P+S+Cl+K+Ca+Ti+Cr+Mn+Fe)=0.7 .. 1.01
Al/Si=0.8 .. 1.2
Ca/Si=0.2 .. 0.7
Na/Si=0 .. 0.1
K/Si=0 .. 0.1
(Cl+2*S)/Na = 0 .. 0.3
(Cl+2*S) / (Al+Si)=0 .. 0.125
(Na+Cl+2*S) / (Al+Si)=0 .. 0.25
~kappa_upper=Cl+S>0 ? (1-f_dust_upper)*(0.68*142.04/2.66*S + 1.12*58.44/2.17*Cl)/(142.04/2.66*S + 58.44/2.17*Cl) : (1-f_dust_upper)*(0.8) :
~kappa_lower=Cl+S>0 ? (1-f_dust_lower)*(0.68*142.04/2.66*S + 1.12*58.44/2.17*Cl)/(142.04/2.66*S + 58.44/2.17*Cl) : (1-f_dust_lower)*(0.8) :


[complex feldspar]
Name=Complex feldspar-like
Class=silicates
(Al+Si+Na+Mg+K+Ca+Fe) / (Na+Mg+Al+Si+P+S+Cl+K+Ca+Ti+Cr+Mn+Fe)=0.7 .. 1.01
Al/Si=0.25 .. 0.5
(Na+K+Ca)/Si=0.125 .. 0.7
Fe/Si=0 .. 0.5
Ca/Si=0 .. 0.5
K/Si=0 .. 0.5
Mg/Si=0 .. 0.5
Na/Si=0 .. 0.5
(Na+Cl+2*S) / (Al+Si)=0 .. 0.25
IsNotInOtherGroup=yes
~kappa_upper=Cl+S>0 ? (1-f_dust_upper)*(0.68*142.04/2.66*S + 1.12*58.44/2.17*Cl)/(142.04/2.66*S + 58.44/2.17*Cl) : (1-f_dust_upper)*(0.8) :
~kappa_lower=Cl+S>0 ? (1-f_dust_lower)*(0.68*142.04/2.66*S + 1.12*58.44/2.17*Cl)/(142.04/2.66*S + 58.44/2.17*Cl) : (1-f_dust_lower)*(0.8) :

[complex clay/Fsp-Mix]
Name=Complex clay/feldspar mixture
Class=silicates
(Al+Si+Na+Mg+K+Ca+Fe) / (Na+Mg+Al+Si+P+S+Cl+K+Ca+Ti+Cr+Mn+Fe)=0.7 .. 1.01
Al/Si=0.25 .. 0.5
(Na+K+Ca)/Si=0 .. 0.125
Fe/Si=0 .. 0.5
Ca/Si=0 .. 0.5
K/Si=0 .. 0.5
Mg/Si=0 .. 0.5
Na/Si=0 .. 0.5
(Na+Cl+2*S) / (Al+Si)=0 .. 0.25
IsNotInOtherGroup=yes
~kappa_upper=Cl+S>0 ? (1-f_dust_upper)*(0.68*142.04/2.66*S + 1.12*58.44/2.17*Cl)/(142.04/2.66*S + 58.44/2.17*Cl) : (1-f_dust_upper)*(0.8) :
~kappa_lower=Cl+S>0 ? (1-f_dust_lower)*(0.68*142.04/2.66*S + 1.12*58.44/2.17*Cl)/(142.04/2.66*S + 58.44/2.17*Cl) : (1-f_dust_lower)*(0.8) :
```

```
;phyllo-silicates

[Muscovite + Biotit]
Name=Mica-like
Class=(phyllo-)silicate/clay mineral
(Ca+Na+K+Fe+Mg+Al+Si) / (Na+Mg+Al+Si+P+S+Cl+K+Ca+Ti+Cr+Mn+Fe)=0.7 .. 1.01
Al/Si=0.2 .. 3
(Na+K+Ca+Mg+Fe)/(Si)=0.5 .. 2.5
(Cl+2*S)/Na = 0 .. 0.3
(Cl+2*S) / (Al+Si)=0 .. 0.125
IsNotInOtherGroup=yes
~kappa_upper=Cl+S>0 ? (1-f_dust_upper)*(0.68*142.04/2.66*S + 1.12*58.44/2.17*Cl)/(142.04/2.66*S + 58.44/2.17*Cl) : (1-f_dust_upper)*(0.8) :
~kappa_lower=Cl+S>0 ? (1-f_dust_lower)*(0.68*142.04/2.66*S + 1.12*58.44/2.17*Cl)/(142.04/2.66*S + 58.44/2.17*Cl) : (1-f_dust_lower)*(0.8) :

[complex clay]
Name=Complex clay-mineral-like
Class=(phyllo-)silicate/clay mineral
(Al+Si+Na+Mg+K+Ca+Fe) / (Na+Mg+Al+Si+P+S+Cl+K+Ca+Ti+Cr+Mn+Fe)=0.7 .. 1.01
Al/Si=0.5 .. 1.5
(Mg+Fe+K)/Si=0.1 .. 1
Fe/Si=0 .. 0.5
Ca/Si=0 .. 0.5
K/Si=0 .. 0.5
Mg/Si=0 .. 0.5
Na/Si=0 .. 0.5
(Na+Cl+2*S) / (Al+Si)=0 .. 0.25
IsNotInOtherGroup=yes
~kappa_upper=Cl+S>0 ? (1-f_dust_upper)*(0.68*142.04/2.66*S + 1.12*58.44/2.17*Cl)/(142.04/2.66*S + 58.44/2.17*Cl) : (1-f_dust_upper)*(0.8) :
~kappa_lower=Cl+S>0 ? (1-f_dust_lower)*(0.68*142.04/2.66*S + 1.12*58.44/2.17*Cl)/(142.04/2.66*S + 58.44/2.17*Cl) : (1-f_dust_lower)*(0.8) :

[Palygorskit]
Name=Palygorskite-like
Class=(phyllo-)silicate/clay mineral
(Mg+Al+Si) / (Na+Mg+Al+Si+P+S+Cl+K+Ca+Ti+Cr+Mn+Fe)=0.7 .. 1.01
Al/Si=0.1 .. 0.5
(Mg)/(Al+Si)=0.2 .. 0.7
Ca/Si=0 .. 0.1
Fe/Si=0 .. 0.1
Na/Si=0 .. 0.1
K/Si=0 .. 0.1
(Na+Cl+2*S) / (Al+Si)=0 .. 0.25
IsNotInOtherGroup=yes
~kappa_upper=Cl+S>0 ? (1-f_dust_upper)*(0.68*142.04/2.66*S + 1.12*58.44/2.17*Cl)/(142.04/2.66*S + 58.44/2.17*Cl) : (1-f_dust_upper)*(0.8) :
~kappa_lower=Cl+S>0 ? (1-f_dust_lower)*(0.68*142.04/2.66*S + 1.12*58.44/2.17*Cl)/(142.04/2.66*S + 58.44/2.17*Cl) : (1-f_dust_lower)*(0.8) :
```

```
; non-silicates

[Calcite]
Name=Calcite-like
Class=Ca-rich
Ca/(Na+Mg+Al+Si+P+S+Cl+K+Ca+Ti+Cr+Mn+Fe)=0.7 .. 1.01
(Al+Si)/Ca=0 .. 0.3
Mg/Ca=0 .. 0.3
S/Ca=0 .. 0.3
Cl/Ca=0 .. 0.3
P/(Ca+P)=0 .. 0.19
S/(Ca+S)=0 .. 0.19
~kappa_upper=Cl+S>0 ? (1-f_dust_upper)*(0.68*142.04/2.66*S + 1.12*58.44/2.17*Cl)/(142.04/2.66*S + 58.44/2.17*Cl) : (1-f_dust_upper)*(0.8) :
~kappa_lower=Cl+S>0 ? (1-f_dust_lower)*(0.68*142.04/2.66*S + 1.12*58.44/2.17*Cl)/(142.04/2.66*S + 58.44/2.17*Cl) : (1-f_dust_lower)*(0.8) :

[Dolomite]
Name=Dolomite-like
Class=Ca-rich
(Mg+Ca) / (Na+Mg+Al+Si+P+S+Cl+K+Ca+Ti+Cr+Mn+Fe)=0.7 .. 1.01
Mg/Ca=0.3 .. 3
S/Ca=0 .. 0.3
Cl/Ca=0 .. 0.3
(Al+Si)/Ca=0 .. 0.3
~kappa_upper=Cl+S>0 ? (1-f_dust_upper)*(0.68*142.04/2.66*S + 1.12*58.44/2.17*Cl)/(142.04/2.66*S + 58.44/2.17*Cl) : (1-f_dust_upper)*(0.8) :
~kappa_lower=Cl+S>0 ? (1-f_dust_lower)*(0.68*142.04/2.66*S + 1.12*58.44/2.17*Cl)/(142.04/2.66*S + 58.44/2.17*Cl) : (1-f_dust_lower)*(0.8) :

[Apatite]
Name=Apatite-like
Class=Ca-rich
(Ca+P) / (Na+Mg+Al+Si+P+S+Cl+K+Ca+Ti+Cr+Mn+Fe)=0.7 .. 1.01
Mg/Ca=0 .. 0.3
P/(Ca+P)=0.2 .. 0.8
Cl/Ca=0 .. 0.3
(Al+Si)/(P+Ca)=0 .. 0.25
~kappa_upper=Cl+S>0 ? (1-f_dust_upper)*(0.68*142.04/2.66*S + 1.12*58.44/2.17*Cl)/(142.04/2.66*S + 58.44/2.17*Cl) : (1-f_dust_upper)*(0.8) :
~kappa_lower=Cl+S>0 ? (1-f_dust_lower)*(0.68*142.04/2.66*S + 1.12*58.44/2.17*Cl)/(142.04/2.66*S + 58.44/2.17*Cl) : (1-f_dust_lower)*(0.8) :

[Gypsum]
Name=Gypsum-like
Class=stable sulfates
(Ca+S) / (Na+Mg+Al+Si+P+S+Cl+K+Ca+Ti+Cr+Mn+Fe)=0.7 .. 1.01
Ca/(Ca+S)=0.2 .. 0.8
Mg/Ca=0 .. 0.3
Cl/Ca=0 .. 0.3
~kappa_upper=Cl+Na>0 ? (1-f_dust_upper)*(0.68*142.04/2.66*Na + 1.12*58.44/2.17*Cl)/(142.04/2.66*Na + 58.44/2.17*Cl) : (1-f_dust_upper)*(0.8) :
~kappa_lower=Cl+Na>0 ? (1-f_dust_lower)*(0.68*142.04/2.66*Na + 1.12*58.44/2.17*Cl)/(142.04/2.66*Na + 58.44/2.17*Cl) : (1-f_dust_lower)*(0.8) :

[Fluorite]
Name=Fluorite-like
Class=Ca-rich
(Ca+F) / (F+Na+Mg+Al+Si+P+S+Cl+K+Ca+Ti+Cr+Mn+Fe)=0.7 .. 1.01
Ca/(Ca+S)=0 .. 0.1999
Ca/(Ca+F)=0.1667 .. 0.5
Mg/Ca=0 .. 0.3
Cl/Ca=0 .. 0.3
~kappa_upper=Cl+Na>0 ? (1-f_dust_upper)*(0.68*142.04/2.66*Na + 1.12*58.44/2.17*Cl)/(142.04/2.66*Na + 58.44/2.17*Cl) : (1-f_dust_upper)*(0.8) :
~kappa_lower=Cl+Na>0 ? (1-f_dust_lower)*(0.68*142.04/2.66*Na + 1.12*58.44/2.17*Cl)/(142.04/2.66*Na + 58.44/2.17*Cl) : (1-f_dust_lower)*(0.8) :

[Mg-rich]
Name=Magnesite-like
Class=other
AdditionalTitle=Density
Additional=3.3
Mg/(Na+Mg+Al+Si+P+S+Cl+K+Ca+Ti+Cr+Mn+Fe)=0.7 .. 1.01
~kappa_upper=Cl+S>0 ? (1-f_dust_upper)*(0.68*142.04/2.66*S + 1.12*58.44/2.17*Cl)/(142.04/2.66*S + 58.44/2.17*Cl) : (1-f_dust_upper)*(0.8) :
~kappa_lower=Cl+S>0 ? (1-f_dust_lower)*(0.68*142.04/2.66*S + 1.12*58.44/2.17*Cl)/(142.04/2.66*S + 58.44/2.17*Cl) : (1-f_dust_lower)*(0.8) :
```

```
;Sulfates

[Na Sulfate]
Name=Sodium sulfate
Class=soluble sulfates
(Na+Mg+S+Cl) / (Na+Mg+Al+Si+P+S+Cl+K+Ca+Ti+Cr+Mn+Fe)=0.7 .. 1.01
S/(Na+0.5*Mg)=0.8 .. 2
Cl/(Na+0.5*Mg)=0 .. 0.2
Cl / (Cl+S)=0 .. 0.3
K/Na=0 .. 0.5
Ca/Na=0 .. 0.5
Mg/Na=0 .. 0.5
(Al+Si)/(Na+Cl+S)=0 .. 0.25
~kappa_upper=Cl+S>0 ? (1-f_dust_upper)*(0.68*142.04/2.66*S + 1.12*58.44/2.17*Cl)/(142.04/2.66*S + 58.44/2.17*Cl) : (1-f_dust_upper)*(0.8) :
~kappa_lower=Cl+S>0 ? (1-f_dust_lower)*(0.68*142.04/2.66*S + 1.12*58.44/2.17*Cl)/(142.04/2.66*S + 58.44/2.17*Cl) : (1-f_dust_lower)*(0.8) :
~SSᵢIB=(Na+2*Mg+K+2*Ca-Cl-2*S)/(Na+2*Mg+K+2*Ca+Cl+2*S)
~FI_Mg_Na=lg(Mg/Na)
~FI_Ca_Na=lg(Ca/Na)
~FI_Mg_Cl=lg(Mg/Cl)
~FI_Na_Cl=lg(Na/Cl)
~FI_S_Cl=lg(S/Cl)

[sulfate]
Name=Ammonium-sulfate-like
Class=soluble sulfates
S/(Na+Mg+Al+Si+P+S+Cl+K+Ca+Ti+Cr+Mn+Fe)=0.7 .. 1.01
Cl / (Cl+S)=0 .. 0.3
Na/S=0 .. 1.01
Cl/S=0 .. 0.2
Si/S=0 .. 0.5
(Al+Si)/S=0 .. 0.25
~kappa_upper=Cl+S>0 ? (1-f_dust_upper)*(0.68*142.04/2.66*S + 1.12*58.44/2.17*Cl)/(142.04/2.66*S + 58.44/2.17*Cl) : (1-f_dust_upper)*(0.8) :
~kappa_lower=Cl+S>0 ? (1-f_dust_lower)*(0.68*142.04/2.66*S + 1.12*58.44/2.17*Cl)/(142.04/2.66*S + 58.44/2.17*Cl) : (1-f_dust_lower)*(0.8) :
~SSRIB=(Na+2*Mg+K+2*Ca-Cl-2*S)/(Na+2*Mg+K+2*Ca+Cl+2*S)
~FI_Mg_Na=lg(Mg/Na)
~FI_Ca_Na=lg(Ca/Na)
~FI_Mg_Cl=lg(Mg/Cl)
~FI_Na_Cl=lg(Na/Cl)
~FI_S_Cl=lg(S/Cl)

[complex sulfate]
Name=Complex sulfate
Class=soluble sulfates
(Na+Mg+K+Ca+S+Cl) / (Na+Mg+Al+Si+P+S+Cl+K+Ca+Ti+Cr+Mn+Fe)=0.7 .. 1.01
(Al+Si)/S=0 .. 0.25
Cl / (Cl+S)=0 .. 0.3
IsNotInOtherGroup=yes
~kappa_upper=Cl+S>0 ? (1-f_dust_upper)*(0.68*142.04/2.66*S + 1.12*58.44/2.17*Cl)/(142.04/2.66*S + 58.44/2.17*Cl) : (1-f_dust_upper)*(0.8) :
~kappa_lower=Cl+S>0 ? (1-f_dust_lower)*(0.68*142.04/2.66*S + 1.12*58.44/2.17*Cl)/(142.04/2.66*S + 58.44/2.17*Cl) : (1-f_dust_lower)*(0.8) :
~SSRIB=(Na+2*Mg+K+2*Ca-Cl-2*S)/(Na+2*Mg+K+2*Ca+Cl+2*S)
~FI_Mg_Na=lg(Mg/Na)
~FI_Ca_Na=lg(Ca/Na)
~FI_Mg_Cl=lg(Mg/Cl)
~FI_Na_Cl=lg(Na/Cl)
~FI_S_Cl=lg(S/Cl)

[complex sulfate-chloride]
Name=Complex soluble salt
Class=soluble sulfates
(Na+Mg+K+Ca+S+Cl) / (Na+Mg+Al+Si+P+S+Cl+K+Ca+Ti+Cr+Mn+Fe)=0.7 .. 1.01
(Al+Si)/S=0 .. 0.25
IsNotInOtherGroup=yes
~kappa_upper=Cl+S>0 ? (1-f_dust_upper)*(0.68*142.04/2.66*S + 1.12*58.44/2.17*Cl)/(142.04/2.66*S + 58.44/2.17*Cl) : (1-f_dust_upper)*(0.8) :
~kappa_lower=Cl+S>0 ? (1-f_dust_lower)*(0.68*142.04/2.66*S + 1.12*58.44/2.17*Cl)/(142.04/2.66*S + 58.44/2.17*Cl) : (1-f_dust_lower)*(0.8) :
~SSRIB=(Na+2*Mg+K+2*Ca-Cl-2*S)/(Na+2*Mg+K+2*Ca+Cl+2*S)
~FI_Mg_Na=lg(Mg/Na)
~FI_Ca_Na=lg(Ca/Na)
~FI_Mg_Cl=lg(Mg/Cl)
~FI_Na_Cl=lg(Na/Cl)
~FI_S_Cl=lg(S/Cl)

[Alunite]
Name=Alunite-like
Class=stable sulfates
(Al+K+S) / (Na+Mg+Al+Si+P+S+Cl+K+Ca+Ti+Cr+Mn+Fe)=0.7 .. 1.01
Ca/(Ca+Al+K+S)=0 .. 0.05
Si/(Si+Al+K+S)=0 .. 0.1
K/(Al+K+S)=0.05 .. 0.3
S/(Al+K+S)=0.15 .. 0.5
Al/(Al+K+S)=0.3 .. 0.8
~kappa_upper=Cl+Na>0 ? (1-f_dust_upper)*(0.68*142.04/2.66*Na + 1.12*58.44/2.17*Cl)/(142.04/2.66*Na + 58.44/2.17*Cl) : (1-f_dust_upper)*(0.8) :
~kappa_lower=Cl+Na>0 ? (1-f_dust_lower)*(0.68*142.04/2.66*Na + 1.12*58.44/2.17*Cl)/(142.04/2.66*Na + 58.44/2.17*Cl) : (1-f_dust_lower)*(0.8) :
```

```
; salt/silicates mixtures

[Sea-salt]
Name=Sea-salt
Class=sea-salt
(Na+Mg+Cl) / (Na+Mg+Al+Si+P+S+Cl+K+Ca+Ti+Cr+Mn+Fe)=0.7 .. 1.01
Cl/(Na+0.5*Mg)=0.5 .. 2
Cl / (Cl+S)=0.7 .. 1.01
S/(Na+0.5*Mg)=0 .. 0.2
K/Na=0 .. 0.5
Ca/Na=0 .. 0.5
Mg/Na=0 .. 0.5
(Al+Si) / (Na+Cl+S)=0 .. 0.25
~SSRIB=(Na+2*Mg+K+2*Ca-Cl-2*S)/(Na+2*Mg+K+2*Ca+Cl+2*S)
~kappa_upper=Cl+S>0 ? (1-f_dust_upper)*(0.68*142.04/2.66*S + 1.12*58.44/2.17*Cl)/(142.04/2.66*S + 58.44/2.17*Cl) : (1-f_dust_upper)*(0.8) :
~kappa_lower=Cl+S>0 ? (1-f_dust_lower)*(0.68*142.04/2.66*S + 1.12*58.44/2.17*Cl)/(142.04/2.66*S + 58.44/2.17*Cl) : (1-f_dust_lower)*(0.8) :
~FI_Mg_Na=lg(Mg/Na)
~FI_Ca_Na=lg(Ca/Na)
~FI_Mg_Cl=lg(Mg/Cl)
~FI_Na_Cl=lg(Na/Cl)
~FI_S_Cl=lg(S/Cl)

[aged Sea salt]
Name=Aged sea-salt
Class=sea-salt
(Na+Mg+Cl+S+Ca) / (Na+Mg+Al+Si+P+S+Cl+K+Ca+Ti+Cr+Mn+Fe)=0.7 .. 1.01
;Cl/(Na+0.5*Mg)=0.2 .. 0.8
;S/(Na+0.5*Mg)=0.2 .. 0.8
(Cl+2*S) / (Na+0.5*Mg+0.5*Ca)=0.3 .. 3.333
Cl / (Cl+S)=0.3 .. 0.7
K / (K+Na)=0 .. 0.3
Ca / (Ca+Na)=0 .. 0.2
Mg / (Mg+Na)=0 .. 0.3
(Al+Si) / (Al+Si+Na+Cl+S)=0 .. 0.25
~kappa_upper=Cl+S>0 ? (1-f_dust_upper)*(0.68*142.04/2.66*S + 1.12*58.44/2.17*Cl)/(142.04/2.66*S + 58.44/2.17*Cl) : (1-f_dust_upper)*(0.8) :
~kappa_lower=Cl+S>0 ? (1-f_dust_lower)*(0.68*142.04/2.66*S + 1.12*58.44/2.17*Cl)/(142.04/2.66*S + 58.44/2.17*Cl) : (1-f_dust_lower)*(0.8) :
~SSRIB=(Na+2*Mg+K+2*Ca-Cl-2*S)/(Na+2*Mg+K+2*Ca+Cl+2*S)
~FI_Mg_Na=lg(Mg/Na)
~FI_Ca_Na=lg(Ca/Na)
~FI_Mg_Cl=lg(Mg/Cl)
~FI_Na_Cl=lg(Na/Cl)
~FI_S_Cl=lg(S/Cl)

[NaCl-Si-Mix]
Name=Sea-salt/silicate mixture
Class=sea-salt/silicate mixtures
(Al+Si+Mg+Fe+Na+Cl+S) / (Na+Mg+Al+Si+P+S+Cl+K+Ca+Ti+Cr+Mn+Fe)=0.7 .. 1.01
Fe / (Na+Mg+Al+Si+P+S+Cl+K+Ca+Ti+Cr+Mn+Fe)=0 .. 0.3
(Na+Cl+2*S) / (Al+Si)=0.25 .. 4
S/Cl=0 .. 0.5
F/(F+Si)=0 .. 0.499
IsNotInOtherGroup=yes
~kappa_upper=Cl+S>0 ? (1-f_dust_upper)*(0.68*142.04/2.66*S + 1.12*58.44/2.17*Cl)/(142.04/2.66*S + 58.44/2.17*Cl) : (1-f_dust_upper)*(0.8) :
~kappa_lower=Cl+S>0 ? (1-f_dust_lower)*(0.68*142.04/2.66*S + 1.12*58.44/2.17*Cl)/(142.04/2.66*S + 58.44/2.17*Cl) : (1-f_dust_lower)*(0.8) :

[NaClS-Si-Mix]
Name=Aged sea-salt/silicate mixture
Class=sea-salt/silicate mixtures
(Al+Si+Mg+Fe+Na+Cl+S) / (Na+Mg+Al+Si+P+S+Cl+K+Ca+Ti+Cr+Mn+Fe)=0.7 .. 1.01
(Na+Cl+2*S) / (Al+Si)=0.25 .. 4
Fe / (Na+Mg+Al+Si+P+S+Cl+K+Ca+Ti+Cr+Mn+Fe)=0 .. 0.3
S/Cl=0.5 .. 1
IsNotInOtherGroup=yes
~kappa_upper=Cl+S>0 ? (1-f_dust_upper)*(0.68*142.04/2.66*S + 1.12*58.44/2.17*Cl)/(142.04/2.66*S + 58.44/2.17*Cl) : (1-f_dust_upper)*(0.8) :
~kappa_lower=Cl+S>0 ? (1-f_dust_lower)*(0.68*142.04/2.66*S + 1.12*58.44/2.17*Cl)/(142.04/2.66*S + 58.44/2.17*Cl) : (1-f_dust_lower)*(0.8) :

[S-Si-Mix]
Name=Sulfate/silicate mixture
Class=sulfate/silicate mixtures
(Al+Si+Mg+Fe+Na+S) / (Na+Mg+Al+Si+P+S+Cl+K+Ca+Ti+Cr+Mn+Fe)=0.7 .. 1.01
Fe / (Na+Mg+Al+Si+P+S+Cl+K+Ca+Ti+Cr+Mn+Fe)=0 .. 0.3
Si / (Al+Si+Mg+Fe) = 0.2 .. 1.01
S/(Al+Si)=0.25 .. 4
Cl/S=0 .. 1
Na/S=0 .. 1
IsNotInOtherGroup=yes
~kappa_upper=Cl+S>0 ? (1-f_dust_upper)*(0.68*142.04/2.66*S + 1.12*58.44/2.17*Cl)/(142.04/2.66*S + 58.44/2.17*Cl) : (1-f_dust_upper)*(0.8) :
~kappa_lower=Cl+S>0 ? (1-f_dust_lower)*(0.68*142.04/2.66*S + 1.12*58.44/2.17*Cl)/(142.04/2.66*S + 58.44/2.17*Cl) : (1-f_dust_lower)*(0.8) :

[complex_mix]
Name=Complex mixture
Class=complex mixtures
(Na+Mg+Al+Si+S+Cl+K+Ca+Fe) / (Na+Mg+Al+Si+P+S+Cl+K+Ca+Ti+Cr+Mn+Fe)=0.7 .. 1.01
(Na+Cl) / (Na+Mg+Al+Si+P+S+Cl+K+Ca+Ti+Cr+Mn+Fe)=0.1 .. 0.9
S/(Na+Mg+Al+Si+P+S+Cl+K+Ca+Ti+Cr+Mn+Fe)=0.1 .. 0.9
(Ca+K+Mg+Fe) / (Na+Mg+Al+Si+P+S+Cl+K+Ca+Ti+Cr+Mn+Fe)=0.1 .. 0.9
(Al+Si) / (Na+Mg+Al+Si+P+S+Cl+K+Ca+Ti+Cr+Mn+Fe)=0.1 .. 0.9
IsNotInOtherGroup=yes
~kappa_upper=Cl+S>0 ? (1-f_dust_upper)*(0.68*142.04/2.66*S + 1.12*58.44/2.17*Cl)/(142.04/2.66*S + 58.44/2.17*Cl) : (1-f_dust_upper)*(0.8) :
~kappa_lower=Cl+S>0 ? (1-f_dust_lower)*(0.68*142.04/2.66*S + 1.12*58.44/2.17*Cl)/(142.04/2.66*S + 58.44/2.17*Cl) : (1-f_dust_lower)*(0.8) :
```

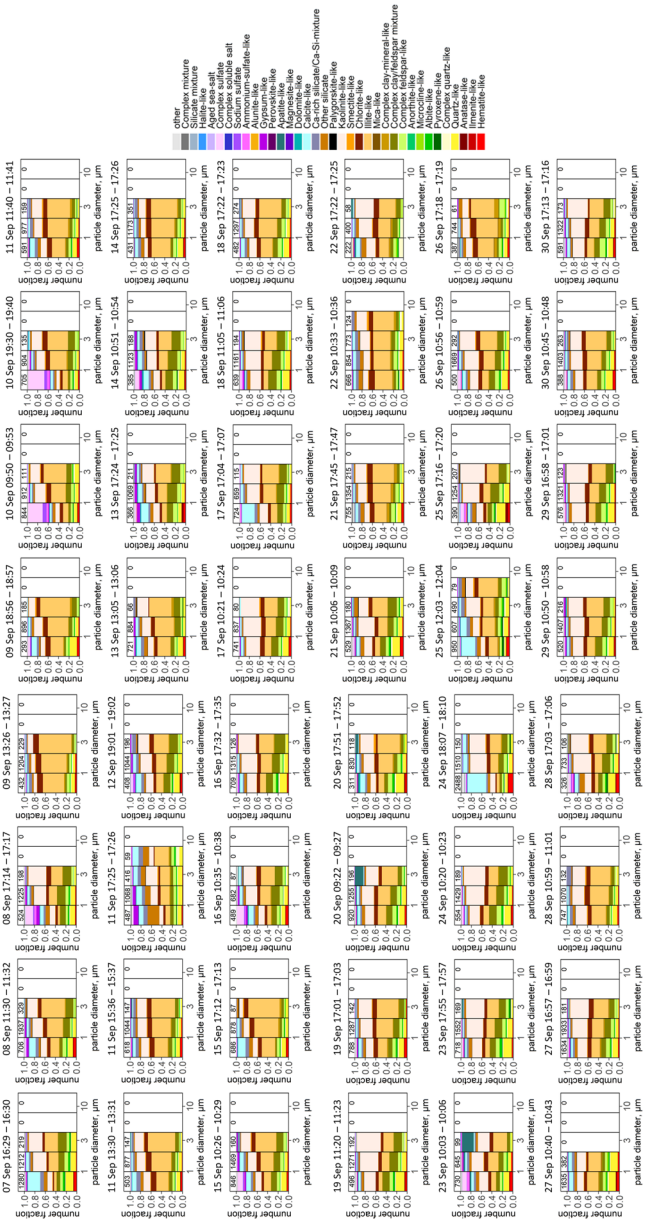

Figure 6.1: Number abundance for MOUDI stage 4. Abundance bars are not shown for size bins with fewer than 50 particles.

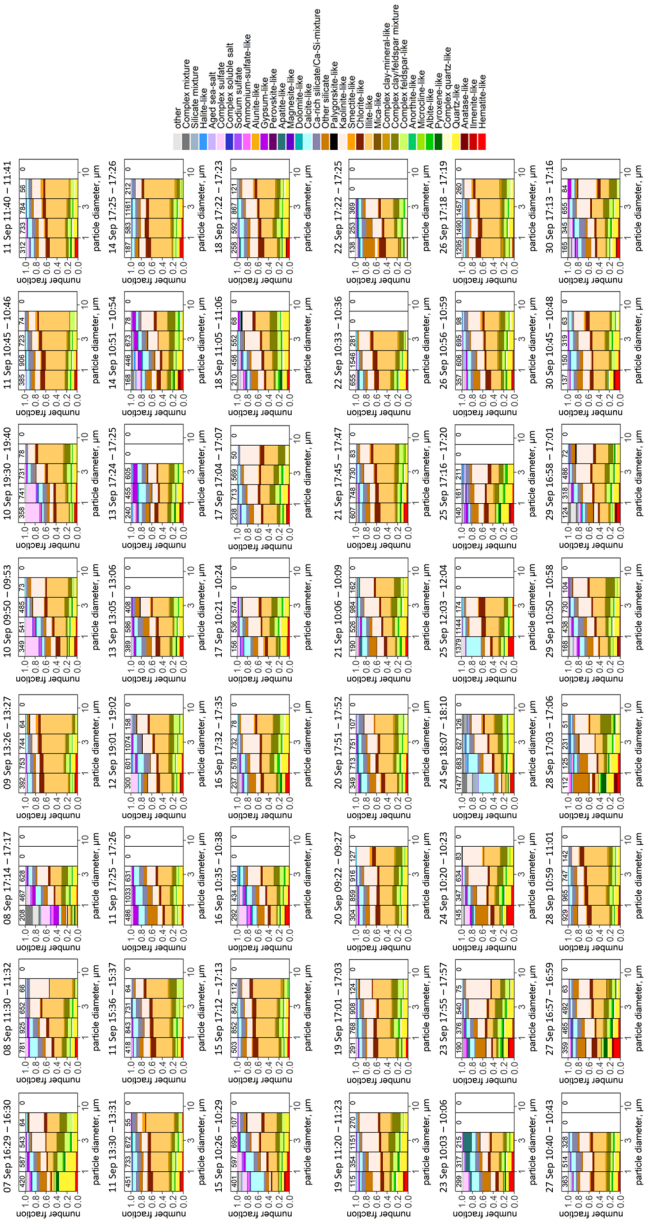

Figure 6.2: Number abundance for MOUDI stage 3. Abundance bars are not shown for size bins with fewer than 50 particles

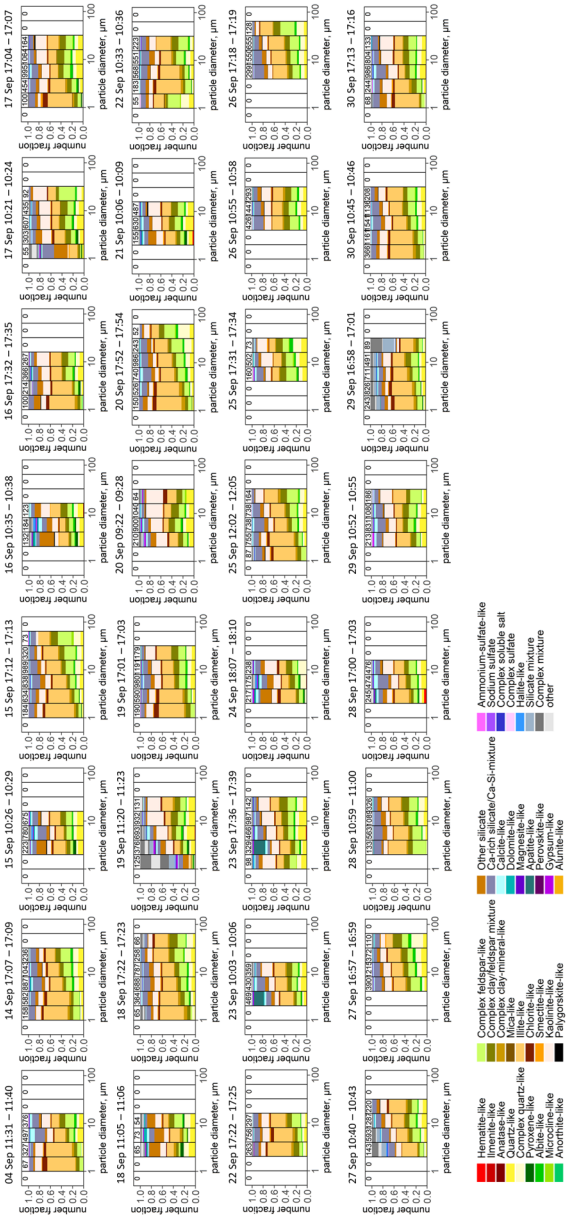

Figure 6.3: Number abundance for FWI. Abundance bars are not shown for size bins with fewer than 50 particles

Temporal evolution of Icelandic dust

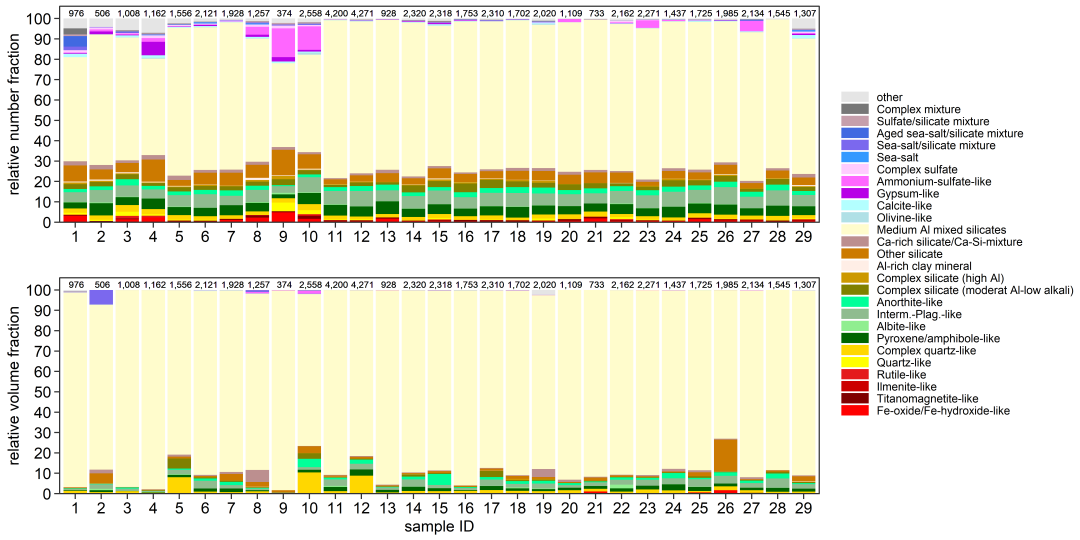

Figure 6.4: Chemical composition (relative number and volume abundance) of different particle groups of aerosol collected in August and September 2021 at Dyngjusandur by deposition plate sampler. Collection time for each Sample ID is provided in table below. The numbers on top represent total particle analysed.

Figure 6.4 and 6.5 shows the relative volume and number fractions for all the analysed flat-plate and free-wing sample substrates respectively at Dyngjusandur. In general, airborne particles at Dyngjusandur is dominated by MAS particles with 70 - 97 % by volume and 40 - 75 % by number fraction. In terms of volume, a rather homogeneous composition is observed among individual samples collected at different days with no particular compositional trend. However, if one looks at the number fraction, the picture is slightly different. MAS is still the dominant particle type but we also see iron-rich particles, other silicates, Intermediate Palygorskite-like, Pyroxene/amphibole-like, with some sulfate episodes. As most of these particles are only present in smaller size bins, they don't show up in significant amount in volume fraction. 17-21 August, 3 and 5 September are characterized by sulfate events. These are mainly confined in the smaller sizes with a median diameter of 1.9 µm and are nearly circular with a median aspect ratio of 1.2. However, some extreme morphology is seen in some coarser particles that are tend to be sulfate needles.

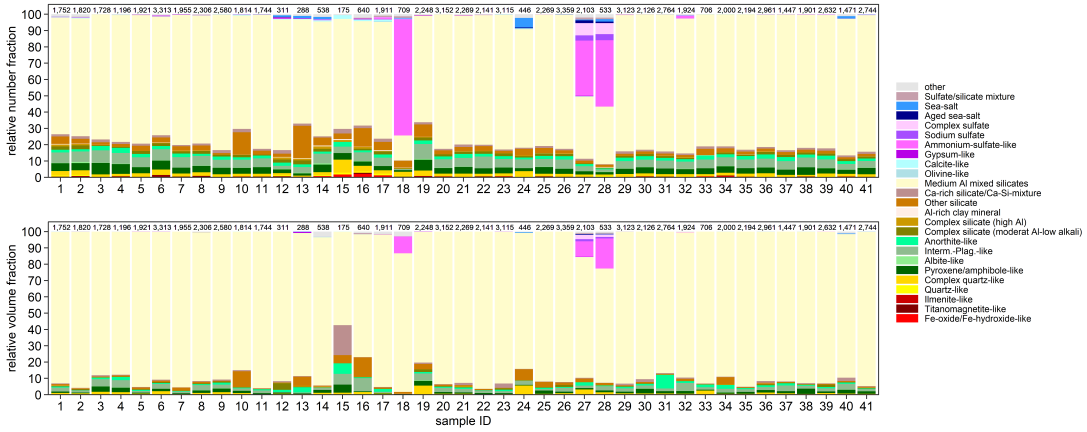

Figure 6.5: Chemical composition (relative number and volume abundance) of different particle groups of aerosol collected in August and September 2021 at Dyngjusandur by free-wing impactor. Collection time for each Sample ID is provided in table below. The numbers on top represent total particle analysed.

Table 6.1: Sampling times for flat-plate samplers at Dyngjusandur

ID	Start date & time	End date & time	Exposure time (min)
1	09.08.2021 12:00	10.08.2021 16:15	1695
2	10.08.2021 16:20	11.08.2021 14:30	1330
3	11.08.2021 14:40	12.08.2021 17:50	1630
4	12.08.2021 18:00	13.08.2021 18:00	1440
5	13.08.2021 18:05	14.08.2021 18:00	1435
6	14.08.2021 18:05	15.08.2021 18:23	1458
7	15.08.2021 18:25	16.08.2021 18:39	1454
8	16.08.2021 18:34	17.08.2021 19:00	1466
9	17.08.2021 19:00	19.08.2021 17:08	2768
10	19.08.2021 17:10	21.08.2021 16:50	2860
11	21.08.2021 16:50	22.08.2021 17:35	1485
12	22.08.2021 20:00	23.08.2021 18:05	1325
13	23.08.2021 18:10	25.08.2021 10:00	2390
14	30.08.2021 19:12	31.08.2021 08:20	788
15	31.08.2021 08:25	31.08.2021 08:35	10
16	31.08.2021 08:45	31.08.2021 10:05	80
17	31.08.2021 10:05	31.08.2021 10:45	40
18	31.08.2021 10:45	31.08.2021 18:30	465
19	31.08.2021 18:40	01.09.2021 09:05	865
20	01.09.2021 09:15	01.09.2021 10:40	85
21	01.09.2021 11:55	01.09.2021 18:15	380
22	01.09.2021 18:30	02.09.2021 18:35	1445
23	02.09.2021 18:35	03.09.2021 19:20	1485
24	03.09.2021 19:20	04.09.2021 18:35	1395
25	04.09.2021 18:35	04.09.2021 19:40	65
26	04.09.2021 19:45	05.09.2021 09:35	830
27	05.09.2021 09:35	05.09.2021 10:30	55
28	05.09.2021 10:30	05.09.2021 20:30	600
29	05.09.2021 20:30	07.09.2021 10:45	2295

Table 6.2: Sampling times for free-wing impactors at Dyngjusandur

ID	Start date & time	End date & time	Exposure time (min)
01	09.08.2021 15:45	09.08.2021 17:45	120
02	10.08.2021 12:35	10.08.2021 14:35	120
03	10.08.2021 17:43	10.08.2021 17:57	14
04	10.08.2021 18:04	10.08.2021 18:07	3
05	11.08.2021 15:08	11.08.2021 15:18	10
06	11.08.2021 15:24	11.08.2021 15:39	15
07	12.08.2021 17:23	12.08.2021 17:38	15
08	14.08.2021 16:08	14.08.2021 17:10	62
09	15.08.2021 16:29	15.08.2021 16:30	1
10	15.08.2021 16:33	15.08.2021 16:36	3
11	15.08.2021 16:41	15.08.2021 16:46	5
12	16.08.2021 18:20	16.08.2021 18:21	1
13	16.08.2021 18:23	16.08.2021 18:26	3
14	16.08.2021 18:27	16.08.2021 18:32	5
15	17.08.2021 18:41	17.08.2021 18:44	3
16	17.08.2021 18:45	17.08.2021 18:50	5
17	19.08.2021 16:40	19.08.2021 17:10	30
18	20.08.2021 15:48	20.08.2021 17:48	120
19	21.08.2021 13:22	21.08.2021 13:52	30
20	22.08.2021 17:02	22.08.2021 17:04	2
21	22.08.2021 17:10	22.08.2021 17:11	1
22	23.08.2021 16:04	23.08.2021 16:08	4
23	23.08.2021 16:15	23.08.2021 16:16	1
24	31.08.2021 19:06	31.08.2021 19:07	1
25	01.09.2021 19:08	01.09.2021 19:09	1
26	01.09.2021 19:14	01.09.2021 19:16	2
27	02.09.2021 10:15	02.09.2021 10:45	30
28	02.09.2021 19:00	02.09.2021 19:30	30
29	03.09.2021 09:30	03.09.2021 10:30	60
30	03.09.2021 11:27	03.09.2021 11:34	7
31	03.09.2021 11:38	03.09.2021 11:47	9
32	03.09.2021 19:10	03.09.2021 19:15	5
33	04.09.2021 09:25	04.09.2021 09:30	5
34	04.09.2021 09:33	04.09.2021 09:38	5
35	04.09.2021 09:45	04.09.2021 10:00	15
36	04.09.2021 18:40	04.09.2021 18:41	1
37	04.09.2021 18:43	04.09.2021 18:45	2
38	05.09.2021 09:35	05.09.2021 09:37	2
39	05.09.2021 09:38	05.09.2021 09:38	0.5
40	05.09.2021 20:06	05.09.2021 20:16	10
41	05.09.2021 20:20	05.09.2021 20:22	2

List of Figures

1.1 Model simulation showing four essential aerosol types and their global occurrence . . . 2
1.2 Conceptual scheme of FRAGMENT with the three objectives (Obj. 1, Obj. 2, and Obj. 3). Image credit: C. Prez Garca-Pando, principal investigator of FRAGMENT. . . . 4
1.3 Overview on the investigated sites . . . 6

2.1 Schematic diagram of mineral dust cycle and interactions between dust and climate and biogeochemistry . . . 10
2.2 Satellite captured image of a Saharan dust plume by the National Aeronautics and Space Administration (NASA)-National Oceanic and Atmospheric Administration (NOAA) Suomi National Polar-orbiting Partnership on June 18, 2020. The dust plume (in light brown) is being transported off the west coast of northern Africa into the Atlantic Ocean. . . . 12
2.3 Climatic and environmental impacts of HLD include direct radiative forcing (blocking sunlight), indirect radiative forcing (clouds and cryosphere), as well as effects on atmospheric chemistry and the marine environment 14
2.4 Mixing state of particle . . . 17
2.5 Radiative forcing bar chart for the period 17502011 based on emitted compounds or other changes . . . 18
2.6 Dust radiation interaction . . . 20
2.7 Dust cloud interaction . . . 22
2.8 Dust interactions with the atmospheric chemistry . . . 24
2.9 Dust interactions with the cryosphere . . . 25
2.10 Dust interactions with biochemistry . . . 26
2.11 Various techniques for observing mineral dust, including aircraft, ground-based, laboratory simulation, and remote sensing. . . . 28

3.1 Electron matter interactions: the different types of signals which are generated 34

3.2 Schematic representation of the types of X-ray spectrum produced by bombardment of incident electron against photon energy 35

3.3 Two-dimensional (2-D) projected area of a dust particle with the two common quantifications of dust width 39

4.1 (a) Northwestern Africa showing area of operation of FRAGMENT campaign. The main location L'Bour is shown by a star sign which is located close to the Drâa river basin. (b) Schematic representation of different instruments used in the campaign with green dots highlighting those instruments used for single particle analysis. (c) Flat-plate deposition sampler (FPS). (d) Free-wing impactor (FWI). (e) Cascade impactor (MOUDI). (f) Sampling schedule of particle collection using different techniques. The horizontal bar represents start and end of sampling time. Note that due to very short sampling time for FWI and MOUDI, the two bars (start and end) appear as one. Image (a) was created using Google Earth (US Dept of State Geographer, Data SIO, NOAA, US Navy, NGA, GEBCO, ©2020 Google, Image Landsat/ Copernicus). 44

4.2 Average elemental composition as a function of particle size for different particle groups. The legend shows element index for each respective element. The numbers on top represent total particle counts in the given size bin. Abundance bars are not shown for size bins with fewer than 10 particles. 45

4.3 Scatter-plot for silicate particle composition. The three main clusters are marked by numbers: (1) quartz cluster, (2) feldspar cluster, and (3) clay mineral/aggregate cluster. 49

4.4 (a) Normalized particle size distribution obtained by different sampling techniques averaged over the entire campaign period. (b) Comparing the atmospheric particle size distribution between FWI and OPC. The bold line is for FWI with error bar showing the Poisson counting error and dashed line indicates the field campaign mean size distribution from OPC and the shaded region shows the 95th and 5th percentile. Note that below $\sim$ 15 µm diameter, the collection efficiency of the FWI drops significantly. 50

4.5 Average size-resolved mass abundance of different particle groups. The numbers on top represent total particle counts in the given size bin. . . . 53

4.6 Average size-resolved mass abundance of different particle groups using different sampling techniques collected over the campaign period. The numbers on top represent total particle counts in the given size bin. Abundance bars are not shown for size bins with fewer than 30 particles. . . 55

4.7 Time series of chemical composition for particles in (a) $0.1 < d < 2.5$ µm, (b) $2.5 < d < 5$ µm and (c) $5 < d < 20$ µm in L'Bour. 56

4.8 Phase compositions of size bins for samples collected under specific meteorological conditions at specific times and on certain days: (a) sulfate episode (b) apatite particle (c) Ca-rich episode and (d) typical average composition. The total number of analyzed particles is given for each size class with fewer than 30 particles not shown. 57

4.9 (a) Size resolved iron indices for silicate particles. n.d. means Fe not detected. The numbers on top represent total particle counts in the given size bin. (b) Silicate particle with iron association based on Al/Si ratio. Abundance bars are not shown for size intervals with fewer than 30 particles because of high statistical uncertainty. 59

4.10 (a) Relative contribution of each particle type to total iron and (b) fraction of elemental iron by mass with respect to all the other elements. 61

4.11 Mass ratio of Feldspar-like, Total feldspar (more strict criterion), and K-feldspar (more strict criterion) to total particles. 62

4.12 (a) Measured and parameterized (solid line) aspect ratio density distribution of dust particles (b) Size-resolved particle aspect ratio. The bar range represents the range between 0.1 and 0.9 quantiles with dot being the median and the bins are color coded by the number of data points within each bin. 64

5.1 Location of the study area. The label DYS represent the location of main measurement site whereas labels MRS, SRS, HRS, and VFS represent the outflow regions where a deposition sampler was placed. 67

5.2 (a) Average elemental composition (atomic fraction) as a function of particle size for the Medium Al mixed silicates (MAS) particles at Dyngjusandur from deposition plate and free-wing impactor samples. The numbers on top represent total particle counts in the given size bin. (b) Two-dimensional histogram with respect to element atomic concentrations ratios for MAS particles. In addition, positions and classifications of particles identified manually by composition and morphology are shown. 69

5.3 Average elemental composition as a function of particle size for (a) Fe-oxide/Fe-hydroxide-like and (b) Titanomagnetite-like. The legend shows element index for each respective element. The numbers on top represent total particle counts in the given size bin. 70
5.4 Typical sulfate particle with presence of a deposition ring of small droplets around the core. 71
5.5 Size-resolved relative volume fraction of different particle groups. 73
5.6 Size resolved iron indices for silicate particles. n.d. means Fe not detected. 74
5.7 (a) Relative contribution of each particle type to total iron and (b) fraction of elemental iron by mass with respect to all the other elements. For comparison iron fraction from Saharan dust is also shown from Panta et al. (2023). 75
5.8 Size-resolved particle AR. The shaded area represents the range between 0.1 and 0.9 quantiles with dot being the median and the bins are color coded by the number of data points within each bin. For comparison the median AR of freshly emitted Saharan dust is also shown from Morocco. . 76
5.9 Parameterized aspect ratio density distributions for fine, coarse, and super-coarse dust as well as distribution for Saharan dust from Panta et al. (2023). 77
5.10 Size-resolved volume-averaged composition of the aerosol at different outflow regions during sulfate intrusion period. 79
5.11 Size-resolved average elemental composition for (a) Icelandic dust and (b) Moroccan dust. 83
5.12 Size-resolved average mineralogical composition for (a) Icelandic dust and (b) Moroccan dust. 84

6.1 Number abundance for MOUDI stage 4. Abundance bars are not shown for size bins with fewer than 50 particles. 102
6.2 Number abundance for MOUDI stage 3. Abundance bars are not shown for size bins with fewer than 50 particles 103
6.3 Number abundance for FWI. Abundance bars are not shown for size bins with fewer than 50 particles 104
6.4 Chemical composition (relative number and volume abundance) of different particle groups of aerosol collected in August and September 2021 at Dyngjusandur by deposition plate sampler. Collection time for each Sample ID is provided in table below. The numbers on top represent total particle analysed. 105

6.5 Chemical composition (relative number and volume abundance) of different particle groups of aerosol collected in August and September 2021 at Dyngjusandur by free-wing impactor. Collection time for each Sample ID is provided in table below. The numbers on top represent total particle analysed. 106

List of Tables

4.1 Size resolved mass fraction (%) of particles in each particle class (number fraction in parentheses). 52
4.2 Parameters of the aspect ratio density distribution, mean, median, and standard deviation (SD) for different particle classes 65

5.1 Classification criteria for different particle groups. The full list is provided in the supplement. 68
5.2 Aspect ratio mean, median and standard deviation (SD) for particle group in fine, coarse, and super-coarse dust mode. Values are not shown for size intervals with less than 40 particles. 78

6.1 Sampling times for flat-plate samplers at Dyngjusandur 107
6.2 Sampling times for free-wing impactors at Dyngjusandur 108

Bibliography

Adebiyi, A. A., & Kok, J. F. (2020). Climate models miss most of the coarse dust in the atmosphere. *Science Advances*, *6*(15), eaaz9507. https://doi.org/10.1126/sciadv.aaz9507

Alfaro, S. C., Gaudichet, A., Gomes, L., & Maillé, M. (1998). Mineral aerosol production by wind erosion: Aerosol particle sizes and binding energies. *Geophysical Research Letters*, *25*(7), 991–994. https://doi.org/10.1029/98GL00502

Amiri-Farahani, A., Allen, R. J., Neubauer, D., & Lohmann, U. (2017). Impact of Saharan dust on North Atlantic marine stratocumulus clouds: importance of the semidirect effect. *Atmospheric Chemistry and Physics*, *17*(10), 6305–6322. https://doi.org/10.5194/acp-17-6305-2017

Amiri-Farahani, A., Allen, R. J., Li, K.-F., & Chu, J.-E. (2019). The Semidirect Effect of Combined Dust and Sea Salt Aerosols in a Multimodel Analysis. *Geophysical Research Letters*, *46*(17-18), 10512–10521. https://doi.org/10.1029/2019GL084590

Anderson, J. R., Buseck, P. R., Patterson, T. L., & Arimoto, R. (1996). Characterization of the Bermuda tropospheric aerosol by combined individual-particle and bulk-aerosol analysis. *Atmospheric Environment*, *30*(2), 319–338. https://doi.org/10.1016/1352-2310(95)00170-4

Ansmann, A., Rittmeister, F., Engelmann, R., Basart, S., Jorba, O., Spyrou, C., Remy, S., Skupin, A., Baars, H., Seifert, P., Senf, F., & Kanitz, T. (2017). Profiling of Saharan dust from the Caribbean to western Africa – Part 2: Shipborne lidar measurements versus forecasts. *Atmospheric Chemistry and Physics*, *17*(24), 14987–15006. https://doi.org/10.5194/acp-17-14987-2017

Anthony, J. W., Bideaux, R. A., Bladh, K., & Nichols, M. C. (2003). *Handbook of Mineralogy*. Mineralogical Society of America, Chantilly, VA 20151-1110, USA.

Arnalds, O. (2010). Dust sources and deposition of aeolian materials in Iceland. *Icelandic Agricultural Sciences*, (23), 3–21.

Arnalds, O., Gisladottir, F., & Sigurjonsson, H. (2001). Sandy deserts of Iceland: an overview. *Journal of Arid Environments*, *47*(3), 359–371. https://doi.org/10.1006/jare.2000.0680

Arnalds, O., Olafsson, H., & Dagsson-Waldhauserova, P. (2014). Quantification of iron-rich volcanogenic dust emissions and deposition over the ocean from Icelandic dust sources. *Biogeosciences*, *11*(23), 6623–6632. https://doi.org/10.5194/bg-11-6623-2014

Arnalds, O., Dagsson-Waldhauserova, P., & Olafsson, H. (2016). The Icelandic volcanic aeolian environment: Processes and impacts — A review. *Aeolian Research*, *20*, 176–195. https://doi.org/10.1016/j.aeolia.2016.01.004

Atkinson, J. D., Murray, B. J., Woodhouse, M. T., Whale, T. F., Baustian, K. J., Carslaw, K. S., Dobbie, S., O'Sullivan, D., & Malkin, T. L. (2013). The importance of feldspar for ice nucleation by mineral dust in mixed-phase clouds. *Nature*, *498*(7454), 355–358. https://doi.org/10.1038/nature12278

Baddock, M., Boskovic, L., Strong, C., McTainsh, G., Bullard, J., Agranovski, I., & Cropp, R. (2013). Iron-rich nanoparticles formed by aeolian abrasion of desert dune sand. *Geochemistry, Geophysics, Geosystems*, *14*(9), 3720–3729. https://doi.org/10.1002/ggge.20229

Baker, A. R., & Jickells, T. D. (2006). Mineral particle size as a control on aerosol iron solubility. *Geophysical Research Letters*, *33*(17). https://doi.org/10.1029/2006GL026557

Baker, A., & Croot, P. (2010). Atmospheric and marine controls on aerosol iron solubility in seawater. *Marine Chemistry*, *120*(1), 4–13. https://doi.org/10.1016/j.marchem.2008.09.003

Baldo, C., Formenti, P., Di Biagio, C., Lu, G., Song, C., Cazaunau, M., Pangui, E., Doussin, J.-F., Dagsson-Waldhauserova, P., Arnalds, O., Beddows, D., MacKenzie, A. R., & Shi, Z. (2023). Complex refractive index and single scattering albedo of Icelandic dust in the shortwave spectrum. *EGUsphere*, *2023*, 1–42. https://doi.org/10.5194/egusphere-2023-276

Baldo, C., Formenti, P., Nowak, S., Chevaillier, S., Cazaunau, M., Pangui, E., Di Biagio, C., Doussin, J.-F., Ignatyev, K., Dagsson-Waldhauserova, P., Arnalds, O., MacKenzie, A. R., & Shi, Z. (2020). Distinct chemical and mineralogical composition of Icelandic dust compared to northern African and Asian dust. *Atmospheric Chemistry and Physics*, *20*(21), 13521–13539. https://doi.org/10.5194/acp-20-13521-2020

Baratoux, D., Mangold, N., Arnalds, O., Bardintzeff, J.-M., Platevoët, B., Grégoire, M., & Pinet, P. (2011). Volcanic sands of Iceland - Diverse origins of aeolian sand deposits revealed at Dyngjusandur and Lambahraun. *Earth Surface Processes and Landforms*, *36*(13), 1789–1808. https://doi.org/10.1002/esp.2201

Bateman, A. P., Belassein, H., & Martin, S. T. (2014). Impactor Apparatus for the Study of Particle Rebound: Relative Humidity and Capillary Forces. *Aerosol Science and Technology*, *48*(1), 42–52. https://doi.org/10.1080/02786826.2013.853866

Bègue, N., Tulet, P., Pelon, J., Aouizerats, B., Berger, A., & Schwarzenboeck, A. (2015). Aerosol processing and CCN formation of an intense Saharan dust plume during the EUCAARI 2008 campaign. *Atmospheric Chemistry and Physics*, *15*(6), 3497–3516. https://doi.org/10.5194/acp-15-3497-2015

Björnsson, H., & Pálsson, F. (2008). Icelandic glaciers. *Jökull*, *58*.

Boose, Y., Sierau, B., García, M. I., Rodríguez, S., Alastuey, A., Linke, C., Schnaiter, M., Kupiszewski, P., Kanji, Z. A., & Lohmann, U. (2016). Ice nucleating particles in the Saharan Air Layer. *Atmospheric Chemistry and Physics*, *16*(14), 9067–9087. https://doi.org/10.5194/acp-16-9067-2016

Bristow, C. S., Hudson-Edwards, K. A., & Chappell, A. (2010). Fertilizing the Amazon and equatorial Atlantic with West African dust. *Geophysical Research Letters*, *37*(14). https://doi.org/10.1029/2010GL043486

Bristow, L. A., Mohr, W., Ahmerkamp, S., & Kuypers, M. M. (2017). Nutrients that limit growth in the ocean. *Current Biology*, *27*(11), R474–R478. https://doi.org/10.1016/j.cub.2017.03.030

Brockmann, J. E. (2011). Aerosol Transport in Sampling Lines and Inlets. In *Aerosol Measurement* (S. 68–105). John Wiley; Sons, Ltd. https://doi.org/10.1002/9781118001684.ch6

Bullard, J. E. (2013). Contemporary glacigenic inputs to the dust cycle. *Earth Surface Processes and Landforms*, *38*(1), 71–89. https://doi.org/10.1002/esp.3315

Bullard, J. E., Baddock, M., Bradwell, T., Crusius, J., Darlington, E., Gaiero, D., Gassó, S., Gisladottir, G., Hodgkins, R., McCulloch, R., McKenna-Neuman, C., Mockford, T., Stewart, H., & Thorsteinsson, T. (2016). High-latitude dust in the Earth system. *Reviews of Geophysics*, *54*(2), 447–485. https://doi.org/10.1002/2016RG000518

Butwin, M. K., Pfeffer, M. A., von Löwis, S., Støren, E. W. N., Bali, E., & Thorsteinsson, T. (2020). Properties of dust source material and volcanic ash in Iceland. *Sedimentology*, *67*(6), 3067–3087. https://doi.org/10.1111/sed.12734

Cakmur, R. V., Miller, R. L., Perlwitz, J., Geogdzhayev, I. V., Ginoux, P., Koch, D., Kohfeld, K. E., Tegen, I., & Zender, C. S. (2006). Constraining the magnitude of the global dust cycle by minimizing the difference between a model and observations. *Journal of Geophysical Research: Atmospheres*, *111*(D6). https://doi.org/10.1029/2005JD005791

Caponi, L., Formenti, P., Massabó, D., Di Biagio, C., Cazaunau, M., Pangui, E., Chevaillier, S., Landrot, G., Andreae, M. O., Kandler, K., Piketh, S., Saeed, T., Seibert, D., Williams, E., Balkanski, Y., Prati, P., & Doussin, J.-F. (2017). Spectral- and size-resolved mass absorption efficiency of mineral dust aerosols in the shortwave spectrum: a simulation chamber study. *Atmospheric Chemistry and Physics*, *17*(11), 7175–7191. https://doi.org/10.5194/acp-17-7175-2017

Carn, S., Clarisse, L., & Prata, A. (2016). Multi-decadal satellite measurements of global volcanic degassing. *Journal of Volcanology and Geothermal Research*, *311*, 99–134. https://doi.org/10.1016/j.jvolgeores.2016.01.002

Carn, S., Fioletov, V., McLinden, C., Li, C., & Krotkov, N. (2017). A decade of global volcanic SO2 emissions measured from space. *Scientific Reports*, *7*(44095). https://doi.org/10.1038/srep44095

Carn, S. A., Krueger, A. J., Krotkov, N. A., Yang, K., & Evans, K. (2009). Tracking volcanic sulfur dioxide clouds for aviation hazard mitigation. *Nat Hazards*, *51*, 325–343. https://doi.org/10.1007/s11069-008-9228-4

Chen, Y., & Siefert, R. L. (2004). Seasonal and spatial distributions and dry deposition fluxes of atmospheric total and labile iron over the tropical and subtropical North Atlantic Ocean. *Journal of Geophysical Research: Atmospheres*, *109*(D9). https://doi.org/10.1029/2003JD003958

Choël, M., Deboudt, K., Osán, J., Flament, P., & Van Grieken, R. (2005). Quantitative Determination of Low-Z Elements in Single Atmospheric Particles on Boron Substrates by Automated Scanning Electron Microscopy−Energy-Dispersive X-ray Spectrometry. *Analytical Chemistry*, *77*(17), 5686–5692. https://doi.org/10.1021/ac050739x

Choobari, O. A., Zawar-Reza, P., & Sturman, A. (2014). The global distribution of mineral dust and its impacts on the climate system: A review. *Atmospheric Research*, *138*, 152–165. https://doi.org/10.1016/j.atmosres.2013.11.007

Chou, C., Formenti, P., Maille, M., Ausset, P., Helas, G., Harrison, M., & Osborne, S. (2008). Size distribution, shape, and composition of mineral dust aerosols collected during the African Monsoon Multidisciplinary Analysis Special Observation Period 0: Dust and Biomass-Burning Experiment field campaign in Niger, January 2006. *Journal of Geophysical Research: Atmospheres*, *113*(D23). https://doi.org/10.1029/2008JD009897

Christiansen, E., & Hamblin, W. (2014). *Dynamic Earth: An Introduction to Physical Geology*. Jones & Bartlett Learning. https://books.google.de/books?id=KEUoAwAAQBAJ

Claquin, T., Schulz, M., & Balkanski, Y. (1999). Modeling the mineralogy of atmospheric dust sources. *Journal of Geophysical Research: Atmospheres*, *104*(D18), 22243–22256. https://doi.org/10.1029/1999JD900416

Cotrim da Cunha, L., Buitenhuis, E. T., Le Quéré, C., Giraud, X., & Ludwig, W. (2007). Potential impact of changes in river nutrient supply on global ocean biogeochemistry. *Global Biogeochemical Cycles*, *21*(4). https://doi.org/10.1029/2006GB002718

Coz, E., Gómez-Moreno, F. J., Pujadas, M., Casuccio, G. S., Lersch, T. L., & Artíñano, B. (2009). Individual particle characteristics of North African dust under different long-range transport scenarios. *Atmospheric Environment*, *43*(11), 1850–1863. https://doi.org/10.1016/j.atmosenv.2008.12.045

Cwiertny, D. M., Young, M. A., & Grassian, V. H. (2008). Chemistry and Photochemistry of Mineral Dust Aerosol [PMID: 18393675]. *Annual Review of Physical Chemistry*, *59*(1), 27–51. https://doi.org/10.1146/annurev.physchem.59.032607.093630

Cziczo, D. J., Froyd, K. D., Gallavardin, S. J., Moehler, O., Benz, S., Saathoff, H., & Murphy, D. M. (2009). Deactivation of ice nuclei due to atmospherically relevant surface coatings. *Environmental Research Letters*, *4*(4), 044013. https://doi.org/10.1088/1748-9326/4/4/044013

Cziczo, D. J., Froyd, K. D., Hoose, C., Jensen, E. J., Diao, M., Zondlo, M. A., Smith, J. B., Twohy, C. H., & Murphy, D. M. (2013). Clarifying the Dominant Sources and Mechanisms of Cirrus Cloud Formation. *Science*, *340*(6138), 1320–1324. https://doi.org/10.1126/science.1234145

Dagsson-Waldhauserova, P., Arnalds, O., & Olafsson, H. (2017). Long-term dust aerosol production from natural sources in Iceland [PMID: 28102779]. *Journal of the Air & Waste Management Association*, *67*(2), 173–181. https://doi.org/10.1080/10962247.2013.805703

Dagsson-Waldhauserova, P., Arnalds, O., & Olafsson, H. (2013). Long-term frequency and characteristics of dust storm events in Northeast Iceland (1949–2011). *Atmospheric Environment*, *77*, 117–127. https://doi.org/10.1016/j.atmosenv.2013.04.075

Dagsson-Waldhauserova, P., Arnalds, O., Olafsson, H., Hladil, J., Skala, R., Navratil, T., Chadimova, L., & Meinander, O. (2015). Snow–Dust Storm: Unique case study from Iceland, March 6–7, 2013. *Aeolian Research*, *16*, 69–74. https://doi.org/10.1016/j.aeolia.2014.11.001

Dang, C., Brandt, R. E., & Warren, S. G. (2015). Parameterizations for narrowband and broadband albedo of pure snow and snow containing mineral dust and black carbon. *Journal of Geophysical Research: Atmospheres*, *120*(11), 5446–5468. https://doi.org/10.1002/2014JD022646

Deboudt, K., Gloter, A., Mussi, A., & Flament, P. (2012). Red-ox speciation and mixing state of iron in individual African dust particles. *Journal of Geophysical Research: Atmospheres*, *117*(D12). https://doi.org/10.1029/2011JD017298

Deer, F., W. A., Howie, R. A., & Zussman, J. (2013, Januar). *An Introduction to the Rock-Forming Minerals*. Mineralogical Society of Great Britain; Ireland. https://doi.org/10.1180/DHZ

Delmonte, B., Petit, J., & Maggi, V. (2002). Glacial to Holocene implications of the new 27000-year dust record from the EPICA Dome C (East Antarctica) ice core. *Climate Dynamics*, *18*(8), 647–660. https://doi.org/10.1007/s00382-001-0193-9

DeMott, P. J., Möhler, O., Cziczo, D. J., Hiranuma, N., Petters, M. D., Petters, S. S., Belosi, F., Bingemer, H. G., Brooks, S. D., Budke, C., Burkert-Kohn, M., Collier, K. N., Danielczok, A., Eppers, O., Felgitsch, L., Garimella, S., Grothe, H., Herenz, P., Hill,

T. C. J., … Zenker, J. (2018). The Fifth International Workshop on Ice Nucleation phase 2 (FIN-02): laboratory intercomparison of ice nucleation measurements. *Atmospheric Measurement Techniques*, *11*(11), 6231–6257. https://doi.org/10.5194/amt-11-6231-2018

DeMott, P. J., Prenni, A. J., Liu, X., Kreidenweis, S. M., Petters, M. D., Twohy, C. H., Richardson, M. S., Eidhammer, T., & Rogers, D. C. (2010). Predicting global atmospheric ice nuclei distributions and their impacts on climate. *Proceedings of the National Academy of Sciences*, *107*(25), 11217–11222. https://doi.org/10.1073/pnas.0910818107

Denjean, C., Cassola, F., Mazzino, A., Triquet, S., Chevaillier, S., Grand, N., Bourrianne, T., Momboisse, G., Sellegri, K., Schwarzenbock, A., Freney, E., Mallet, M., & Formenti, P. (2016). Size distribution and optical properties of mineral dust aerosols transported in the western Mediterranean. *Atmospheric Chemistry and Physics*, *16*(2), 1081–1104. https://doi.org/10.5194/acp-16-1081-2016

Di Biagio, C., Balkanski, Y., Albani, S., Boucher, O., & Formenti, P. (2020). Direct Radiative Effect by Mineral Dust Aerosols Constrained by New Microphysical and Spectral Optical Data. *Geophysical Research Letters*, *47*(2), e2019GL086186. https://doi.org/10.1029/2019GL086186

Di Biagio, C., Formenti, P., Balkanski, Y., Caponi, L., Cazaunau, M., Pangui, E., Journet, E., Nowak, S., Andreae, M. O., Kandler, K., Saeed, T., Piketh, S., Seibert, D., Williams, E., & Doussin, J.-F. (2019). Complex refractive indices and single-scattering albedo of global dust aerosols in the shortwave spectrum and relationship to size and iron content. *Atmospheric Chemistry and Physics*, *19*(24), 15503–15531. https://doi.org/10.5194/acp-19-15503-2019

Duce, R. A., Unni, C. K., Ray, B. J., Prospero, J. M., & Merrill, J. T. (1980). Long-Range Atmospheric Transport of Soil Dust from Asia to the Tropical North Pacific: Temporal Variability. *Science*, *209*(4464), 1522–1524. https://doi.org/10.1126/science.209.4464.1522

Ebert, M., Weigel, R., Kandler, K., Günther, G., Molleker, S., Grooß, J.-U., Vogel, B., Weinbruch, S., & Borrmann, S. (2016). Chemical analysis of refractory stratospheric aerosol particles collected within the arctic vortex and inside polar stratospheric clouds. *Atmospheric Chemistry and Physics*, *16*(13), 8405–8421. https://doi.org/10.5194/acp-16-8405-2016

Engelbrecht, J. P., Moosmüller, H., Pincock, S., Jayanty, R. K. M., Lersch, T., & Casuccio, G. (2016). Technical note: Mineralogical, chemical, morphological, and optical interrelationships of mineral dust re-suspensions. *Atmospheric Chemistry and Physics*, *16*(17), 10809–10830. https://doi.org/10.5194/acp-16-10809-2016

Engelbrecht, J. P., Stenchikov, G., Prakash, P. J., Lersch, T., Anisimov, A., & Shevchenko, I. (2017). Physical and chemical properties of deposited airborne particulates over the Arabian Red Sea coastal plain. *Atmospheric Chemistry and Physics*, *17*(18), 11467–11490. https://doi.org/10.5194/acp-17-11467-2017

Engelbrecht, J. P., McDonald, E. V., Gillies, J. A., Jayanty, R. K. J., Casuccio, G., & Gertler, A. W. (2009). Characterizing Mineral Dusts and Other Aerosols from the Middle East—Part 2: Grab Samples and Re-Suspensions. *Inhalation Toxicology*, *21*(4), 327–336. https://doi.org/10.1080/08958370802464299

Engelstaedter, S., Tegen, I., & Washington, R. (2006). North African dust emissions and transport. *Earth-Science Reviews*, *79*(1), 73–100. https://doi.org/10.1016/j.earscirev.2006.06.004

Eriksen Hammer, S., Ebert, M., & Weinbruch, S. (2019). Comparison of operator- and computer-controlled scanning electron microscopy of particles from different atmospheric aerosol types. *Anal Bioanal Chem*, *411*, 1633–1645. https://doi.org/10.1007/s00216-019-01614-7

Eriksen Hammer, S., Mertes, S., Schneider, J., Ebert, M., Kandler, K., & Weinbruch, S. (2018). Composition of ice particle residuals in mixed-phase clouds at Jungfraujoch (Switzerland): enrichment and depletion of particle groups relative to total aerosol. *Atmospheric Chemistry and Physics*, *18*(19), 13987–14003. https://doi.org/10.5194/acp-18-13987-2018

Evan, A. T., Flamant, C., Fiedler, S., & Doherty, O. (2014). An analysis of aeolian dust in climate models. *Geophysical Research Letters*, *41*(16), 5996–6001. https://doi.org/10.1002/2014GL060545

Falkovich, A. H., Ganor, E., Levin, Z., Formenti, P., & Rudich, Y. (2001). Chemical and mineralogical analysis of individual mineral dust particles. *Journal of Geophysical Research: Atmospheres*, *106*(D16), 18029–18036. https://doi.org/10.1029/2000JD900430

Falkowski, P., Scholes, R. J., Boyle, E., Canadell, J., Canfield, D., Elser, J., Gruber, N., Hibbard, K., Högberg, P., Linder, S., Mackenzie, F. T., III, B. M., Pedersen, T., Rosenthal, Y., Seitzinger, S., Smetacek, V., & Steffen, W. (2000). The Global Carbon Cycle: A Test of Our Knowledge of Earth as a System. *Science*, *290*(5490), 291–296. https://doi.org/10.1126/science.290.5490.291

Fang, C. P., McMurry, P. H., Marple, V. A., & Rubow, K. L. (1991). Effect of Flow-induced Relative Humidity Changes on Size Cuts for Sulfuric Acid Droplets in the Microorifice Uniform Deposit Impactor (MOUDI). *Aerosol Science and Technology*, *14*(2), 266–277. https://doi.org/10.1080/02786829108959489

Fishwick, M. P., Ussher, S. J., Sedwick, P. N., Lohan, M. C., Worsfold, P. J., Buck, K. N., & Church, T. M. (2018). Impact of surface ocean conditions and aerosol provenance

on the dissolution of aerosol manganese, cobalt, nickel and lead in seawater. *Marine Chemistry*, *198*, 28–43. https://doi.org/10.1016/j.marchem.2017.11.003

Fitzgerald, E., Ault, A. P., Zauscher, M. D., Mayol-Bracero, O. L., & Prather, K. A. (2015). Comparison of the mixing state of long-range transported Asian and African mineral dust. *Atmospheric Environment*, *115*, 19–25. https://doi.org/10.1016/j.atmosenv.2015.04.031

Flanner, M. G., Arnheim, J. B., Cook, J. M., Dang, C., He, C., Huang, X., Singh, D., Skiles, S. M., Whicker, C. A., & Zender, C. S. (2021). SNICAR-ADv3: a community tool for modeling spectral snow albedo. *Geoscientific Model Development*, *14*(12), 7673–7704. https://doi.org/10.5194/gmd-14-7673-2021

Flanner, M. G., Zender, C. S., Randerson, J. T., & Rasch, P. J. (2007). Present-day climate forcing and response from black carbon in snow. *Journal of Geophysical Research: Atmospheres*, *112*(D11). https://doi.org/10.1029/2006JD008003

Formenti, P., Schütz, L., Balkanski, Y., Desboeufs, K., Ebert, M., Kandler, K., Petzold, A., Scheuvens, D., Weinbruch, S., & Zhang, D. (2011). Recent progress in understanding physical and chemical properties of African and Asian mineral dust. *Atmospheric Chemistry and Physics*, *11*(16), 8231–8256. https://doi.org/10.5194/acp-11-8231-2011

Froyd, K. D., Yu, P., Schill, G. P., Brock, C. A., Kupc, A., Williamson, C. J., Jensen, E. J., Ray, E., Rosenlof, K. H., Bian, H., et al. (2022). Dominant role of mineral dust in cirrus cloud formation revealed by global-scale measurements. *Nature Geoscience*, *15*, 177–183. https://doi.org/10.1038/s41561-022-00901-w

Geiger, H., Mattsson, T., Deegan, F. M., Troll, V. R., Burchardt, S., Gudmundsson, Ó., Tryggvason, A., Krumbholz, M., & Harris, C. (2016). Magma plumbing for the 2014–2015 Holuhraun eruption, Iceland. *Geochemistry, Geophysics, Geosystems*, *17*(8), 2953–2968. https://doi.org/10.1002/2016GC006317

Giannadaki, D., Pozzer, A., & Lelieveld, J. (2014). Modeled global effects of airborne desert dust on air quality and premature mortality. *Atmospheric Chemistry and Physics*, *14*(2), 957–968. https://doi.org/10.5194/acp-14-957-2014

Gillette, D. A., Adams, J., Endo, A., Smith, D., & Kihl, R. (1980). Threshold velocities for input of soil particles into the air by desert soils. *Journal of Geophysical Research: Oceans*, *85*(C10), 5621–5630. https://doi.org/10.1029/JC085iC10p05621

Gillette, D. A., & Passi, R. (1988). Modeling dust emission caused by wind erosion. *Journal of Geophysical Research: Atmospheres*, *93*(D11), 14233–14242. https://doi.org/10.1029/JD093iD11p14233

Ginoux, P. (2003). Effects of nonsphericity on mineral dust modeling. *Journal of Geophysical Research: Atmospheres*, *108*(D2). https://doi.org/10.1029/2002JD002516

Ginoux, P., Chin, M., Tegen, I., Prospero, J. M., Holben, B., Dubovik, O., & Lin, S.-J. (2001). Sources and distributions of dust aerosols simulated with the GOCART model. *Journal of Geophysical Research: Atmospheres*, *106*(D17), 20255–20273. https://doi.org/10.1029/2000JD000053

Ginoux, P., Prospero, J. M., Gill, T. E., Hsu, N. C., & Zhao, M. (2012). Global-scale attribution of anthropogenic and natural dust sources and their emission rates based on MODIS Deep Blue aerosol products. *Reviews of Geophysics*, *50*(3). https://doi.org/10.1029/2012RG000388

Glaccum, R. A., & Prospero, J. M. (1980). Saharan aerosols over the tropical North Atlantic — Mineralogy. *Marine Geology*, *37*(3), 295–321. https://doi.org/10.1016/0025-3227(80)90107-3

Gomes, L., Bergametti, G., Coudé-Gaussen, G., & Rognon, P. (1990). Submicron desert dusts: A sandblasting process. *Journal of Geophysical Research: Atmospheres*, *95*(D9), 13927–13935. https://doi.org/10.1029/JD095iD09p13927

González-Flórez, C., Klose, M., Alastuey, A., Dupont, S., Escribano, J., Etyemezian, V., Gonzalez-Romero, A., Huang, Y., Kandler, K., Nikolich, G., Panta, A., Querol, X., Reche, C., Yus-Díez, J., & Pérez García-Pando, C. (2022). Insights into the size-resolved dust emission from field measurements in the Moroccan Sahara. *Atmospheric Chemistry and Physics Discussions*, *2022*, 1–65. https://doi.org/10.5194/acp-2022-758

González-Romero, A., González-Flórez, C., Panta, A., Yus-Díez, J., Reche, C., Córdoba, P., Alastuey, A., Kandler, K., Klose, M., Querol, X., & Pérez García-Pando, C. (in prep). Properties of dust-source sediment and their importance on dust emission: the case of Dyngjusandur, Iceland.

González-Romero, A., González-Flórez, C., Panta, A., Yus-Díez, J., Reche, C., Córdoba, P., Alastuey, A., Kandler, K., Klose, M., Querol, X., & Pérez García-Pando, C. (2023). Variability in grain size, mineralogy, and mode of occurrence of Fe in surface sediments of preferential dust-source inland drainage basins: The case of the Lower Drâa Valley, S Morocco. *EGUsphere*, *2023*, 1–32. https://doi.org/10.5194/egusphere-2023-1120

Groot Zwaaftink, C. D., Grythe, H., Skov, H., & Stohl, A. (2016). Substantial contribution of northern high-latitude sources to mineral dust in the Arctic. *Journal of Geophysical Research: Atmospheres*, *121*(22), 13, 678–13, 697. https://doi.org/10.1002/2016JD025482

Hall, A. (2004). The Role of Surface Albedo Feedback in Climate. *Journal of Climate*, *17*(7), 1550–1568. https://doi.org/10.1175/1520-0442(2004)017<1550:TROSAF>2.0.CO;2

Hamilton, D. S., Perron, M. M., Bond, T. C., Bowie, A. R., Buchholz, R. R., Guieu, C., Ito, A., Maenhaut, W., Myriokefalitakis, S., Olgun, N., Rathod, S. D., Schepanski, K., Tagliabue, A., Wagner, R., & Mahowald, N. M. (2022). Earth, Wind, Fire, and Pollution: Aerosol Nutrient Sources and Impacts on Ocean Biogeochemistry. *Annual Review of Marine Science*, *14*(1), 303–330. https://doi.org/10.1146/annurev-marine-031921-013612

Hand, J. L., Mahowald, N. M., Chen, Y., Siefert, R. L., Luo, C., Subramaniam, A., & Fung, I. (2004). Estimates of atmospheric-processed soluble iron from observations and a global mineral aerosol model: Biogeochemical implications. *Journal of Geophysical Research: Atmospheres*, *109*(D17). https://doi.org/10.1029/2004JD004574

Harrison, A. D., O'Sullivan, D., Adams, M. P., Porter, G. C. E., Blades, E., Brathwaite, C., Chewitt-Lucas, R., Gaston, C., Hawker, R., Krüger, O. O., Neve, L., Pöhlker, M. L., Pöhlker, C., Pöschl, U., Sanchez-Marroquin, A., Sealy, A., Sealy, P., Tarn, M. D., Whitehall, S., … Murray, B. J. (2022). The ice-nucleating activity of African mineral dust in the Caribbean boundary layer. *Atmospheric Chemistry and Physics*, *22*(14), 9663–9680. https://doi.org/10.5194/acp-22-9663-2022

Harrison, A. D., Whale, T. F., Carpenter, M. A., Holden, M. A., Neve, L., OŚullivan, D., Vergara Temprado, J., & Murray, B. J. (2016). Not all feldspars are equal: a survey of ice nucleating properties across the feldspar group of minerals. *Atmospheric Chemistry and Physics*, *16*(17), 10927–10940. https://doi.org/10.5194/acp-16-10927-2016

He, C. (2022). Modelling light-absorbing particle–snow–radiation interactions and impacts on snow albedo: fundamentals, recent advances and future directions. *Environmental Chemistry*, 296–311. https://doi.org/10.1071/EN22013

He, C., Liou, K.-N., Takano, Y., Chen, F., & Barlage, M. (2019). Enhanced Snow Absorption and Albedo Reduction by Dust-Snow Internal Mixing: Modeling and Parameterization. *Journal of Advances in Modeling Earth Systems*, *11*(11), 3755–3776. https://doi.org/10.1029/2019MS001737

He, C., Takano, Y., & Liou, K.-N. (2017). Close packing effects on clean and dirty snow albedo and associated climatic implications. *Geophysical Research Letters*, *44*(8), 3719–3727. https://doi.org/10.1002/2017GL072916

Helgren, D. M., & Prospero, J. M. (1987). Wind Velocities Associated with Dust Deflation Events in the Western Sahara. *Journal of Applied Meteorology and Climatology*, *26*(9), 1147–1151. https://doi.org/10.1175/1520-0450(1987)026<1147:WVAWDD>2.0.CO;2

Hettiarachchi, E., Ivanov, S., Kieft, T., Goldstein, H. L., Moskowitz, B. M., Reynolds, R. L., & Rubasinghege, G. (2021). Atmospheric Processing of Iron-Bearing Mineral Dust Aerosol and Its Effect on Growth of a Marine Diatom, Cyclotella meneghiniana.

Environmental Science & Technology, *55*(2), 871–881. https://doi.org/10.1021/acs.est.0c06995

Heymsfield, A. J., Krämer, M., Luebke, A., Brown, P., Cziczo, D. J., Franklin, C., Lawson, P., Lohmann, U., McFarquhar, G., Ulanowski, Z., & Tricht, K. V. (2017). Cirrus Clouds. *Meteorological Monographs*, *58*, 2.1–2.26. https://doi.org/10.1175/AMSMONOGRAPHS-D-16-0010.1

Hinds, W. C. (1999). *Aerosol technology: properties, behavior, and measurement of airborne particles*. John Wiley & Sons.

Hoose, C., & Möhler, O. (2012). Heterogeneous ice nucleation on atmospheric aerosols: a review of results from laboratory experiments. *Atmospheric Chemistry and Physics*, *12*(20), 9817–9854. https://doi.org/10.5194/acp-12-9817-2012

Huang, J., Wang, T., Wang, W., Li, Z., & Yan, H. (2014). Climate effects of dust aerosols over East Asian arid and semiarid regions. *Journal of Geophysical Research: Atmospheres*, *119*(19), 11, 398–11, 416. https://doi.org/10.1002/2014JD021796

Huang, Y., Adebiyi, A. A., Formenti, P., & Kok, J. F. (2021). Linking the Different Diameter Types of Aspherical Desert Dust Indicates That Models Underestimate Coarse Dust Emission. *Geophysical Research Letters*, *48*(6), e2020GL092054. https://doi.org/10.1029/2020GL092054

Huang, Y., Kok, J. F., Kandler, K., Lindqvist, H., Nousiainen, T., Sakai, T., Adebiyi, A., & Jokinen, O. (2020). Climate Models and Remote Sensing Retrievals Neglect Substantial Desert Dust Asphericity. *Geophysical Research Letters*, *47*(6), e2019GL086592. https://doi.org/10.1029/2019GL086592

Huang, Z., Huang, J., Hayasaka, T., Wang, S., Zhou, T., & Jin, H. (2015). Short-cut transport path for Asian dust directly to the Arctic: a case study. *Environmental Research Letters*, *10*(11), 114018. https://doi.org/10.1088/1748-9326/10/11/114018

Huneeus, N., Schulz, M., Balkanski, Y., Griesfeller, J., Prospero, J., Kinne, S., Bauer, S., Boucher, O., Chin, M., Dentener, F., Diehl, T., Easter, R., Fillmore, D., Ghan, S., Ginoux, P., Grini, A., Horowitz, L., Koch, D., Krol, M. C., … Zender, C. S. (2011). Global dust model intercomparison in AeroCom phase I. *Atmospheric Chemistry and Physics*, *11*(15), 7781–7816. https://doi.org/10.5194/acp-11-7781-2011

Ilyinskaya, E., Schmidt, A., Mather, T. A., Pope, F. D., Witham, C., Baxter, P., Jóhannsson, T., Pfeffer, M., Barsotti, S., Singh, A., Sanderson, P., Bergsson, B., McCormick Kilbride, B., Donovan, A., Peters, N., Oppenheimer, C., & Edmonds, M. (2017). Understanding the environmental impacts of large fissure eruptions: Aerosol and gas emissions from the 2014–2015 Holuhraun eruption (Iceland). *Earth and Planetary Science Letters*, *472*, 309–322. https://doi.org/10.1016/j.epsl.2017.05.025

IPCC. (2018). Framing and Context, in: Global Warming of 1.5°C: IPCC Special Report on Impacts of Global Warming of 1.5°C above Pre-industrial Levels in Context of Strengthening Response to Climate Change, Sustainable Development, and Efforts to Eradicate Poverty, edited by: Masson-Delmotte, V., Zhai, P., Pörtner, H.-O., Roberts, D., Skea, J., Shukla, P. R., Pirani, A., Moufouma-Okia, W., Péan, C., Pidcock, R., Connors, S., Matthews, J. B. R., Chen, Y., Zhou, X., Gomis, M. I., Lonnoy, E., Maycock, T., Tignor, M., and Waterfield, T. *Cambridge University Press, Cambridge, UK and New York, NY, USA*, 49–92. https://doi.org/10.1017/9781009157940.003

Ito, A., Adebiyi, A. A., Huang, Y., & Kok, J. F. (2021). Less atmospheric radiative heating by dust due to the synergy of coarser size and aspherical shape. *Atmospheric Chemistry and Physics*, *21*(22), 16869–16891. https://doi.org/10.5194/acp-21-16869-2021

Jakobsson, S. P., Jónasson, K., & Sigurdsson, I. A. (2008). The three igneous rock series of Iceland. *Jökull*, *58*, 117–138. https://doi.org/10.33799/jokull2008.58.117

Jeong, D., Kim, K., & Choi, W. (2012). Accelerated dissolution of iron oxides in ice. *Atmospheric Chemistry and Physics*, *12*(22), 11125–11133. https://doi.org/10.5194/acp-12-11125-2012

Jeong, G. Y., Park, M. Y., Kandler, K., Nousiainen, T., & Kemppinen, O. (2016). Mineralogical properties and internal structures of individual fine particles of Saharan dust. *Atmospheric Chemistry and Physics*, *16*(19), 12397–12410. https://doi.org/10.5194/acp-16-12397-2016

Jeong, G. Y. (2008). Bulk and single-particle mineralogy of Asian dust and a comparison with its source soils. *Journal of Geophysical Research: Atmospheres*, *113*(D2). https://doi.org/10.1029/2007JD008606

Jickells, T. D., An, Z. S., Andersen, K. K., Baker, A. R., Bergametti, G., Brooks, N., Cao, J. J., Boyd, P. W., Duce, R. A., Hunter, K. A., Kawahata, H., Kubilay, N., laRoche, J., Liss, P. S., Mahowald, N., Prospero, J. M., Ridgwell, A. J., Tegen, I., & Torres, R. (2005). Global Iron Connections Between Desert Dust, Ocean Biogeochemistry, and Climate. *Science*, *308*(5718), 67–71. https://doi.org/10.1126/science.1105959

Jish Prakash, P., Stenchikov, G., Tao, W., Yapici, T., Warsama, B., & Engelbrecht, J. P. (2016). Arabian Red Sea coastal soils as potential mineral dust sources. *Atmospheric Chemistry and Physics*, *16*(18), 11991–12004. https://doi.org/10.5194/acp-16-11991-2016

Johnson, R. (1996). *ENVIRONMENTAL SCANNING ELECTRON MICROSCOPY An Introduction to ESEM*. Philips Electron Optics. https://nanoscience.ch/wp-content/uploads/sites/8/2017/08/an_introduction_to_esem.pdf

Journet, E., Balkanski, Y., & Harrison, S. P. (2014). A new data set of soil mineralogy for dust-cycle modeling. *Atmospheric Chemistry and Physics*, *14*(8), 3801–3816. https://doi.org/10.5194/acp-14-3801-2014

Journet, E., Desboeufs, K. V., Caquineau, S., & Colin, J.-L. (2008). Mineralogy as a critical factor of dust iron solubility. *Geophysical Research Letters*, *35*(7). https://doi.org/10.1029/2007GL031589

Kaaden, N., Massling, A., Schladitz, A., Müller, T., Kandler, K., SchüTZ, L., Weinzierl, B., Petzold, A., Tesche, M., Leinert, S., Deutscher, C., Ebert, M., Weinbruch, S., & Wiedensohler, A. (2009). State of mixing, shape factor, number size distribution, and hygroscopic growth of the Saharan anthropogenic and mineral dust aerosol at Tinfou, Morocco. *Tellus B: Chemical and Physical Meteorology*, *61*(1), 51–63. https://doi.org/10.1111/j.1600-0889.2008.00388.x

Kandler, K., Benker, N., Bundke, U., Cuevas, E., Ebert, M., Knippertz, P., Rodriguez, S., Schütz, L., & Weinbruch, S. (2007). Chemical composition and complex refractive index of Saharan Mineral Dust at Izaña, Tenerife (Spain) derived by electron microscopy. *Atmospheric Environment*, *41*(37), 8058–8074. https://doi.org/10.1016/j.atmosenv.2007.06.047

Kandler, K., Lieke, K., Benker, N., Emmel, C., Küpper, M., Müller-Ebert, D., Ebert, M., Scheuvens, D., Schladitz, A., Schütz, L., & Weinbruch, S. (2011b). Electron microscopy of particles collected at Praia, Cape Verde, during the Saharan Mineral Dust Experiment: particle chemistry, shape, mixing state and complex refractive index. *Tellus B: Chemical and Physical Meteorology*, *63*(4), 475–496. https://doi.org/10.1111/j.1600-0889.2011.00550.x

Kandler, K., Schneiders, K., Ebert, M., Hartmann, M., Weinbruch, S., Prass, M., & Pöhlker, C. (2018). Composition and mixing state of atmospheric aerosols determined by electron microscopy: method development and application to aged Saharan dust deposition in the Caribbean boundary layer. *Atmospheric Chemistry and Physics*, *18*(18), 13429–13455. https://doi.org/10.5194/acp-18-13429-2018

Kandler, K., Schneiders, K., Heuser, J., Waza, A., Aryasree, S., Althausen, D., Hofer, J., Abdullaev, S. F., & Makhmudov, A. N. (2020). Differences and Similarities of Central Asian, African, and Arctic Dust Composition from a Single Particle Perspective. *Atmosphere*, *11*(3). https://doi.org/10.3390/atmos11030269

Kandler, K., Schütz, L., Deutscher, C., Ebert, M., Hofmann, H., Jäckel, S., Jaenicke, R., Knippertz, P., Lieke, K., Massling, A., Petzold, A., Schladitz, A., Weinzierl, B., Wiedensohler, A., Zorn, S., & Weinbruch, S. (2009). Size distribution, mass concentration, chemical and mineralogical composition and derived optical parameters of the boundary layer aerosol at Tinfou, Morocco, during SAMUM 2006. *Tellus B:*

Chemical and Physical Meteorology, *61*(1), 32–50. https://doi.org/10.1111/j.1600-0889.2008.00385.x

Kandler, K., Schütz, L., Jäckel, S., Lieke, K., Emmel, C., Müller-Ebert, D., Ebert, M., Scheuvens, D., Schladitz, A., Šegvić, B., Wiedensohler, A., & Weinbruch, S. (2011a). Ground-based off-line aerosol measurements at Praia, Cape Verde, during the Saharan Mineral Dust Experiment: microphysical properties and mineralogy. *Tellus B: Chemical and Physical Meteorology*, *63*(4), 459–474. https://doi.org/10.1111/j.1600-0889.2011.00546.x

Kanji, Z. A., Ladino, L. A., Wex, H., Boose, Y., Burkert-Kohn, M., Cziczo, D. J., & Krämer, M. (2017). Overview of Ice Nucleating Particles. *Meteorological Monographs*, *58*, 1.1–1.33. https://doi.org/10.1175/AMSMONOGRAPHS-D-16-0006.1

Karydis, V. A., Kumar, P., Barahona, D., Sokolik, I. N., & Nenes, A. (2011). On the effect of dust particles on global cloud condensation nuclei and cloud droplet number. *Journal of Geophysical Research: Atmospheres*, *116*(D23204). https://doi.org/10.1029/2011JD016283

Karydis, V. A., Tsimpidi, A. P., Bacer, S., Pozzer, A., Nenes, A., & Lelieveld, J. (2017). Global impact of mineral dust on cloud droplet number concentration. *Atmospheric Chemistry and Physics*, *17*(9), 5601–5621. https://doi.org/10.5194/acp-17-5601-2017

Kawai, K., Matsui, H., & Tobo, Y. (2023). Dominant Role of Arctic Dust With High Ice Nucleating Ability in the Arctic Lower Troposphere. *Geophysical Research Letters*, *50*(8), e2022GL102470. https://doi.org/10.1029/2022GL102470

Klaver, A., Formenti, P., Caquineau, S., Chevaillier, S., Ausset, P., Calzolai, G., Osborne, S., Johnson, B., Harrison, M., & Dubovik, O. (2011). Physico-chemical and optical properties of Sahelian and Saharan mineral dust: in situ measurements during the GERBILS campaign. *Quarterly Journal of the Royal Meteorological Society*, *137*(658), 1193–1210. https://doi.org/10.1002/qj.889

Koehler, K. A., Kreidenweis, S. M., DeMott, P. J., Petters, M. D., Prenni, A. J., & Carrico, C. M. (2009). Hygroscopicity and cloud droplet activation of mineral dust aerosol. *Geophysical Research Letters*, *36*(8). https://doi.org/10.1029/2009GL037348

Kok, J., Parteli, E. J., Michaels, T. I., & Karam, D. B. (2012). The physics of wind-blown sand and dust. *Reports on Progress in Physics*, *75*(10), 106901. https://doi.org/10.1088/0034-4885/75/10/106901

Kok, J. F., Adebiyi, A. A., Albani, S., Balkanski, Y., Checa-Garcia, R., Chin, M., Colarco, P. R., Hamilton, D. S., Huang, Y., Ito, A., Klose, M., Leung, D. M., Li, L., Mahowald, N. M., Miller, R. L., Obiso, V., Pérez García-Pando, C., Rocha-Lima, A., Wan, J. S., & Whicker, C. A. (2021b). Improved representation of the global dust cycle using

observational constraints on dust properties and abundance. *Atmospheric Chemistry and Physics*, *21*(10), 8127–8167. https://doi.org/10.5194/acp-21-8127-2021

Kok, J. F., Adebiyi, A. A., Albani, S., Balkanski, Y., Checa-Garcia, R., Chin, M., Colarco, P. R., Hamilton, D. S., Huang, Y., Ito, A., Klose, M., Li, L., Mahowald, N. M., Miller, R. L., Obiso, V., Pérez García-Pando, C., Rocha-Lima, A., & Wan, J. S. (2021a). Contribution of the worldś main dust source regions to the global cycle of desert dust. *Atmospheric Chemistry and Physics*, *21*(10), 8169–8193. https://doi.org/10.5194/acp-21-8169-2021

Kok, J. F., Ridley, D. A., Zhou, Q., Miller, R. L., Zhao, C., Heald, C. L., Ward, D. S., Albani, S., & Haustein, K. (2017). Smaller desert dust cooling effect estimated from analysis of dust size and abundance. *Nature Geoscience*, *10*(4), 274–278. https://doi.org/10.1038/ngeo2912

Kok, J. F., Storelvmo, T., Karydis, V. A., Adebiyi, A. A., Mahowald, N. M., Evan, A. T., He, C., & Leung, D. M. (2023). Mineral dust aerosol impacts on global climate and climate change. *Nature Reviews Earth & Environment*, *4*(2), 71–86. https://doi.org/10.1038/s43017-022-00379-5

Kong, S. S.-K., Pani, S. K., Griffith, S. M., Ou-Yang, C.-F., Babu, S. R., Chuang, M.-T., Ooi, M. C. G., Huang, W.-S., Sheu, G.-R., & Lin, N.-H. (2022). Distinct transport mechanisms of East Asian dust and the impact on downwind marine and atmospheric environments. *Science of The Total Environment*, *827*, 154255. https://doi.org/10.1016/j.scitotenv.2022.154255

Korolev, A., McFarquhar, G., Field, P. R., Franklin, C., Lawson, P., Wang, Z., Williams, E., Abel, S. J., Axisa, D., Borrmann, S., Crosier, J., Fugal, J., Krämer, M., Lohmann, U., Schlenczek, O., Schnaiter, M., & Wendisch, M. (2017). Mixed-Phase Clouds: Progress and Challenges. *Meteorological Monographs*, *58*, 5.1–5.50. https://doi.org/10.1175/AMSMONOGRAPHS-D-17-0001.1

Krejci, R., Ström, J., de Reus, M., & Sahle, W. (2005). Single particle analysis of the accumulation mode aerosol over the northeast Amazonian tropical rain forest, Surinam, South America. *Atmospheric Chemistry and Physics*, *5*(12), 3331–3344. https://doi.org/10.5194/acp-5-3331-2005

Krishnamurthy, A., Moore, J. K., Mahowald, N., Luo, C., Doney, S. C., Lindsay, K., & Zender, C. S. (2009). Impacts of increasing anthropogenic soluble iron and nitrogen deposition on ocean biogeochemistry. *Global Biogeochemical Cycles*, *23*(3). https://doi.org/10.1029/2008GB003440

Kumar, P., Sokolik, I. N., & Nenes, A. (2011b). Cloud condensation nuclei activity and droplet activation kinetics of wet processed regional dust samples and minerals. *Atmospheric Chemistry and Physics*, *11*(16), 8661–8676. https://doi.org/10.5194/acp-11-8661-2011

Kumar, P., Sokolik, I. N., & Nenes, A. (2011a). Measurements of cloud condensation nuclei activity and droplet activation kinetics of fresh unprocessed regional dust samples and minerals. *Atmospheric Chemistry and Physics*, *11*(7), 3527–3541. https://doi.org/10.5194/acp-11-3527-2011

Kurosaki, Y., & Mikami, M. (2007). Threshold wind speed for dust emission in east Asia and its seasonal variations. *Journal of Geophysical Research: Atmospheres*, *112*(D17). https://doi.org/10.1029/2006JD007988

Lafon, S., Sokolik, I. N., Rajot, J. L., Caquineau, S., & Gaudichet, A. (2006). Characterization of iron oxides in mineral dust aerosols: Implications for light absorption. *Journal of Geophysical Research: Atmospheres*, *111*(D21). https://doi.org/10.1029/2005JD007016

Lamotte, C., Guth, J., Marécal, V., Cussac, M., Hamer, P. D., Theys, N., & Schneider, P. (2021). Modeling study of the impact of SO2 volcanic passive emissions on the tropospheric sulfur budget. *Atmospheric Chemistry and Physics*, *21*(14), 11379–11404. https://doi.org/10.5194/acp-21-11379-2021

Laskin, A., Cowin, J., & Iedema, M. (2006). Analysis of individual environmental particles using modern methods of electron microscopy and X-ray microanalysis [Science and Spectroscopy of Environmentally Important Interfaces]. *Journal of Electron Spectroscopy and Related Phenomena*, *150*(2), 260–274. https://doi.org/10.1016/j.elspec.2005.06.008

Laskin, A., & Cowin, J. P. (2001). Automated Single-Particle SEM/EDX Analysis of Submicrometer Particles down to 0.1 µm. *Analytical Chemistry*, *73*(5), 1023–1029. https://doi.org/10.1021/ac0009604

Laskin, A., Iedema, M. J., & Cowin, J. P. (2002). Quantitative Time-Resolved Monitoring of Nitrate Formation in Sea Salt Particles Using a CCSEM/EDX Single Particle Analysis. *Environmental Science & Technology*, *36*(23), 4948–4955. https://doi.org/10.1021/es020551k

Laskin, A., Iedema, M. J., & Cowin, J. P. (2003). Time-Resolved Aerosol Collector for CCSEM/EDX Single-Particle Analysis. *Aerosol Science and Technology*, *37*(3), 246–260. https://doi.org/10.1080/02786820300945

Laskin, A., Iedema, M. J., Ichkovich, A., Graber, E. R., Taraniuk, I., & Rudich, Y. (2005). Direct observation of completely processed calcium carbonate dust particles. *Faraday Discuss.*, *130*, 453–468. https://doi.org/10.1039/B417366J

Lasne, J., Urupina, D., Maters, E. C., Delmelle, P., Romanias, M. N., & Thevenet, F. (2022). Photo-enhanced uptake of SO2 on Icelandic volcanic dusts. *Environ. Sci.: Atmos.*, *2*, 375–387. https://doi.org/10.1039/D1EA00094B

Li, W., Shao, L., Zhang, D., Ro, C.-U., Hu, M., Bi, X., Geng, H., Matsuki, A., Niu, H., & Chen, J. (2016). A review of single aerosol particle studies in the atmosphere of East Asia:

morphology, mixing state, source, and heterogeneous reactions. *Journal of Cleaner Production*, *112*, 1330–1349. https://doi.org/10.1016/j.jclepro.2015.04.050

Lieke, K., Kandler, K., Scheuvens, D., Emmel, C., Glahn, C. V., Petzold, A., Weinzierl, B., Veira, A., Ebert, M., Weinbruch, S., & Schütz, L. (2011). Particle chemical properties in the vertical column based on aircraft observations in the vicinity of Cape Verde Islands. *Tellus B: Chemical and Physical Meteorology*, *63*(4), 497–511. https://doi.org/10.1111/j.1600-0889.2011.00553.x

Lindqvist, H., Jokinen, O., Kandler, K., Scheuvens, D., & Nousiainen, T. (2014). Single scattering by realistic, inhomogeneous mineral dust particles with stereogrammetric shapes. *Atmospheric Chemistry and Physics*, *14*(1), 143–157. https://doi.org/10.5194/acp-14-143-2014

Liou, K. N., Takano, Y., He, C., Yang, P., Leung, L. R., Gu, Y., & Lee, W. L. (2014). Stochastic parameterization for light absorption by internally mixed BC/dust in snow grains for application to climate models. *Journal of Geophysical Research: Atmospheres*, *119*(12), 7616–7632. https://doi.org/10.1002/2014JD021665

Liu, C.-M., Young, C.-Y., & Lee, Y.-C. (2006). Influence of Asian dust storms on air quality in Taiwan. *Science of The Total Environment*, *368*(2), 884–897. https://doi.org/10.1016/j.scitotenv.2006.03.039

Luo, C., Mahowald, N., Bond, T., Chuang, P. Y., Artaxo, P., Siefert, R., Chen, Y., & Schauer, J. (2008). Combustion iron distribution and deposition. *Global Biogeochemical Cycles*, *22*(1). https://doi.org/10.1029/2007GB002964

Mahowald, N., Albani, S., Kok, J. F., Engelstaeder, S., Scanza, R., Ward, D. S., & Flanner, M. G. (2014). The size distribution of desert dust aerosols and its impact on the Earth system. *Aeolian Research*, *15*, 53–71. https://doi.org/10.1016/j.aeolia.2013.09.002

Mahowald, N. M., Engelstaedter, S., Luo, C., Sealy, A., Artaxo, P., Benitez-Nelson, C., Bonnet, S., Chen, Y., Chuang, P. Y., Cohen, D. D., Dulac, F., Herut, B., Johansen, A. M., Kubilay, N., Losno, R., Maenhaut, W., Paytan, A., Prospero, J. M., Shank, L. M., & Siefert, R. L. (2009). Atmospheric Iron Deposition: Global Distribution, Variability, and Human Perturbations. *Annual Review of Marine Science*, *1*(1), 245–278. https://doi.org/10.1146/annurev.marine.010908.163727

Mallios, S. A., Drakaki, E., & Amiridis, V. (2020). Effects of dust particle sphericity and orientation on their gravitational settling in the earth's atmosphere. *Journal of Aerosol Science*, *150*, 105634. https://doi.org/10.1016/j.jaerosci.2020.105634

Marcotte, A. R., Anbar, A. D., Majestic, B. J., & Herckes, P. (2020). Mineral Dust and Iron Solubility: Effects of Composition, Particle Size, and Surface Area. *Atmosphere*, *11*(5). https://doi.org/10.3390/atmos11050533

Maring, H., Savoie, D. L., Izaguirre, M. A., Custals, L., & Reid, J. S. (2003). Mineral dust aerosol size distribution change during atmospheric transport. *Journal of Geophysical Research: Atmospheres*, *108*(D19). https://doi.org/10.1029/2002JD002536

Marsden, N. A., Ullrich, R., Möhler, O., Eriksen Hammer, S., Kandler, K., Cui, Z., Williams, P. I., Flynn, M. J., Liu, D., Allan, J. D., & Coe, H. (2019). Mineralogy and mixing state of north African mineral dust by online single-particle mass spectrometry. *Atmospheric Chemistry and Physics*, *19*(4), 2259–2281. https://doi.org/10.5194/acp-19-2259-2019

Marticorena, B., & Bergametti, G. (1995). Modeling the atmospheric dust cycle: 1. Design of a soil-derived dust emission scheme. *Journal of Geophysical Research: Atmospheres*, *100*(D8), 16415–16430. https://doi.org/10.1029/95JD00690

Maters, E. C., Dingwell, D. B., Cimarelli, C., Müller, D., Whale, T. F., & Murray, B. J. (2019). The importance of crystalline phases in ice nucleation by volcanic ash. *Atmospheric Chemistry and Physics*, *19*(8), 5451–5465. https://doi.org/10.5194/acp-19-5451-2019

Matsuki, A., Schwarzenboeck, A., Venzac, H., Laj, P., Crumeyrolle, S., & Gomes, L. (2010). Cloud processing of mineral dust: direct comparison of cloud residual and clear sky particles during AMMA aircraft campaign in summer 2006. *Atmospheric Chemistry and Physics*, *10*(3), 1057–1069. https://doi.org/10.5194/acp-10-1057-2010

May, K. R., & Clifford, R. (1967). The Impaction of Aerosol Particles on Cylinders, Spheres, Ribbons and Discs. *The Annals of Occupational Hygiene*, *10*(2), 83–95. https://doi.org/10.1093/annhyg/10.2.83

McGraw, Z., Storelvmo, T., David, R. O., & Sagoo, N. (2020). Global Radiative Impacts of Mineral Dust Perturbations Through Stratiform Clouds. *Journal of Geophysical Research: Atmospheres*, *125*(23), e2019JD031807. https://doi.org/10.1029/2019JD031807

Meinander, O., Dagsson-Waldhauserova, P., Amosov, P., Aseyeva, E., Atkins, C., Baklanov, A., Baldo, C., Barr, S. L., Barzycka, B., Benning, L. G., Cvetkovic, B., Enchilik, P., Frolov, D., Gassó, S., Kandler, K., Kasimov, N., Kavan, J., King, J., Koroleva, T., … Vukovic Vimic, A. (2022). Newly identified climatically and environmentally significant high-latitude dust sources. *Atmospheric Chemistry and Physics*, *22*(17), 11889–11930. https://doi.org/10.5194/acp-22-11889-2022

Meinander, O., Dagsson-Waldhauserova, P., & Arnalds, O. (2016). Icelandic volcanic dust can have a significant influence on the cryosphere in Greenland and elsewhere. *Polar Research*, *35*. https://doi.org/10.3402/polar.v35.31313

Middleton, N. (2017). Desert dust hazards: A global review. *Aeolian Research*, *24*, 53–63. https://doi.org/10.1016/j.aeolia.2016.12.001

Monteiro, A., Basart, S., Kazadzis, S., Votsis, A., Gkikas, A., Vandenbussche, S., Tobias, A., Gama, C., García-Pando, C. P., Terradellas, E., Notas, G., Middleton, N., Kushta, J., Amiridis, V., Lagouvardos, K., Kosmopoulos, P., Kotroni, V., Kanakidou, M., Mihalopoulos, N., … Nickovic, S. (2022). Multi-sectoral impact assessment of an extreme African dust episode in the Eastern Mediterranean in March 2018. *Science of The Total Environment*, *843*, 156861. https://doi.org/10.1016/j.scitotenv.2022.156861

Moosmüller, H., Engelbrecht, J. P., Skiba, M., Frey, G., Chakrabarty, R. K., & Arnott, W. P. (2012). Single scattering albedo of fine mineral dust aerosols controlled by iron concentration. *Journal of Geophysical Research: Atmospheres*, *117*(D11). https://doi.org/10.1029/2011JD016909

Morel, F. M., Rueter, J. G., & Price, N. M. (1991). Iron Nutrition of Phytoplankton and its Possible Importance in the Ecology of Ocean Regions with High Nutrient and Low Biomass. *Oceanography*, *4*(2), 56–61. Verfügbar 14. Oktober 2022 unter http://www.jstor.org/stable/43924569

Moroni, B., Arnalds, O., Dagsson-Waldhauserová, P., Crocchianti, S., Vivani, R., & Cappelletti, D. (2018). Mineralogical and Chemical Records of Icelandic Dust Sources Upon Ny-Ålesund (Svalbard Islands). *Frontiers in Earth Science*, *6*. https://doi.org/10.3389/feart.2018.00187

Morrison, H., De Boer, G., Feingold, G., Harrington, J., Shupe, M. D., & Sulia, K. (2012). Resilience of persistent Arctic mixed-phase clouds. *Nature Geoscience*, *5*(1), 11–17. https://doi.org/10.1038/ngeo1332

Moskowitz, B. M., Reynolds, R. L., Goldstein, H. L., Berquó, T. S., Kokaly, R. F., & Bristow, C. S. (2016). Iron oxide minerals in dust-source sediments from the Bodélé Depression, Chad: Implications for radiative properties and Fe bioavailability of dust plumes from the Sahara. *Aeolian Research*, *22*, 93–106. https://doi.org/10.1016/j.aeolia.2016.07.001

Muhs, D. R. (2013). The geologic records of dust in the Quaternary. *Aeolian Research*, *9*, 3–48. https://doi.org/10.1016/j.aeolia.2012.08.001

Murray, B. J., Carslaw, K. S., & Field, P. R. (2021). Opinion: Cloud-phase climate feedback and the importance of ice-nucleating particles. *Atmospheric Chemistry and Physics*, *21*(2), 665–679. https://doi.org/10.5194/acp-21-665-2021

Myhre, G., Samset, B. H., Schulz, M., Balkanski, Y., Bauer, S., Berntsen, T. K., Bian, H., Bellouin, N., Chin, M., Diehl, T., Easter, R. C., Feichter, J., Ghan, S. J., Hauglustaine, D., Iversen, T., Kinne, S., Kirkevåg, A., Lamarque, J.-F., Lin, G., … Zhou, C. (2013). Radiative forcing of the direct aerosol effect from AeroCom Phase II simulations. *Atmospheric Chemistry and Physics*, *13*(4), 1853–1877. https://doi.org/10.5194/acp-13-1853-2013

Myriokefalitakis, S., Bergas-Massó, E., Gonçalves-Ageitos, M., Pérez García-Pando, C., van Noije, T., Le Sager, P., Ito, A., Athanasopoulou, E., Nenes, A., Kanakidou, M., Krol, M. C., & Gerasopoulos, E. (2022). Multiphase processes in the EC-Earth model and their relevance to the atmospheric oxalate, sulfate, and iron cycles. *Geoscientific Model Development*, *15*(7), 3079–3120. https://doi.org/10.5194/gmd-15-3079-2022

Ndour, M., Conchon, P., D'Anna, B., Ka, O., & George, C. (2009). Photochemistry of mineral dust surface as a potential atmospheric renoxification process. *Geophysical Research Letters*, *36*(5). https://doi.org/10.1029/2008GL036662

Ndour, M., D'Anna, B., George, C., Ka, O., Balkanski, Y., Kleffmann, J., Stemmler, K., & Ammann, M. (2008). Photoenhanced uptake of NO2 on mineral dust: Laboratory experiments and model simulations. *Geophysical Research Letters*, *35*(5). https://doi.org/10.1029/2007GL032006

Neuman, C. M. (1993). A review of aeolian transport processes in cold environments. *Progress in Physical Geography: Earth and Environment*, *17*(2), 137–155. https://doi.org/10.1177/030913339301700203

Nickovic, S., Vukovic, A., Vujadinovic, M., Djurdjevic, V., & Pejanovic, G. (2012). Technical Note: High-resolution mineralogical database of dust-productive soils for atmospheric dust modeling. *Atmospheric Chemistry and Physics*, *12*(2), 845–855. https://doi.org/10.5194/acp-12-845-2012

Nousiainen, T., Kahnert, M., & Lindqvist, H. (2011). Can particle shape information be retrieved from light-scattering observations using spheroidal model particles? [Polarimetric Detection, Characterization, and Remote Sensing]. *Journal of Quantitative Spectroscopy and Radiative Transfer*, *112*(13), 2213–2225. https://doi.org/10.1016/j.jqsrt.2011.05.008

Nousiainen, T., & Kandler, K. (2015). Light scattering by atmospheric mineral dust particles. In *Light Scattering Reviews 9* (S. 3–52). Springer. https://doi.org/10.1007/978-3-642-37985-7_1

Okada, K., Heintzenberg, J., Kai, K., & Qin, Y. (2001). Shape of atmospheric mineral particles collected in three Chinese arid-regions. *Geophysical Research Letters*, *28*(16), 3123–3126. https://doi.org/10.1029/2000GL012798

Okin, G. S., Baker, A. R., Tegen, I., Mahowald, N. M., Dentener, F. J., Duce, R. A., Galloway, J. N., Hunter, K., Kanakidou, M., Kubilay, N., Prospero, J. M., Sarin, M., Surapipith, V., Uematsu, M., & Zhu, T. (2011). Impacts of atmospheric nutrient deposition on marine productivity: Roles of nitrogen, phosphorus, and iron. *Global Biogeochemical Cycles*, *25*(2). https://doi.org/10.1029/2010GB003858

Onishi, K., Kurosaki, Y., Otani, S., Yoshida, A., Sugimoto, N., & Kurozawa, Y. (2012). Atmospheric transport route determines components of Asian dust and health

effects in Japan. *Atmospheric Environment*, *49*, 94–102. https://doi.org/10.1016/j.atmosenv.2011.12.018

Onishi, K., Otani, S., Yoshida, A., Mu, H., & Kurozawa, Y. (2015). Adverse Health Effects of Asian Dust Particles and Heavy Metals in Japan. *Asia Pacific Journal of Public Health*, *27*(2), NP1719–NP1726. https://doi.org/10.1177/1010539511428667

O'Sullivan, D., Marenco, F., Ryder, C. L., Pradhan, Y., Kipling, Z., Johnson, B., Benedetti, A., Brooks, M., McGill, M., Yorks, J., & Selmer, P. (2020). Models transport Saharan dust too low in the atmosphere: a comparison of the MetUM and CAMS forecasts with observations. *Atmospheric Chemistry and Physics*, *20*(21), 12955–12982. https://doi.org/10.5194/acp-20-12955-2020

Ott, D. K., & Peters, T. M. (2008). A Shelter to Protect a Passive Sampler for Coarse Particulate Matter, PM10 − 2.5. *Aerosol Science and Technology*, *42*(4), 299–309. https://doi.org/10.1080/02786820802054236

Otto, S., Trautmann, T., & Wendisch, M. (2011). On realistic size equivalence and shape of spheroidal Saharan mineral dust particles applied in solar and thermal radiative transfer calculations. *Atmospheric Chemistry and Physics*, *11*(9), 4469–4490. https://doi.org/10.5194/acp-11-4469-2011

Painter, T. H., Deems, J. S., Belnap, J., Hamlet, A. F., Landry, C. C., & Udall, B. (2010). Response of Colorado River runoff to dust radiative forcing in snow. *Proceedings of the National Academy of Sciences*, *107*(40), 17125–17130. https://doi.org/10.1073/pnas.0913139107

Panta, A., Kandler, K., Alastuey, A., González-Flórez, C., González-Romero, A., Klose, M., Querol, X., Reche, C., Yus-Díez, J., & Pérez García-Pando, C. (2023). Insights into the single-particle composition, size, mixing state, and aspect ratio of freshly emitted mineral dust from field measurements in the Moroccan Sahara using electron microscopy. *Atmospheric Chemistry and Physics*, *23*(6), 3861–3885. https://doi.org/10.5194/acp-23-3861-2023

Paramonov, M., David, R. O., Kretzschmar, R., & Kanji, Z. A. (2018). A laboratory investigation of the ice nucleation efficiency of three types of mineral and soil dust. *Atmospheric Chemistry and Physics*, *18*(22), 16515–16536. https://doi.org/10.5194/acp-18-16515-2018

Paris, R., Desboeufs, K., & Journet, E. (2011). Variability of dust iron solubility in atmospheric waters: Investigation of the role of oxalate organic complexation. *Atmospheric Environment*, *45*(36), 6510–6517. https://doi.org/10.1016/j.atmosenv.2011.08.068

Pérez, C., Nickovic, S., Pejanovic, G., Baldasano, J. M., & Özsoy, E. (2006). Interactive dust-radiation modeling: A step to improve weather forecasts. *Journal of Geophysical Research: Atmospheres*, *111*(D16). https://doi.org/10.1029/2005JD006717

Pérez García-Pando, C., Thomson, M. C., Stanton, M. C., Diggle, P. J., Hopson, T., Pandya, R., Miller, R. L., & Hugonnet, S. (2014). Meningitis and climate: from science to practice. *Earth Perspectives*, *1*(1), 1–15. https://doi.org/10.1186/2194-6434-1-14

Perlwitz, J., & Miller, R. L. (2010). Cloud cover increase with increasing aerosol absorptivity: A counterexample to the conventional semidirect aerosol effect. *Journal of Geophysical Research: Atmospheres*, *115*(D8). https://doi.org/10.1029/2009JD012637

Piedra, P., & Moosmüller, H. (2017). Optical losses of photovoltaic cells due to aerosol deposition: Role of particle refractive index and size. *Solar Energy*, *155*, 637–646. https://doi.org/10.1016/j.solener.2017.06.047

Price, H. C., Baustian, K. J., McQuaid, J. B., Blyth, A., Bower, K. N., Choularton, T., Cotton, R. J., Cui, Z., Field, P. R., Gallagher, M., Hawker, R., Merrington, A., Miltenberger, A., Neely III, R. R., Parker, S. T., Rosenberg, P. D., Taylor, J. W., Trembath, J., Vergara-Temprado, J., … Murray, B. J. (2018). Atmospheric Ice-Nucleating Particles in the Dusty Tropical Atlantic. *Journal of Geophysical Research: Atmospheres*, *123*(4), 2175–2193. https://doi.org/10.1002/2017JD027560

Prospero, J. M. (1999). Long-range transport of mineral dust in the global atmosphere: Impact of African dust on the environment of the southeastern United States. *Proceedings of the National Academy of Sciences*, *96*(7), 3396–3403. https://doi.org/10.1073/pnas.96.7.3396

Prospero, J. M., Ginoux, P., Torres, O., Nicholson, S. E., & Gill, T. E. (2002). Environmental characterization of global sources of atmospheric soil dust identified with the Nimbus 7 Total Ozone Mapping Spectrometer (TOMS) absorbing aerosol product. *Reviews of Geophysics*, *40*(1), 2-1-2–31. https://doi.org/10.1029/2000RG000095

Pu, B., Ginoux, P., Guo, H., Hsu, N. C., Kimball, J., Marticorena, B., Malyshev, S., Naik, V., O'Neill, N. T., Pérez García-Pando, C., Paireau, J., Prospero, J. M., Shevliakova, E., & Zhao, M. (2020). Retrieving the global distribution of the threshold of wind erosion from satellite data and implementing it into the Geophysical Fluid Dynamics Laboratory land–atmosphere model (GFDL AM4.0/LM4.0). *Atmospheric Chemistry and Physics*, *20*(1), 55–81. https://doi.org/10.5194/acp-20-55-2020

Querol, X., Tobías, A., Pérez, N., Karanasiou, A., Amato, F., Stafoggia, M., Pérez García-Pando, C., Ginoux, P., Forastiere, F., Gumy, S., Mudu, P., & Alastuey, A. (2019). Monitoring the impact of desert dust outbreaks for air quality for health studies. *Environment International*, *130*, 104867. https://doi.org/10.1016/j.envint.2019.05.061

Raiswell, R., & Canfield, D. (2012). The iron biogeochemical cycle past and present. *Geochemical Perspectives*, *1*(1), 1–220. https://doi.org/10.7185/geochempersp.1.1

Raupach, M. R., Gillette, D. A., & Leys, J. F. (1993). The effect of roughness elements on wind erosion threshold. *Journal of Geophysical Research: Atmospheres*, *98*(D2), 3023–3029. https://doi.org/10.1029/92JD01922

Reed, S. J. B. (2005). Electron–specimen interactions. In *Electron Microprobe Analysis and Scanning Electron Microscopy in Geology* (2. Aufl., S. 7–20). Cambridge University Press. https://doi.org/10.1017/CBO9780511610561.003

Reid, E. A., Reid, J. S., Meier, M. M., Dunlap, M. R., Cliff, S. S., Broumas, A., Perry, K., & Maring, H. (2003a). Characterization of African dust transported to Puerto Rico by individual particle and size segregated bulk analysis. *Journal of Geophysical Research: Atmospheres*, *108*(D19). https://doi.org/10.1029/2002JD002935

Reid, J. S., Jonsson, H. H., Maring, H. B., Smirnov, A., Savoie, D. L., Cliff, S. S., Reid, E. A., Livingston, J. M., Meier, M. M., Dubovik, O., & Tsay, S.-C. (2003b). Comparison of size and morphological measurements of coarse mode dust particles from Africa. *Journal of Geophysical Research: Atmospheres*, *108*(D19). https://doi.org/10.1029/2002JD002485

Reynolds, R. L., Cattle, S. R., Moskowitz, B. M., Goldstein, H. L., Yauk, K., Flagg, C. B., Berquó, T. S., Kokaly, R. F., Morman, S., & Breit, G. N. (2014). Iron oxide minerals in dust of the Red Dawn event in eastern Australia, September 2009. *Aeolian Research*, *15*, 1–13. https://doi.org/10.1016/j.aeolia.2014.02.003

Richards-Thomas, T., McKenna-Neuman, C., & Power, I. M. (2021). Particle-scale characterization of volcaniclastic dust sources within Iceland. *Sedimentology*, *68*(3), 1137–1158. https://doi.org/10.1111/sed.12821

Riemer, N., Ault, A. P., West, M., Craig, R. L., & Curtis, J. H. (2019). Aerosol Mixing State: Measurements, Modeling, and Impacts. *Reviews of Geophysics*, *57*(2), 187–249. https://doi.org/10.1029/2018RG000615

Rocha-Lima, A., Martins, J. V., Remer, L. A., Todd, M., Marsham, J. H., Engelstaedter, S., Ryder, C. L., Cavazos-Guerra, C., Artaxo, P., Colarco, P., & Washington, R. (2018). A detailed characterization of the Saharan dust collected during the Fennec campaign in 2011: in situ ground-based and laboratory measurements. *Atmospheric Chemistry and Physics*, *18*(2), 1023–1043. https://doi.org/10.5194/acp-18-1023-2018

Rodríguez, S., Alastuey, A., & Querol, X. (2012). A review of methods for long term in situ characterization of aerosol dust. *Aeolian Research*, *6*, 55–74. https://doi.org/10.1016/j.aeolia.2012.07.004

Rodríguez, S., Prospero, J. M., López-Darias, J., García-Alvarez, M.-I., Zuidema, P., Nava, S., Lucarelli, F., Gaston, C. J., Galindo, L., & Sosa, E. (2021). Tracking the changes of iron solubility and air pollutants traces as African dust transits the Atlantic in the Saharan dust outbreaks. *Atmospheric Environment*, *246*, 118092. https://doi.org/10.1016/j.atmosenv.2020.118092

Rubasinghege, G., Lentz, R. W., Scherer, M. M., & Grassian, V. H. (2010). Simulated atmospheric processing of iron oxyhydroxide minerals at low pH: Roles of particle size and acid anion in iron dissolution. *Proceedings of the National Academy of Sciences*, *107*(15), 6628–6633. https://doi.org/10.1073/pnas.0910809107

Rubin, M., Berman-Frank, I., & Shaked, Y. (2011). Dust-and mineral-iron utilization by the marine dinitrogen-fixer *Trichodesmium*. *Nature Geoscience*, *4*(8), 529–534. https://doi.org/10.1038/ngeo1181

Ryder, C. L., Highwood, E. J., Lai, T. M., Sodemann, H., & Marsham, J. H. (2013b). Impact of atmospheric transport on the evolution of microphysical and optical properties of Saharan dust. *Geophysical Research Letters*, *40*(10), 2433–2438. https://doi.org/10.1002/grl.50482

Ryder, C. L., Highwood, E. J., Rosenberg, P. D., Trembath, J., Brooke, J. K., Bart, M., Dean, A., Crosier, J., Dorsey, J., Brindley, H., Banks, J., Marsham, J. H., McQuaid, J. B., Sodemann, H., & Washington, R. (2013a). Optical properties of Saharan dust aerosol and contribution from the coarse mode as measured during the Fennec 2011 aircraft campaign. *Atmospheric Chemistry and Physics*, *13*(1), 303–325. https://doi.org/10.5194/acp-13-303-2013

Ryder, C. L., Highwood, E. J., Walser, A., Seibert, P., Philipp, A., & Weinzierl, B. (2019). Coarse and giant particles are ubiquitous in Saharan dust export regions and are radiatively significant over the Sahara. *Atmospheric Chemistry and Physics*, *19*(24), 15353–15376. https://doi.org/10.5194/acp-19-15353-2019

Ryder, C. L., Marenco, F., Brooke, J. K., Estelles, V., Cotton, R., Formenti, P., McQuaid, J. B., Price, H. C., Liu, D., Ausset, P., Rosenberg, P. D., Taylor, J. W., Choularton, T., Bower, K., Coe, H., Gallagher, M., Crosier, J., Lloyd, G., Highwood, E. J., & Murray, B. J. (2018). Coarse-mode mineral dust size distributions, composition and optical properties from AER-D aircraft measurements over the tropical eastern Atlantic. *Atmospheric Chemistry and Physics*, *18*(23), 17225–17257. https://doi.org/10.5194/acp-18-17225-2018

Sagoo, N., & Storelvmo, T. (2017). Testing the sensitivity of past climates to the indirect effects of dust. *Geophysical Research Letters*, *44*(11), 5807–5817. https://doi.org/10.1002/2017GL072584

Samset, B. H., Stjern, C. W., Andrews, E., Kahn, R. A., Myhre, G., Schulz, M., & Schuster, G. L. (2018). Aerosol Absorption: Progress Towards Global and Regional Constraints. *Current climate change reports*, *4*, 65–83. https://doi.org/10.1007/s40641-018-0091-4

Sanchez-Marroquin, A., Arnalds, O., Baustian-Dorsi, K. J., Browse, J., Dagsson-Waldhauserova, P., Harrison, A. D., Maters, E. C., Pringle, K. J., Vergara-Temprado, J., Burke, I. T., McQuaid, J. B., Carslaw, K. S., & Murray, B. J. (2020). Iceland is an episodic source

of atmospheric ice-nucleating particles relevant for mixed-phase clouds. *Science Advances*, *6*(26), eaba8137. https://doi.org/10.1126/sciadv.aba8137

Sanchez-Marroquin, A., Hedges, D. H. P., Hiscock, M., Parker, S. T., Rosenberg, P. D., Trembath, J., Walshaw, R., Burke, I. T., McQuaid, J. B., & Murray, B. J. (2019). Characterisation of the filter inlet system on the FAAM BAe-146 research aircraft and its use for size-resolved aerosol composition measurements. *Atmospheric Measurement Techniques*, *12*(11), 5741–5763. https://doi.org/10.5194/amt-12-5741-2019

Sand, M., Samset, B. H., Myhre, G., Gliß, J., Bauer, S. E., Bian, H., Chin, M., Checa-Garcia, R., Ginoux, P., Kipling, Z., Kirkevåg, A., Kokkola, H., Le Sager, P., Lund, M. T., Matsui, H., van Noije, T., Olivié, D. J. L., Remy, S., Schulz, M., … Watson-Parris, D. (2021). Aerosol absorption in global models from AeroCom phase III. *Atmospheric Chemistry and Physics*, *21*(20), 15929–15947. https://doi.org/10.5194/acp-21-15929-2021

Sarangi, C., Qian, Y., Rittger, K., Ruby Leung, L., Chand, D., Bormann, K. J., & Painter, T. H. (2020). Dust dominates high-altitude snow darkening and melt over high-mountain Asia. *Nature Climate Change*, *10*(11), 1045–1051. https://doi.org/10.1038/s41558-020-00909-3

Schepanski, K. (2018). Transport of Mineral Dust and Its Impact on Climate. *Geosciences*, *8*(5). https://doi.org/10.3390/geosciences8050151

Scheuvens, D., Kandler, K., Küpper, M., Lieke, K., Zorn, R., Ebert, M., Schütz, L., & Weinbruch, S. (2011). Individual-particle analysis of airborne dust samples collected over Morocco in 2006 during SAMUM 1. *Tellus B: Chemical and Physical Meteorology*, *63*(4), 512–530. https://doi.org/10.1111/j.1600-0889.2011.00554.x

Schmale, J., Zieger, P., & Ekman, A. M. (2021). Aerosols in current and future Arctic climate. *Nature Climate Change*, *11*(2), 95–105. https://doi.org/10.1038/s41558-020-00969-5

Schulz, M., Prospero, J. M., Baker, A. R., Dentener, F., Ickes, L., Liss, P. S., Mahowald, N. M., Nickovic, S., García-Pando, C. P., Rodríguez, S., Sarin, M., Tegen, I., & Duce, R. A. (2012). Atmospheric Transport and Deposition of Mineral Dust to the Ocean: Implications for Research Needs. *Environmental Science & Technology*, *46*(19), 10390–10404. https://doi.org/10.1021/es300073u

Seinfeld, J., & Pandis, S. (2016). *Atmospheric Chemistry and Physics: From Air Pollution to Climate Change* (3. Aufl.). Wiley.

Shao, Y. (2008). *Physics and Modelling of Wind Erosion*. Springer. https://doi.org/10.1007/978-1-4020-8895-7

Shao, Y., Wyrwoll, K.-H., Chappell, A., Huang, J., Lin, Z., McTainsh, G. H., Mikami, M., Tanaka, T. Y., Wang, X., & Yoon, S. (2011). Dust cycle: An emerging core theme in

Earth system science. *Aeolian Research*, *2*(4), 181–204. https://doi.org/10.1016/j.aeolia.2011.02.001

Shi, Z., Krom, M. D., Bonneville, S., Baker, A. R., Bristow, C., Drake, N., Mann, G., Carslaw, K., McQuaid, J. B., Jickells, T., & Benning, L. G. (2011). Influence of chemical weathering and aging of iron oxides on the potential iron solubility of Saharan dust during simulated atmospheric processing. *Global Biogeochemical Cycles*, *25*(2). https://doi.org/10.1029/2010GB003837

Shi, Z., Krom, M. D., Bonneville, S., Baker, A. R., Jickells, T. D., & Benning, L. G. (2009). Formation of Iron Nanoparticles and Increase in Iron Reactivity in Mineral Dust during Simulated Cloud Processing. *Environmental Science & Technology*, *43*(17), 6592–6596. https://doi.org/10.1021/es901294g

Shi, Z., Krom, M. D., Jickells, T. D., Bonneville, S., Carslaw, K. S., Mihalopoulos, N., Baker, A. R., & Benning, L. G. (2012). Impacts on iron solubility in the mineral dust by processes in the source region and the atmosphere: A review. *Aeolian Research*, *5*, 21–42. https://doi.org/10.1016/j.aeolia.2012.03.001

Skiles, S. M., Flanner, M., Cook, J. M., Dumont, M., & Painter, T. H. (2018). Radiative forcing by light-absorbing particles in snow. *Nature Climate Change*, *8*(11), 964–971. https://doi.org/10.1038/s41558-018-0296-5

Sokolik, I. N., Winker, D. M., Bergametti, G., Gillette, D. A., Carmichael, G., Kaufman, Y. J., Gomes, L., Schuetz, L., & Penner, J. E. (2001). Introduction to special section: Outstanding problems in quantifying the radiative impacts of mineral dust. *Journal of Geophysical Research: Atmospheres*, *106*(D16), 18015–18027. https://doi.org/10.1029/2000JD900498

Sokolik, I. N., & Toon, O. B. (1999). Incorporation of mineralogical composition into models of the radiative properties of mineral aerosol from UV to IR wavelengths. *Journal of Geophysical Research: Atmospheres*, *104*(D8), 9423–9444. https://doi.org/10.1029/1998JD200048

Sokolik, I. N., Toon, O. B., & Bergstrom, R. W. (1998). Modeling the radiative characteristics of airborne mineral aerosols at infrared wavelengths. *Journal of Geophysical Research: Atmospheres*, *103*(D8), 8813–8826. https://doi.org/10.1029/98JD00049

Solomon, S., Qin, D., Manning, M., Averyt, K., & Marquis, M. (2007). *Climate change 2007-the physical science basis: Working group I contribution to the fourth assessment report of the IPCC* (Bd. 4). Cambridge university press.

Stevens, B., & Feingold, G. (2009). Untangling aerosol effects on clouds and precipitation in a buffered system. *Nature*, *461*(7264), 607–613. https://doi.org/10.1038/nature08281

Stockdale, A., Krom, M. D., Mortimer, R. J. G., Benning, L. G., Carslaw, K. S., Herbert, R. J., Shi, Z., Myriokefalitakis, S., Kanakidou, M., & Nenes, A. (2016). Understanding the

nature of atmospheric acid processing of mineral dusts in supplying bioavailable phosphorus to the oceans. *Proceedings of the National Academy of Sciences*, *113*(51), 14639–14644. https://doi.org/10.1073/pnas.1608136113

Stocker, T. F., Qin, D., Plattner, G.-K., Tignor, M., Allen, S. K., Boschung, J., Nauels, A., Xia, Y., Bex, V., Midgley, P. M., et al. (2013). Climate change 2013: The physical science basis. *Contribution of Working Group I to the Fifth Assessment Report of the Intergovernmental Panel on Climate Change*, *1535*.

Stokes, G. G. (1901). On the Effect of the Internal Friction of Fluids on the Motion of Pendulums. In *Mathematical and Physical Papers* (S. 1–10, Bd. 3). Cambridge University Press. https://doi.org/10.1017/CBO9780511702266.002

Storelvmo, T. (2017). Aerosol Effects on Climate via Mixed-Phase and Ice Clouds. *Annual Review of Earth and Planetary Sciences*, *45*(1), 199–222. https://doi.org/10.1146/annurev-earth-060115-012240

Strong, J. D. O., Vecchi, G. A., & Ginoux, P. (2018). The Climatological Effect of Saharan Dust on Global Tropical Cyclones in a Fully Coupled GCM. *Journal of Geophysical Research: Atmospheres*, *123*(10), 5538–5559. https://doi.org/10.1029/2017JD027808

Tegen, I., Harrison, S. P., Kohfeld, K., Prentice, I. C., Coe, M., & Heimann, M. (2002). Impact of vegetation and preferential source areas on global dust aerosol: Results from a model study. *Journal of Geophysical Research: Atmospheres*, *107*(D21), AAC 14-1-AAC 14–27. https://doi.org/10.1029/2001JD000963

Tegen, I., & Lacis, A. A. (1996). Modeling of particle size distribution and its influence on the radiative properties of mineral dust aerosol. *Journal of Geophysical Research: Atmospheres*, *101*(D14), 19237–19244. https://doi.org/10.1029/95JD03610

Textor, C., Schulz, M., Guibert, S., Kinne, S., Balkanski, Y., Bauer, S., Berntsen, T., Berglen, T., Boucher, O., Chin, M., Dentener, F., Diehl, T., Easter, R., Feichter, H., Fillmore, D., Ghan, S., Ginoux, P., Gong, S., Grini, A., … Tie, X. (2006). Analysis and quantification of the diversities of aerosol life cycles within AeroCom. *Atmospheric Chemistry and Physics*, *6*(7), 1777–1813. https://doi.org/10.5194/acp-6-1777-2006

Thompson, J. M. T., & Ridgwell, A. J. (2002). Dust in the Earth system: the biogeochemical linking of land, air and sea. *Philosophical Transactions of the Royal Society of London. Series A: Mathematical, Physical and Engineering Sciences*, *360*(1801), 2905–2924. https://doi.org/10.1098/rsta.2002.1096

Urupina, D., Lasne, J., Romanias, M., Thiery, V., Dagsson-Waldhauserova, P., & Thevenet, F. (2019). Uptake and surface chemistry of SO2 on natural volcanic dusts. *Atmospheric Environment*, *217*, 116942. https://doi.org/10.1016/j.atmosenv.2019.116942

Usher, C. R., Michel, A. E., & Grassian, V. H. (2003). Reactions on mineral dust. *Chemical reviews*, *103*(12), 4883–4940. https://doi.org/10.1021/cr020657y

Valentin, C., & Bresson, L.-M. (1992). Morphology, genesis and classification of surface crusts in loamy and sandy soils. *Geoderma*, *55*(3), 225–245. https://doi.org/10.1016/0016-7061(92)90085-L

van der Does, M., Knippertz, P., Zschenderlein, P., Harrison, R. G., & Stuut, J.-B. W. (2018). The mysterious long-range transport of giant mineral dust particles. *Science Advances*, *4*(12), eaau2768. https://doi.org/10.1126/sciadv.aau2768

Varga, G., Dagsson-Waldhauserová, P., Gresina, F., & Helgadottir, A. (2021). Saharan dust and giant quartz particle transport towards Iceland. *Scientific reports*, *11*(1), 1–12. https://doi.org/10.1038/s41598-021-91481-z

Vasiliou, J. G., Sorensen, D., & McMurry, P. H. (1999). Sampling at controlled relative humidity with a cascade impactor. *Atmospheric Environment*, *33*(7), 1049–1056. https://doi.org/10.1016/S1352-2310(98)00323-9

Vet, R., Artz, R. S., Carou, S., Shaw, M., Ro, C.-U., Aas, W., Baker, A., Bowersox, V. C., Dentener, F., Galy-Lacaux, C., Hou, A., Pienaar, J. J., Gillett, R., Forti, M. C., Gromov, S., Hara, H., Khodzher, T., Mahowald, N. M., Nickovic, S., … Reid, N. W. (2014). A global assessment of precipitation chemistry and deposition of sulfur, nitrogen, sea salt, base cations, organic acids, acidity and pH, and phosphorus. *Atmospheric Environment*, *93*, 3–100. https://doi.org/10.1016/j.atmosenv.2013.10.060

Warren, S. G., & Wiscombe, W. J. (1980). A Model for the Spectral Albedo of Snow. II: Snow Containing Atmospheric Aerosols. *Journal of Atmospheric Sciences*, *37*(12), 2734–2745. https://doi.org/10.1175/1520-0469(1980)037<2734:AMFTSA>2.0.CO;2

Waza, A., Schneiders, K., May, J., Rodríguez, S., Epple, B., & Kandler, K. (2019). Field comparison of dry deposition samplers for collection of atmospheric mineral dust: results from single-particle characterization. *Atmospheric Measurement Techniques*, *12*(12), 6647–6665. https://doi.org/10.5194/amt-12-6647-2019

Wendisch, M., & Brenguier, J.-L. (2013). Airborne Measurements for Environmental Research: Methods and Instruments. *John Wiley and Sons, Ltd*. https://doi.org/10.1002/9783527653218

WHO. (2021). *W.H.O global air quality guidelines: particulate matter (PM2.5 and PM10), ozone, nitrogen dioxide, sulfur dioxide and carbon monoxide*. World Health Organization. https://apps.who.int/iris/handle/10665/345329

Winkler, P. (1973). The growth of atmospheric aerosol particles as a function of the relative humidity—II. An improved concept of mixed nuclei. *Journal of Aerosol Science*, *4*(5), 373–387. https://doi.org/10.1016/0021-8502(73)90027-X

Wittmann, M., Groot Zwaaftink, C. D., Steffensen Schmidt, L., Guðmundsson, S., Pálsson, F., Arnalds, O., Björnsson, H., Thorsteinsson, T., & Stohl, A. (2017). Impact of dust

deposition on the albedo of Vatnajökull ice cap, Iceland. *The Cryosphere*, *11*(2), 741–754. https://doi.org/10.5194/tc-11-741-2017

Xi, Y., Xu, C., Downey, A., Stevens, R., Bachelder, J. O., King, J., Hayes, P. L., & Bertram, A. K. (2022). Ice nucleating properties of airborne dust from an actively retreating glacier in Yukon, Canada. *Environ. Sci.: Atmos.*, *2*, 714–726. https://doi.org/10.1039/D1EA00101A

Yang, W., Marshak, A., Kostinski, A. B., & Várnai, T. (2013). Shape-induced gravitational sorting of Saharan dust during transatlantic voyage: Evidence from CALIOP lidar depolarization measurements. *Geophysical Research Letters*, *40*(12), 3281–3286. https://doi.org/10.1002/grl.50603

Ye, Y., & Völker, C. (2017). On the Role of Dust-Deposited Lithogenic Particles for Iron Cycling in the Tropical and Subtropical Atlantic. *Global Biogeochemical Cycles*, *31*(10), 1543–1558. https://doi.org/10.1002/2017GB005663

Yoshida, A., Moteki, N., Ohata, S., Mori, T., Tada, R., Dagsson-Waldhauserová, P., & Kondo, Y. (2016). Detection of light-absorbing iron oxide particles using a modified single-particle soot photometer. *Aerosol Science and Technology*, *50*(3), 1–4. https://doi.org/10.1080/02786826.2016.1146402

Young, G., Jones, H. M., Darbyshire, E., Baustian, K. J., McQuaid, J. B., Bower, K. N., Connolly, P. J., Gallagher, M. W., & Choularton, T. W. (2016). Size-segregated compositional analysis of aerosol particles collected in the European Arctic during the ACCACIA campaign. *Atmospheric Chemistry and Physics*, *16*(6), 4063–4079. https://doi.org/10.5194/acp-16-4063-2016

Yu, H., Chin, M., Yuan, T., Bian, H., Remer, L. A., Prospero, J. M., Omar, A., Winker, D., Yang, Y., Zhang, Y., Zhang, Z., & Zhao, C. (2015). The fertilizing role of African dust in the Amazon rainforest: A first multiyear assessment based on data from Cloud-Aerosol Lidar and Infrared Pathfinder Satellite Observations. *Geophysical Research Letters*, *42*(6), 1984–1991. https://doi.org/10.1002/2015GL063040

Yus-Díez, J., Pandolfi, M., González-Flórez, C., Escribano, J., Gonzalez-Romero, J., Ivančič, M., Rigler, M., Klose, M., Kandler, K., Panta, A., Querol, X., Reche, C., Perez García-Pando, C., & Alastuey, A. (2023). *Quantifying variations in multi-wavelength optical properties of freshly-emitted Saharan dust from the Lower Drâa Valley, Moroccan Sahara*.

Zender, C. S., Bian, H., & Newman, D. (2003a). Mineral Dust Entrainment and Deposition (DEAD) model: Description and 1990s dust climatology. *Journal of Geophysical Research: Atmospheres*, *108*(D14). https://doi.org/10.1029/2002JD002775

Zender, C. S., Newman, D., & Torres, O. (2003b). Spatial heterogeneity in aeolian erodibility: Uniform, topographic, geomorphic, and hydrologic hypotheses. *Journal*

of Geophysical Research: Atmospheres, *108*(D17). https://doi.org/10.1029/2002JD003039

Zhang, X. L., Wu, G. J., Zhang, C. L., Xu, T. L., & Zhou, Q. Q. (2015). What is the real role of iron oxides in the optical properties of dust aerosols? *Atmospheric Chemistry and Physics*, *15*(21), 12159–12177. https://doi.org/10.5194/acp-15-12159-2015

Zhao, A., Ryder, C. L., & Wilcox, L. J. (2022). How well do the CMIP6 models simulate dust aerosols? *Atmospheric Chemistry and Physics*, *22*(3), 2095–2119. https://doi.org/10.5194/acp-22-2095-2022

Zhao, X., Huang, K., Fu, J. S., & Abdullaev, S. F. (2022). Long-range transport of Asian dust to the Arctic: identification of transport pathways, evolution of aerosol optical properties, and impact assessment on surface albedo changes. *Atmospheric Chemistry and Physics*, *22*(15), 10389–10407. https://doi.org/10.5194/acp-22-10389-2022

Zimmermann, F., Weinbruch, S., Schütz, L., Hofmann, H., Ebert, M., Kandler, K., & Worringen, A. (2008). Ice nucleation properties of the most abundant mineral dust phases. *Journal of Geophysical Research: Atmospheres*, *113*(D23). https://doi.org/10.1029/2008JD010655

Zubko, N., Muñoz, O., Zubko, E., Gritsevich, M., Escobar-Cerezo, J., Berg, M. J., & Peltoniemi, J. (2019). Light scattering from volcanic-sand particles in deposited and aerosol form. *Atmospheric Environment*, *215*, 116813. https://doi.org/10.1016/j.atmosenv.2019.06.051

Acknowledgement

I'd like to thank my advisor, Prof. Dr. K. Kandler. Firstly, for accepting me as a PhD student and giving me the opportunity to work in FRAGMENT project and secondly, for the supervision of my work. His constant support has helped me immensely in finishing this work. I am equally thankful to my co-advisor, Dr. C. Pérez García-Pando for his excellent mentorship as well as countless discussions.

Likewise, I would like to thank Prof. Dr. M. Bigalke and Prof. Dr. C. Schüth for their willingness to act as examiners for this thesis.

A special thanks to Prof. Dr. S. Weinbruch and Prof. Dr. M. Ebert for answering all of my questions.

My great thanks goes to colleagues Adolfo, Cristina, Jesús, Claudia, Mara, Hannah. We've had lot of adventures together: from working under the "mild" Moroccan sun to "breath-taking" Icelandic dust, we've certainly created life-long memories. I've truly cherished all our moments and am grateful for the time we shared.

Many thanks to the participants of the FRAGMENT and HiLDA field campaigns especially Andres, Martina, Xavier, Cristina, and Kerstin. All these brilliant scientists have taught me that doing good research is a joy. In addition, the comments and advice I have received from my co-authors on the manuscripts has been invaluable and has greatly improved the quality of my work.

Also, I recognize that doing a PhD involves a lot of "fun" aspects: making purchases, handling reimbursements, building instruments, and arranging travel. Thank you Astrid for the administrative support over the years. Many thanks to Thomas for the technical support and for the good times in Iceland. Luciana and Alexis from Barcelona Supercomputing Center, thank you for providing the necessary administrative support.

Last but not least, I would like to thank all past and present members of the Atmospheric Aerosol group: Arya, Andebo, Ayuk, Dani, Janina, Johannes, Kilian, Lisa, Luis, Melanie,

Sadath, and Selina for all the good times and discussions.

Funding support for this dissertation was provided by the project FRontiers in dust mineRAloGical coMposition and its Effects upoN climaTe (FRAGMENT), a European Research Council (ERC) Consolidator Grant funded by the European Union (grant agreement number: 773051).

Darmstadt, 31. August 2023

A.P.